Surface Properties and Electrocatalytic Applications of Metallophthalocyanines confined on Electrode Surfaces

A thesis submitted in fulfillment of the requirement for the degree of

Doctor of Philosophy
of
Rhodes University
by

Isaac Adebayo Akinbulu

November 2010

DEDICATION

This work is dedicated to the glory of God, the source of knowledge, wisdom, understanding and life.

I also dedicate this work to my wife and children:

Juliet Osarhiemen Akinbulu (Mrs)

Caleb Oluwatomisin Akinbulu

and

Timothy Oluwatimileyin Akinbulu

ACKNOWLEDGMENTS

Except the Lord build the house, they labor in vain that build it, except the Lord keep the city, the watchman waketh but in vain (Psalm 127: 1). I appreciate the Lord almighty, for his mercy endureth forever. I give God the glory for his faithfulness and for granting me the perseverance, knowledge, wisdom and understanding to complete this programme.

I appreciate my Supervisor, Prof. Tebello Nyokong, for her positive criticism, guidance and supervision that made this programme a success, thanks.

I appreciate my wife, Juliet Osarhiemen Akinbulu, my children, Caleb Oluwatomisin Akinbulu and Timothy Oluwatimileyin Akinbulu, for their love and support. Your love and support, throughout the programme, can not be measured. You are the pillar upon which this success is built. I am, indeed, very grateful, thanks. I also appreciate my Parents, Mr. Johnson Adeyemi Akinbulu, Mrs. Beatrice Oluwasegun Akinbulu and my in-law, Mr. John Ogbeifun, for their prayer and support. Also, my sincere appreciation goes to my Sister, Janet Ireti Alewi (Mrs), my brother Isaiah Adetunji Akinbulu and all my siblings, for their prayer and support.

I appreciate my family at Rhodes, Lab. S 22, for their support and love; S 22 was indeed home away from home. I say thanks to everyone.

I also appreciate the National Research Foundation of South Africa (NRF) for funding this programme.

I equally appreciate the Department of Chemistry, University of Lagos for study leave.

Finally, my appreciation goes to all the staff of the Department of Chemistry, Rhodes University.

ABSTRACT

New cobalt (**13**, **16 19** and **22**), manganese (**14**, **17**, **20** and **23**) and iron (**15**, **18**, **21** and **24**) phthalocyanine complexes were synthesized and characterized. The UV-Vis spectral properties of the complexes were typical of the nature of central metal and position of substituent on the Pc ligand. Their electrochemical behaviors were signatures of the central metals, with varying influences of the nature and position of substituents. Nano-composite of complex **18** and single walled carbon nanotubes (SWCNTs) (SWCNT-**18**) was fabricated. Formation of this nano-composite was confirmed by infrared (IR) spectroscopy, X-ray diffraction (XRD) spectroscopy and transmission electron microscopy (TEM). Self-assembled monolayers (SAMs) of SWCNT-**18**, complexes **13-15**, **18** and **22-24** were formed on polycrystalline gold disc electrodes, while complexes **17** and **20** were electropolymerized on glassy carbon electrodes (GCE). Complex **14** was also electrodeposited on GCE. Surface properties of the SAMs were consistent with the molecular feature of the substituent and the nature of central metal in the adsorbed species, while those of the MnPc modified GCEs were dependent on point of substitution and number of substituent. The SAM-modified gold electrodes were used for the electrocatalytic oxidation of the carbamate insecticide, carbofuran. Amplification of the current signal of the insecticide, at more energetically feasible oxidation potentials, on the SAM-modified gold electrodes, relative to bare gold electrode, justified electrocatalysis. There was enhanced sensitivity (attributed to the presence of SWCNT) of the SWCNT-**18**-SAM-modified gold electrode towards carbofuran, relative to the signals observed on the other SAMs. Current response of the insecticide, bendiocarb, was also intensified, at more favorable oxidation potentials, on the MnPc (**14** and **17**) modified GCEs, relative to the response on bare GCE, substantiating electrocatalysis. Also, catalysis of the oxidation of the herbicide, bentazon, was observed on polymeric film of complex **20**. The current response of the herbicide on this film was better than that observed on bare GCE. Electrocatalysis of the analytes, on the respective modified electrodes, occurred via closely related mechanisms.

TABLE OF CONTENTS

CHAPTER 4:
SURFACE PROPERTIES OF MODIFIED ELECTRODES

LIST OF ABBREVIATIONS

Ac	=	Acetyl
AFM	=	Atomic force microscopy
CME	=	Chemically modified electrode
CV	=	Cyclic voltammetry
CV	=	Cyclic voltammogram
DBU	=	1,8-diazabicyclo [5.4.0] undec-7-ene
DCC	=	Dicyclohexylcarbodiimide
DCM	=	Dichloromethane
DMA	=	Dimethylacetamide
DMF	=	Dimethylformamide
DMSO	=	Dimethylsulfoxide
EIS	=	Electrochemical impedance spectroscopy
GCE	=	Glassy carbon electrode
HOMO	=	Highest occupied molecular orbital
ICDD	=	International center for diffraction data
IR	=	Infrared
ITO	=	Indium tin oxide
LB	=	*Langmuir-Blodgett*
LMCT	=	Ligand-to-metal charge transfer

LUMO	=	Lowest unoccupied orbital
MLCT	=	Metal-to-ligand charge transfer
MPc	=	Metallophthalocyanine
MPc-SAM	=	Metallophthalocyanine-self assembled monolayer
MWCNTs	=	Multi walled carbon nanotubes
NMR	=	Nuclear magnetic resonance
NIR	=	Near infrared
OTTLE	=	Optically transparent thin layer electrode.
Pc	=	Phthalocyanine
RDE	=	Rotating disc electrode
SAM	=	Self-assembled monolayer
SEM	=	Scanning electron microscopy
SERS	=	Surface enhanced raman spectroscopy
SWCNTs	=	Single walled carbon nanotubes
SWV	=	Square wave voltammetry
$TBABF_4$	=	Tetrabutylammonium tetrafluoroborate
TEM	=	Transmission electron microscopy
THF	=	Tetrahydrofuran
UV-Vis	=	Ultraviolet-visible
UPD	=	Underpotential deposition

LIST OF SYMBOLS

A	=	Electrode surface area in cm^2
α	=	Electron transfer coefficient
ε	=	Extinction coefficient
Γ_{MPc}	=	Surface coverage or concentration of metallophthalocyanine
Γ_{ibf}	=	Ion barrier factor
λ	=	Wavelength in nm
C	=	Molar concentration of analyte
C	=	Columbs
C_{dl}	=	Double layer capacitance
CPE	=	Constant phase element
D	=	Diffusion coefficient
E	=	Potential
E_{pa}	=	Anodic peak potential
E_{pc}	=	Cathodic peak current
$E_{1/2}$	=	Half-wave potential
ΔE	=	Anodic-to-cathodic peak splitting
f	=	Frequency
F	=	Faraday's constant
Hz	=	Hertz

I_L	=	Mass transport limiting current
I_{pa}	=	Anodic peak current
I_{pc}	=	Cathodic peak current
k	=	Heterogeneous reaction rate constant
k_o	=	Standard heterogeneous reaction rate constant
K	=	Kelvin
n	=	Number of electron
Q	=	Quantity of electric charge
Q_{Bare}	=	Integrated electric charge due to bare gold electrode
Q_{SAM}	=	Integrated electric charge due to SAM-modified electrode
R	=	Molar gas constant
R_{CT}	=	Charge transfer resistance
R_S	=	Solution or electrolyte resistance
υ	=	Scan rate
V	=	Volume
V	=	Volts
Z_{im}	=	Imaginary impedance
Z_{re}	=	Real impedance
Z_W	=	Warburg impedance

LIST OF FIGURES

Figure 4.15: SEM images of bare, **18**-SAM and SWCNT-**18**-SAM-modified gold-coated glasses.

LIST OF SCHEMES

LIST OF TABLES

CHAPTER 1

INTRODUCTION

1.1 Basics of Metallophthalocyanines

1.1.1 Discovery

Metallophthalocyanines (MPcs) are some of the most researched molecules in modern chemistry. These versatile macrocyclic compounds have attracted enormous research interest since their discovery almost a century ago. Discovery of these macrocycles was accidental; a blue colored 'impurity' was detected during a synthesis expected to produce colorless products [1]. Preliminary research work revealed that the colored substance was an exceptionally stable pigment, thus encouraging further research interest on other important properties of this interesting material. Linstead and coworkers [2], from Imperial College, London, U.K., pioneered further studies on the elucidation of the molecular structure of this promising pigment. Their findings and that of Dent and Robertson [3-6] became the recipe for further studies that unraveled the enormous potentials of these macrocycles. A review of the general applications and some important properties of these compounds are presented.

1.1.2 Structural properties

Figure 1.1A shows the geometric structure of metallophthalocyanine, elucidated by x-ray diffraction [4]. Metallophthalocyanine is an 18-π-electron aromatic macrocyclic compound, consisting of four isoindole units linked via azamethine bridges. This structure is closely related to that of porphyrin, Figure 1.1B, but with major structural differences. The differences in structural features [7,8] are:

(i) The isoindole units in phthalocyanine (Pc) are replaced with pyrrole units in porphyrin

(ii) The pyrrole units in porphyrin are connected via carbon atoms, in place of the azamethine bridges linking the isoindole units in phthalocyanine.

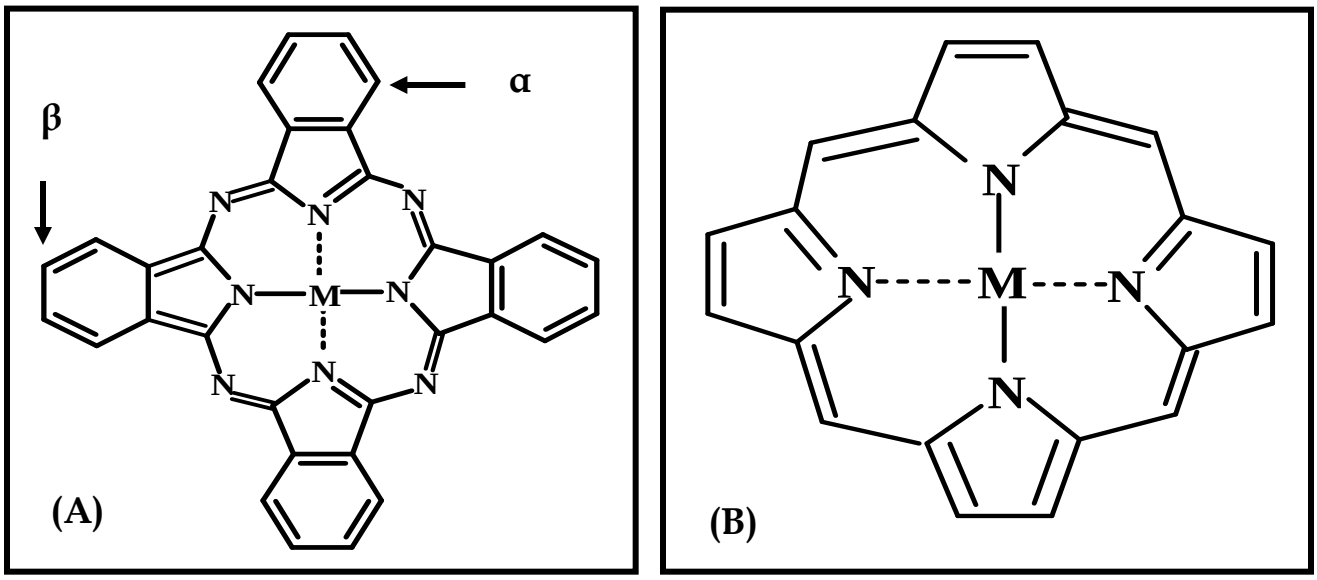

Figure 1.1: Geometric structures of (A) metallophthalocyanine and (B) metalloporphyrin complexes, **M** indicate the central metal in these complexes.

The cavity of phthalocyanine can host different metals, designated **M** in figure 1.1A, while the ring can accommodate different substituents at the peripheral (β) or non-peripheral (α) positions. These give room for considerable architectural flexibility, hence the versatility of these fascinating compounds. The central metal can be in or out of the plane of the macrocycle, depending on its size [9]. The radius of the Pc cavity, which allows minimum strain on the relatively rigid macrocyclic frame, is *ca* 1.90 Å [10]. An atom smaller or larger than this size distorts the conformation of the Pc skeleton, while ring deformation may result from an exceptionally larger atom. Generally, the nature of central atom, position and type of substituent influence the electronic, physical, electrochemical and other important properties of these macrocycles.

1.1.3 General applications

Applications of phthalocyanines can be attributed to their chemical structure, unique electronic property, high degree of aromaticity and architectural flexibility. MPcs are used as dyes and pigments in the paint, printing, paper and textile industries, due to

their intense blue-green color, high dyeing power, chemical inertness, photostability and insolubility in most solvents [11-14]. Most phthalocyanine dyes are derivatives of CuPc. MPc complexes are also employed in catalysis of many chemical reactions [15,16], notably, industrial catalytic desulphurization of gasoline [15,17-19], which makes use of CoPc derivatives. Also, applications of phthalocyanines have been reported in compact disc (CD) technology, electrophotography and ink jet printing [20,21]. Emerging applications of these molecules include their uses as: chemical sensors [22,23], molecular metals [24,25], liquid crystals [26], semiconductors [23], electrochemical sensors [27-29] and non-linear optical limiters [30,31]. Medical applications of MPc complexes have also been reported, like their use in photodynamic therapy of cancer (PDT) [32,33], an alternative method to chemotherapy. Application of MPcs for this purpose relies on their photosensitizing properties and ability to absorb strongly in the far red region of the visible region, where the body tissue is very transparent.

1.1.4 Synthesis

MPc complexes are generally synthesized by condensation reaction involving substituted precursors. This method is cleaner and easier to control, in terms of extent of substitution, compared to direct substitution onto the ring of a preexisting phthalocyanine. Commonly used phthalocyanine precursors are the derivatives of aromatic *ortho*-dicarboxylic acid, such as phthalonitriles (**1**), phthalic acids (**2**), phthalimides (**3**), phthalic anhydrides (**4**), diiminoisoindolines (**5**) and o-cyanobenzamides (**6**) (Figure 1.2). Phthalonitriles are the most useful of these precursors. They can be prepared via many synthetic pathways and can easily undergo condensation reaction to give the desired MPc complexes. Phthalocyanine complexes of most metals, with the exception of silver and mercury, are often obtained in good yields using phthalonitriles (**1**). Heating in the presence of the required metal salt, in suitable high boiling solvent, gives the desired complex. When high premium is attached to purity, phthalonitriles are the most suitable, but most expensive, for the synthesis of MPc complexes. The use of other precursors has some limitations. For instance, MPc

complexes can only be formed from phthalic acids (**2**) and phthalimides (**3**) in the presence of a catalyst, such as ammonium molybdate, and a nitrogen source, like urea. Other limitations of the use of phthalimides and some derivatives of phthalic acid are: formation of unpredictable products and restriction on the type of functional groups required for condensation reaction to occur. Nonetheless, phthalic anhydrides are relatively cheap [4-6,11,34], hence the preferred starting materials for large scale production of phthalocyanines.

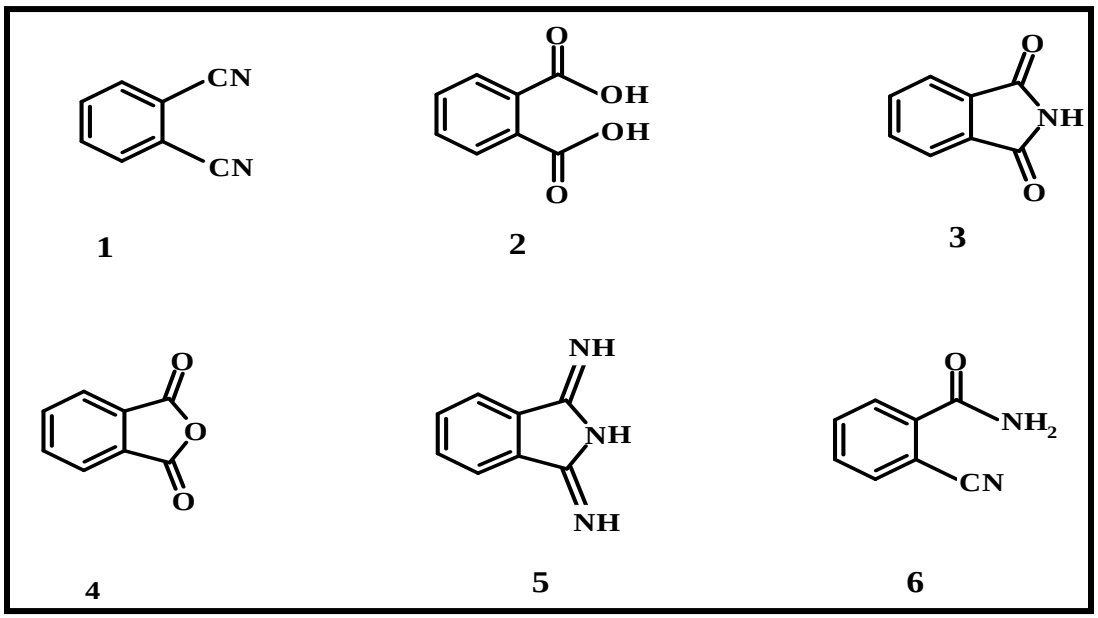

Figure 1.2: Some phthalocyanine precursors

Prior to synthesis, substituted phthalonitriles are modified, depending on the substituent to be introduced onto the phthalocyanine ligand. Modifications are normally effected via nucleophilic aromatic substitution reaction. Electron-withdrawing nature of the two nitrile groups increases the susceptibility of phthalonitriles to nucleophilic attack. Apart from the presence of appropriate (good) leaving group (NO_2 for mono-substituted phthalonitriles, **7**, and Cl for disubstituted phthalonitriles, **9**) (Scheme 1.1), the success of this reaction is equally dependent on the degree of nucleophilicity of the desired substituent. Commonly used nucleophilic substituents are

alcohols [35-37], amines [38-40] and thiols [31,41,42]. The nucleophilic substituents employed in this work are thiols (**8**, **10** and **12**) (Scheme 1.1). Monosubstituted phthalonitriles are traditionally employed as precursors for tetra- (non-peripheral **7**, or peripheral **9**) and disubstituted phthalonitriles for octa-substituted MPc complexes.

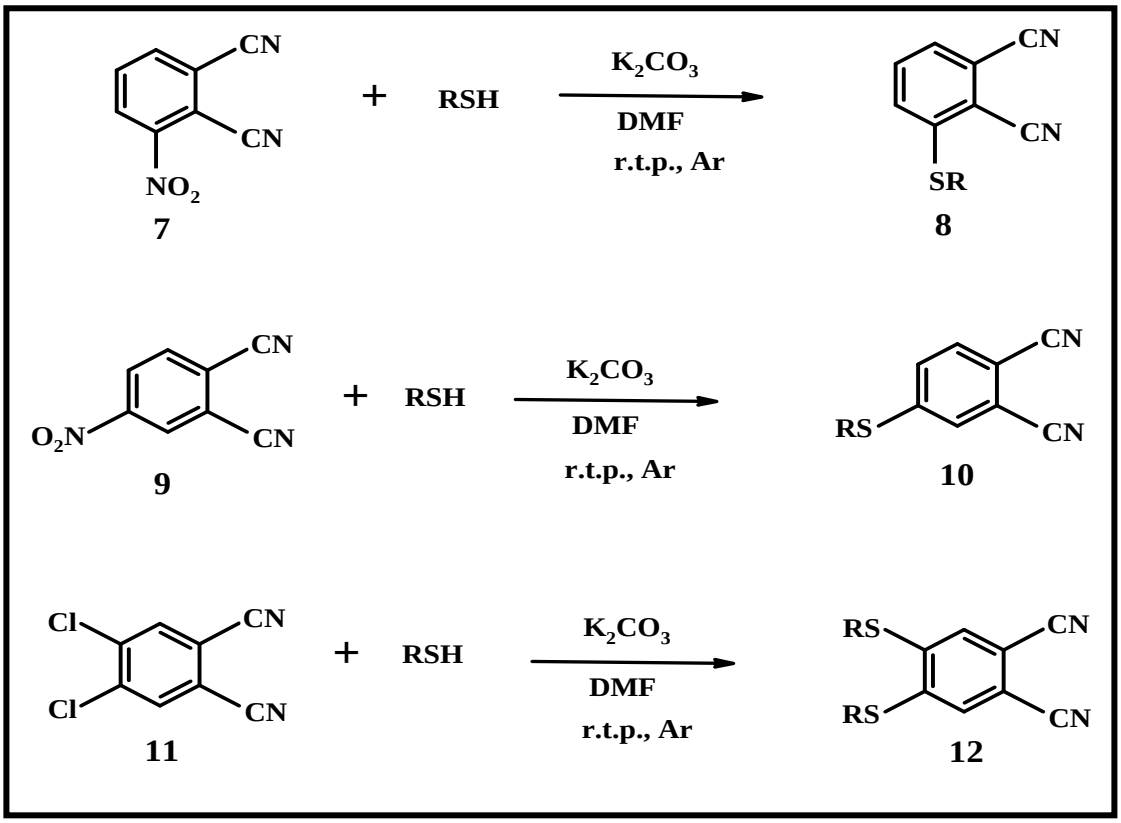

Scheme 1.1: Synthesis of substituted phthalonitriles

Phthalonitriles substituted with the appropriate functionalities are converted to the desired MPc complexes, in the presence of suitable metal salts via a metal template assisted cyclotetrametrization reaction, at elevated temperature. Scheme 1.2 shows generalized synthetic pathways for the thio-derivatised MPc complexes used in this work. Mechanism of formation involves stepwise combination of phthalonitrile precursors or reactive intermediate, coordination of the central metal ion, and ring cyclisation to form the desired complex [43-47]. High boiling solvents, such as chlorobenzene, quinoline and nitrobenzene are the solvents of choice for the synthesis

of MPc complexes. Refluxing pentan-1-ol or similar alcohol, in the presence of an organic base, such as 1,8-diazabicyclo[5.4.0]undec-7-ene (DBU), Piperidine, or cyclohexylamine [43,48,49], can also be employed for the synthesis of MPc complexes. In this work, the solvent employed for synthesis is 2-(diethylaminoethanol).

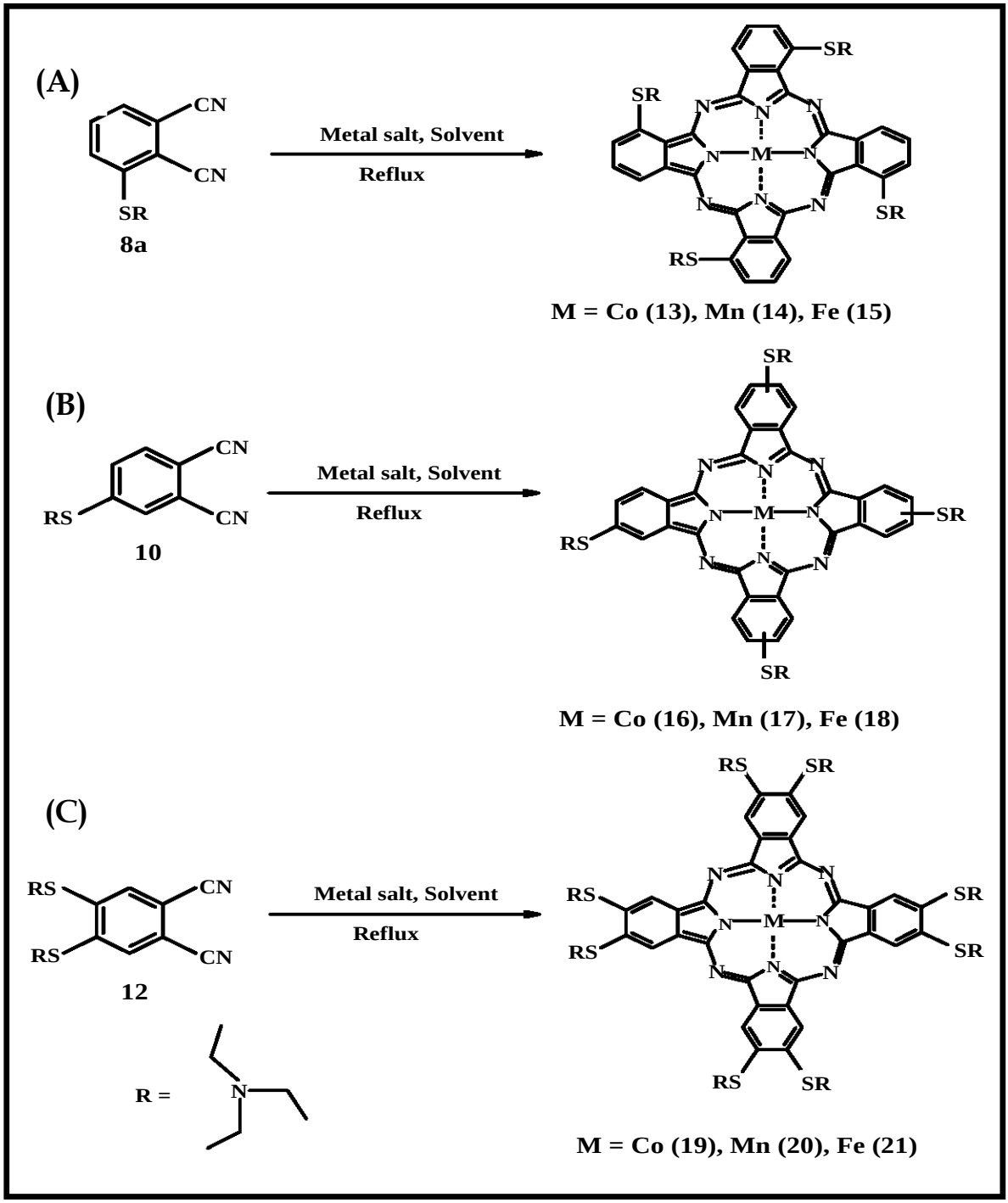

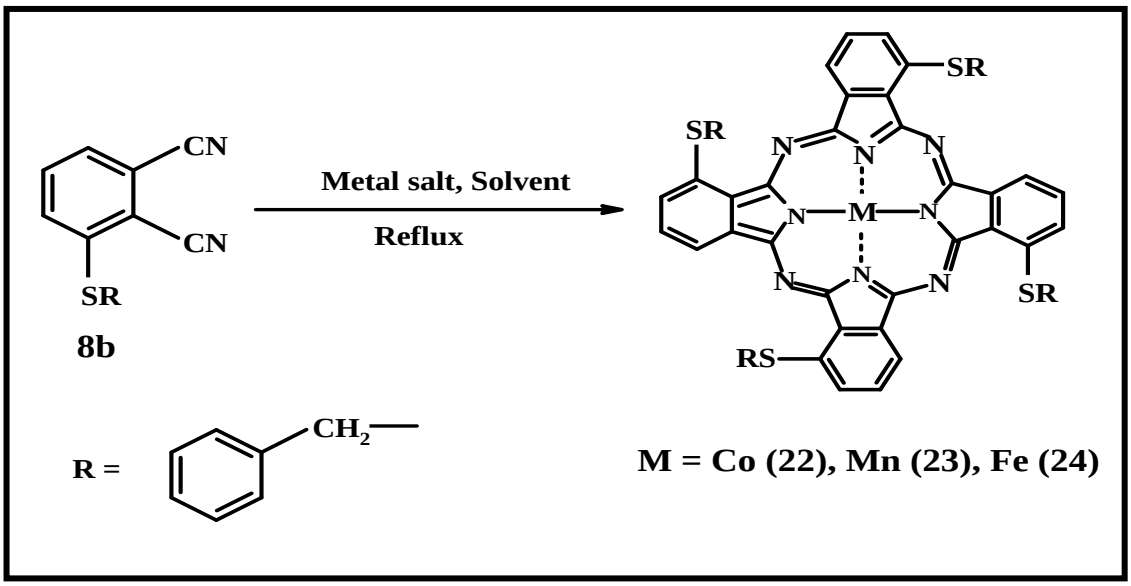

Scheme 1.2: Generalized synthetic pathways for (A) non-peripherally tetra-substituted, (B) peripherally tetra-substituted, and (C) peripherally octa-substituted alkylthio- and (D) non-peripherally tetra-substituted arylthio derivatised metallophthalocyanine complexes.

Purification of phthalocyanines can be achieved using different methods. Very often, the method is determined by the expected degree of purity, stability and solubility in certain organic solvents. Ultra-purity can be attained by sublimation at temperatures up to 600°C in vacuo [13,50,51]. This method relies extensively on the remarkable thermal stability of these macrocycles. Purification can also be achieved by recrystallisation. Sparingly soluble metal free and metal complexes of phthalocyanines can be purified by this method in high-boiling aromatic solvents (such as 1-chloronaphthalene and quinoline) [13,20,50]. Coordinating solvent, such as pyridine, can also be used for recrystallisation of unsubstituted Pcs containing suitable metal ions (e.g. Zn^{2+}, Co^{2+}, Fe^{2+}, Ru^{2+} etc.). Chromatographic methods are also fashionable purification strategies for MPcs.

MPc complexes are generally characterized using classical methods employed for organic compounds, including elemental analysis, infra-red (IR) and ultraviolet-visible (UV-Vis) spectroscopies. Single crystal X-ray analysis has also proved invaluable in

structural characterization of phthalocyanines [4,5,52,53]. Nuclear magnetic resonance (NMR) spectroscopy is also a very reliable analytical technique for structural elucidation, especially for more soluble MPc complexes. Major limitation of the use of NMR is broadening of signals, due to the strong tendency of MPcs to aggregate in solution. Interestingly, choice of solvent (e.g. d_6-benzene or d_5-pyridine), reduced aggregation and high temperature [54] can improve the quality of NMR spectra of MPc complexes. Mass spectrometry has also become an indispensable technique for characterization of MPcs, complimenting other methods discussed above. Field desorption (FD) [55,56], fast atom bombardment (FAB) [57] and matrix-assisted laser desorption ionization (MALDI) [58-60] mass spectrometry methods have been employed.

1.1.5 Absorption spectra of metallophthalocyanines

Electronic transitions in metallophthalocyanines are characterized by the presence of intense band (Q-band) in the red end (near 700 nm) of the visible region (or near-IR for some derivatives) of the electromagnetic spectrum and less-intense band (B-band) in the blue end (near 350 nm) (Figure 1.3A). The B-band is made up of two transitions: B1 and B2. There is also the possibility of other $\pi \rightarrow \pi^*$ transitions (N, L and C), at lower wavelength than the B transitions [61]. The model employed for the interpretation of electronic transitions in metalloporphyrins, proposed by Gouterman and coworkers [62], has been modified to explain the origin of the spectra of metallophthalocyanines. Unlike metallophthalocyanines, electronic transitions in metalloporphyrins are characterized by weak Q-band and intense B-band (near 410 nm) (Figure 1.3B).

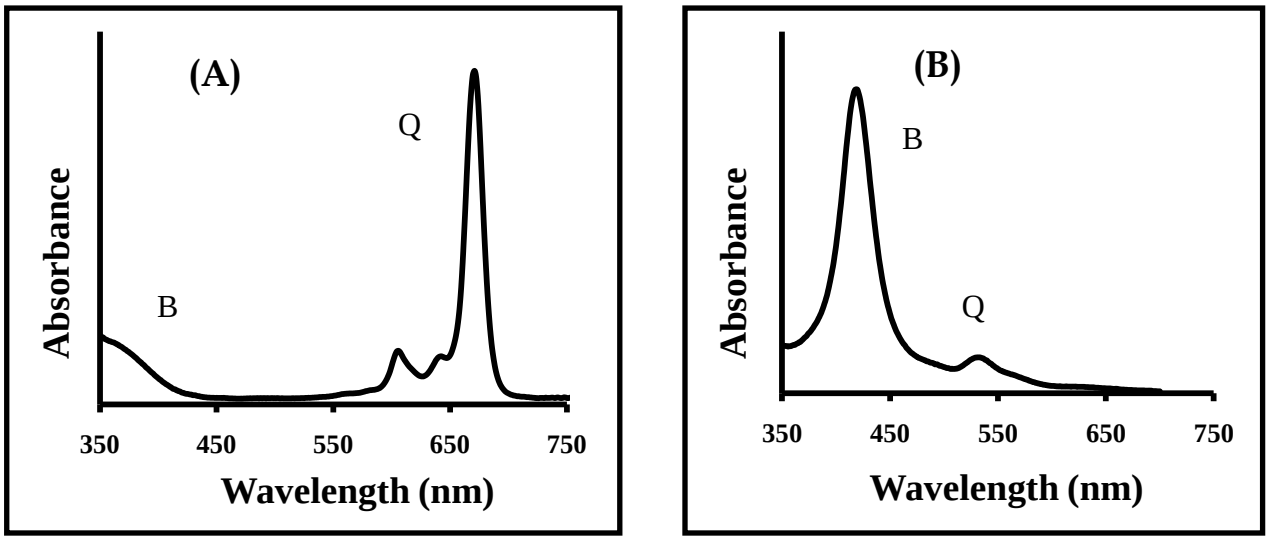

Figure 1.3: Characteristic electronic absorption spectra of (A) metallophthalocyanine and (B) metalloporphyrin

Gouterman *et al* [62] used a 4-orbital model (Figure 1.4), based on linear combination of atomic orbitals (LCAO), to account for the electronic properties of porphyrins. The optical spectrum of phthalocyanine is explained using a modified form of this model. Electronic transitions in these macrocycles (phthalocyanine and porphyrin) are essentially governed by the energies of the highest occupied molecular orbital (HOMO) and the lowest unoccupied molecular orbital (LUMO), which is influenced by the symmetry of these molecules. Generally, metal-free Pcs are of lower symmetry (D_{2h}) than their metallated analogues (D_{4h}). D_{2h} symmetry is associated with a split Q-band [63], due to transitions from $1a_{1u}$ of the HOMO to a non-degenerate $1e_g^*$ of the LUMO, while a single Q-band (due to a degenerate $1e_g^*$ of the LUMO) is characteristic of D_{4h} symmetry.

Apart from enhanced intensity, Q-band in phthalocyanine is relatively red-shifted compared to that of porphyrin (Figure 1.3). This is attributed to longer conjugated pathway around the 18-π system of the inner 16-atom phthalocyanine ring, compared to porphyrin (Figure 1.1). Position of Q-band in MPc complexes can be affected by (i) nature of central metal, (ii) type of solvent, (iii) presence of axial ligand, (iv) nature of

substituent, and (v) expansion of the conjugated π-system of the Pc ring [63-66]. Specifically, ring expansion, electron-releasing substituents (substituents containing nitrogen and sulphur), axial ligation and metals, such as manganese [67,68] and titanium [69,70], give red-shifted Q-band in MPc complexes.

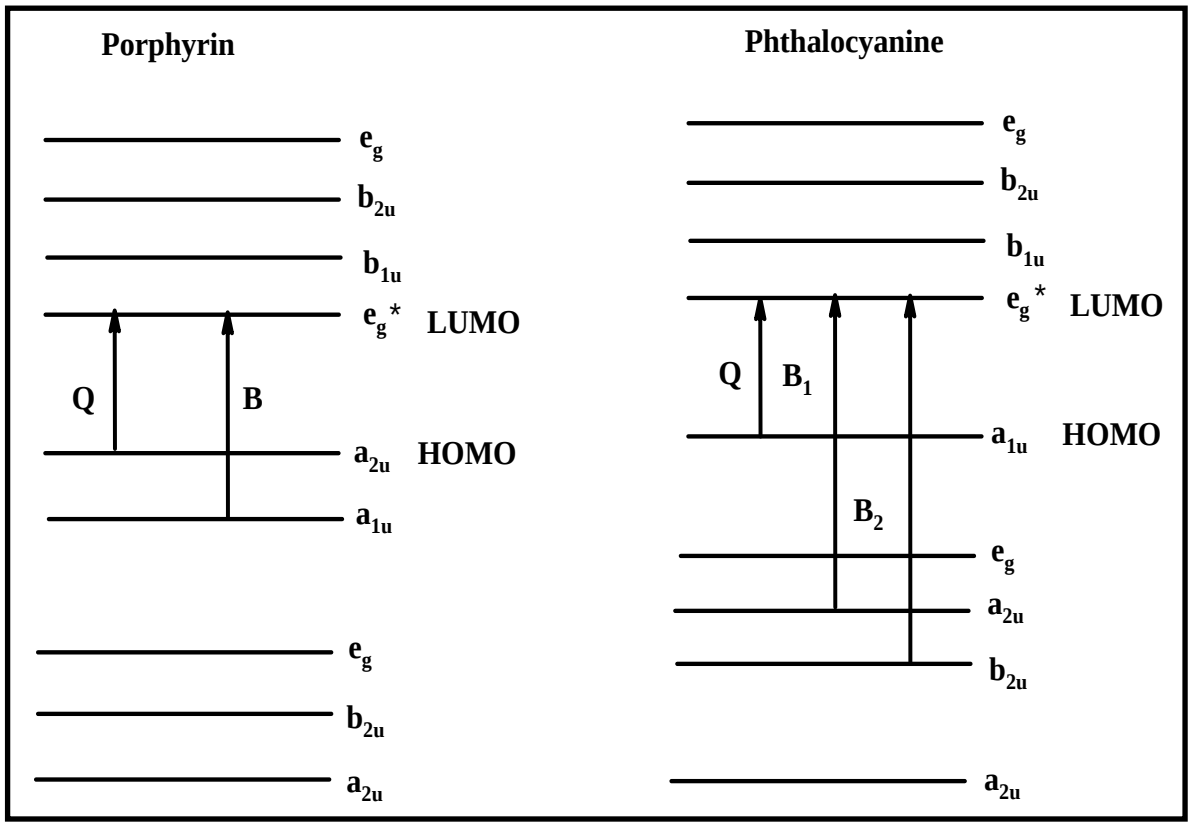

Figure 1.4: Gouterman's four-orbital description of electronic transitions in metalloporphyrin and metallophthalocyanine [62]

Electronic transitions in MPcs are not limited to the π → π* transitions discussed above, vibronic components, metal-to-ligand (MLCT) or ligand-to-metal charge transfer (LMCT) (in the 400-500 nm region) [71,72] may occur. MLCT and LMCT (Figure 1.5) [73] are usually observed in phthalocyanine complexes containing metals such as Co, Mn, Fe and Cr, whose energy levels lie between the HOMO-LUMO energy envelope of the Pc ring.

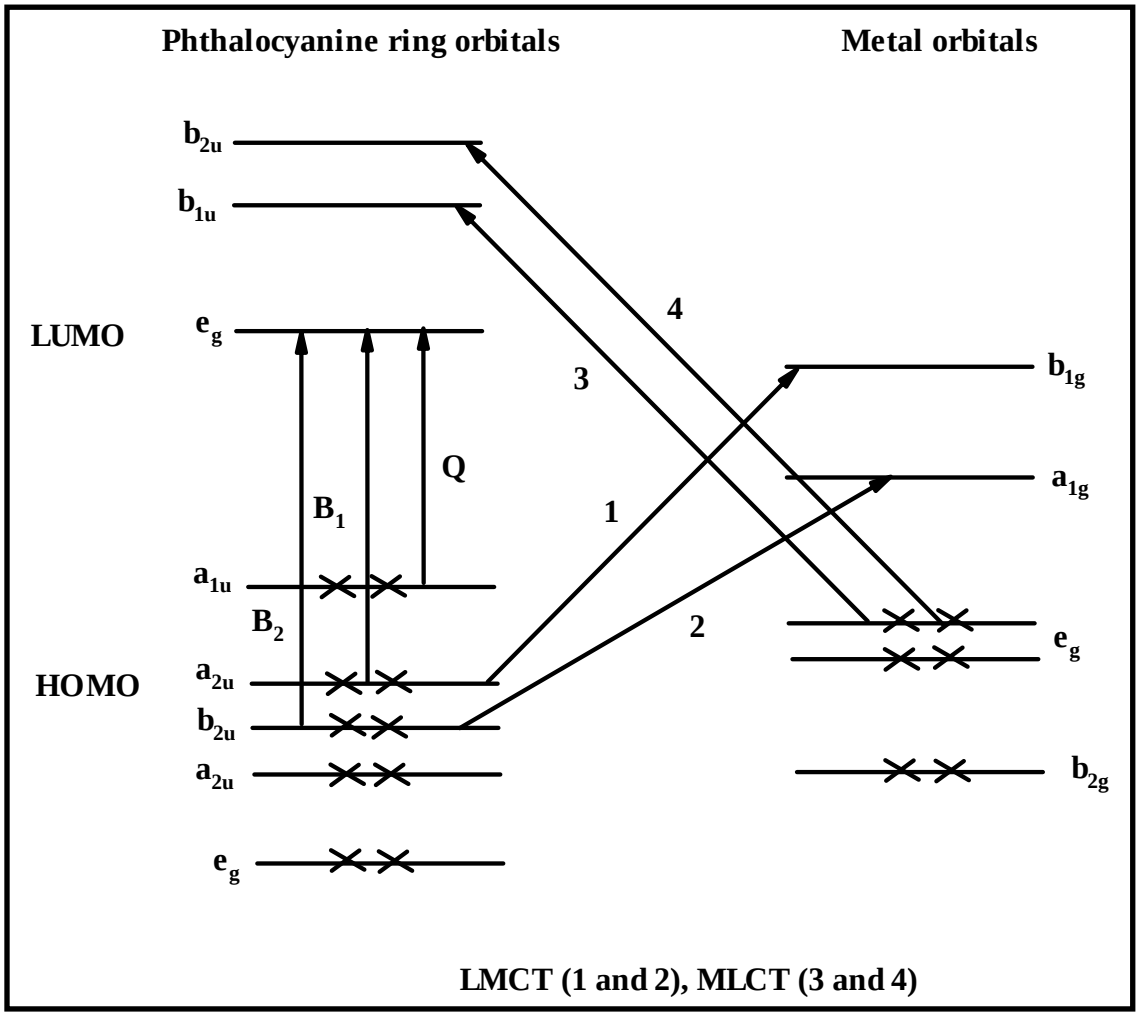

Figure 1.5: Charge transfer transitions in metallophthalocyanine complex

1.1.6 Electrochemical properties of Metallophthalocyanines

Electroactivity of metal-free phthalocyanine (H_2Pc) and that of the metallated analogues is, undoubtedly, why these macrocyclic compounds are the candidates of choice in the design of electrochemical sensors and fabrication of chemically modified electrodes (CMEs). The molecular orbital system in Figure 1.4 is relevant in explaining the redox behavior of these macrocycles. Essentially, the Pc ligand is divalent negative (Pc^{2-}). It can be oxidized to Pc^{1-} and Pc^{0} by successive loss of two electrons from the $1a_{1u}$ of the

HOMO, while reduction is effected by addition of four electrons, in succession, to the doubly degenerate e_g of the LUMO, to give Pc^{3-}, Pc^{4-}, Pc^{5-} and Pc^{6-}.

Phthalocyanine complexes of electroactive metals (such as Ag, Cr, Co, Fe, Mn, Rh, etc) have richer redox chemistry, due to the involvement of both the central metals and the Pc ring. Redox properties of these metal ions can be attributed to their vacant or partially filled d-orbitals, and favorable energies of these orbitals, relative to that of the π-orbital of the Pc ring. In Pc complexes containing redox inactive metals (such as Zn, Al, Ba, Cd, Ge, Mg, Pb, etc), redox activities are restricted to the ring, thus limiting their electrocatalytic relevance. Electrochemical properties of MPc complexes can be influenced by the nature of central metal, type of solvent, position (peripheral or non-peripheral) and nature of substituent (electron-donating or electron-withdrawing), among others. MPc complexes with substituents bearing sulphur and nitrogen groups are frequently employed in the fabrication of CMEs, via self-assembly and electrochemical polymerization, thus the interest in the electrochemical properties of these complexes [74-76]. Electrochemical properties of new thio-substituted Co (**13**, **16**, **19** and **22**) Mn (**14**, **17**, **20** and **23**) and Fe (**15**, **18**, **21** and **24**) phthalocyanine complexes (Scheme 1.2) are reported in this work.

1.1.6.1 Electrochemical properties of cobalt phthalocyanine complexes

Cobalt phthalocyanines (CoPc) are the most extensively studied metal complexes of phthalocyanines [77-79] because of their potential use as electrocatalysts and for the design of electrochemical sensors; which are encouraged by the interesting coordination chemistry of cobalt. Cobalt exhibits three oxidation states: Co^{I}, Co^{II} and Co^{III}. Co^{I} does not bind any axial ligand; hence exist essentially in a square planar environment. Co^{II} does bind axial ligands but with low affinity, which suggests this species may exhibit coordination number of (i) four (square planar), (ii) five (penta-coordinate) and rarely (iii) six (hexa-coordinate). Co^{III} has high affinity for axial ligands and is usually stabilized by two axial ligands; hence exist predominantly in an octahedral

environment. Axial ligation has direct effect on the solution electrochemistry of CoPc complexes. $Co^{I}Pc^{2-}$ and $Co^{II}Pc^{2-}$ species can be observed in both coordinating and non-coordinating solvents but $Co^{III}Pc^{2-}$ species is normally observed in coordinating solvents, such as dimethyl sulphoxide (DMSO), dimethylformamide (DMF) and pyridine (Py). These solvents coordinate, as ligands, to the coordination sites on Co^{III}, offering significant stability to this oxidation state, hence the possibility of observing $Co^{III}Pc^{2-}$ species in solution. Apart from coordinating solvents, Co^{III} ion can also be stabilized through axial ligation of anionic species, such as cyanide, halogen and hydroxide. This suggests that the type of electrolyte in solution may significantly affect the electrochemical properties of CoPc complexes. Like all phthalocyanine complexes containing electroactive metals, redox activities are not restricted to the metal in CoPc. The formation of $Co^{III}Pc^{2-}$ species is usually followed by the first ring oxidation (formation of $Co^{III}Pc^{1-}$ species); while the first ring reduction (formation of $Co^{I}Pc^{3-}$ species) is preceded by the formation of $Co^{I}Pc^{2-}$ species. Generally, the first reduction process in CoPc is metal-centered, since reduction of Pc^{2-} to Pc^{3-} is much more difficult than the reduction of Co^{II} [80].

Table 1.1 shows the electrochemical data of some reported CoPc complexes, with substituents containing sulphur group [74,81,82]. Thio-substituted CoPc complexes are still limited; hence the relevance of their study in this work. Table 1.1 suggests that oxidative processes are more energetically feasible with the alkylthio-derivatised complexes than their arylthio-substituted analogues. This explains the preference of the former to the latter in most of the oxidative electrocatalytic processes (discussed later) investigated in this work. The observed trend in Table 1.1 may be attributed to the electron-withdrawing nature of the benzyl group of the arylthio substituent. Nonetheless, presence of sulphur-bearing substituents satisfies a necessary condition for the formation of self-assembled monolayer (SAM) of each of the complexes on gold electrode. Interestingly, the alkylthio-derivatised MPc complexes reported in this work (**13-21**) have both nitrogen and sulphur-bearing substituent (2-diethylaminoethanethio)

(Scheme 1.2), encouraging polymer formation, via the oxidation of the nitrogen group, in addition to the prospect of forming SAMs of the complexes on gold electrode. Electrochemical properties of CoPc complexes containing this substituent are reported for the first time in this work. The zinc analogue has been reported [83], but unsuitable for electrocatalytic application due to the redox inactivity of Zn.

Table 1.1: Electrochemical data of some aryl- and alkylthio-substituted CoPc complexes, values in V vs. Ag|AgCl

Complex	$Co^{I}Pc^{-2}$/ $Co^{I}Pc^{-3}$	$Co^{II}P^{-2}$/ $Co^{I}Pc^{-2}$	$Co^{III}Pc^{-2}$/ $Co^{II}Pc^{-2}$	$Co^{III}Pc^{-1}$/ $Co^{III}Pc^{-2}$	Solvent	Reference
CoOBMPc	-0.58	-0.10	+0.72	+1.16	DMF	81
CoTDMPc		-0.46	+0.44	+0.66	DCM	74
CoOBTPc	-1.07	-0.38	+0.40	+0.77	DMF	82
$CoTBMPc^{\beta}$	-1.41	-0.38	+0.42	+0.89	DMF	74

OBM = octa benzylmercapto, TDM = tetra dodecylmercapto, OBT = octa butylthio and Pc = phthalocyanine.

1.1.6.2 Electrochemical properties of manganese phthalocyanine complexes

Electrochemical properties of manganese phthalocyanine (MnPc) complexes have also generated considerable interest [84-86]. Variable oxidation states of Mn (Mn^{I}, Mn^{II}, Mn^{III} and Mn^{IV}) [87-89] makes MnPc complexes attractive for electrocatalytic purposes. $Mn^{II}Pc^{2-}$ gets readily oxidized to $Mn^{III}Pc^{2-}$ at moderate potential, varying from -0.08 to -0.15 V in many coordinating solvents (DMSO, DMF and Py). Apart from recent reports [67,90], oxidation of $Mn^{III}Pc^{2-}$ to $Mn^{IV}Pc^{2-}$ rarely occurs; conversion of Pc^{2-} to Pc^{1-} is normally favored. Reduction of $Mn^{II}Pc^{2-}$ species is still a subject of debate; ring reduction

(formation of $Mn^{II}Pc^{3-}$) [67] and reduction of the central metal (formation of $Mn^{I}Pc^{2-}$) [91] have been reported. Formation of MnPc μ-oxo complex [92] is also a major feature of the electrochemical properties of MnPc complexes, especially in an oxygen-rich solution of

$$PcMn^{II} + O_2 \rightleftharpoons PcMn^{III}(O_2) \quad 1.1$$

$$PcMn^{III}(O_2) + PcMn^{II} \rightleftharpoons PcMn^{III}\text{-}O_2\text{-}Mn^{III}Pc \quad 1.2$$

$$PcMn^{III}\text{-}O_2\text{-}Mn^{III}Pc \rightleftharpoons 2PcMn^{IV}O \quad 1.3$$

$$2PcMn^{IV}O + 2PcMn^{II} \rightleftharpoons 2PcMn^{III}\text{-}O\text{-}Mn^{III}Pc \quad 1.4$$

$$4PcMn^{II} + O_2 \longrightarrow 2PcMn^{III}\text{-}O\text{-}Mn^{III}Pc \text{ (Net equation)} \quad 1.5$$

Table 1.2: Electrochemical data of some aryl- and alkylthio substituted MnPc complexes, values in V vs. Ag | AgCl

Complex	$Mn^{II}Pc^{-2}$/ $Mn^{II}Pc^{-2}$	$Mn^{III}Pc^{-2}$/ $Mn^{II}Pc^{-2}$	$Mn^{IV}Pc^{-2}$/ $Mn^{III}Pc^{-2}$	$Mn^{III}Pc^{-1}$/ $Mn^{III}Pc^{-2}$	$Mn^{IV}Pc^{-1}$/ $Mn^{III}Pc^{-2}$	Reference
[a]MnTMPyPc		-0.06		+1.34		94
[a]MnOPTPc	-1.24	-0.46	+0.47		+0.75	90
[a]MnTBMPcβ	-0.98	-0.26		+0.83		95
[b]MnTHTPcα	-1.45	-0.16		+1.03		96
[b]MnTHTPcβ	-1.34	-0.16		+1.00		96

TMPy = tetra mercaptopyridine, OPT = octa pentylthio, TBM = tetra benzylmercapto, THT = tetrakis (6-hydroxyhexylthio), Pc = phthalocyanine, [a]Values recorded in DCM, [b]Value recorded in DMSO, using SCE as reference electrode.

MnPc in DMF. This process is triggered by the transformation of $Mn^{II}Pc^{2-}$ species to an oxygen adduct (equation 1.1). Further transformations generate the species in equations 1.2-1.4, with the overall process represented by (equation 1.5) [93]. Electrochemical data of some aryl- and alkylthio substituted MnPc complexes is shown in Table 1.2 [90,94-96]. Like their Co derivatives, thio-substituted MnPc complexes are still limited, hence their relevance in this work. As discussed above for CoPc complexes, MnPc complexes containing diethylaminoethanethio substituent, with the dual attribute of facilitating SAM and polymer formation, are reported here for the first time.

1.1.6.3 Electrochemical properties of iron phthalocyanine complexes

Like the cobalt analogues, electrochemical properties of iron phthalocyanine (FePc) complexes have been extensively investigated [84,97-99]. Redox behaviors of FePc complexes can be influenced by solvents and electrolytes (as axial ligands). $Fe^{II}Pc^{2-}$ species is predominantly an octahedral complex in coordinating solvents, such as dimethylacetamide (DMA), dimethylformamide (DMF), pyridine (Py) and dimethylsulfoxide (DMSO) [99,100]. The ease of oxidation of $Fe^{II}Pc^{2-}$ to $Fe^{III}Pc^{2-}$ is dependent on the anion in solution. This process is more energetically feasible (occurs at more negative potential) in the presence of Cl^- or OH^-, which offers more stability than ClO_4^-. Further oxidation occurs on the ring in FePc complexes, forming the $Fe^{III}Pc^{1-}$ species. Two reduction processes are usually observed for $Fe^{II}Pc^{2-}$. Metal reduction (formation of penta-coordinate $Fe^{I}Pc^{2-}$ species) is normally followed by ring reduction (Pc^{2-} to Pc^{3-}) [100]. Table 1.3 shows the electrochemical data of some aryl- and alkylthio substituted FePc complexes [74,81,82]. Studies on thio-substituted FePc complexes are also limited, as highlighted above for the Co and Mn derivatives, hence the importance of their study in this work. Like the CoPc and MnPc complexes, electrochemical properties of diethylaminoethanethio substituted FePc complexes are reported for the first time in this work.

Table 1.3: Electrochemical data of some aryl- and alkylthio substituted FePc complexes, values in V vs. Ag|AgCl

Complex	$Fe^{I}Pc^{-2}$/ $Fe^{I}Pc^{-3}$	$Fe^{II}Pc^{-2}$/ $Fe^{I}Pc^{-2}$	$Fe^{III}Pc^{-2}$/ $Fe^{II}Pc^{-2}$	$Fe^{III}Pc^{-1}$/ $Fe^{III}Pc^{-2}$	Solvent	Reference
FeOBMPc	-0.70	-0.26	+0.25	+0.60	DMF	81
FeTBMPc	-078	-0.37	+0.36	+0.70	DMF	74
FeTDMPc	-0.84	-0.53	+0.62	+1.01	DCM	74
FeOBTPc	-1.00	-0.49	+0.26	+0.90	DMF	82

OBM = octa benzylmercapto, TBM = tetra benzylmercapto, OBT = octa butylthio, TDM = tetra dodecylmercapto and Pc = phthalocyanine

1.1.6.4 Spectroelectrochemical properties of metallophthalocyanines

Electronic transitions in MPc complexes are influenced by the oxidation states of the central metal and that of the Pc ligand. Thus, useful information can be obtained from UV-Vis spectroscopic measurements hyphenated to an electrochemical system. This is the basis of spectroelectrochemistry. Comparative analysis of the spectral properties of the starting complex and that of the electro-generated species provides valuable information on the nature of redox processes. In this work, effects of the nature and position of substituent on the resolution of such spectral transformations are investigated for the CoPc complexes. Contributions of the manganese μ-oxo species to the quality of spectral changes, and how these are affected by point of substitution, are also investigated for the MnPc analogues. Possible spectral transformations during spectroelectrochemical experiment include: shift in position or collapse of Q-band and

emergence of new bands, depending on whether the electrochemical process involved is ligand-based or metal-centered.

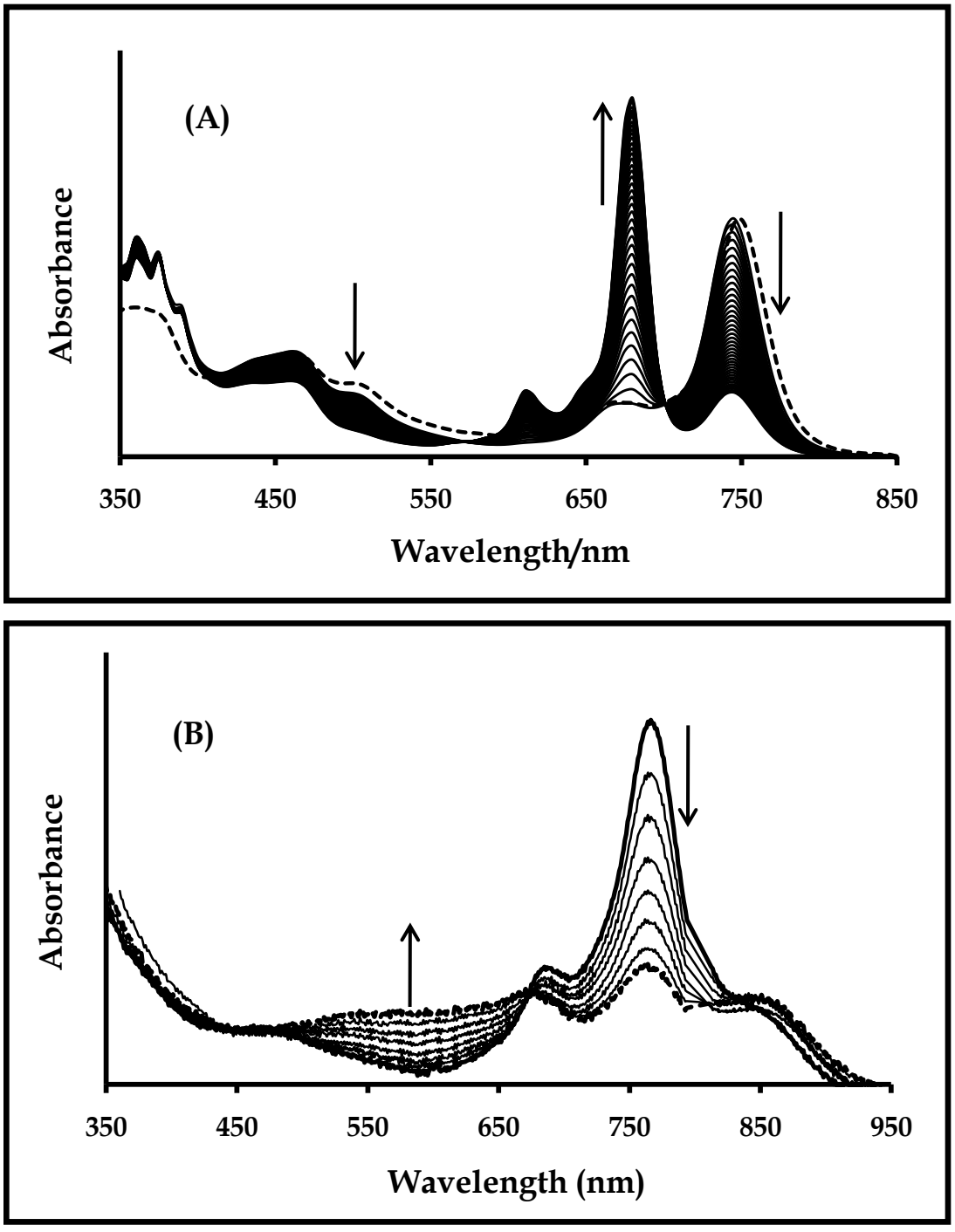

Figure 1.6: Spectral transformations showing (A) reduction of $Mn^{III}Pc$ to $Mn^{II}Pc$ [101] and (B) ring reduction (Pc^{-2} to Pc^{-3}) [102].

Metal oxidation or reduction results in shift in Q-band position (Figure 1.6A) [101] and change in color of the solution (green to blue for CoPc and FePc, and brown to green for MnPc). In some MnPc complexes, a strong new peak in the 500 nm region is characteristic of the formation of $Mn^{I}Pc$ species [91]. Reduction of the Pc ring (formation of Pc^{-3} species) results in collapse of Q-band and new weak peaks in the 500-600 nm region (Figure 1.6B) [102], while emergence of new weak peak around 500 nm, in addition to the collapse of Q-band, is typical of ring oxidation (formation of Pc^{-1} species).

1.1.7 Aims of this thesis

The main focus of this thesis is to exploit the electrocatalytic properties of some aryl- and alkylthio- substituted Co, Mn and Fe phthalocyanine complexes (Scheme 1.2), with the aim of fabricating (using self assembly and electrochemical polymerization techniques) sensitive and selective electrochemical sensing surfaces, for detection of pesticides of environmental importance; carbofuran, bendiocarb and bentazon. Also, this work investigates the possibility of enhancing the sensitivity of these surfaces, by covalent integration of the remarkable electronic attributes of single walled carbon nanotubes, within the limit of the electrocatalytic domain of one of the iron analogues of the complexes studied.

1.2 Chemically Modified Electrodes (CMEs)

A chemically modified electrode (CME) is an electrode having a chemical substance (organic or inorganic), deliberately immobilized on its surface, such that it exhibits the chemical, electrochemical, optical, and other important properties of the immobilized molecule(s). The pioneering works of Hubbard and coworkers [103,104], Murray and coworkers [105] and Millar *et al* [106] unraveled the enormous potentials of CMEs and initiated a wide area of research in this field [107-111]. Chemical modification offers the possibility of intelligently reconstructing the surface of conventional electrodes, to enhance their functionality, by making use of the intrinsic properties of the modifier for selective electrochemical reactions. Usually, chemical modifiers of interest in

electroanalysis are: organic redox compounds, organometallic redox complexes (like MPcs), conducting polymers and fine metallic particles. Chemical modification increases heterogeneous electron transfer rates of solution species (analytes), for which electron transfer process is thermodynamically possible, but kinetically limited. Kinetic limitation is attributed to high overpotentials associated with redox processes involving such species on bare electrodes. Surface modification does not necessarily incorporate the electronic orbital system of the surface-immobilized species into the conduction band of the electrodes, but electron transfer rates are customarily fast for these species, because of their close proximity to the electronically conducting electrodes. This enhances their ability to mediate, via surfaced-confined redox couples, in electron transfer processes involving the electrodes and the analytes. Efficient mediatory role encompasses: (i) electrochemical reversibility, (ii) fast electron transfer between mediator, electrode and analyte, and (iii) chemical stability in the reaction environment. In this work, gold and glassy carbon electrodes are chemically modified with redox active MPc complexes, using suitable modification strategies (discussed below), to enhance the electrodes' sensitivity towards the analytes of interest.

1.2.1 General Methods of Electrode Modification

There are various strategies for modifying electrode surfaces, depending on the nature of the electrode (substrate), molecular identity of the modifier, and proposed application of the modified electrode, among others. The *Langmuir-Blodgett* (LB) method is the oldest technique of constructing molecular assemblies on solid substrate (e.g. glass). This method has been adopted in the formation of thin films of MPc on solid substrates [112,113]. CMEs can also be fabricated by layer-by-layer assemblies of thin films. This method is particular attractive in the formation of inorganic and composite films on electrodes [114-117]. Another method of constructing CMEs is the use of organic polymers as chemical modifiers. Electronically conducting polymers, such as polypyrrole, polythiophene, polyaniline, and their derivatives, can easily be formed on suitable electrodes by oxidative polymerization of the corresponding monomers. The

polymers could be doped with appropriate inorganic ions [118-120], organic compounds [121,122], heteropolyanions [123-126], and metal complexes [127-129], thus the attraction for their use as chemical modifiers. Doping incorporates the specials attributes of the dopants to the conducting polymers. Conducting polymers of MPc complexes have been employed in the fabrication of CMEs by electrochemical polymerization [76,130-132]. Formation of polymeric films of MPc complexes is facilitated by the presence of substituents containing oxidizable groups (sulphur and nitrogen atoms). Another widely used method of electrode modification is the self-assembly technique. This method is especially popular because it is one of the simplest and easiest methods of fabricating CMEs. The affinity of sulfur for metal electrodes (such as Au, Hg and Pt) promotes the popularity and simplicity of this method. Electrochemical polymerization and self-assembly methods are employed for electrode modification in this work. A general overview of these two methods is presented

1.2.2 Overview of Self-assembly Technique

A self-assembled monolayer (SAM) is a single molecular layer in which the constituents share similar orientation. SAMs are formed by adsorption of molecules, via covalent bond formation, onto a suitable substrate from a homogeneous solution. This monolayer is highly organized and stable, due to the affinity of the head group for the substrate and possible interactions between closely packed tail groups (Figure 1.7). Construction of CMEs by self-assembly technique is not new, but this method was popularized by the series of works published by Sagiv and coworkers [133-135], on highly stable SAMs of alkanesilanes, formed on glass and aluminium oxide substrates. Thio-substituted MPc complexes are employed in this study, a general overview of their SAMs is presented.

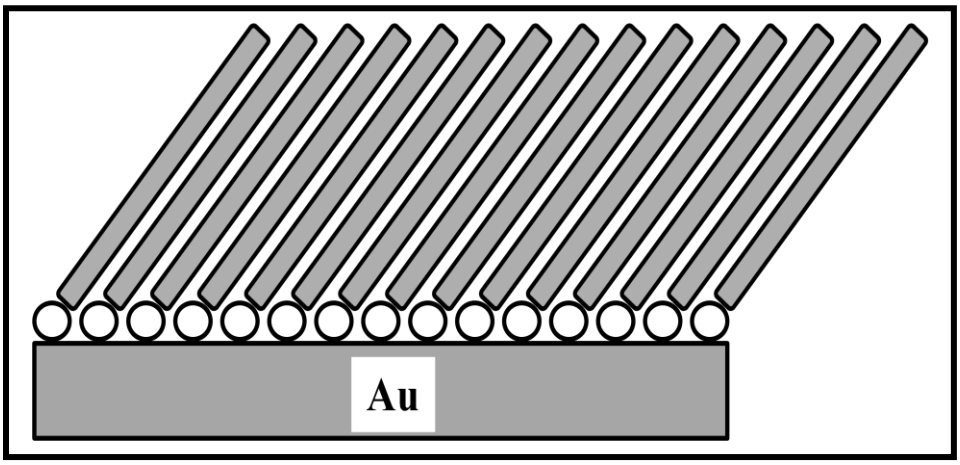

Figure 1.7: Schematic representation of organized monolayer of alkanethiols on gold.

The most popular method of forming self-assembled monolayers of thio-substituted MPc complexes is by immersing the substrate (particularly gold) of interest in homogeneous solution of the desired MPc complex [82,136,137]. Self-assembled monolayers of thio-derivatised metallophthalocyanine complexes containing disulphide functionality has also been investigated [138]. Generally, monolayers of metallophthalocyanine complexes are characterized by the following features:

(i) Orientation and nature of packing of the monolayers are dependent on chain length, nature, number and position of substituents on the phthalocyanine ligand.

(ii) Possible orientations of MPc monolayers are described as vertical (Figure 1.8A), umbrella (Figure 1.8B) (facilitated by the presence of axial thiol group) and octopus (Figure 1.8C) (characteristic feature of monolayers of octa-substituted MPc derivatives).

(iii) Monolayers of MPc complexes containing single tethers are formed with the molecules tilted at different angles to the substrate, depending on the length of the tether chain, while monolayers of MPc with disulphide functionality have characteristically parallel orientation [138].

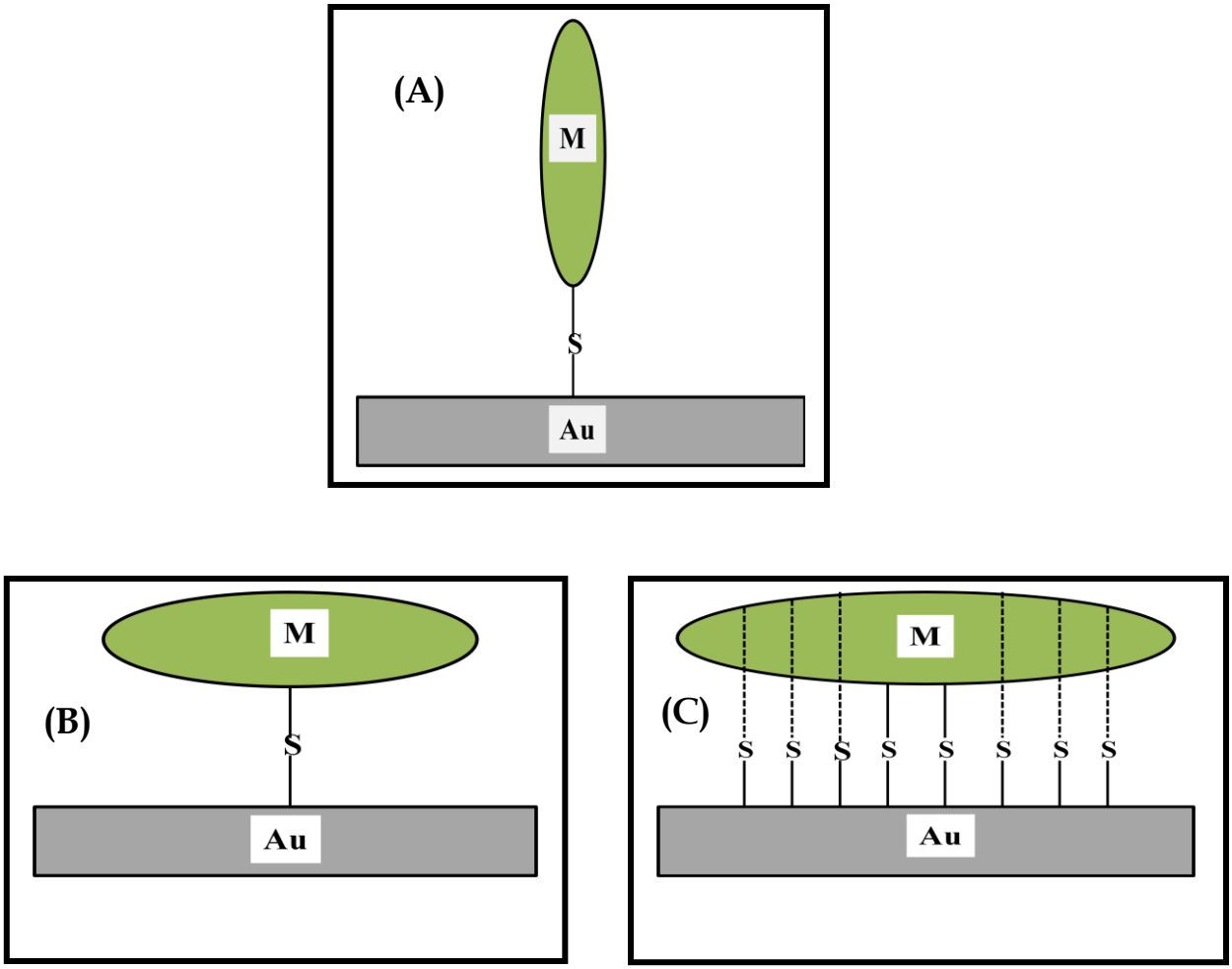

Figure 1.8: (A) Vertical, (B) Umbrella and (C) Octopus orientations of MPc-SAM

In this work, self-assembled monolayers of tetra-substituted arylthio- and alkylthio-derivatised metallophthalocyanine complexes are formed on polycrystalline gold disc electrode, and their surface properties investigated. The alkylthio-substituted MPc complexes (Scheme 1.2) have the dual attribute of forming both self-assembled monolayer and electropolymerized films, thus their relevance in this study. Electrochemical data of the SAMs of some arylthio and alkylthio-substituted MPc complexes (M = Co, Fe, Mn), formed on gold electrode, is shown in Table 1.4 [82,136,137]. Table 1.4 shows that SAM of alkylthio-substituted MPc (FeOBTPc) has the best surface coverage, while the worst surface coverage can be identified with arylthio-derivatised MPc-SAM (MnTBMPc). This informed the choice of diethylaminoethanethio-substituted

MPcs for SAM formation in this work. Electrochemical properties of these SAMs are compared with those of their benzylthio-derivatised analogues.

Table 1.4: Electrochemical data of the SAMs of thio-substituted MPcs formed on gold electrode

MPc-SAM	Medium	Γ_{ibf}	Γ_{MPcSAM}/mol cm^{-2} ×10^{-10}	M^{III}/M^{II}	$E_{1/2}$/V vs. Ag|AgCl	Reference
CoOBTPc	Acidic	0.99	0.96	Co^{III}/Co^{II}	+0.36	136
CoTBMPc	pH 4	0.98	0.86	Co^{III}/Co^{II}	+0.32	137
CoTDMPc	pH 4	0.96	0.91	Co^{III}/Co^{II}	+0.24	137
FeOBTPc	Acidic	0.99	0.98	Fe^{III}/Fe^{II}	+0.26	82
FeTDMPc	pH 4	0.99	0.78	Fe^{III}/Fe^{II}	+0.37	137
MnTBMPc	pH 4	0.97	0.69	Mn^{IV}/Mn^{III}	+0.27	137

OBT = octa butylthio, TBM = tetra benzylmercapto and TDM = tetra dodecylmercapto

1.2.3 Overview of Electropolymerization Technique

Electrochemical polymerization is one of the numerous methods of forming polymeric films of MPc complexes on conductive substrates. Polymers of MPc complexes can also be formed by plasma polymerization [139] and the LB method [140]. Alternatively, functional properties of MPc complex can be imprinted onto pre-formed polymers by direct incorporation of the complex. In this work, polymeric films of MPc complexes are formed on glassy carbon electrode by electrochemical polymerization. The polymer-modified electrodes are employed for the electrochemical detection of the neuro-toxic carbamate insecticide, bendiocarb, and the toxic, contact herbicide, bentazon. The

presence of polymerizable group (sulfur or nitrogen) on the substituent is a prerequisite for forming polymers of MPc complexes, thus the relevance of the MPc complexes studied in this work.

Electrochemical polymerization is carried out by repetitive cycling, within suitable potential window, of a conductive substrate in a homogeneous solution of the monomer. Differences between successive voltammetry scans and emergence of new voltammetric peaks (Figure 1.9) [141] are characteristic of polymer formation. The elegance of this method is underscored by its simplicity and the ability to control polymer growth, with a fixed number of cyclic voltammetry cycles. Importantly, the quality of an MPc-based polymer is dependent on the nature of solvent, purity of the monomer and potential range employed during voltammetry scanning. The most studied polymers of MPc complexes are those of tetraamino-substituted complexes [76,130-132]. Polymer formation is driven by the oxidation of amino groups (Scheme 1.3), which form radicals that attack the phenyl groups of neighbouring molecules [76,130-132]. Oxidation potential of the amino group and the number of monolayer formed were reported to be dependent on the nature of central metal [142]. Formation of polymeric films of pyrrole-substituted MPc complexes has also been reported [141,143]. Polymer formation was attributed to the oxidation of the pyrrole groups, with the resulting radicals facilitating polymer formation in a style reminiscent of the formation of polypyrrole.

1.2.4 Methods of characterizing chemically modified electrodes

Generally, CMEs are characterized using non-electrochemical or/and electrochemical methods. The most popular electrochemical method is cyclic voltammetry, and recently, electrochemical impedance spectroscopy (EIS). SAM-modified electrodes (particularly gold) can be characterized by using any of the following non-electrochemical methods: measurement of wetting contact angle, infrared and Raman spectroscopy, ellipsometry,

x-ray photoelectron spectroscopy (XPS) and microscopy (scanning tunneling, scanning electron and atomic force microscopy).

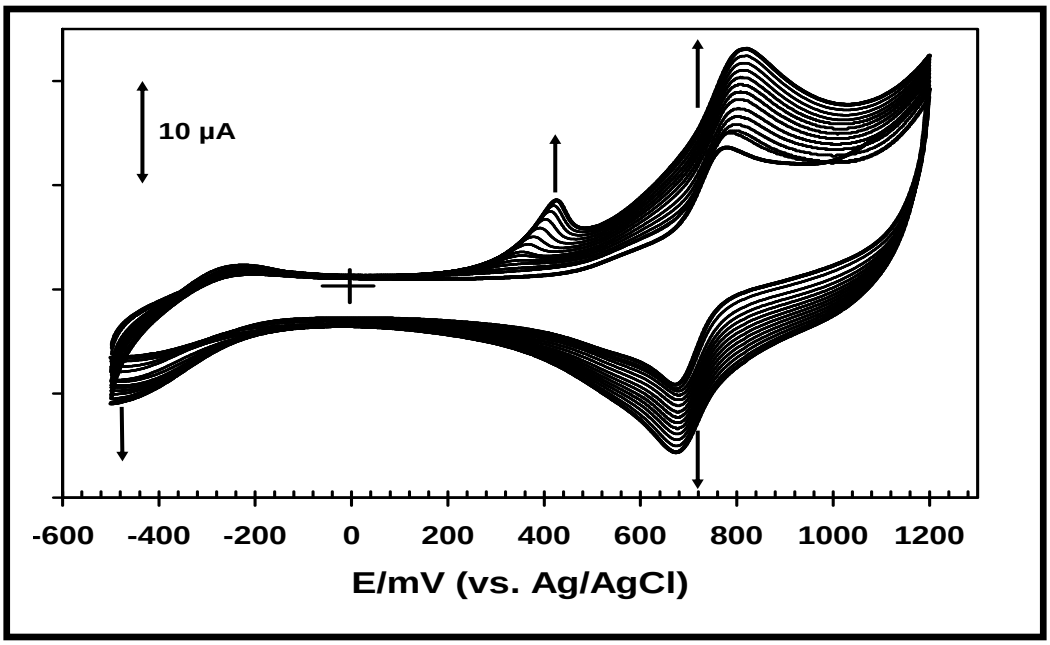

Figure 1.9: Typical cyclic voltammetry profiles showing formation of MPc-polymer [141]

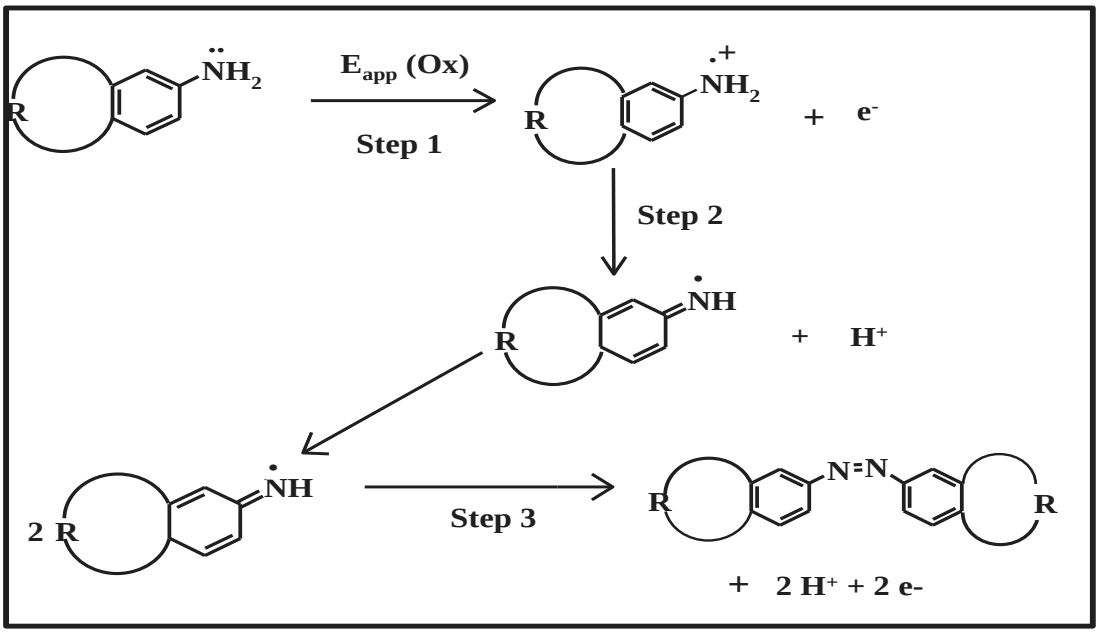

Scheme 1.3: Schematic representation of electropolymerization of amino substituted phthalocyanine monomer, R is the remaining part of the molecule.

Electropolymerized film modified electrodes can also be characterized by microscopic methods; in addition to the use of quartz crystal microbalance and UV-Vis spectroscopy [130,144]. In this work, surface properties of modified electrodes are investigated using cyclic voltammetry, electrochemical impedance spectroscopy, and microscopic techniques. An overview of these methods is presented.

1.2.4.1 Cyclic voltammetry

One of the most widely used electrochemical methods of characterizing redox-active modifiers on electrodes is cyclic voltammetry. For the characterization of SAM-modified gold electrodes, this method relies on the blocking behavior of monolayers. In principle, SAM formation on gold electrode is justified by the inhibition of the redox processes characteristic of bare gold surface: gold oxidation, underpotential deposition (UPD) of metals (Cu and Pb), and oxidation or reduction of solution species.

Investigation of the inhibition of gold oxidation can be performed by subjecting a gold electrode to a positive potential scan from the double-layer region to potentials that facilitate gold oxidation. This is normally carried out in aqueous acid or alkaline solution. On a bare gold surface, a well-resolved anodic peak is observed (Figure 1.10). The shape and position of the peak are diagnostic of both the crystallinity of the gold and presence or absence of oxidizable contaminants. The gold oxide layer is reduced when the potential is returned in the negative direction, with the cathodic peak at potential negative of the onset of oxidation. The area under this peak is a measure of the surface area of the electrode. These processes are suppressed on a SAM-modified gold electrode (Figure 1.10). Inhibition of gold oxidation is best explained by the exclusion of water or hydroxide ion from the gold surface. Thus, oxide stripping current, on SAM-modified gold electrode, is indicative of the presence of pinhole (a site at which the electrode surface is exposed to the electrolyte) in the monolayer. The extent of this occurrence can be evaluated by calculating the ion barrier factor of the SAM (equation

1.6). A value close to unity is indicative of the presence of minimal pinhole, and a closely packed monolayer.

$$\Gamma_{\text{ibf}} = 1 - \frac{Q_{SAM}}{Q_{Bare}} \qquad 1.6$$

where Q_{SAM} and Q_{Bare} are the integrated charges associated with the oxide stripping peak on the SAM-modified and bare gold electrodes, respectively.

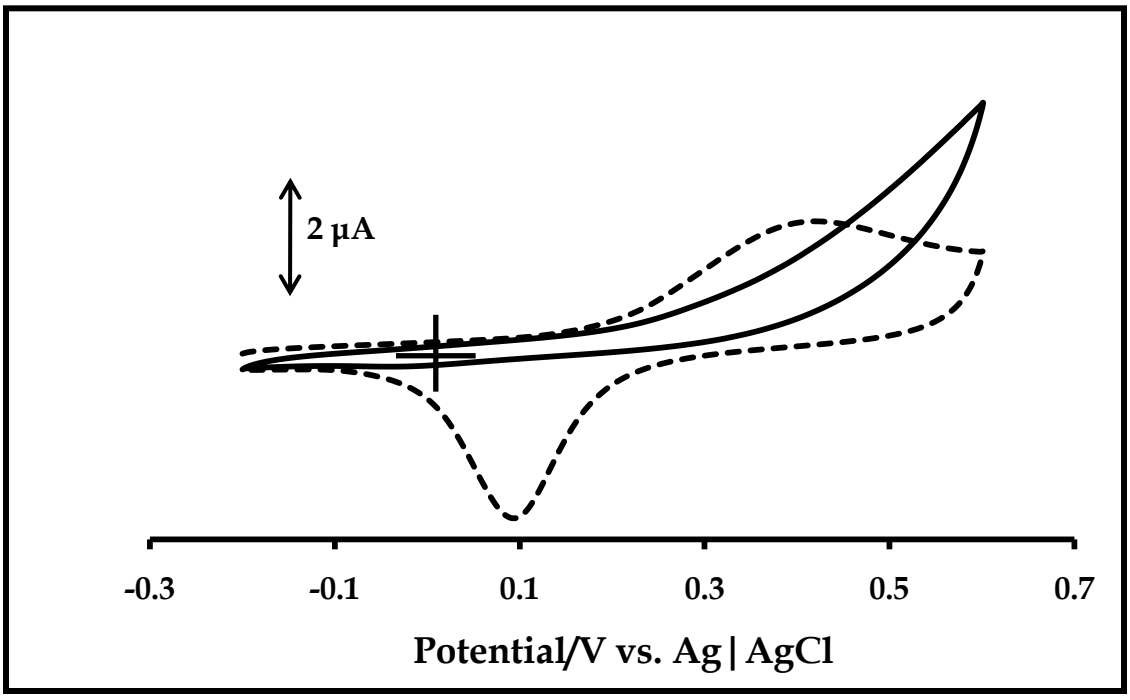

Figure 1.10: Cyclic voltammograms of bare (dashed line) and MPc-SAM-modified (solid line) gold electrodes in 0.1 M KOH solution.

SAM-modified gold electrode can also be characterized by the blocking of metal deposition on gold electrode. Metal deposition is characterized by the bulk deposition of the metal at potentials close to the thermodynamic potential and underpotential deposition (UPD) at potentials well positive of the thermodynamic potential. For example, the cyclic voltammetry response of a bare gold electrode in a Cu^{2+}/H_2SO_4 solution (Figure 1.11) can be used to describe this phenomenon. The onset of bulk deposition of Cu is normally observed near the standard potential of the Cu^{2+}/Cu half reaction (~ +0.03 V vs. Ag|AgCl) in the negative-going scan and a large stripping peak in the return scan (Figure 1.11) [145]. Like the gold oxide stripping peak, the area under

the copper stripping peak is indicative of the electrode surface area. The formation of a monolayer is characterized by the inhibition of these processes.

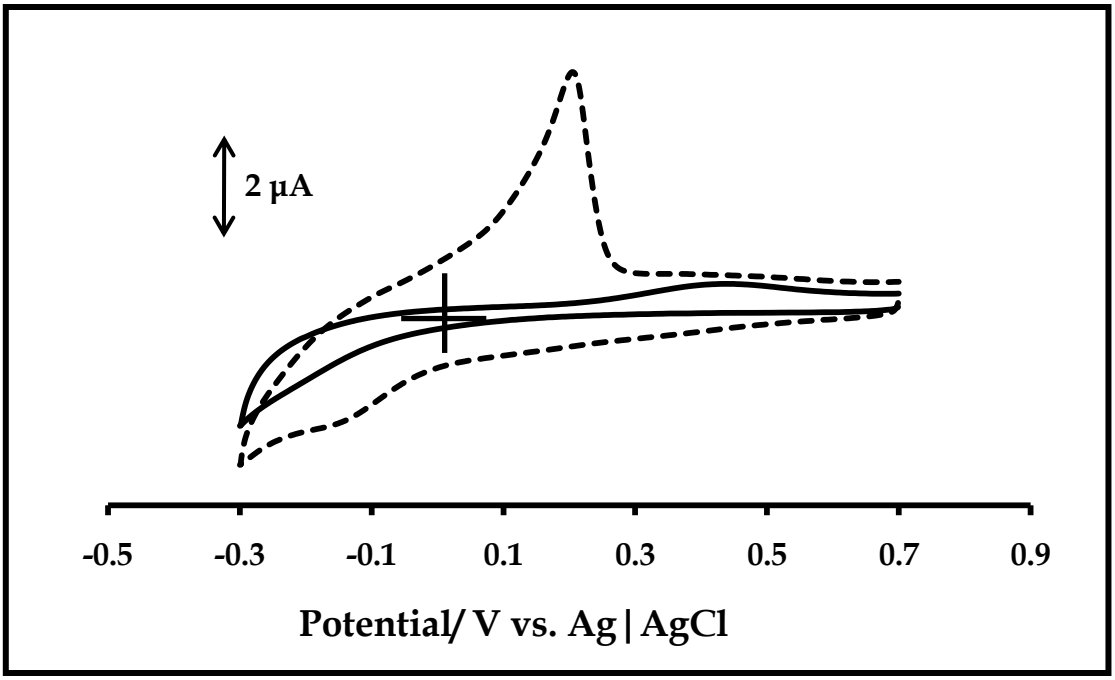

Figure 1.11: Cyclic voltammograms of bare (dashed line) and MPc-SAM-modified gold electrodes in 1×10^{-3} M $CuSO_4$/0.5 M H_2SO_4 solution [145].

Suppression of simple faradaic process involving soluble oxidized and reduced species can also be used to characterize SAM, but meaningful explanation of the blocking behavior of a monolayer, in this respect, is often complicated by the interplay of other factors. For example, the Fe^{3+}/Fe^{2+} redox couple is usually inhibited on most SAMs of aryl and alkylthio-derivatised MPc complexes in aqueous medium (Figure 1.12), with no discernable blocking properties to the $[Fe(CN)_6]^{3+/2+}$ redox process in the same medium [137] (Figure 1.13). This behavior has also been observed in monolayers of alkanethiols [146]. Suppression of the Fe^{3+}/Fe^{2+} redox process was observed in water but no blocking behavior was observed for the ferrocene/ferricenium redox couple in acetonitrile [146].This is explained in terms of the favorable heterogeneous rate constant for electron transfer in the $[Fe(CN)_6]^{3+/2+}$ and ferrocene/ferricenium redox couples. Other factors that may account for these observations are size and hydrophilicity of the

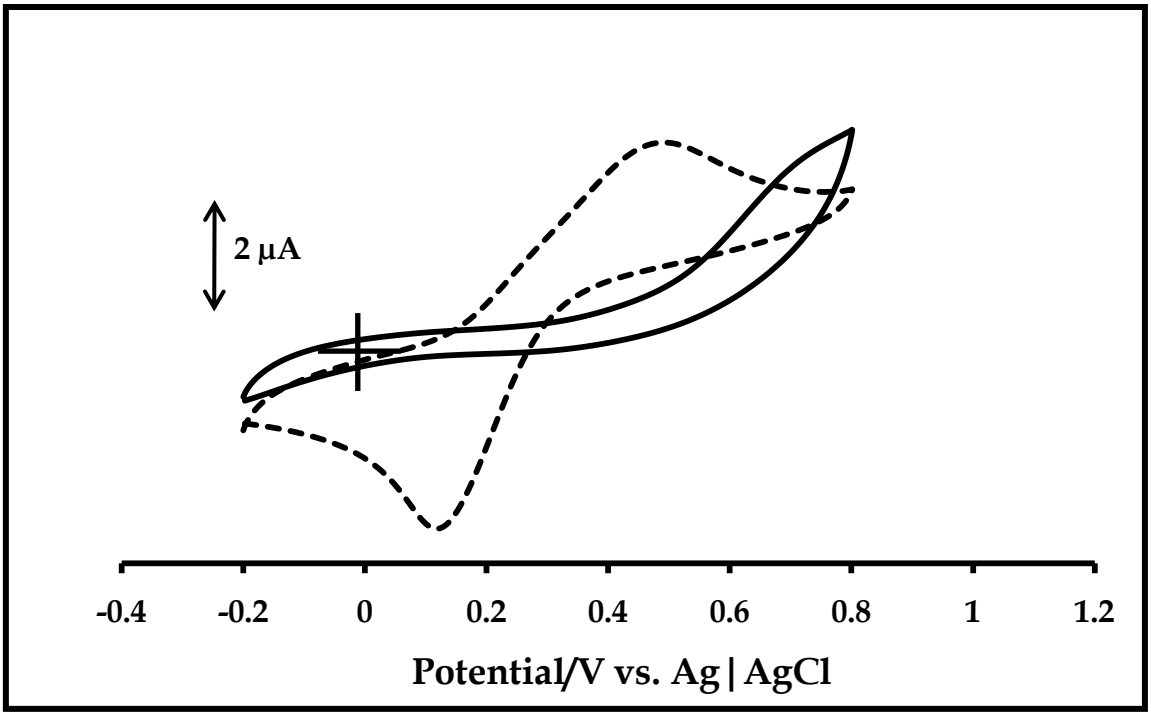

Figure 1.12: Cyclic voltammograms of bare (dashed line) and MPc-SAM-modified gold electrodes in 1×10^{-3} M $(Fe(NH_4)(SO_4)_2$/ 1×10^{-3} M $HClO_4$ solution.

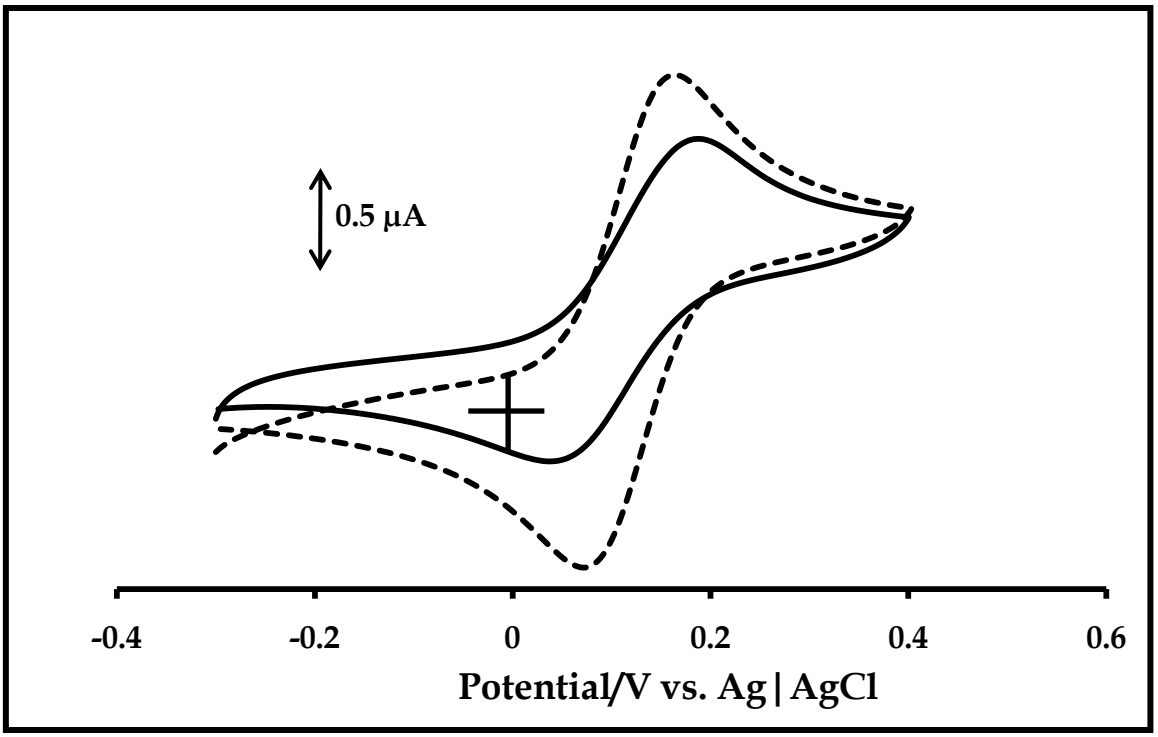

Figure 1.13: Cyclic voltammograms of bare (dashed line) and MPc-SAM-modified (solid line) gold electrodes in 1×10^{-3} M $[Fe(CN)_6]^{4-}$/ 0.1 M KCl solution.

redox ions and the difference in the mechanism of electron transfer (outer-sphere versus inner-sphere).

Finally, modified electrodes can be characterized by using cyclic voltammetry to investigate the redox activities of the adsorbed species, especially for CMEs with redox-active modifiers. Electrolytes of choice in this regard are buffer solutions of suitable pH values. Usually, the half wave potentials of the observed redox processes are very close their former potentials in solution. The charge under the observed redox peak (Figure 1.14) [147] can be used to calculate the concentration (surface coverage, mol cm^{-2}) of the adsorbed complex (equation 1.7). For SAM-modified electrode, value of surface coverage is also informative of the possible orientation of the molecules on the substrate.

$$\Gamma_{MPc} = \frac{Q}{nFA} \qquad 1.7$$

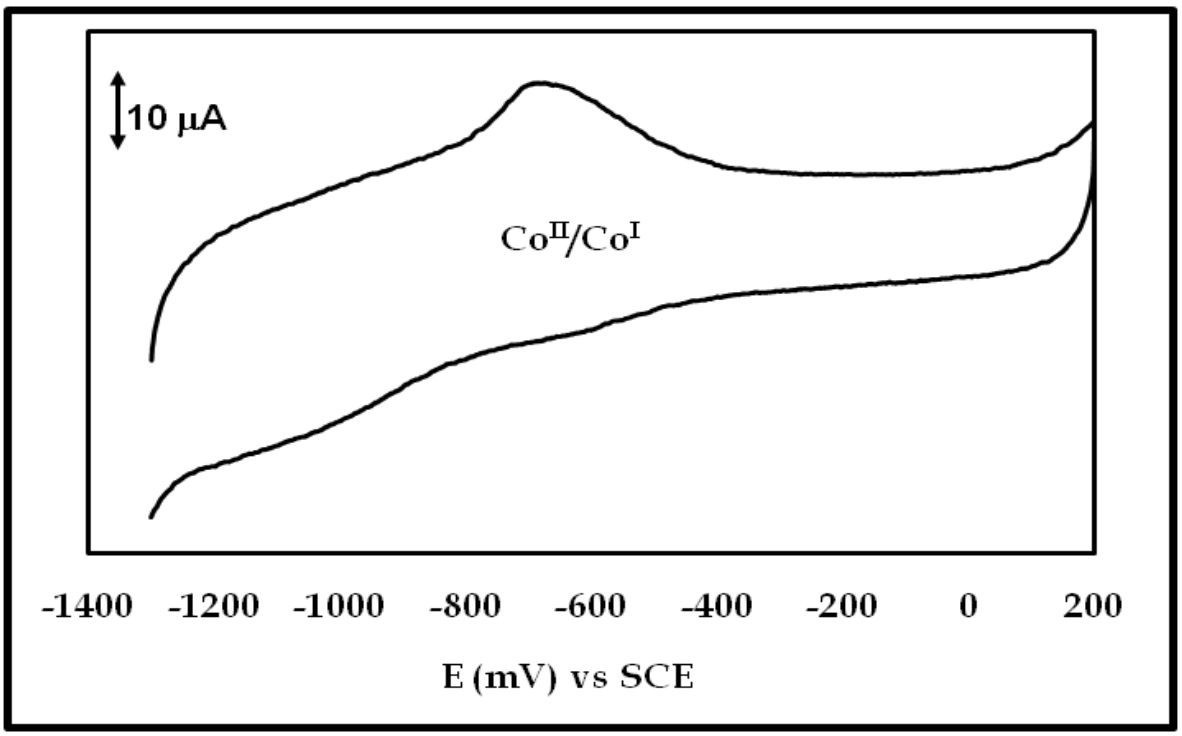

Figure 1.14: Typical cyclic voltammetry profile of adsorbed MPc complex in buffer solution [147].

Q = charge under the observed redox peak

n = number of electrons transferred

F = Faraday's constant

A = real surface are of the electrode

1.2.4.2 Electrochemical impedance spectroscopy (EIS) method

Impedance (Z) is a complex quantity associated with an alternating current (ac) circuit, analogous to resistance (R) in a direct current (dc) circuit. Generally, substantial perturbation of an electrochemical system occurs on the application of an electrical stimulus, in the form of a sinusoidal voltage.

1.2.4.2.1 Nyquist plots

In electrochemical impedance spectroscopy (EIS), an electrical stimulus, in the form of a specified voltage (the former potential of the electroactive species of interest), is applied to the working electrode, resulting in the polarization of the electrode/solution interface [148]. Impedance of the cell is then sampled over a specified range of frequencies; to give a plot of imaginary versus real impedance (Nyquist plot) (Figures 1.15A and B). Application of this technique to electrochemical phenomena relies on the use of different circuit models (the equivalent circuits) (Figure 1.15C and D), depending on the impedance spectrum in the complex plane, to explain the physical electrochemistry of the cell. Electrical properties of the elements in the proposed circuit must be representative of the real physical (e.g. diffusion) and chemical (e.g. charge transfer) processes occurring in the electrochemical cell of interest. For electrode characterization, the impedance spectra of the bare and modified electrodes, in a given redox probe, are recorded. Difference in impedance responses of the bare and modified electrodes is indicative of successful modification.

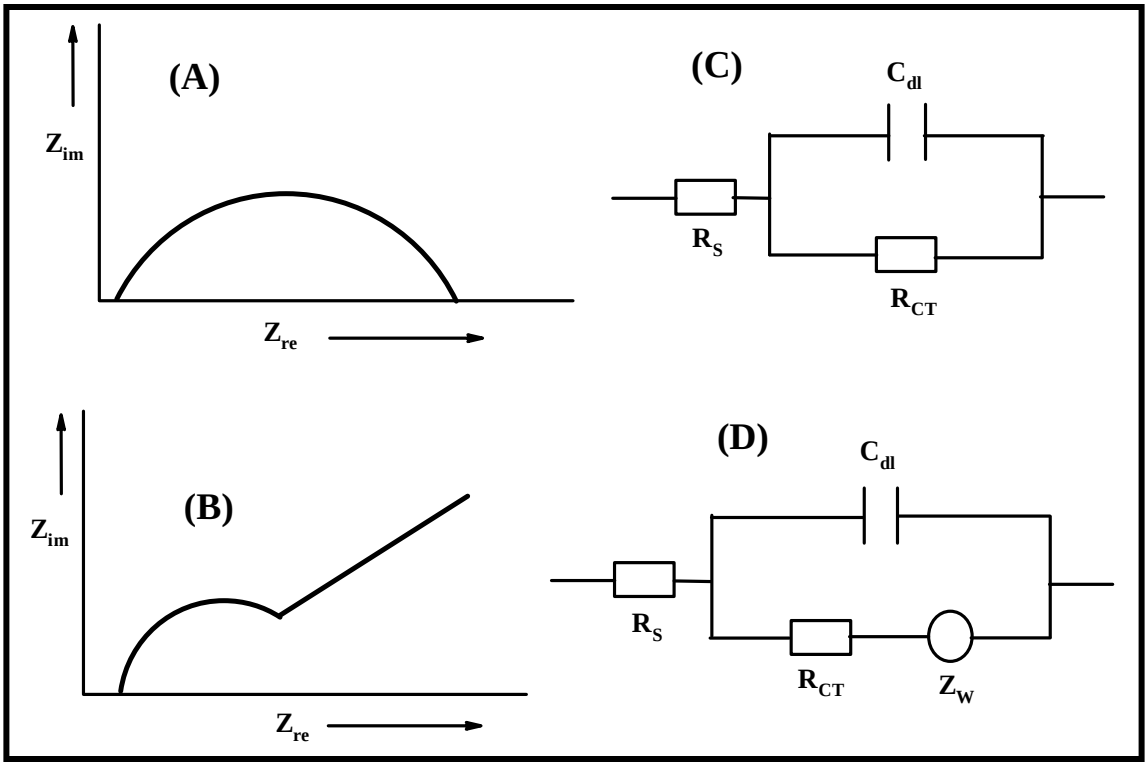

Figure 1.15: Typical Nyquist plots (A and B) and corresponding equivalent circuits (C and D).

EIS data can be analyzed using a mathematical model that predicts the theoretical impedance of the cell, or networks of electrical circuit elements, referred to as equivalent circuits. The latter is used in this work. In principle, the use of equivalent circuit to explain the physical electrochemistry of a three-electrode electrochemical cell takes into account three important parameters in the cell. The first parameter is the resistance of the electrolyte solution between the reference and the working electrodes (R_S). A resistor, with resistance (impedance) equal to R_S accounts for this parameter in the equivalent circuit. Another relevant parameter is the double-layer capacitance (C_{dl}) of the electrochemical double layer, a capacitor-like interfacial region in the cell. This parameter is taken into consideration by the inclusion of a capacitor, with capacitance equal to C_{dl}, in the equivalent circuit. The third parameter is the resistance (impedance) of the charge-transfer process (R_{CT}). In the equivalent circuit, this is represented by a resistor, with resistance equal to R_{CT}. The Nyquist plot depicting this scenario is shown in Figure 1.15A. The equivalent circuit comprising of these parameters is a parallel

combination of R_{CT} and C_{dl}, in series with R_S (Figure 1.15C). This circuit can be modified to account for other physical processes in the cell, depending on the impedance spectrum of interest. One of such modification is the inclusion of the Warburg impedance, Z_W, to account for diffusion-related process in the cell. The impedance spectrum and the corresponding equivalent circuit (***Randles circuit***) describing this phenomenon are shown in Figure 1.15B and D.

1.2.4.2.2 The Bode Plots

Bode plots are subsets of the Nyquist plot. Information obtainable from a Bode plot compliments that of the Nyquist plot [148]. Generally, Bode plots are plots of impedance (Z) and phase angle (Φ) versus frequency (ω), usually over a wide range of values, on a logarithmic scale (Figure 1.16). Unlike the Nyquist plot, the value of ω corresponding to

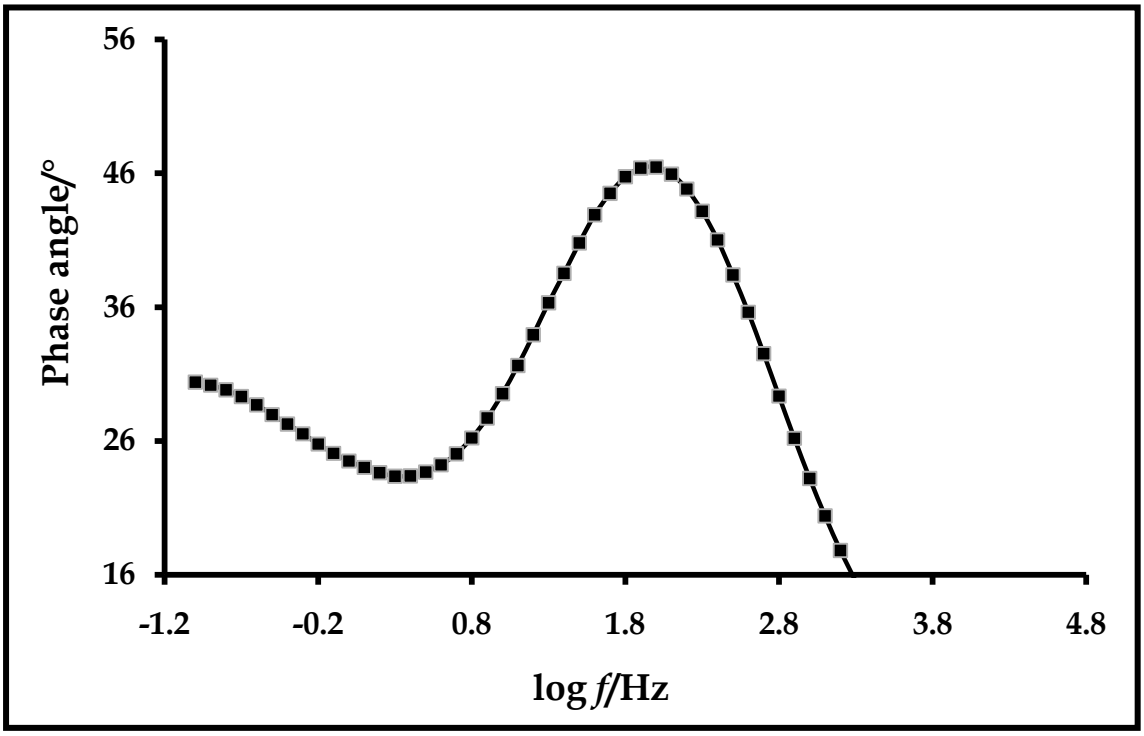

Figure 1.16: Typical bode plot

a given value of Z can be evaluated on the Bode plot. In the phase-angle plot (Φ versus ω), $\Phi \rightarrow$ -90°, at low ω, denotes pure capacitive behavior. Deviation from this behavior

requires the use of constant phase element, CPE, in place of C_{dl}, in the equivalent circuit modeling the cell. Reaction rate constant can also be qualitatively estimated from the Bode plots. The phase peak (ω corresponding to a given Φ) in a Bode plot is derived from a serial combination of R_S with a parallel combination of R_{CT} and C_{dl}. As R_{CT} decreases, phase peak shifts to higher value and vice versa. In most cases, modification of electrode is evidenced by higher R_{CT} and shift of phase peak to lower value.

1.2.4.3 Microscopic methods

1.2.4.3.1 Atomic Force Microscopy (AFM)

Atomic force microscopy (AFM) is a scanning probe technique used for imaging of surfaces. Significant difference in morphology is expected between the bare and modified electrodes. Also, increase in roughness factor is indicative of the presence of the species of interest on a given substrate. In this work, morphological features of the modified electrodes are investigated using AFM in the non-contact mode. The porosity of MPc-polymer films is also investigated using this technique. Figure 1.17 shows typical atomic force microscopic images of (A) bare and (B) MPc modified substrates [149]. Figure 1.17 shows that increase in mean roughness can be identified after modification.

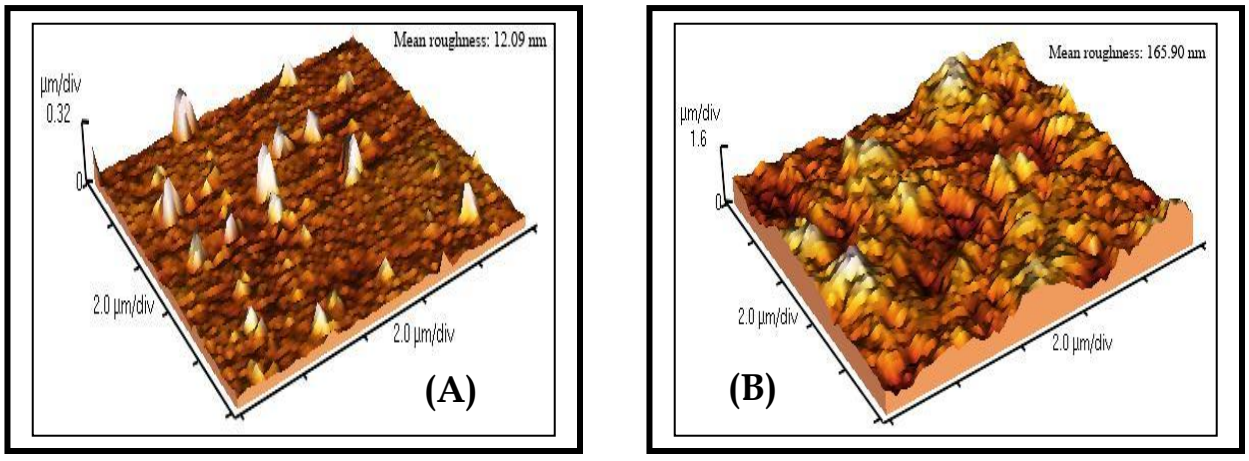

Figure 1.17: Typical AFM images of (A) bare and (B) MPc modified substrates [149].

1.2.4.3.2 Scanning Electron Microscopy (SEM)

Like transmission electron microscope, scanning electron microscope (SEM) makes use of electrons, rather than light, to image a sample. The clarity of SEM images makes this technique one of the most useful microscopic techniques in modern research. In this work, SEM is used to probe the microscopic properties of SAM-modified gold electrodes.

1.3 Electrocatalysis

1.3.1 Characteristics of electrocatalytic behavior: Cyclic voltammetry

In cyclic voltammetry, electrocatalysis is typified by reduction in overpotential (less positive oxidation potential or less negative reduction potential) and/or amplification of current response of redox active species. In most cases, oxidation/reduction of the analyte is not reversible, due to formation of redox inactive products or products which

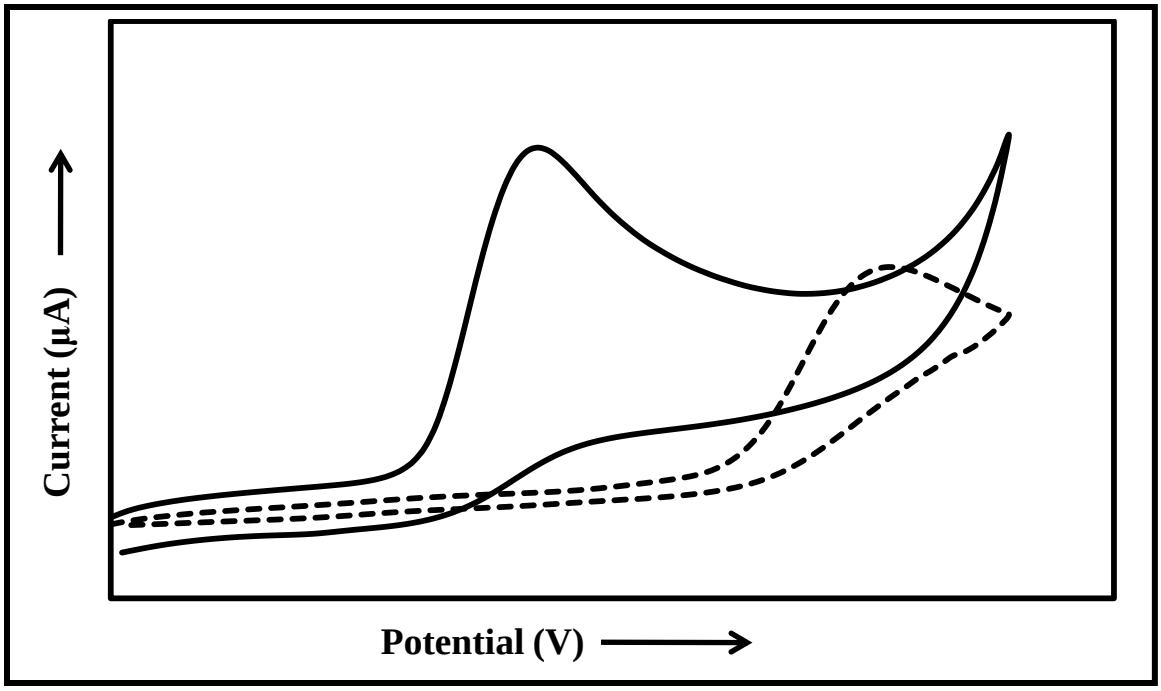

Figure 1.18: Hypothetical model illustrating MPc-mediated electrocatalytic oxidation of an analyte.

undergo redox reaction at extreme potentials. Figure 1.18 is a hypothetical model illustrating electrocatalytic oxidation of an analyte. Dashed and solid lines are the cyclic voltammetry responses of the species in the absence and presence of electrocatalysts, respectively. Redox active MPc complexes are good electrocatalysts toward many analytes [76,130-132]. In this work, electrocatalytic properties of Fe, Mn and Co complexes of phthalocyanine are employed for electrochemical detection of selected pesticides.

1.3.2 Electrode kinetics: Rotating Disc Electrode (RDE) Voltammetry

Rotating disc electrode (RDE) voltammetry is a technique in which the solution near a disc-shaped electrode is subjected to forced mechanical convection (stirring). In this technique, the electrode is placed in the desired solution and rotated at a controlled rotation speed, ω, (rad s^{-1}) to induce stirring [150]. The rotated electrode acts as a pump, drawing the solution toward the electrode along the z-axis, flinging it out radially across the electrode surface. Uniform accessibility [151] of the electrode ensures constant flux of solution across its surface. In RDE voltammetry, mass transport is by diffusion only, but products are normally swept away radially from the electrode surface by convection. A typical RDE voltammogram is shown in Figure 1.19. Three distinct portions can be identified on the voltammogram: (I) foot of the wave, (II) rising part of the wave and (III) a plateau-like portion. I_L on the voltammogram is the mass transport limiting current. At this current, heterogeneous rate constant, k, of the redox process concerned is very large, the electrode is highly reactive and the concentration of redox species is zero on the electrode surface. The relationship between I_L and ω was defined by Levich [152], while the measured current in RDE voltammetry was evaluated using the Koutecky-Levich equation [153], discussed later. RDE voltammetry is particularly fashionable in elucidating the electrode kinetics of electroactive films (modified electrodes) because of: (i) uniform accessibility of the electrode, which ensures constant flux of analyte across its surface and (ii) constant and reproducible analyte concentration at the surface of the electrocatalytic film.

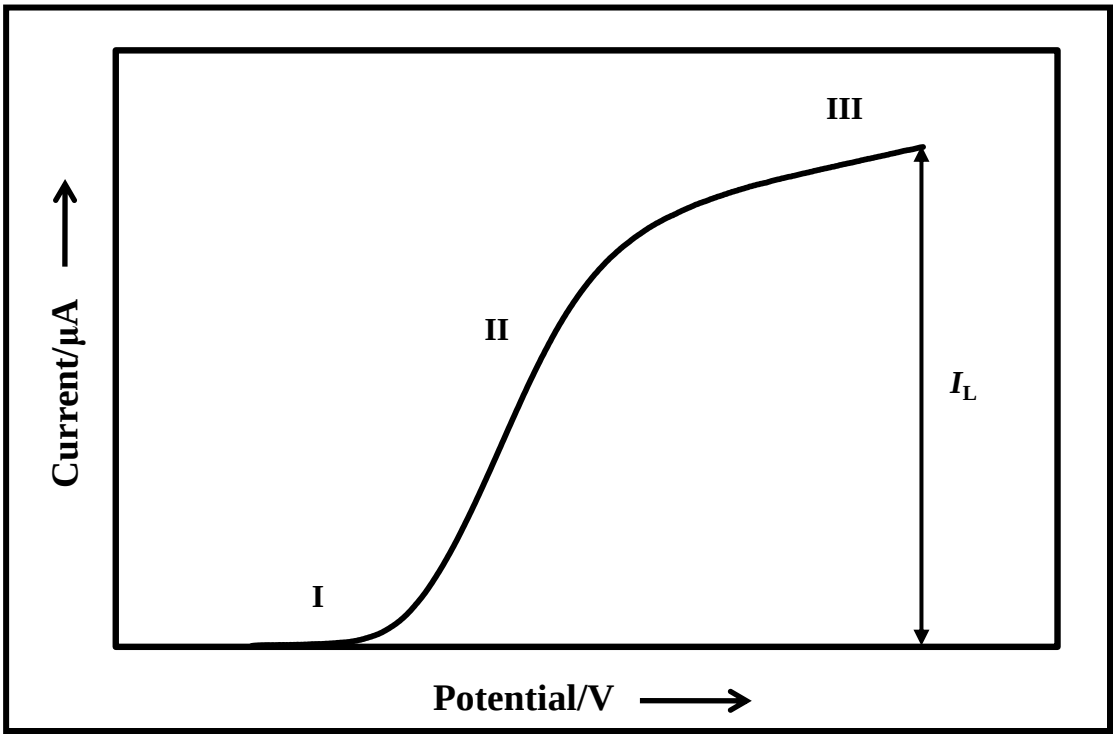

Figure 1.19: Typical RDE voltammogram

1.3.3 Mechanism of electrocatalysis using metallophthalocyanine complexes

Electrocatalysis involving MPc complexes may be metal-centered or ring-based, depending on the oxidation or reduction potential of the electroreactant of interest. In principle, electrocatalytic oxidative process, mediated by the metal center of MPc complex, is represented by the following equations

$$M^nPc \longrightarrow M^{n+1}Pc + e^- \qquad 1.8$$

$$M^{n+1}Pc + \mathbf{A} \longrightarrow M^nPc + \mathbf{A}^+ \qquad 1.9$$

The above hypothesizes the electrocatalytic oxidation of '**A**' via outer sphere mechanism. The oxidation of '**A**' is accompanied by the regeneration of the electrocatalysts (equation 1.9). Electrocatalytic oxidation of '**A**' via inner sphere is depicted by equations 1.10 to 1.12

$$M^nPc \longrightarrow M^{n+1}Pc + e^- \qquad 1.10$$

$$M^{n+1}Pc + \mathbf{A} \longrightarrow [M^{n+1}Pc\text{-}\mathbf{A}]^{n-1} \qquad 1.11$$

$$[M^{n+1}Pc\text{-}\mathbf{A}]^{n-1} \longrightarrow M^{n}Pc + \mathbf{A}^{+} \qquad 1.12$$

Equation 1.11 denotes the presence of analyte-catalyst intermediate.

UV-Vis spectroscopy can also offer reliable mechanistic information. Change in the position or intensity of the Q-band of MPc complex, in the presence of the analyte of interest, suggests catalyst-substrate interaction. In most cases, such interaction involves the metal centre, via axial ligation [154].

In this work, the remarkable electronic attributes of single-walled carbon nanotubes (SWCNTs) are covalently integrated with the electrocatalytic properties of FePc, with a view to enhancing the electrocatalytic relevance of the complex. An overview of the general properties of these one dimensional nanostructures is presented.

1.4 Overview of the general properties of Carbon nanotubes

1.4.1 Structural properties and general applications

Carbon nanotubes (CNTs) were discovered two decades ago in electric arc-discharge experiments, during the synthesis of fullerene [155]. They are made up of rolled-up sheets of graphene (single sheet of sp^2 hybridized carbon atoms). The parent graphene sheet is a flexible, single layer of carbon atoms, densely packed in a honeycomb crystal lattice. It is not purely planar, but exhibits intrinsic microscopic roughening [156,157], enhancing the possibility of rolling up to form tube-like, single- (SWCNTs) or multi-walled (MWCNTs) structures (Figure 1.20). SWCNT (Figure 1.20A) [158] is a single cylinder of graphene, while MWCNT (Figure 1.20B) [158] consists of concentric cylinders.

CNTs are usually obtained from different carbon sources, using different synthetic methods [159,160]: electric arc discharge (EAD), laser ablation (LA), plasma and chemical vapor deposition (CVD). Reorganization into tube-like structures takes place in the presence of transition metal catalyst. CNTs have unique thermal, electronic, mechanical

and optical properties [161-165], which explains why they are the most investigated nanomaterials in recent years. Their uses in the design of biosensors, nanodevices and nanoelectronics have been reported [166-170]. Also, they are essential component of electrochemical supercapacitors (ESs) [171-173] and electrochemical sensors [174-178]. Their use in the fabrication of electrochemical sensors underscores the high electrical conductivity of these nanostructures. Also, the relevance of CNTs to energy storage has been intensively investigated, resulting in increased demand for their uses in hydrogen storage [179-181] and in the design of fuel cells [182,183].

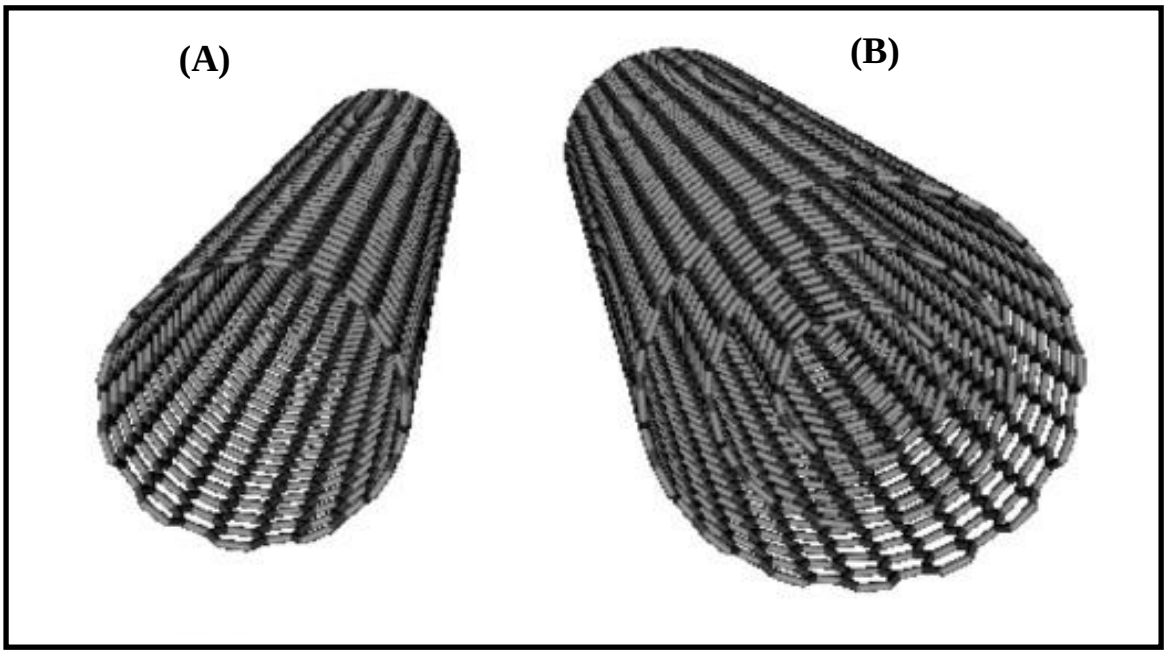

Figure 1.20: (A) Single walled and (B) Multi walled carbon nanotubes [158]

1.4.2 Methods of coordinating carbon nanotubes to functional molecules

Most applications of CNTs require functionalization of these nanostructures, depending on the desired application. Functionalization may occur at the side walls, defect sites or open ends of the tube. Functional materials, such as anthracene [184], MPc complex [185] and porphyrin derivatives [186] or biomolecules, such as DNA [187,188] and peptides [189,190], can be coordinated to CNTs by covalent or non-covalent attachment. Covalent attachment is normally carried out in the presence of coupling agents, like the carbodiimides

{dicyclohexylcarbodiimide (DCC), diisopropylcarbodiimide (DIC) and 1-ethyl-3-(3-dimethylaminopropylcarbodiimide (EDC)}. In non-covalent functionalization, aromatic molecules are attached on the walls of the nanotubes via π-π interaction, preserving the sp^2 hybridized status of the carbon atoms and the electronic properties of the CNTs. Covalent functionalization is often less favored because of the likely perturbation of the electronic properties of the nanotubes [191,192]. Nonetheless, recent report [185] suggests nanoconjugate, obtained from covalent combination of tetraamino-substituted CoPc and SWCNTs, has higher electrical conductivity than any of its individual units. In this work, acid functionalized SWCNTs are decorated with diethylaminoethanethio-derivatised iron phthalocyanine complex by covalent attachment, via amide linkage. The self-assembled monolayer (SAM) film of the resulting nanocomposite is employed for electrocatalytic oxidation of the neuro-toxic pesticide, carbofuran.

1.4.3 Methods of characterizing carbon nanotube-metallophthalocyanine composites

Structural properties of CNT-MPc nanocomposite can be elucidated using spectroscopic techniques, such as infrared and X-ray diffraction spectroscopy. Particularly, X-ray diffraction (XRD) spectroscopy has become a very useful analytical tool in probing the structural integrity of CNTs [193], thus its relevance in the investigation of the structural properties of CNTs-based materials, such as CNT-MPc composite. In this work, XRD spectroscopy is employed for the characterization of nanostructures of interest. A brief overview of this technique is presented. Transmission electron microscopy (TEM) is also employed in the evaluation of the microscopic natures of the nanostructures used in this work, while SEM is used for the characterization of self-assembled monolayer film of the CNT-MPc composite on gold electrode.

1.4.3.1 X-ray diffraction spectroscopy

X-ray diffraction spectroscopy is a technique used for the elucidation of the structural properties of materials. Generally, materials can be described as amorphous or

crystalline. Atoms constituting amorphous materials are arranged in a random manner, similar to the disordered arrangement found in a liquid. Examples of amorphous materials are glasses. In crystalline materials, atoms are arranged in a well defined, regular pattern. For an unknown sample, XRD spectral interpretation and subsequent structural elucidation require the use of the International Centre for Diffraction Data (ICDD) database, which contains the XRD spectra and the corresponding structural information of known organic and inorganic samples. Structural properties of an unknown sample are elucidated by matching its XRD spectrum with that of closely related materials in the database. Figure 1.21 shows typical XRD spectrum of SWCNT [194]. The peaks at 2θ = 26.2°, 44° and 51.2° are associated with {002}, {111} and [200} reflections of carbon, respectively.

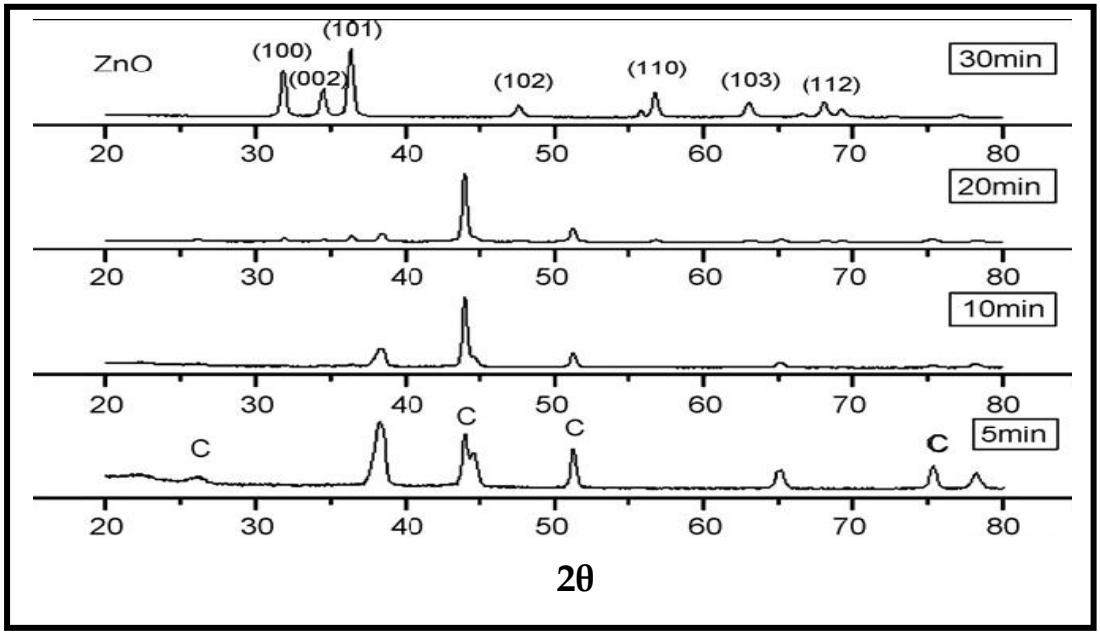

Figure 1.21: XRD spectra of SWCNT-ZnO composite [194].

1.4.3.2 Transmission Electron microscopy (TEM)

Transmission electron microscopy (TEM) is a microscopy technique that makes use of a beam of electron, transmitted through an ultra thin sample, to reveal the microscopic integrity of the sample. In this work, this technique is used to characterize the

nanomaterials used for electrode modification. Figure 1.22 shows the TEM image of raw SWCNT [195].

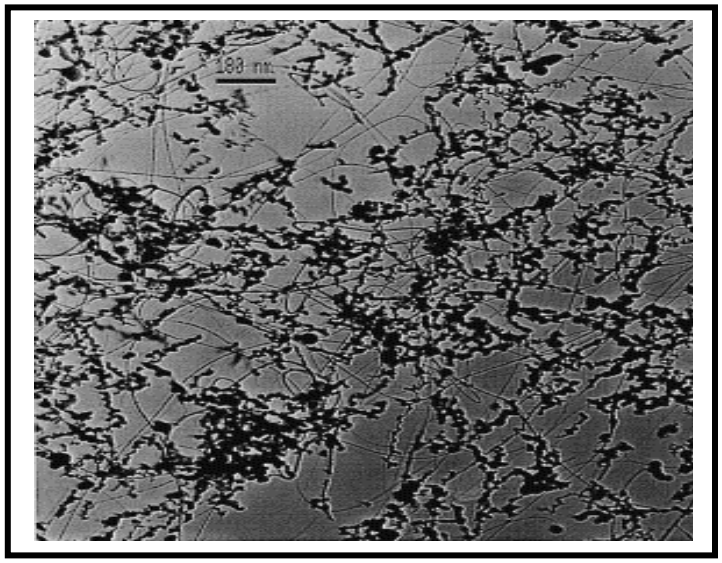

Figure 1.22: TEM image of raw SWCNT [195].

1.5 Analytes of interest: Pesticides

1.5.1 Classification of Pesticides

Pesticides are classified using different criteria. Some of these criteria include: (i) the target pest, (ii) their active ingredients, and (iii) degree of toxicity, among others.

The first mode of classification is the most widely used. Based on this criterion, pesticides can be classified as: (a) insecticides (target pests are insects), (b) fungicides (target pests are fungi), (c) herbicides (target pests are weeds), (d) bactericides (target pests are bacteria), and (e) rotenticides (target pests are rodents), among others. Carbofuran (Figure 1.23A) and bendiocarb (Figure 1.23B) are insecticides, while bentazon (Figure 1.23C) is an herbicide.

The second mode of classification takes into account the class of chemical that makes up the pesticide. Although, some pesticides may contain more than one active component,

majority of them are often identified with a single active ingredient. Based on this style of classification, the following categories of pesticides can be identified: (a) carbamates, (b) organochlorines, (c) organophosphates, and (d) thiocarbamates, among others. Carbofuran and bendiocarb are carbamate pesticides.

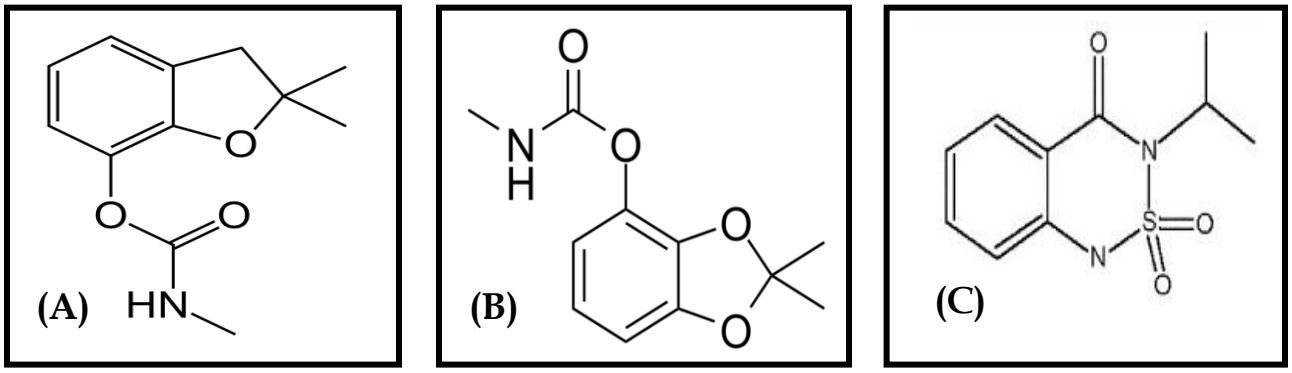

Figure 1.23: Molecular structures of (A) Carbofuran, (B) Bendiocarb and (C) Bentazon

The third mode of classification is commonly used for regulatory purposes. The most notable regulatory body in this respect is the world health organization (WHO). This style of classification, often referred to as the WHO hazard classes, takes into account the potential risk of the pesticide to human health. WHO has developed a globally-harmonized system (GHS) [196] to address classification of chemicals, labels, and safety data sheets. This system is subject to review periodically. Based on this criterion, pesticides can be classified as: (a) class Ia (extremely hazardous), (b) class Ib (highly hazardous), (c) class II (moderately hazardous), (d) class III (slightly hazardous), and (e) class IV (unlikely to present acute hazard in normal use). Carbofuran and bendiocarb fall into class Ib (i.e. they are highly hazardous), while bentazon is moderately hazardous (class II). Therefore, fabrication of sensitive electrochemical sensors for fast and routine evaluation of these pesticides in environmental samples is imperative; this underscores one of the primary objectives of this work. As carbamate pesticides, carbofuran and bendiocarb are neuro-toxic. This underlines the mechanism of their insecticidal action; it is also the essence of their toxicity.

1.5.2 Overview of the methods of detection of carbofuran, bendiocarb and bentazon

1.5.2.1 Carbofuran and bendiocarb

Carbofuran and bendiocarb are N-methyl carbamate insecticides, thus can be detected using the same method. Various methods of analysis of N-methyl carbamate pesticides have been reported in the literature. One of the most widely used methods relies on their ability to inhibit the activity of acetylcholinesterase, in the presence of a suitable substrate, such as N-methylindoxyl acetate [197]. In the absence of carbofuran or bendiocarb, the non-fluorescent N-methylindoxyl acetate is hydrolyzed to the fluorescent yellow-colored N-methyl-3-hydroxyindole. In the presence of any of these pesticides, hydrolysis of this substrate is inhibited, resulting in decrease in fluorescence. The decrease in fluorescence is a measure of the amount of carbofuran or bendiocarb in the sample under investigation.

Chromatographic methods are also commonly used for the analysis of these pesticides. Analysis of carbofuran and bendiocarb by microcoulometric gas-liquid chromatography has been reported [198]. It was reported that a quantity as low as 0.025 ppm can be detected.

The use of enzyme-based methods for the analysis of pesticides is plagued by the challenge of providing a biologically compactable environment, which ensures enzymes retain their activities for reasonable period of time. The possibility of enzymes getting denatured and loosing their activities can not be completely ruled out, hence the preference of other methods to enzyme-based methods. The major drawback of chromatographic methods is extensive sample preparation. Although, very low limits of detection are often reported, these methods are unsuitable for routine evaluation.

Electrochemical methods are the most suitable methods for rapid, routine and sensitive analysis of pesticides in environmental samples. The inability to detect non-electroactive pesticides is the major limitation of electrochemical methods. Selectivity could also be a challenge in the presence of electroactive interferent. Ordinarily, most

carbamate pesticides are not electroactive, but their electroactive phenolic derivatives can be formed on alkaline hydrolysis.

Low detection limits and electrode stability were reported for the use of boron-doped diamond thin-film electrode (0.6-1 ng/ml) [199] for detection of carbamate insecticides, but the redox signals of the insecticides were observed at very high overpotential (+0.90 V versus Ag|AgCl), thus increasing the chance of interference from other electroactive species. High sensitivity (5.0×10^{-8} mol/L) and selectivity were also reported for detection of carbofuran on disposable heated screen printed carbon electrode [200], but reproducible measurements can not be obtained, since the electrode is disposable. The process of fabricating this electrode is also relatively more complicated than the methods employed in this work. Ironically, the use of metallophthalocyanine modified electrodes for detection of these environmentally significant insecticides (carbofuran and bendiocarb) has not been reported before, despite the well-documented electrocatalytic properties of MPc complexes towards many analytes [76,130-132], hence the use of MPcs for electrocatalytic detection of these pesticides is reported in this work, for the first time.

1.5.2.2 Bentazon

Like carbofuran and bendiocarb, chromatographic techniques have been widely used for quantifying bentazon in environmental samples. Chromatographic methods such as gas chromatography [201,202] and high performance liquid chromatography (HPLC) [203,204] have been reported. The use of bare glassy carbon electrode for the detection of bentazon in commercial sample has also been reported [205]. Severe poisoning of the electrode, coupled with high limit of detection, is a major limitation of the use of bare electrode. Conducting polymers of polyaniline and polypyrole, modified with carbon paste, have also been employed for detection of bentazon [206]. The measured voltammetry signal was depended on the amount of bentazon sopped from the solution, which may not truly reflect the actual concentration of the herbicide in a given sample. In this work, the use of MPc-polymer modified electrodes for electrochemical detection of this herbicide is reported. Table 1.5 presents a survey of the electrocatalytic

applications of MPc-SAM and MPc-polymer modified electrodes for detection of various analytes [76,82,130-132,207-211]. Carbofuran, bendiocarb and bentazon have not been detected before on MPc modified electrodes, hence the relevance of this work.

Table 1.5: Electrocatalytic applications of MPc-SAM and MPc-polymer modified electrodes, E_p versus Ag|AgCl

MPc-SAM modified electrodes						
Complex	Electrode	[a]Analyte	E_p, V	LoD/M	Medium	Reference
CoOBTPc	Au	L-cysteine	+0.42	$3.1\pm0.8 \times 10^{-7}$	pH 4	136
FeOBTPc	Au	L-cysteine	+0.33	3.0×10^{-7}	pH 4	82
CoOBTPc	Au	Thiocyanate	+0.78	$1.1\pm0.8 \times 10^{-7}$	pH 4	136
CoTAPc	Au	Oxygen	-0.21	_	pH 7	207
FeOBTPc	Au	Penicillamine	+0.45	$2.7\pm0.6 \times 10^{-6}$	pH 4	82
CoOBTPc	Au	Homocysteine	+0.52	$5.2\pm0.6 \times 10^{-7}$	pH 4	136
FePc	4-MPy-Au	Hydrazine	+0.35	5×10^{-6}	pH 7	208
MPc-Polymer modified electrodes						
Complex	Electrode	[a]Analyte	E_p, V	LoD/M	Medium	Reference
CoTAPc	GCE	Sulphide	~+0.01	_	pH 9	130
MnTAPc	GCE	[b]Glycine	-0.63	_	pH 4	76
CrTAPc	GCE	Nitrite	+0.80	_	pH 7.3	131
NiTpPPc	VCE or Pt	Chlorophenol	+0.43	_	0.1 M NaOH	209
NiTAPc	VCE	Dopamine	+0.19	_	pH 7.4	132
FeTAPc	GCE	[b]Oxygen	-0.15	_	pH 13	210
CoTAPc	VCE	L-cysteine	-0.08	1.3×10^{-4}	0.5 M NaOH	211

[a]Electrocatalysis via oxidation, [b]Reduction, GCE = glassy carbon electrode; VCE = Vitreous carbon electrode, TA = tetra amino, TpP = tetra-4-(pyrrol-1-yl)phenoxy, MPy-Au = preformed SAM on gold using 4-mercaptopyridine, OBT = octa butylthio, Pc = phthalocyanine

1.6 Summary of Aims of Thesis

A summary of the aims of this thesis is highlighted below:

(a) Synthesis and investigation of the spectral, electrochemical and spectroelectrochemical properties of some selected peripherally and non-peripherally thio-substituted cobalt, iron and manganese phthalocyanine complexes, Scheme 1.2.

(b) Design of electrodes modified with the self-assembled monolayer and polymeric films of these complexes.

(c) Fabrication of single walled carbon nanotubes-metallophthalocyanine nano-composite and design of electrode modified with the self-assembled monolayer film of this composite.

(d) Investigation of the surface properties of the modified electrodes using electrochemical and non-electrochemical methods.

(e) Application of the modified electrodes for electrochemical detection of the pesticides carbofuran, bendiocarb and bentazon.

(f) Investigation of the electrode kinetics associated with the electrochemical detection of these pesticides.

(g) Investigation of the stability, selectivity and sensitivity of the modified electrodes.

CHAPTER 2

EXPERIMENTAL

2.1 Materials

Dimethylformamide (DMF), dimethylsulphoxide (DMSO), dichloromethane (DCM), sulphuric acid, tetrahydrofuran (THF), perchloric acid, methanol, ethanol, hydrogen peroxide, acetic acid, sodium hydroxide, anhydrous copper(II) sulphate, potassium hydroxide, silica gel 60 (0.04-0.063 mm) (for column chromatography) and ferrous ammonium sulphate were obtained from Merck. Potassium carbonate, cobalt(II) chloride, manganese(II) acetate, iron(II) chloride tetrahydrate, 2-(diethylaminoethanethiol) hydrochloride, 2-diethylaminoethanol, carbofuran, bendiocarb, bentazon, diazinon, chlorpyrifos, dichlorvos, tetrabutylammonium tetrafluoroborate ($TBABF_4$) (electrolyte for electrochemical experiments involving MPc complexes), 4-nitrophthalimide, 3-nitrophthalimide, 4,5-dichlorophthalic acid, dicyclohexylcarbodiimide (DCC), single walled carbon nanotubes (SWCNTs, 7 – 1.2 nm in diameter and 2 – 20 μm in length), phosphate buffer tablets and aluminum oxide (WN-3: neutral) (for column chromatography) were obtained from Sigma-Aldrich. Anhydrous form of iron(II) chloride was obtained by heating the hydrated form in an oven. Potassium chloride and potassium ferrocyanide were obtained from SAARCHEM. Benzylthiol was obtained from Fluka. All solvents were distilled before use. Stock solutions of carbofuran, bendiocarb, bentazon, diazinon, chlorpyrifos and dichlorvos were prepared in freshly distilled methanol due to their limited solubility in water. Where necessary, solutions were prepared with ultra pure water of resistivity 18.2 MΩ.cm obtained from a Milli-Q Water system. Prior to electrochemical analysis, carbofuran and bendiocarb were hydrolyzed in 0.5 M NaOH solution for 0.5 h, and the pH of the resulting solutions adjusted to 4 with acetic acid.

2.2 Instrumentation

Various spectroscopic techniques were employed for characterization of MPc complexes and the nanomaterials. For UV/Vis spectral characterization, a Shimadzu UV-2550 UV-Vis/NIR spectrophotometer was used. Infra red spectra (KBr discs) were recorded on Bruker Vertex 70-Ram II spectrophotometer, while ^{1}H nuclear magnetic resonance spectral characterization was carried out in $CDCl_3$, using a Bruker EMX 400 NMR spectrometer. X-ray powder diffraction (XRD) patterns were recorded on a Bruker D8 Discover, equipped with a proportional counter, using Cu-Kα radiation (λ = 1.5405 Å, nickel filter). For XRD experiments, samples were placed on a silicon wafer slide and data recorded within the range $2\theta = 5^{o}$ to 60^{o}, scanning at 1^{o} min^{-1} with a filter time-constant of 2.5 s per step and a slit width of 6.0 mm. X-ray diffraction data were fitted using Eva (evaluation curve fitting) software, while analysis of data was done using International Center Diffraction Data (ICDD) database. Microscopic properties of materials were investigated with scanning electron microscope (SEM) (Tescan Digital Microscope model) or/and transmission electron microscope (TEM) (JEOL JEM 1210 model) at 100 KV accelerating voltage. Also atomic force microscopy (AFM) was used for microscopic characterization. AFM images were obtained in the non-contact mode in air with a CP-11 Scanning Probe Microscope from Veeco Instruments (Carl Zeiss, South Africa) at a scan rate of 1 Hz. TEM images were recorded, using ultra thin film of the sample, on a carbon grid, while SEM and AFM images were recorded on gold coated glass and indium tin oxide (ITO) glass, respectively.

2.3 Synthesis

2.3.1 Alkylthio-derivatised metallophthalocyanine complexes

2.3.1.1 3-Nitrophthalonitrile (7), Scheme 3.1, and 4-nitrophthalonitriles (9), Scheme 3.2

The synthesis of compounds **7** and **9** have been reported before [212]

2.3.1.2 3-(2-Diethylaminoethanethio) phthalonitrile (8a) Scheme 3.1

Compound **8a** was synthesized (Scheme 3.1) using the method reported for the synthesis of 1,2-bis-(diethylaminoethanethio)-4,5-dicyanobenzene [213] with some modifications as follows: compound **7** (3.05 g, 17.6 mmol) was dissolved in anhydrous DMF (150 ml) under nitrogen and 2-diethylaminoethanethiol hydrochloride (2.99 g, 17.6 mmol) added. After stirring for 10 min., finely ground anhydrous K_2CO_3 (29.3 g, 212.0 mmol) was added in portions over 2 h, with stirring. The reaction mixture was stirred at room temperature for 48 h under nitrogen. Then the solution was poured into ice (900 g). The precipitate was filtered off and washed with water, until the filtrate was neutral. The product was then dried in air. Yield: 2.74 g (60%). IR (KBr) υ_{max}/cm^{-1}: 2969-2814 (CH_2), 2229 (υ_{CN}), 1565, 1520, 1445, 1372, 1290, 1231, 1193, 1133, 1065, 1029, 987, 855, 787, 730, 547, 439. ^{1}H NMR ($CDCl_3$) δ = 7.73-7.56 (m, 3H, Ar-H), 3.22-3.19 (t, 2H, SCH_2), 2.82-2.79 (t, 2H, NCH_2), 2.61-2.58 (dd, 4H, CH_2C), 1.06-1.02 (t, 6H, CH_3) ppm.

2.3.1.3 Cobalt tetrakis-(2-diethylaminoethanethio) phthalocyanine (nonperipheral) (13), Scheme 3.1

A mixture of compound **8a** (0.40 g, 1.54 mmol) and cobalt(II) chloride (0.049 g, 0.38 mmol) was refluxed in 2-(diethylaminoethanol) (1.2 ml) for 12 h under nitrogen. Thereafter, the mixture was cooled to room temperature and treated with excess MeOH: H_2O (1:1) to precipitate the crude deep blue product. The product was filtered and dried in air. Purification was achieved using column chromatography with neutral alumina as column material and DCM/MeOH (10:1) as eluent. Yield: 1.01 g (60%). Calc.

for $C_{56}H_{68}N_{12}S_4Co$: C, 61.37%; H, 6.21%; N, 15.34%; S, 11.69%: Found: C, 60.96%; H, 6.31%; N, 14.80%; S, 12.11%. UV-Vis (DMF): λ_{max} (nm) (log ε): 693 (5.3), 628 (4.8), 478 (4.2); IR (KBr) υ_{max}/cm^{-1}; 2966-2799 (CH_2), 1619, 1572, 1514, 1462, 1384, 1318, 1239, 1113, 919, 739, 595.

2.3.1.4 Manganese(III) acetate tetrakis-(2-diethylaminoethanethio) phthalocyanine (nonperipheral) (14), Scheme 3.1

Complex **14** was synthesized (Scheme 3.1) and purified as described for complex **13**, using compound **8a** (0.40 g, 1.54 mmol) as the starting material, with manganese(II) acetate (0.065 g, 0.38 mmol) as the metal salt, in place of cobalt(II) chloride. Yield: 1.20 g (67%). Calc. for $C_{56}H_{68}N_{12}S_4MnOAc$: C, 57.93%; H, 5.86%; N, 14.48%; S, 11.03%). Found: C, 57.65%; H, 5.96%; N, 13.98%; S, 11.33%. UV-Vis (DMF): λ_{max} (nm) (log ε): 770 (5.4), 696 (4.7), 510 (4.5), 357 (5.0); IR (KBr) υ_{max}/cm^{-1}; 2967-2805 (Aliph-CH_2), 1719, 1568, 1466, 1379, 1235, 1190, 1067, 915, 877 (Mn-O) 766, 738, 592.

2.3.1.5 Iron tetrakis-(2-diethylaminoethanethio) phthalocyanine (non-peripheral) (15), Scheme 3.1

Complex **15** was synthesized (Scheme 3.1) and purified as described for complex **13**, using compound **8a** (0.40 g, 1.54 mmol) as the starting material, with anhydrous iron(II) chloride (0.048 g, 0.38 mmol) as the metal salt, in place of cobalt(II) chloride. Yield: 1.13 g (67%). Calc. for $C_{56}H_{68}N_{12}S_4Fe.CH_2Cl_2$: C, 57.09%; H, 5.78%; N, 14.27%; S, 11.88%. Found: C, 57.34%; H, 5.78%; N, 13.79%; S, 11.01%; UV-Vis (CH_3OH): λ_{max} (nm) (log ε): 689 (5.1), 626 (4.6); IR (KBr) υ_{max}/cm^{-1}; 2966-2803 (Aliph-CH_2), 1600 (aromatic C═C stretch), 1496, 1457, 1384 (CH_2 and CH_3 bends), 1324, 1196, 1140, 1071, 914, 823, 745.

2.3.1.6 4-(2-diethylaminoethanethio) phthalonitrile (10) Scheme 3.2

Compound **10**, Scheme 3.2, was synthesized following the method described above for compound **8a**, using 4-nitrophthalonitrile (compound **9**) (3.05 g, 17.6 mmol) in place of 3-nitrophthalonitrile (compound **7**). Yield: 3.42 g (75%). IR (KBr) υ_{max}/cm^{-1}: 3084-3018

(Ar-C-H), 2968-2807 (CH_2), 2229 (CN), 1582, 1542, 1471, 1384, 1289, 1225, 1198, 1142, 1072, 987, 906, 825, 732, 609, 521. ^{1}H NMR ($CDCl_3$) δ = 7.66-7.54 (m, 3H, Ar-H), 3.15-31.2 (t, 2H, SCH_2), 2.80-2.77 (t, 2H, NCH_2), 2.62-2.57 (qnt, 4H, CH_2C), 1.07-1.03 (t, 6H, CH_3) ppm.

2.3.1.7 Cobalt tetrakis-(2-diethylaminoethanethio) phthalocyanine (peripheral) (16), Scheme 3.2

Complex **16** was synthesized (Scheme 3.2) and purified following the same method described for complex **13**, using compound **10** (0.40 g, 1.54 mmol) as the starting material, in place of compound **8a**. Yield: 1.08 g (64%). Calc. for $C_{56}H_{68}N_{12}S_4Co.CH_2Cl_2$: C, 56.95%; H, 5.76%; N, 14.23%; S, 10.85%); Found: C, 56.87%; H, 5.78%; N, 13.89%; S, 11.25%. UV-Vis (DMF): λ_{max} (nm) (log ε): 675 (5.6), 615 (5.1), 406 (4.8), 352 (5.1); IR (KBr) υ_{max}/cm^{-1}; 2965-2800 (CH_2), 1601, 1519, 1449, 1393, 1312, 1143, 1091, 930, 815, 771, 748, 689.

2.3.1.8 Manganese(III) acetate tetrakis-(2-diethylaminoethanethio) phthalocyanine (peripheral) (17), Scheme 3.2

Complex **17** was synthesized (Scheme 3.2) and purified as described for complex **16**, using compound **10** as the starting material (0.40 g, 1.54 mmol), with manganese(II) acetate (0.065 g, 0.38 mmol) as the metal salt, in place of cobalt(II) chloride. Yield: 1.28 g (72%). Calc. for $C_{56}H_{68}N_{12}S_4MnOAc.H_2O$. C, 57.04%; H, 5.77%; N, 14.26%; S, 10.87%. Found: C, 56.76%; H, 5.72%; N, 14.10%; S, 11.41%. UV-Vis (DMF): λ_{max} (nm) (log ε): 739 (5.1), 662 (4.5), 500 (4.4), 432 (5.5), 365 (4.7); IR (KBr) υ_{max}/cm^{-1}; 2966-2802 (Aliph-CH_2), 1597, 1504, 1450, 1389, 1325, 1067, 924, 878 (Mn-O), 822, 769, 741.

2.3.1.9 Iron tetrakis-(2-diethylaminoethanethio) phthalocyanine (peripheral) (18), Scheme 3.2

Complex **18** was synthesized (Scheme 3.2) and purified as described for complex **16**, using compound **10** as the starting material (0.40 g, 1.54 mmol), with anhydrous iron(II) chloride (0.048 g, 0.38 mmol) as the metal salt, in place of cobalt(II) chloride.

Yield: 1.24 g (74%). Calc. for $C_{56}H_{68}N_{12}S_4Fe.CH_2Cl_2$: C, 57.09%; H, 5.78%; N, 14.27%; S, 11.88%. Found: C, 56.62%; H, 5.61%; N, 14.12%; S, 11.30%; UV-Vis (DCM): λ_{max} (nm) (logε): 704 (5.3), 584 (4.6), 422 (5.0), 354 (5.3); IR: υ_{max}/cm^{-1}: 2972 (CH_2 stretch), 1602 (aromatic C=C stretch) , 1460, 1393 (CH_2 and CH_3 bends), 826, 746 (aromatic C-H bends).

2.3.1.10 1, 2-Bis-(diethylaminoethanethio) phthalonitrile (12), Scheme 3.3

1, 2-Dichlorophthalonitrile (**11**) was synthesized according to reported procedures [214]. Compound **12** (Scheme 3.3) was also synthesized following literature procedure [213], with slight modification as follows: compound **11** (3.49g, 17.67 mmol) was dissolved in anhydrous DMF (100 ml) under nitrogen, followed by the addition of 2-diethylaminoethanethiol hydrochloride (6g, 35.34 mmol). After stirring for 10 min, finely ground anhydrous K_2CO_3 (19.5g, 141.36 mmol) was added in portions over 2 h with stirring. The reaction mixture was stirred at room temperature for 48 h under nitrogen. Thereafter, the solution was poured into ice water (600 g). The precipitate was filtered off, washed with water, until the filtrate was neutral. The product was then dried in air. Yield: 3.61 g (52%). IR (KBr) υ_{max}/cm^{-1}: 3075, 2970-2812, 2229, 1562, 1459, 1382, 1343, 1275, 1200, 1113, 1066, 991, 733, 529. ^{1}H NMR ($CDCl_3$) δ = 7.54 (s, 2H, Ar-H), 3.12-3.08 (t, 4H, SCH_2), 2.80-2.77 (t, 4H, NCH_2), 2.61-2.55 (qnt, 8H, CH_2C), 1.05-1.01 (t, 12H, CH_3) ppm.

The synthesis of cobalt octakis-(2-diethylaminiethanethio) phthalocyanine (peripheral) (complex **19**), scheme 3.3, has been reported before [213].

2.3.1.11 Manganese(III) acetate octakis-(2-diethylaminoethanethio) phthalocyanine (peripheral) (20), Scheme 3.3

Complex **20** was synthesized (Scheme 3.3) according to the method reported for the cobalt analogue (**19**) [213]. A mixture of compound **12** (0.6g, 1.54 mmol), manganese acetate (0.066g, 0.38 mmol) and 2-(diethylaminoethanol) (1.2 ml) was refluxed for 12 h under nitrogen. After cooling to room temperature, the mixture was treated with excess

MeOH: H_2O (1:1 ml) in order to precipitate the product. The product was filtered and dried in air. The product was then purified using column chromatography with neutral alumina as column material and DCM/methanol (20:1) as eluent. Yield: 0.54g (80%). Calc. for $C_{80}H_{120}N_{16}S_8MnOAc.CH_2Cl_2$: C, 58.51%; H, 7.34%; N, 13.16%. Found: C, 57.11%; H, 6.72%; N, 12.63%; UV-Vis (DMF): λ_{max} (nm) (log ε): 440(4.8), 473(4.8), 503(4.8), 681(4.6), 760(5.3); IR (KBr) υ_{max}/cm^{-1}; 2966-2805 (CH_2), 1413, 1377, 1327, 1070, 781, 744, 705, 606.

2.3.1.12 Iron octakis-(2-diethylaminoethanethio) phthalocyanine (peripheral) (21), Scheme 3.3

Complex **21** was synthesized following the method described above for **20**, using anhydrous iron(II) chloride (0.049g, 0.38mmol) in place of manganese(II) acetate. Yield: 0.28g (41%). Calc. for $C_{80}H_{120}N_{16}S_8Fe.2CH_2Cl_2$: C, 55.07%; H, 6.93%; N, 12.52%. Found: C, 54.71%; H, 6.71%; N, 12.34%; UV-Vis (DMF): λ_{max} (nm) (log ε): 360(4.4), 451(3.9), 621(3.7), 657(3.9), 686(4.1), 746(3.8); IR (KBr) υ_{max}/cm^{-1} 2972-2805 (CH_2), 1412, 1357, 1317, 1080, 789, 758, 735, 688.

2.3.2 Arylthio-derivatised metallophthalocyanine complexes

2.3.2.1 3-(Benzylthio) phthalonitrile (8b), Scheme 3.4

Compound **8b** was synthesized (Scheme 3.4) following the procedure reported for 4-(benzylthio) phthalonitrile [74], with some modifications as follows: compound **7** (6 g, 34.68 mmol) was dissolved in anhydrous DMSO (50 ml) under nitrogen, followed by the addition of benzylthiol (5.55 g, 45 mmol). After stirring strongly for 20 min, finely ground anhydrous K_2CO_3 (15 g, 108.7 mmol) was added in portions over 2 h with stirring. The reaction mixture was stirred at room temperature for 12 h under nitrogen. Thereafter, the crude product was precipitated out from the reaction mixture with ice (600 g). The precipitate was filtered off, washed with water, until the filtrate was neutral. The product was crystallized twice from ethanol and dried in air. Yield: 1.91 g (22%). IR (KBr) υ_{max}/cm^{-1}: 3067-3031 (Ar-C-H), 2936-2852 (CH_2), 2226 (υ_{CN}), 1961, 1561,

1500, 1447, 1289, 1187, 1155, 1066, 1030, 911, 854, 785, 709, 589, 555, 483, 434. ^{1}H NMR ($CDCl_3$) δ = 7.62-7.55 (m, 3H, S-Ar-H), 7.36-7.30 (m, 5H, C-Ar-H), 4.31 (s, 2H, CH_2) ppm.

2.3.2.2 Cobalt tetrakis-(benzylthio) phthalocyanine (non-peripheral) (22), Scheme 3.4

Complex **22** was synthesized following the method reported for the peripheral derivative [74], with some modifications. A mixture of compound **8b** (0.6 g, 1.85 mmol) and cobalt(II) chloride (0.063 g, 0.49 mmol) was refluxed in 2-(diethylaminoethanol) (3 ml) for 6 h under nitrogen. The deep green crude product was precipitated, after cooling, in excess methanol. The precipitate was filtered and dried in air. Purification was performed using column chromatography with silica gel as column material and $CHCl_3$/MeOH (10:1) as eluent. Yield: 1.06 g, (42%). Calc. for $C_{60}H_{40}N_8S_4Co.CH_2Cl_2$: C, 62.93%; H, 3.50%; N, 9.79%; S, 11.19%. Found: C, 62.61%; H, 3.91%; N, 9.42%; S, 10.68 %;). UV-Vis (DMF): λ_{max} (nm) (log ε): 692 (5.5), 355 (5.3); IR (KBr) υ_{max}/cm^{-1}; 3059 (*w*, Ar-C-H), 2920 (*w*, CH_2) 1584, 1448, 1318, 1241, 1114, 746, 702.

2.3.2.3 Manganese(III) acetate tetrakis-(benzylthio) phthalocyanine (non-peripheral) (23), Scheme 3.4

Complex **23** was synthesized following the procedure reported for **22** above, using manganese(II) acetate (0.085 g, 0.49 mmol) in place of cobalt(II) chloride. Yield: 1.08 g, (52%). Calc. for $C_{60}H_{40}N_8S_4MnOAc$: C, 64.06%; H, 3.56%; N, 9.96%; S, 11.39%. Found: C, 63.64%; H, 4.02%; N, 9.46%; S, 11.58%; UV-Vis (DMF): λ_{max} (nm) (log ε): 768 (5.4), 690 (4.8), 511 (4.5), 477 (4.5), 357 (5.1); IR (KBr) υ_{max}/cm^{-1}; 3191-3067 (*w*, Ar-C-H), 1763, 1716, 1374, 1308, 1236, 1109, 1064.

2.3.2.4 Iron tetrakis-(benzylthio) phthalocyanine (non-peripheral) (24), Scheme 3.4

Complex **24** was synthesized (Scheme 3.4) following the procedure reported for **22** above, using anhydrous iron(II) chloride (0.062 g, 0.49 mmol) in place of cobalt(II) chloride. Yield: 0.92 g, (47%). Calc. for $C_{60}H_{40}N_8S_4Fe$: C, 68.19%; H, 3.79%; N, 10.61%; S,

12.12%. Found: C, 67.89%; H, 4.04%; N, 10.62%; S, 12.19%; UV-Vis (DMF): λ_{max} (nm) (log ε): 672 (5.4), 609 (5.0), 442 (5.2), 353 (5.6); IR (KBr) υ_{max}/cm^{-1}; 3059-3025 (*w*, Ar-C-H), 2921 (*w*, CH_2) 1722, 1569, 1457, 1312, 1236, 1106, 743, 705.

2.3.3 Formation of acid functionalized single walled carbon nanotubes, Scheme 3.5

Single walled carbon nanotubes (SWCNTs) were purified and oxidized to form SWCNT-COOH by adding raw SWCNTs (100 mg) to a mixture of HNO_3 and H_2SO_4 (3:1) [215]. The resulting suspension was stirred at a temperature of 70°C for 2 h. The final mixture was cooled to room temperature and washed with excess millipore water until a pH of 5 was obtained. The purified SWCNTs (SWCNT-COOH) were dried in an oven for 12 h.

2.3.4 Formation of SWCNT-18 nano-composite, Scheme 3.5

SWCNT-COOH (10 mg) was added to 4 ml of freshly distilled DMF. The mixture was sonicated for 1 h, to aid the solubility of SWCNT-COOH in DMF. DCC (1 mg) was added to the resulting mixture to convert the carboxyl groups of the SWCNT-COOH to active carbodiimide esters. The mixture was stirred under nitrogen for 72 h. Thereafter, 10 mg of complex **18** was added to the black solution and stirred for 72 h under nitrogen. Nucleophilic reaction between the activated –COOH of SWCNT-COOH and tertiary amine group (-NR_3) of the substituent of complex **18** (Scheme 3.2) resulted in the formation of amide bond (coordinate covalent), that links the units together in the nano-composite. The composite was dried in an oven for 12 h and characterized using IR spectroscopy, TEM and XRD techniques.

2.4 Methods

2.4.1 Electrochemical methods

Electrochemical experiments were performed using Autolab potentiostat PGSTAT 302 (Eco Chemie, Utrecht, The Netherlands) driven by the general purpose Electrochemical System data processing software (GPES, software version 4.9) or BioAnalytical Systems (BAS) model 100B/W Electrochemical Workstation (for rotating disc electrode, RDE, voltammetry). Square wave voltammetric analysis was carried out at a frequency of 10 Hz, amplitude of 50 mV and step potential of 5 mV. For all electrochemical experiments, a conventional three-electrode system was used. The working electrode was bare or MPc-modified glassy carbon electrode (GCE, with geometric area of 0.07 cm^2) or MPc-SAM-modified polycrystalline gold disc electrode (Au, with geometric area of 0.02 cm^2). The bare GCE was used for electrochemical characterization of MPc complexes, while MPc-modified gold and glassy carbon electrodes were used for electrocatalytic detection of the analytes investigated in this work. Ag|AgCl wire and platinum wire were used as the pseudo reference and auxiliary (counter) electrodes respectively. The potential response of the Ag|AgCl pseudo-reference electrode was less than the Ag|AgCl (3 M KCl) by 0.015 ± 0.003V. Electrochemical experiments involving MPc complexes were performed in freshly distilled DMF, containing $TBABF_4$ as supporting electrolyte. All electrochemical experiments were carried out in argon saturated solutions. Electrochemical impedance spectroscopy (EIS) measurements were performed with Autolab FRA software between 1.0 MHz and 10 KHz using a 5 mV rms sinusoidal modulation. A non-linear least squares (NNLS) method based on the EQUIVCRT programme [216] was used for automatic fitting of EIS data.

Spectroelectrochemical data were obtained using a home-made optically transparent thin-layer electrochemical (OTTLE) cell (containing Pt grit working and auxiliary electrodes, and a Ag|AgCl pseudo reference electrode) connected to a Bioanalytical Systems (BAS) CV 27 voltammograph.

2.4.2 Design of modified electrodes

2.4.2.1 Electrode pre-treatment

Prior to use, the electrode (GCE) surface was polished with alumina on a Buehler felt pad and rinsed with excess millipore water. The gold electrode surface was also polished in aqueous slurry of alumina on sic-emery paper and subjected to ultrasonic vibration in absolute ethanol to remove residual alumina. The electrode was then etched in hot 'piranha' solution (30% H_2O_2 and concentrated H_2SO_4) (1:3 v/v) for two minutes and rinsed with excess millipore water. It was then scanned in 0.5 M H_2SO_4 between -0.5 to 1.5 V vs. Ag|AgCl to obtain a reproducible scan. Gold-coated glass, employed for surface characterization of SAM films, was used without further pre-treatment. Indium tin oxide (ITO) coated glass, the substrate used for solid state UV-Vis spectral and atomic force microscopic characterizations, was soaked in acetone for six hours and rinsed with the same solvent before use.

2.4.2.2 Self-assembly

The pre-treated polycrystalline gold disc electrode was rinsed with freshly distilled DMF and then immersed in a homogenous solution of the desired MPc complex (1×10^{-4} M) in DMF for 24 hr.

2.4.2.3 Electropolymerization/Electrodeposition

Polymeric or electrodeposited films of MPc were formed on GCE by repetitive cyclic voltammetry scanning of the bare electrode in 1×10^{-3} M of the desired MPc complex in freshly distilled DMF containing 0.1 M $TBABF_4$ supporting electrolyte. Formation of MPc-polymer or electrodeposited film of MPc on ITO glass was also achieved using the same method described for bare GCE.

RESULTS AND DISCUSSIONS

List of Publications

The results reported in this thesis have been published in the following journals

(1) I.A. Akinbulu and T. Nyokong

Synthesis, spectroscopic and electrochemical properties of manganese, nickel and iron octakis-(2-diethylaminoethanethio) phthalocyanines: ***Polyhedron*, 28 (2009) 2831-2838**

(2) I.A. Akinbulu and T. Nyokong

Characterization of polymeric films of new manganese phthalocyanine complex octa-substituted with 2-diethylaminoethanethiol, and its use for the electrochemical detection of bentazon: ***Electrochim. Acta*, 55 (2009) 37-45**

(3) I.A. Akinbulu and T. Nyokong

Syntheses and investigation of the effects of position and nature of substituent on the spectral, electrochemical and spectroelectrochemical properties of new cobalt phthalocyanine complexes: ***Polyhedron*, 29 (2010) 1257-1270**

(4) I.A. Akinbulu and T. Nyokong

The effects of point of substitution on the electrochemical behavior of new manganese phthalocyanines, tetra-substituted with diethylaminoethanethiol: ***Inorg. Chim. Acta*, 363 (2010) 3229-3237**

(5) I.A. Akinbulu, S. Khene and T. Nyokong

Surface properties of self-assembled monolayer films of tetra-substituted cobalt, iron and manganese alkylthio phthalocyanine complexes: ***Electrochim. Acta*, 55 (2010) 7085-7093**

(6) I.A. Akinbulu, S. Khene and T. Nyokong

The effects of point of substitution on the formation of manganese phthalocyanine based molecular materials: surface characterization and electrocatalysis: ***Thin Solid Films*****, 519 (2010) 911-918**

(7) I.A. Akinbulu and T. Nyokong

Fabrication and characterization of single walled carbon nanotubes-iron phthalocyanine nano-composite: Surface properties and electron transport dynamics of its self assembled monolayer film: ***New J. Chem.*****, 34 (2010) 2875-2886**

(8) I.A. Akinbulu and T. Nyokong

Formation, surface characterization and electrocatalytic application of self assembled monolayer films of tetra-substituted manganese, iron and cobalt benzylthio phthalocyanine complexes: ***J. Solid State Electrochem.*** **in press**

CHAPTER 3

CHARACTERIZATION

3.1 Metallophthalocyanine complexes

3.1.1 Synthesis

The synthetic pathway for complexes **13-15** is shown in Scheme 3.1. Compound **8a** was obtained via a based-catalyzed (K_2CO_3) nucleophilic aromatic substitution reaction. Cyclotetramerization of **8a** occurred in the presence of the desired metal salts: $CoCl_2$, $Mn(CH_3COO)_2$ and $FeCl_2$ to form complexes **13**, **14** and **15**, respectively. The complexes were purified using column chromatography on alumina and are soluble in solvents such as DMF, THF and DMSO.

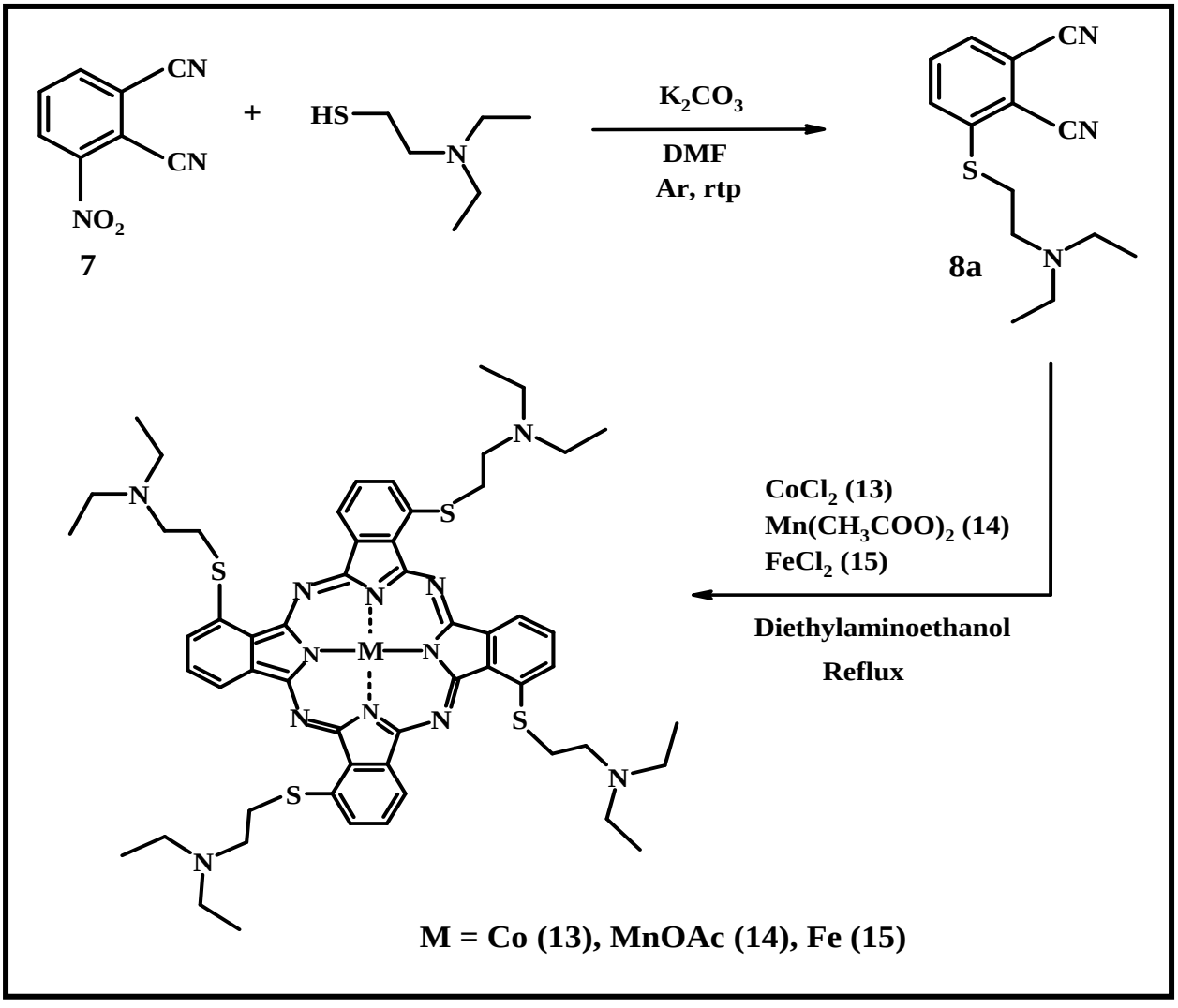

Scheme 3.1: Synthetic pathway for complexes **13-15**

Scheme 3.2 shows the synthetic route for complexes **16-18**. Formation of compound **10** was also effected via a based-catalyzed (K_2CO_3) aromatic nucleophilic attack. Cyclization of compound **10** in the presence of $CoCl_2$ (for **16**), $Mn(CH_3COO)_2$ (for **17**) and $FeCl_2$ (for **18**) resulted in the formation of the target complexes. The resulting complexes were soluble in solvents like DMF, DMSO, THF and DCM. Purification of these complexes was done using the same method described for complexes **13-15**.

It is important to mention that, in each case, formation of complexes **13-18** may be accompanied by the formation of the mixture of four possible structural isomers (C_{4h}, C_{2v}, C_s and D_{2h}). However, no attempt was made to separate these isomers.

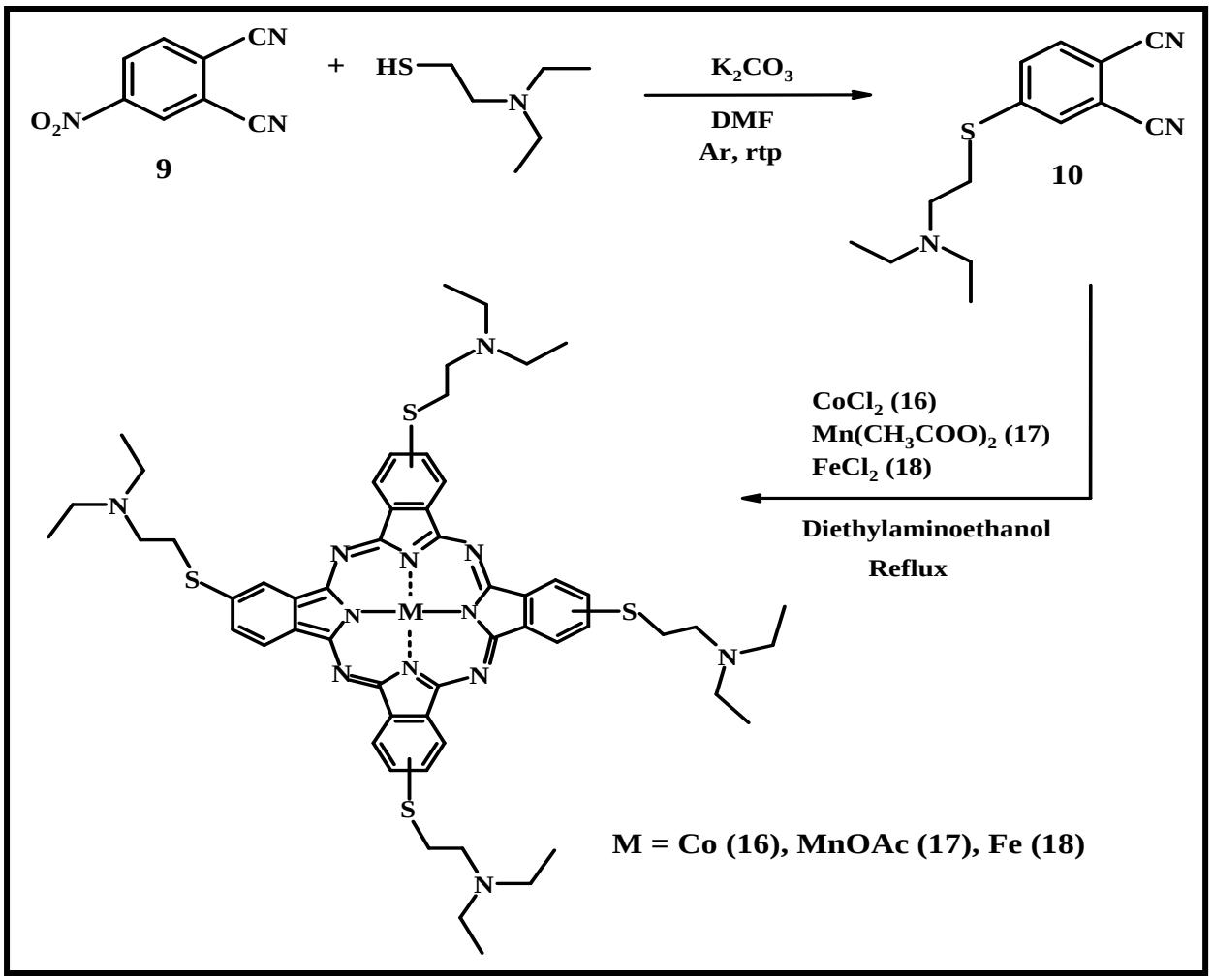

Scheme 3.2: Synthetic pathway for complexes **16-18**

The synthetic route for complexes **19-21** is depicted in Scheme 3.3. The phthalonitrile precursor for these complexes (compound **12**) was also formed via nucleophilic aromatic substitution reaction in the presence of a catalyst (K_2CO_3). Cyclization of this precursor occurred, in the presence of the appropriate metal template, $CoCl_2$ (for **19**), $Mn(CH_3COO)_2$ (for **20**) and $FeCl_2$ (for **21**), to form the target complexes. Like the other complexes discussed above, complexes **19-21** were soluble in solvents such as DMF, DMSO and DCM. Purification was effected as discussed for complexes **13-15**.

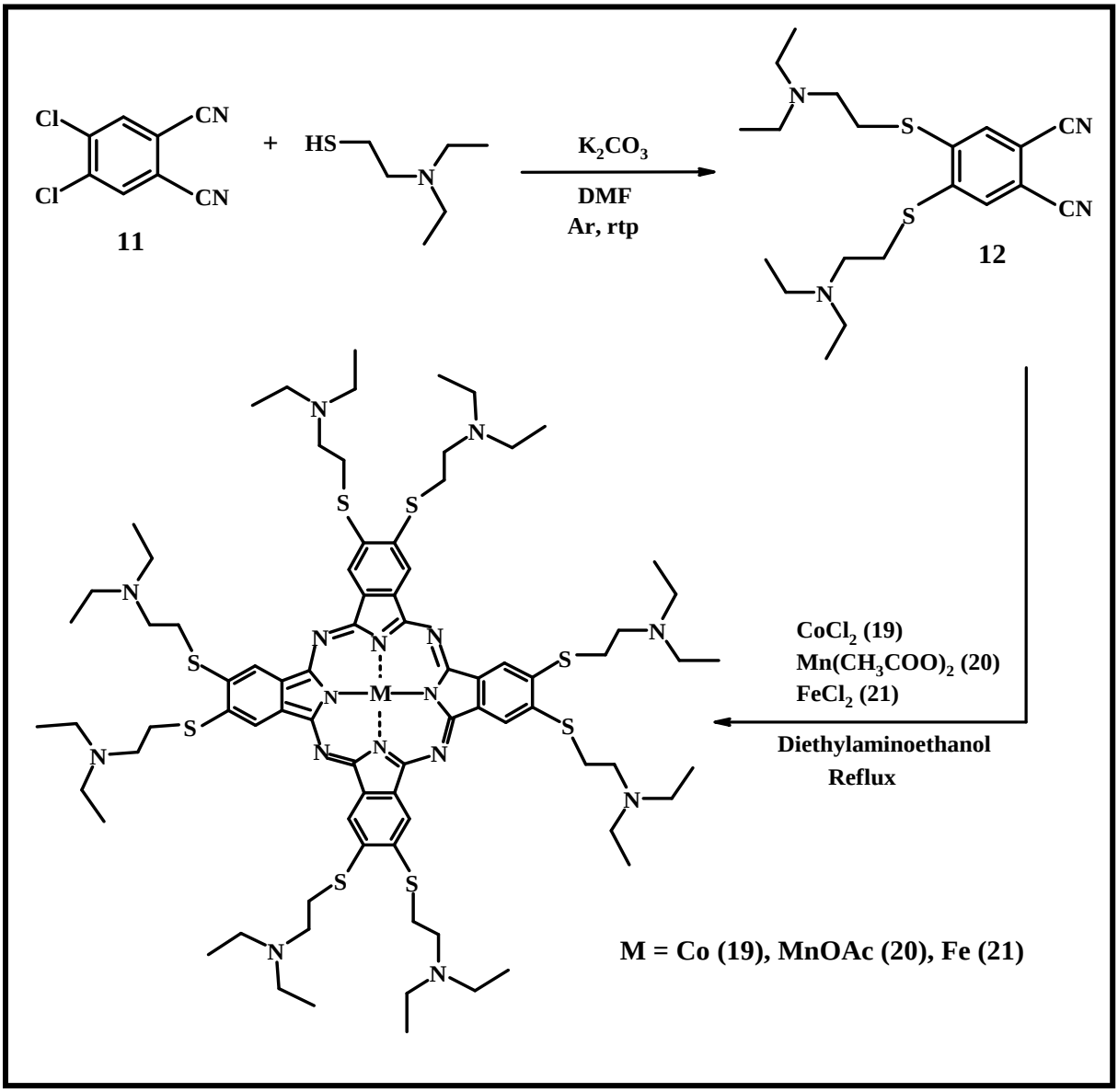

Scheme 3.3: Synthetic pathway for complexes **19-21**.

Complexes **22-24** were synthesized as shown in Scheme 3.4. Like the other complexes, their phthalonitrile precursor (compound **8b**) was formed via aromatic nucleophilic substitution reaction, catalyzed by a base (K_2CO_3). The nucleophilic substituent engaged in this respect was benzylthiol. Cyclization of compound **8b** took place in the presence of the desired metal salts, $CoCl_2$ (for **22**), $Mn(CH_3COO)_2$ (for **23**) and $FeCl_2$ (for **24**), to give the corresponding MPc complexes. These complexes are soluble in DMF, DMSO, THF and DCM. Like complexes **13-21**, column chromatography was employed for purification of complexes **22-24**, but silica gel was used as column material, instead of alumina, due to the non-polar nature of the substituent.

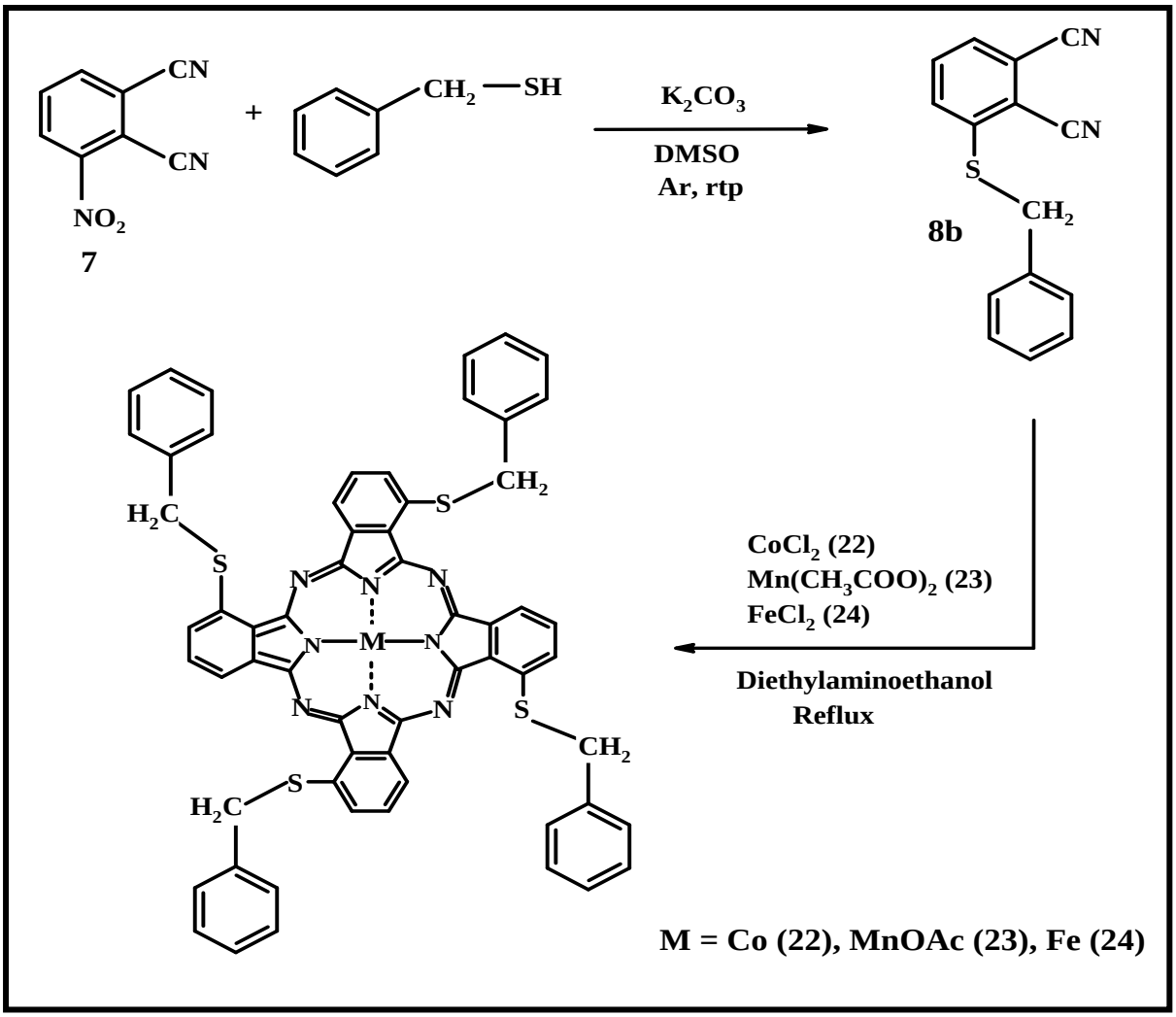

Scheme 3.4: Synthetic pathway for complexes **22-24**.

All the complexes (**13-24**) were characterized by IR and UV-Vis spectroscopies as well as elemental analysis. The results obtained are in agreement with the predicted structures in Schemes 3.1, 3.2, 3.3 and 3.4. The disappearance of the strong C≡N stretches at 2229 cm^{-1} (for compounds **8a, 10 and 12**) and 2226 cm^{-1} (for compound **8b**) confirmed the formation of the complexes. All the MnPc complexes (**14, 17, 20 and 23***)* contain acetate axial ligand, evidenced from the presence of Mn-O stretch (877 cm^{-1}) in their IR spectra.

3.1.2 UV-Vis Spectral Properties

3.1.2.1 Complexes 13, 16, 19 and 22 (CoPcs)

Fig. 3.1 shows the UV-Vis spectra, in DMF, of the cobalt complexes {4.41 × 10^{-6} M (**13**), 4.22 × 10^{-6} M (**16**), 4.21 × 10^{-6} M (**19**) and 2.75 × 10^{-6} M (**22**)} studied in this work. The effects of position {non-peripheral (**13)** versus peripheral (**16**)} and number {tera-substituted (**16**) versus octa-substituted (**19**)} of substituent on the spectral qualities of these complexes are clearly observable. However, the nature of substituent {diethylaminoethanethio (**13**) versus benzylthio (**22**)} has no significant effect on the position of Q-band in these complexes. The shift in Q-band position and changes in absorption behavior have been explained in terms of conformational distortion caused by the stress of the substituents in MPcs complexes [217]. Coordination of certain ligands to the central metal, enlargement of the π-system of the Pc [218-220] and aggregation behavior have also been implicated.

Complex **13** (non-peripheral) shows Q-band absorption at 693 nm in DMF, while that of complex **16** (peripheral) is observed at 675 nm (Table 3.1). The Q-band of complex **22** (692 nm) (Table 3.1) is also red-shifted (bathochromic effect) compared to that of the previously reported peripheral analogue (674 nm) [74]. Usually, non-peripheral substitution in MPc complexes imposes some measure of steric strain on these macrocycles, leading to conformational distortion of the Pc skeleton, resulting in change in absorbance and shift in the position of Q-band. The degree of steric strain is closely

related to the complexity of the substituent. The position of Q-band in complex **19** (peripherally octa-substituted) (699 nm), Table 3.1, is also red-shifted relative to that of complex **16** (peripherally tetra-substituted) (675 nm). This observation can be interpreted in terms of enhanced electron-releasing tendency, due to the plurality of electron-donating substituent on the Pc ligand. However, the Q-band position in complex **13** (693 nm) (diethylaminoethanethio-substituted CoPc) shows no distinct difference from that of complex **22** (692 nm) (benzylthio-substituted CoPc), Table 3.1. Also, it is important to note the broad nature of the absorption band in complex **22**, this is characteristic of some aggregations in MPc complexes. Fig. 3.2 (1.27 to 8.89 × 10^{-6} M) shows the effect of changing concentration on the spectra of complex **13** (representative of the other CoPc complexes). Beer's law was obeyed within the range of concentrations investigated for all the complexes.

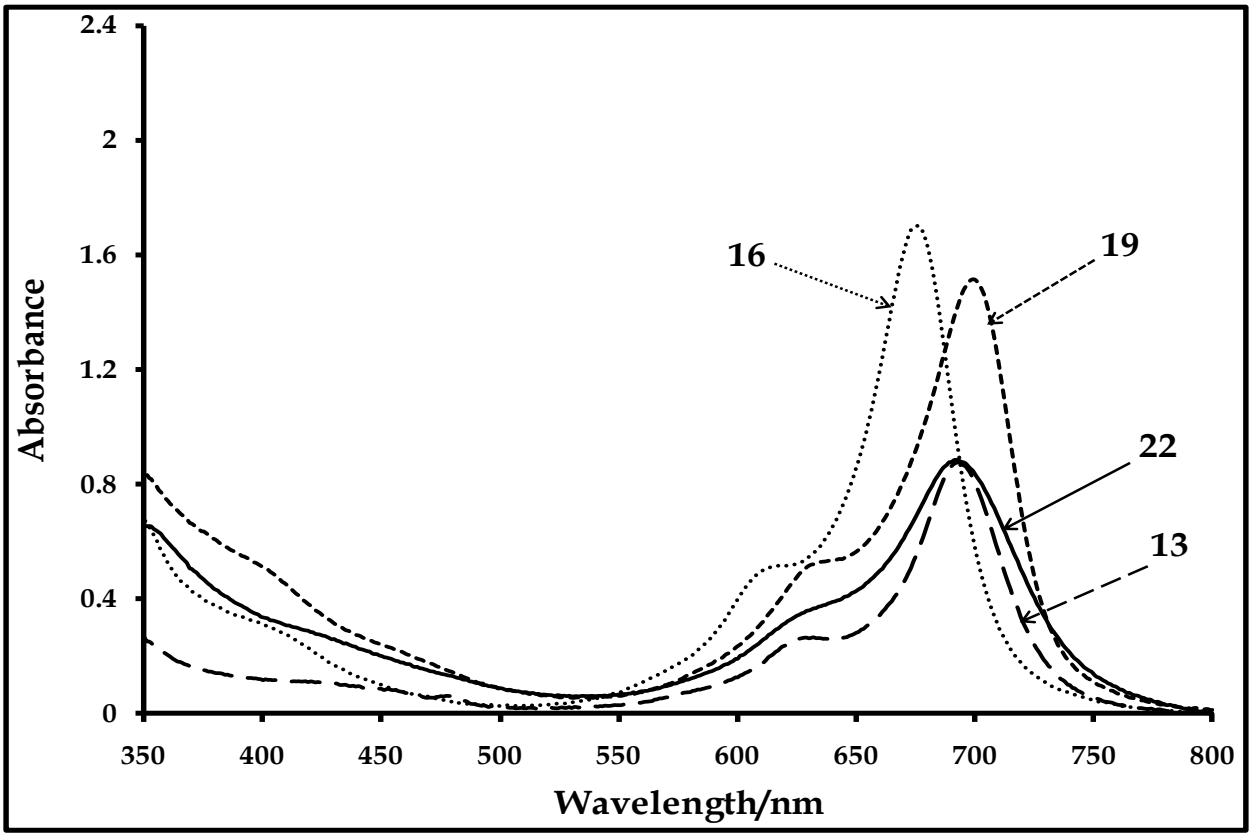

Figure 3.1: UV-Vis spectra of complexes **13** (4.41 × 10^{-6} M), **16** (4.22 × 10^{-6} M), **19** (4.20 × 10^{-6} M) and **22** (2.75 × 10^{-6} M) in DMF.

Table 3.1: Summary of Q-band maxima of complexes **13-24**

Complex	Q-band/nm	Solvent
13 (CoPc)	693	DMF
14 (MnPc)	770	DMF
15 (FePc)	689	MeOH
16 (CoPc)	675	DMF
17 (MnPc)	739	DMF
18 (FePc)	704	DCM
19 (CoPc)	699	DMF
20 (MnPc)	760	DMF
21 (FePc)	686	DMF
22 (CoPc)	692	DMF
23 (MnPc)	768	DMF
24 (FePc)	672	DMF

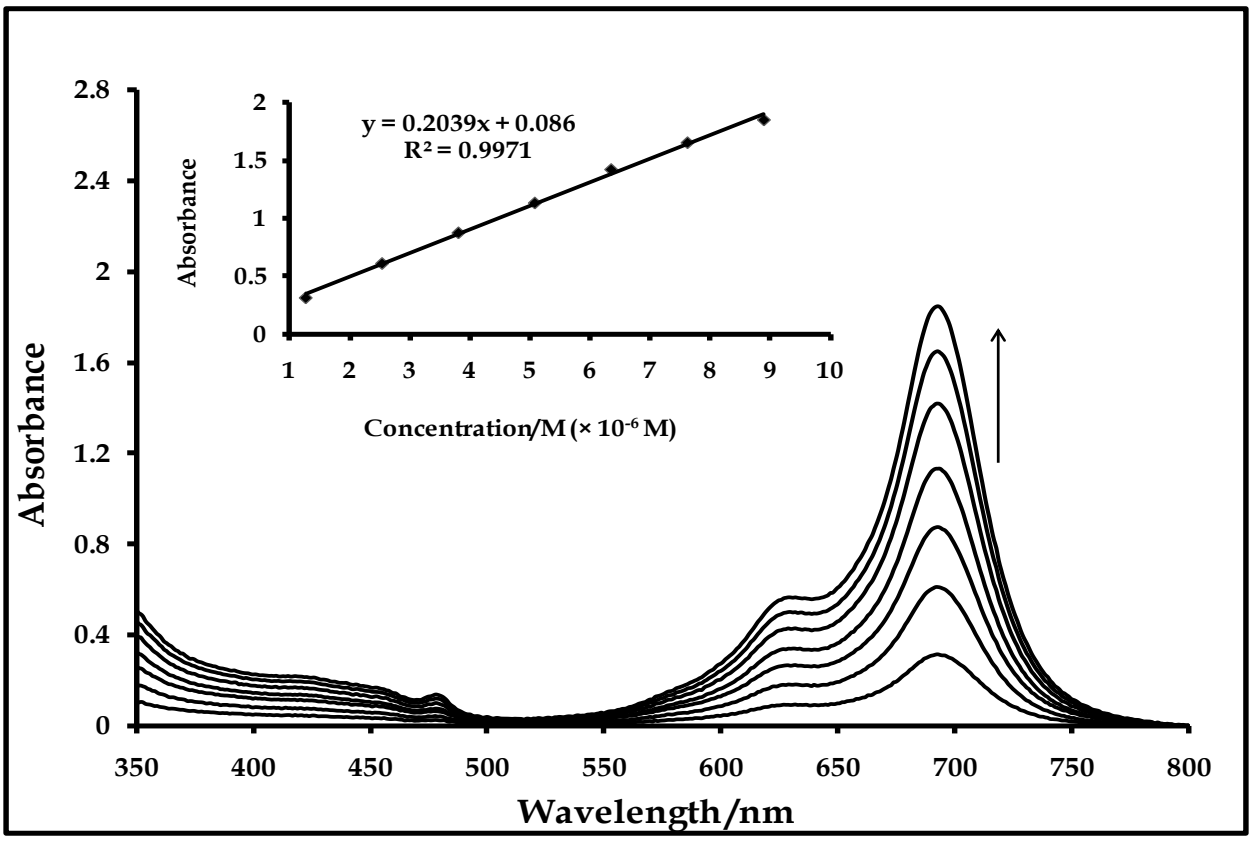

Figure 3.2: UV-Vis spectra of complex **13** (1.27 - 8.89 × 10^{-6} M) in DMF.

3.1.2.2 Complexes 14, 17, 20 and 23 (MnPcs)

The UV-Vis spectra of the MnPc complexes studied in this work are shown in Fig. 3.3. Q-band maxima of the complexes are indicated in Table 3.1. The spectra were measured in DMF, for 8.82 × 10^{-6} M of complex **14**, 1.26 × 10^{-5} M of complex **17**, 8.82 × 10^{-6} M of complex **20** and 7.56 × 10^{-6} M of complex **23**. Like the cobalt derivatives, the spectral properties of these complexes are influenced by the position and number of substituent on the Pc ligand. Also, the nature of substituent has no substantial effect on the position of Q-band. As expected, the Q-band of the non-peripherally tetra-substituted complex (**14**) (770 nm) is red-shifted with respect to the peripheral derivative (**17**) (739 nm). Similar spectral feature was also observed between complexes **20** and **17** (octa- versus tetra-substituted). The Q-band of **20** (octa-substituted) (760 nm) is red-shifted relative to that of **17** (tetra-substituted) (739 nm). The interpretation of this observation is the same as that offered, previously, for the CoPc analogues. The Q-band of **23** (768 nm)

(benzylthio substituted) is slightly blue-shifted compared to that of the diethylaminoethanethio substituted derivative, **14**, (770 nm), Table 3.1, which underscores the minimal effect of the nature of substituent on the spectral properties of these complexes. The other bands in the 420 – 530 nm region are due to charge transfer transitions, while the weak band around 630 nm in complex **17** is characteristic of MnPc μ-oxo species.

It is important to mention the effect of the Mn central metal ion, relative to that of a Co centre, on the spectral qualities of these complexes (Table 3.1). The Q-bands of the MnPc complexes are red-shifted compared to the corresponding CoPc complexes. This is typical of MnPc complexes [91]. Also, it is imperative to highlight that the positions of Q-band in all the MnPc complexes are consistent with that of $Mn^{III}Pc$ species. Although, manganese(II) acetate was the metal salt employed for synthesis (Schemes 3.1-3.4), the

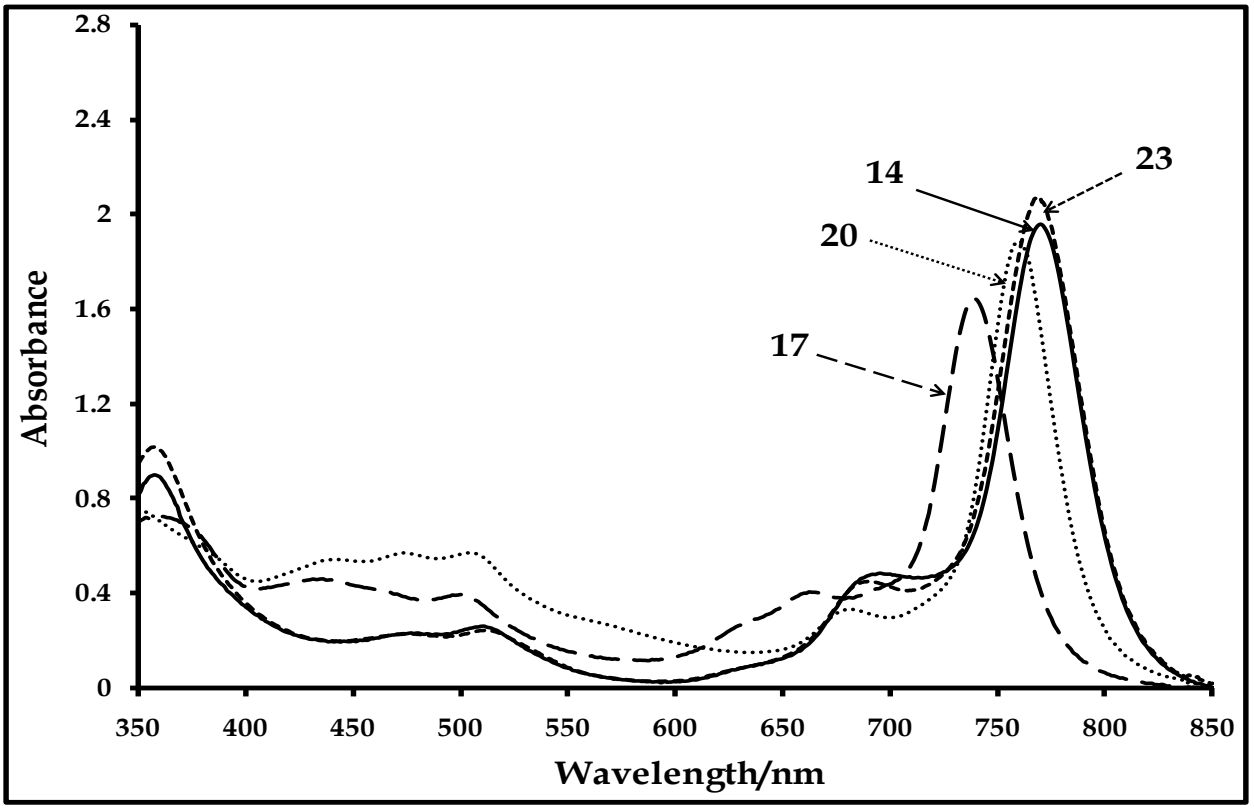

Figure 3.3: UV-Vis spectra of complexes **14** (8.82×10^{-6} M), **17** (1.26×10^{-5} M), **20** (8.82×10^{-6} M) and **23** (7.56×10^{-6} M) in DMF.

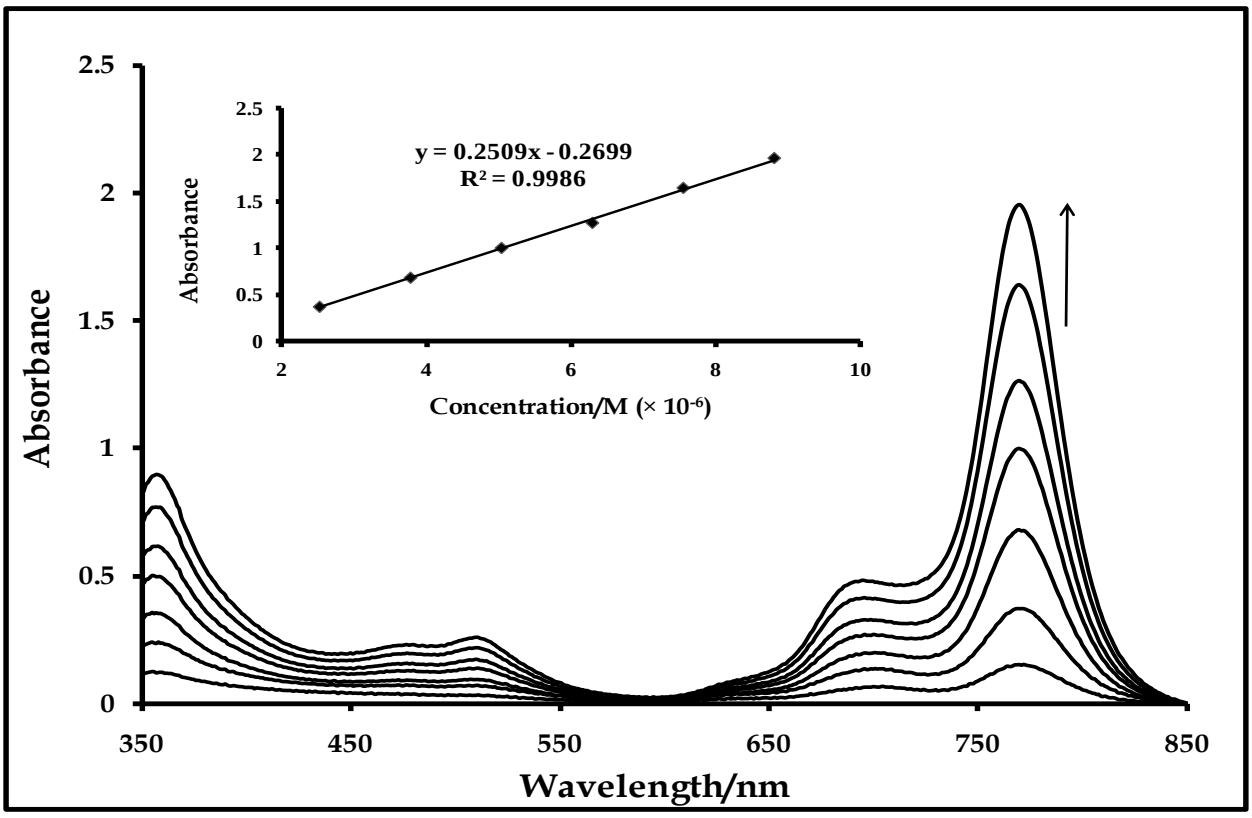

Figure 3.4: UV-Vis spectra of complex **14** (1.26 - 8.82 × 10^{-6} M) in DMF.

negative potential of the Mn^{III}/Mn^{II} species makes it air sensitive, facilitating the oxidation of Mn^{II} to Mn^{III} during synthesis and purification [67]. The dependence of absorbance on concentration of these complexes is shown in Fig. 3.4, for complex **14** (representative of the other MnPc complexes). For all the complexes, Beer's law was obeyed within the concentration ranges investigated.

3.1.2.3 Complexes 15, 18, 21 and 24 (FePcs)

Although, all the complexes are soluble in DMF, the observed trend in the UV-Vis spectral properties of the Co and MnPc complexes, in DMF, can not be investigated for the Fe analogues, due to the complicated nature of their spectra in this solvent, especially the alkylthio-substituted derivatives (**15**, **18** and **21**). Also, the complexes were not soluble in the same solvent, hence the use of different solvents for the

investigation of their UV-Vis spectral properties, Table 3.1. However, the spectroscopic properties of complex **21** were evaluated in DMF.

Fig. 3.5A shows the UV-Vis spectrum of 5.16×10^{-6} M of complex **15** in methanol, with the Q-band absorption at 689 nm. The UV-Vis spectrum of complex **18** (5.50×10^{-6} M), in DCM (Fig. 3.5B), shows a broad Q-band, characteristic of aggregation, at 704 nm. The bands at 422 and 354 nm are typical of charge transfer and B-band, respectively.

Complex **21** exhibits spectral behavior (Fig. 3.5C) characteristic of a stacked monomer in FePc complexes. This is normally observed at about 630 nm in DMF [221]. The UV/visible spectral analysis of FePc complexes has been a subject of extensive research due to the complexity and the wide variety of species that may be formed in solution. For example, perchlorinated iron(II) phthalocyanine dissolved in DMF is known [222] to react with oxygen, resulting in oxidation and formation of a μ-oxo species, $Pc^{-2}Fe^{III}$-O-$Fe^{III}Pc^{-2}$, which changes back to the original monomeric species upon reduction. In the present study, the spectra in Fig. 3.5C were obtained in freshly prepared, dearated DMF solutions, suggesting that the peak near 630 nm is not related to the μ-oxo species, but the presence of monomeric species, as well as cofacially aggregated one. On dilution (5.2×10^{-5} M to 7.42×10^{-6} M), the peak near 630 nm decreased faster than the main peak at 686 nm. Aggregation (the presence of the band near 630 nm) was evident, even at concentration as low as 7.42×10^{-6} M, Fig. 3.5C. The split in the main Q band suggests the presence of $Fe^{III}Pc$ species [91].

The UV-Vis spectrum of complex **24** (benzythio-derivatised, non-peripherally tetra-substituted derivative), in DMF, is shown in Fig. 3.5D. The Q-band appeared at 672 nm, while peaks at 442 and 353 nm are characteristic of charge transfer and B band, respectively. The peak around 638 nm can be associated with aggregation.

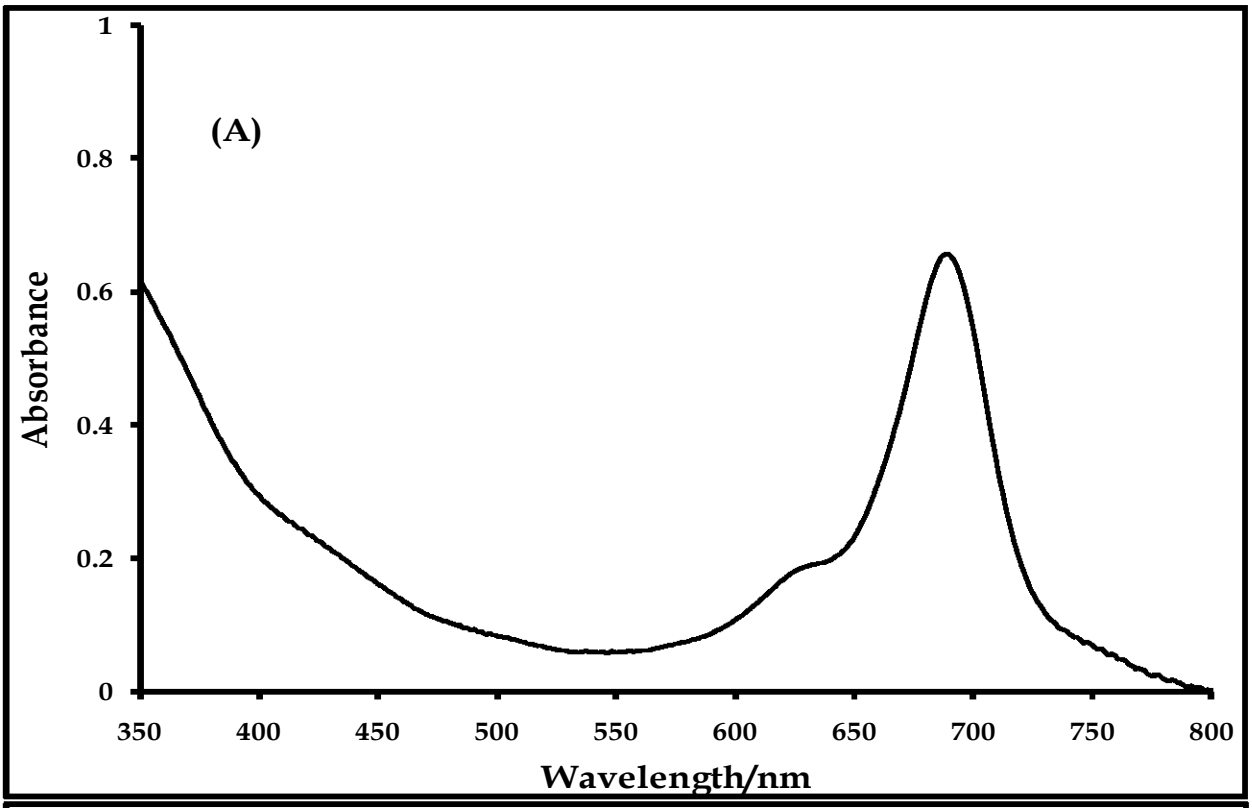
(A)
Absorbance
1
0.8
0.6
0.4
0.2
0
350
400
450
500
550
600
650
700
750
800
Wavelength/nm

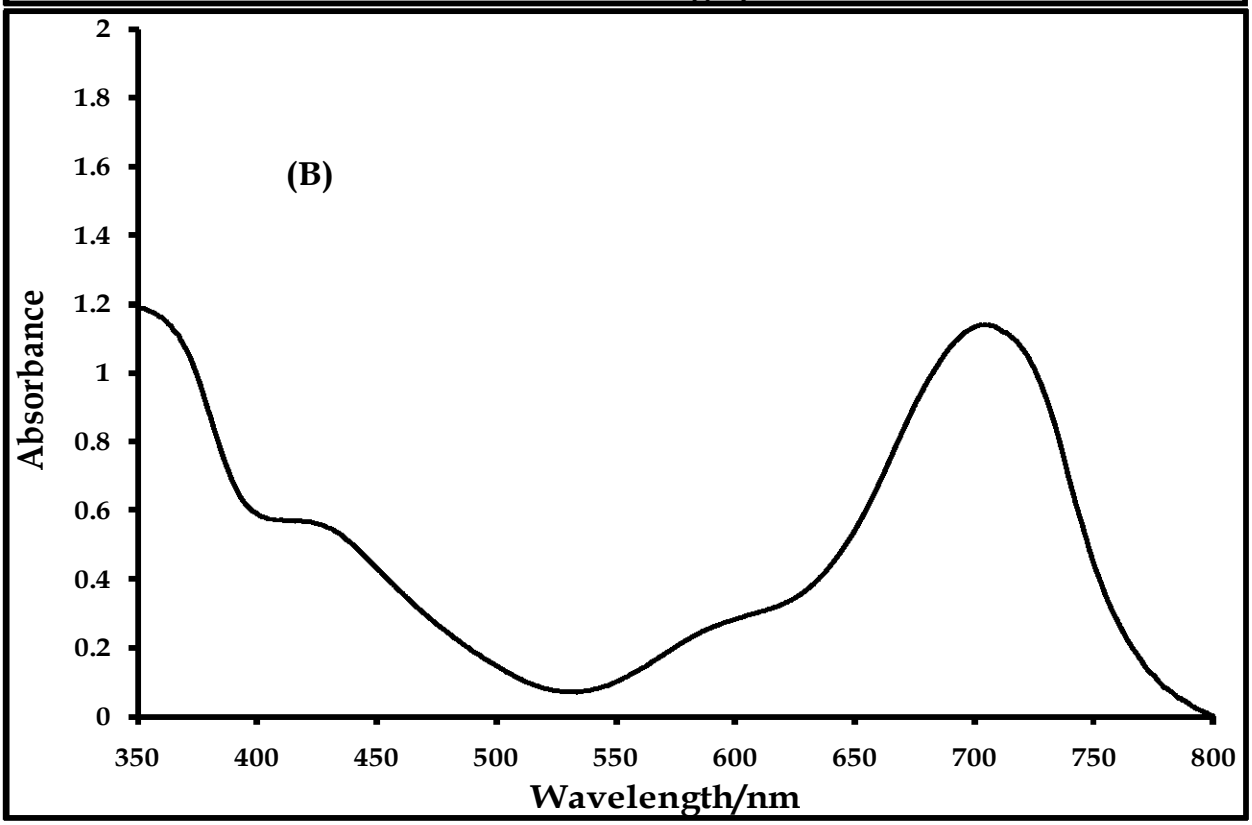
(B)
Absorbance
2
1.8
1.6
1.4
1.2
1
0.8
0.6
0.4
0.2
0
350
400
450
500
550
600
650
700
750
800
Wavelength/nm

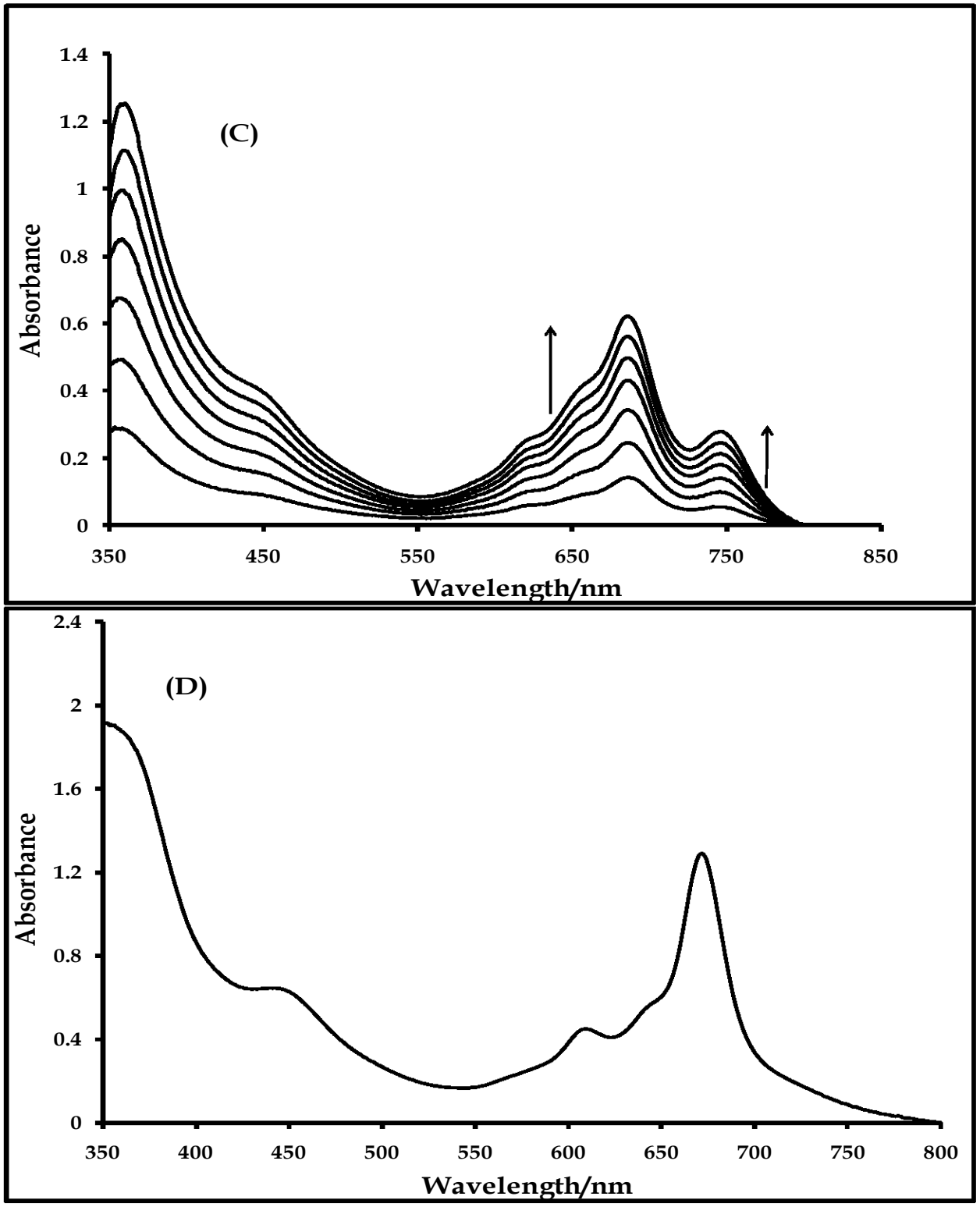

Figure 3.5: UV-Vis spectra of (A) complexes **15** (5.16×10^{-6} M) in MeOH, (B) **18** (5.50×10^{-6} M) in DCM, (C) **21** (7.42×10^{-6} - 5.2×10^{-5} M) in DMF and (D) **24** (4.25×10^{-6} M) in DMF.

3.1.3 Electrochemical and Spectroelectrochemical Properties

3.1.3.1 Cobalt phthalocyanine complexes

3.1.3.1.1 Complex 13

Figs. 3.6A and B show, respectively, the square wave and cyclic voltammetry of 1×10^{-3} M of complex **13**, in freshly distilled, dried DMF, containing 0.1 M $TBABF_4$ (supporting electrolyte). Two irreversible oxidations (processes **III** and **IV**) were observed. Process **III**, at E_p = +0.41 V vs. Ag|AgCl, is assigned to a metal-based oxidation: $Co^{III}Pc^{-2}/Co^{II}Pc^{-2}$, while process **IV**, at E_p = +0.86 V vs. Ag|AgCl, is a ring-based oxidation: $Co^{III}Pc^{-1}/Co^{III}Pc^{-2}$, Table 3.2. The larger current observed for **IV** may be attributed to the oxidation of the Pc ring, plus contribution from the ring substituents, as typical of sulfur containing MPc complexes [95,223]. Two reduction processes (**I** and **II**) were observed. The metal reduction, process **II** ($E_{1/2}$ = -0.38 V vs. Ag|AgCl), is reversible, with ΔE value of 81 mV and cathodic to anodic peak current ratio close to unity. This is assigned to $Co^{II}Pc^{-2}/Co^{I}Pc^{-2}$ species, Table 3.2. Process **I**, at $E_{1/2}$ = -1.46 V vs. Ag|AgCl, Table 3.2, is assigned to ring reduction ($Co^{I}Pc^{-2}/Co^{I}Pc^{-3}$), typical of CoPc complexes in DMF solutions. This couple is quasi-reversible, with ΔE value of 110 mV. The extra peaks observed in Fig. 3.6 (more pronounced on the more sensitive square wave voltammogram) can be attributed to aggregation.

Table 3.2: Summary of electrochemical data of CoPc complexes in DMF, values in Volt vs. Ag|AgCl.

Complex	$Co^{I}Pc^{-2}/Co^{I}Pc^{-3}$	$Co^{II}Pc^{-2}/Co^{I}Pc^{-2}$	$Co^{III}Pc^{-2}/Co^{II}Pc^{-2}$	$Co^{III}Pc^{-1}/Co^{III}Pc^{-2}$
13	-1.46	-0.38	+0.41	+0.86
16	-1.26	-0.24	+0.64	_
19	-1.40	-0.32	+0.80	_
22	-1.25	-0.26	+0.59	_

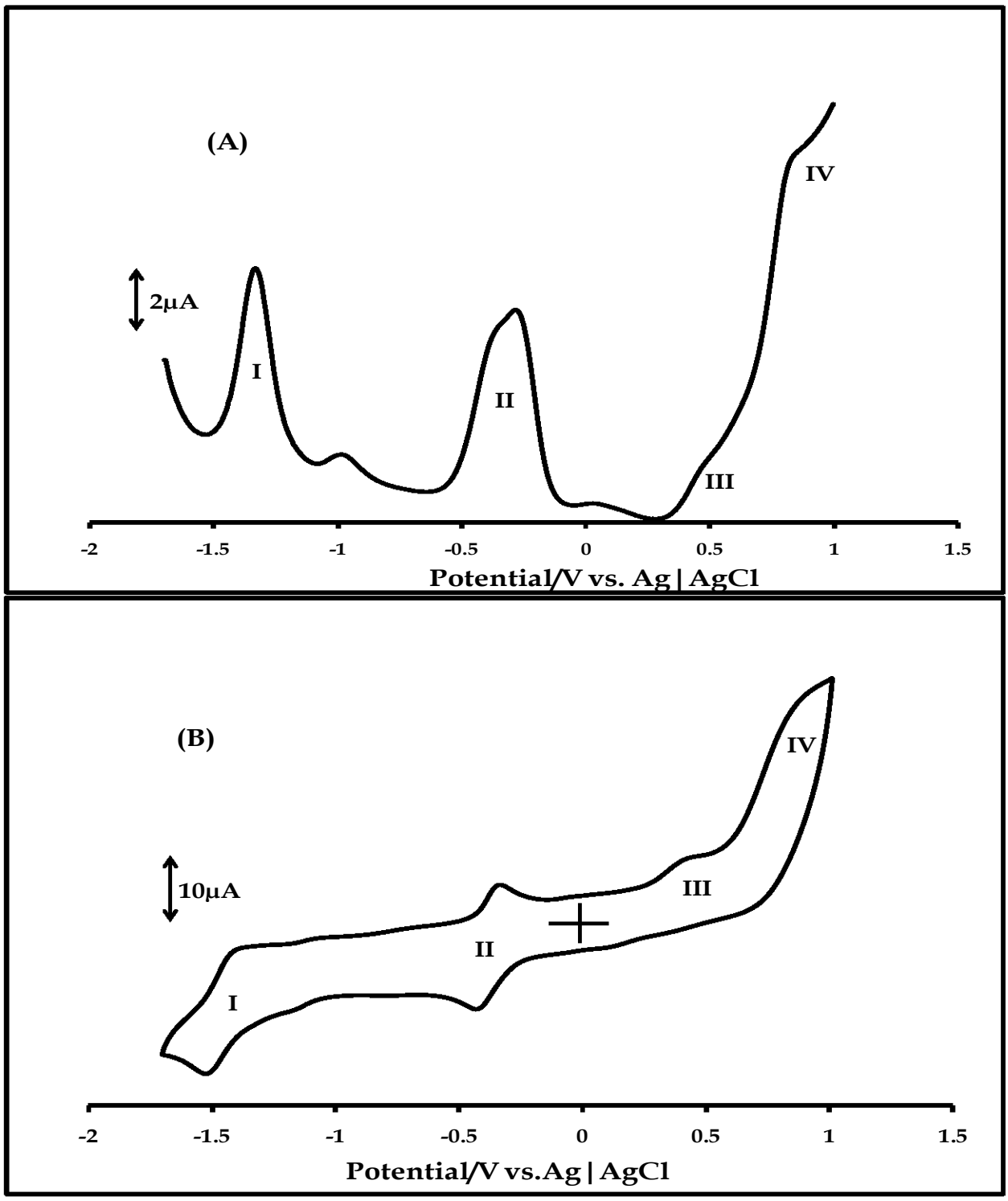

Figure 3.6: (A) Square wave and (B) cyclic voltammetry profiles of 1 × 10^{-3} M of complex **13** in freshly distilled DMF containing 0.1 M $TBABF_4$ supporting electrolyte. Step potential: 5 mV, amplitude: 50 mV, frequency: 10 Hz. Scan rate: 100 mVs^{-1}.

The above redox processes were confirmed using spectroelectrochemistry. Fig. 3.7 shows the spectral transformations obtained during spectroelectrochemical investigation of the properties of complex **13**. The spectral changes in Fig. 3.7A were observed on the application of potential more negative of process **II** ($E_{1/2}$ = -0.38 V vs. Ag|AgCl, Fig. 3.6B). The Q-band of the starting spectrum (bold solid line) (694 nm) is similar to the spectrum of complex **13** (693 nm) in Fig. 3.1, showing minimal effects of the electrolyte. Reduction resulted in shift in Q-band from 694 to 712 nm (bold dashed line), Table 3.3, with constant intensity. Also, there was the emergence of new intense band at 473 nm. Presence of new intense peaks, between 400 to 500 nm region, typifies the formation of $Co^{I}Pc$ species [91]. The shift in Q-band, without change in intensity, is characteristic of metal-based reduction in MPc complexes. Thus, the spectral changes noticed in Fig. 3.7A confirm the assignment of process **II** (Fig. 3.6B) to $Co^{II}Pc^{-2}/Co^{I}Pc^{-2}$ species. Clear isobestic points, noticed at 570 and 705 nm, show that process **II** (Fig. 3.6B) is a clean reduction involving two species. Regeneration of over 90% of the starting spectrum, on the application of zero potential, confirmed reversibility.

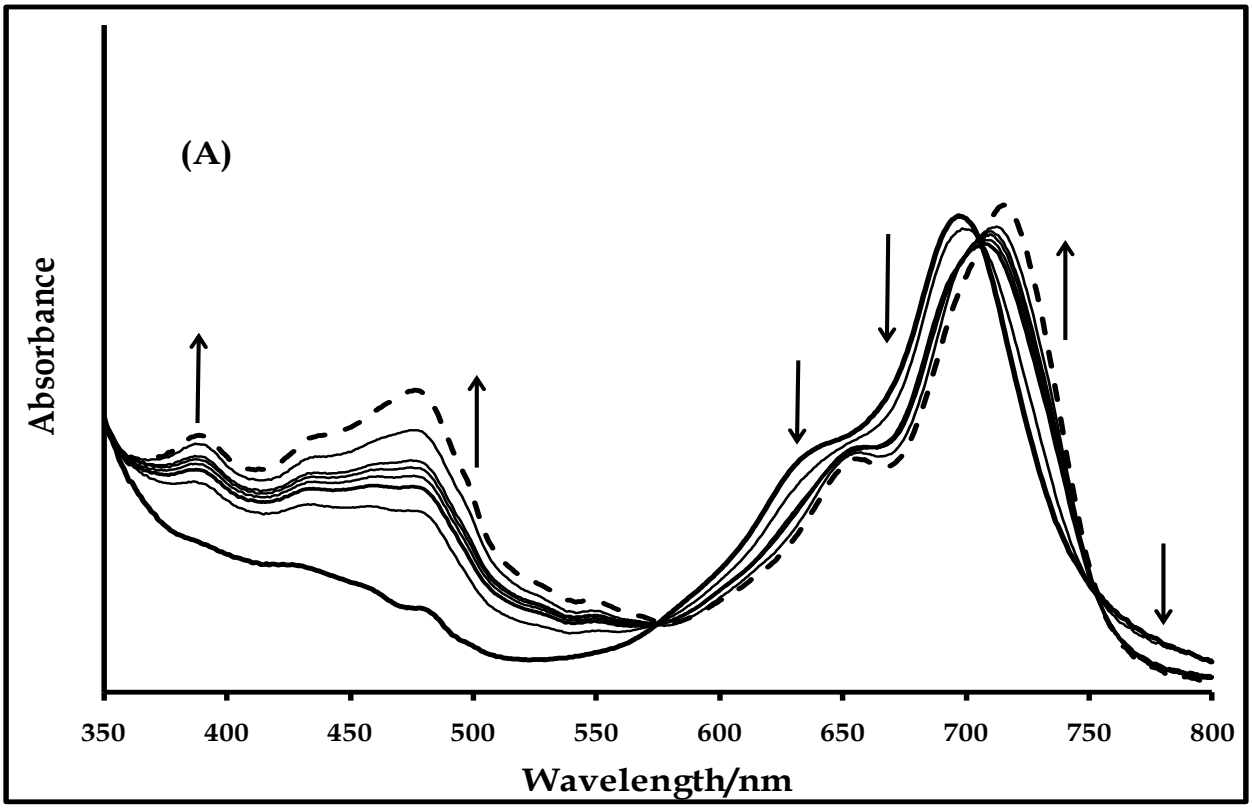

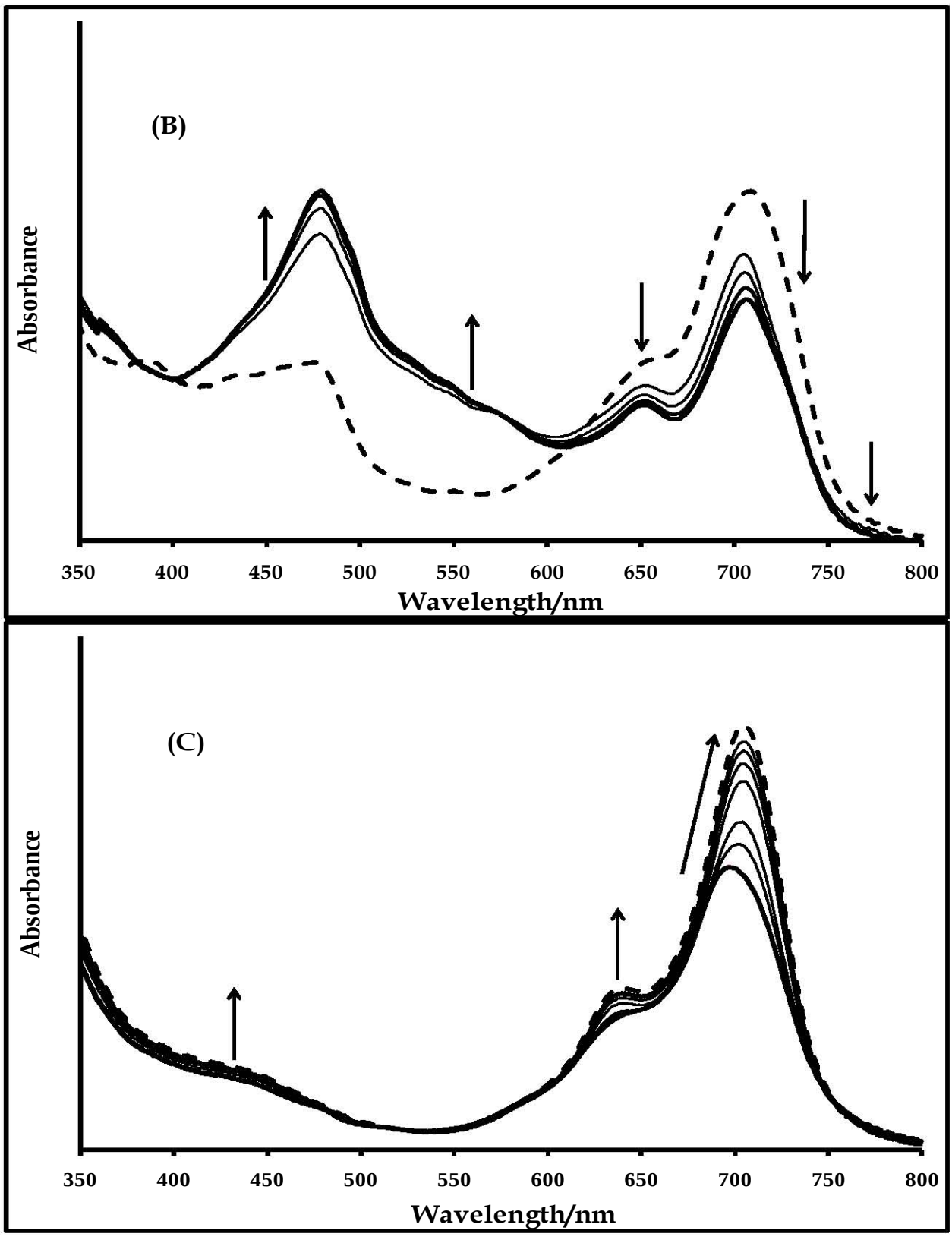
(B)
Absorbance
350
400
450
500
550
600
650
700
750
800
Wavelength/nm
(C)
Absorbance
350
400
450
500
550
600
650
700
750
800
Wavelength/nm

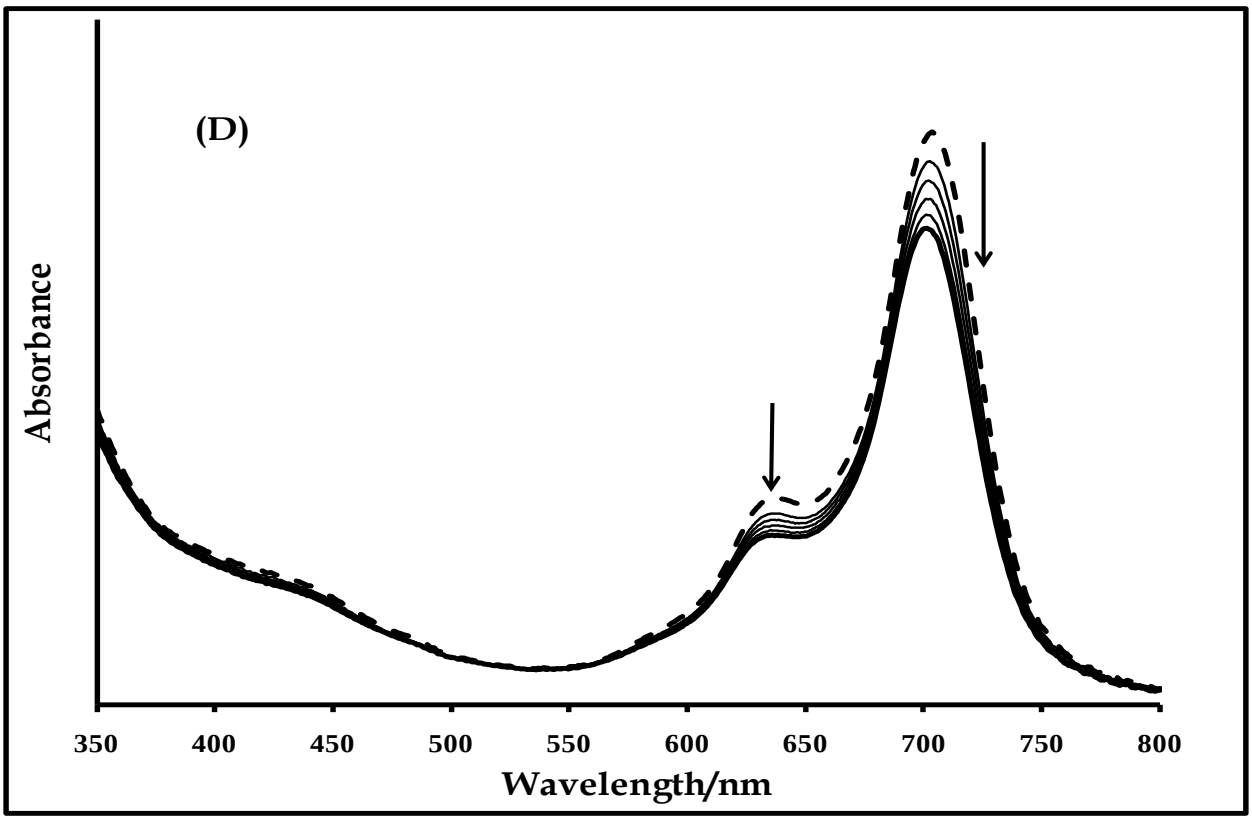

Figure 3.7: UV-Vis spectral changes observed for complex **13** during controlled potential electrolysis at (**A**) -0.45 V (process **II**), (**B**) -1.5V (process **I**), (**C**) +0.5 V (process **III**) and (**D**) +0.9 V (process **IV**) vs. Ag|AgCl. Electrolyte = DMF containing 0.1 M $TBABF_4$. The final spectra in (**A**) and (**C**) are the starting spectra in (**B)** and (**D**) respectively.

The number of electrons transferred in Fig. 3.7A was calculated to be approximately 1, using equation 3.1.

$$Q = nFVC \qquad 3.1$$

where n, F, V and C are the number of electrons transferred, Faraday's constant, volume and concentration of the electroactive species, respectively.

The species obtained in Fig. 3.7A was further reduced (Fig. 3.7B) by the application of a potential more negative of that of couple **I** ($E_{1/2}$ = -1.46 V vs. Ag|AgCl, Fig. 3.6B). There was a decrease in intensity of the new Q-band (bold dashed line) and emergence of a new band (bold solid line) at 570 nm. These spectral changes are consistent with the

formation of a Pc^{-3} species [224]. This confirms the assignment of couple **I** (Fig. 3.6B) to $Co^{I}Pc^{-2}/Co^{I}Pc^{-3}$ species.

Application of a potential positive of process **III** (E_p = +0.41 V vs. Ag|AgCl, Fig. 3.6B) resulted in the spectral changes shown in Fig. 3.7C**.** The Q-band of the starting spectrum (bold solid line) was red-shifted (from 694 to 702 nm) (Table 3.3), with increased intensity, upon oxidation. These spectral changes are consistent with the oxidation of Co^{II} to Co^{III}, Table 3.3. Hence, confirming the assignment of process **III** (Fig. 3.6B) to $Co^{III}Pc^{-2}/Co^{II}Pc^{-2}$ species.

Table 3.3: Q-band maxima of initial, oxidized and reduced species for CoPc and MnPc complexes in DMF containing $TBABF_4$ supporting electrolyte.

	Q-band/nm		
Complex	$M^{I}Pc^{-2}$	$M^{II}Pc^{-2}$	$M^{III}Pc^{-2}$
13	712	694	702
14	_	713	778
16	710	672	677
17	_	692	743
19	726	692	_
20	_	705	760
22	707	692	697
23	_	710	768

Further oxidations are expected to occur on the ring, by virtue of the nature of CoPcs [223]. However, application of a potential more positive of process **IV** (E_p = +0.86 V vs. Ag|AgCl, Fig. 3.6B) resulted in the spectral changes shown in Fig. 3.7D. A decrease in

the Q-band intensity, without any appreciable increase in intensity around the 500 nm region, was observed. Increased intensity around the 500 nm region is characteristic of ring oxidation in MPc [223]. Hence, spectral changes observed in Fig. 3.7D may be attributed to degradation of the complex, as reported previously for other thio-derivatised MPc complexes [225]. Nonetheless, the assignment of process **IV** to $Co^{III}Pc^{-1}/Co^{III}Pc^{-2}$ is consistent with the redox behavior of CoPc complexes (Table 1.1)

3.1.3.1.2 Complex 16

Electrochemical properties of complex **16** were slightly different from those of complex **13**. As discussed previously, non-peripheral positions are sterically crowded positions that may impose some conformational stress on MPc complexes, thus the slight difference in the electrochemical behaviors of these complexes. Figs. 3.8A and 3.8B show, respectively, the square wave and cyclic voltammetry profiles of 1×10^{-3} M of complex **16** in freshly distilled, dried DMF, containing 0.1 M $TBABF_4$, as supporting electrolyte. Three distinctly defined redox processes (labeled **I**, **II** and **III**) can be identified. Process **III** (Fig. 3.8B) is assigned to metal oxidation, $Co^{III}Pc^{-2}/Co^{II}Pc^{-2}$ ($E_{1/2}$ = +0.64 V vs. Ag|AgCl) (Table 3.2) in accordance with literature [226]. Metal oxidation is expected, since this species is usually observed in coordinating solvents [226]. This process is virtually irreversible. The irreversibility of the oxidation processes of sulfur containing MPc complexes is well documented [95,223], hence the irreversible nature of process **III** is not surprising. Process **II** is assigned to metal reduction, $Co^{II}Pc^{-2}/Co^{I}Pc^{-2}$ ($E_{1/2}$ = -0.24 V vs. Ag|AgCl), Table 3.2. It has a cathodic to anodic peak current ratio of near unity, but quasi-reversible, because of peak to peak separation (ΔE) of 161 mV (ΔE for ferrocene was 90 mV within the same potential window, with the same scan rate (100 mVs^{-1}). Reversibility of this couple ($Co^{II}Pc^{-2}/Co^{I}Pc^{-2}$) did not improve at shorter potential window. Process **I** is assigned to ring reduction, $Co^{I}Pc^{-2}/Co^{I}Pc^{-3}$ ($E_{1/2}$ = -1.26 V vs. Ag|AgCl), Table 3.2. This process is also quasi-reversible, with ΔE value of 151 mV, although with cathodic to anodic current ratio of near unity. Spectroelectrochemistry, discussed shortly, was used to confirm these processes.

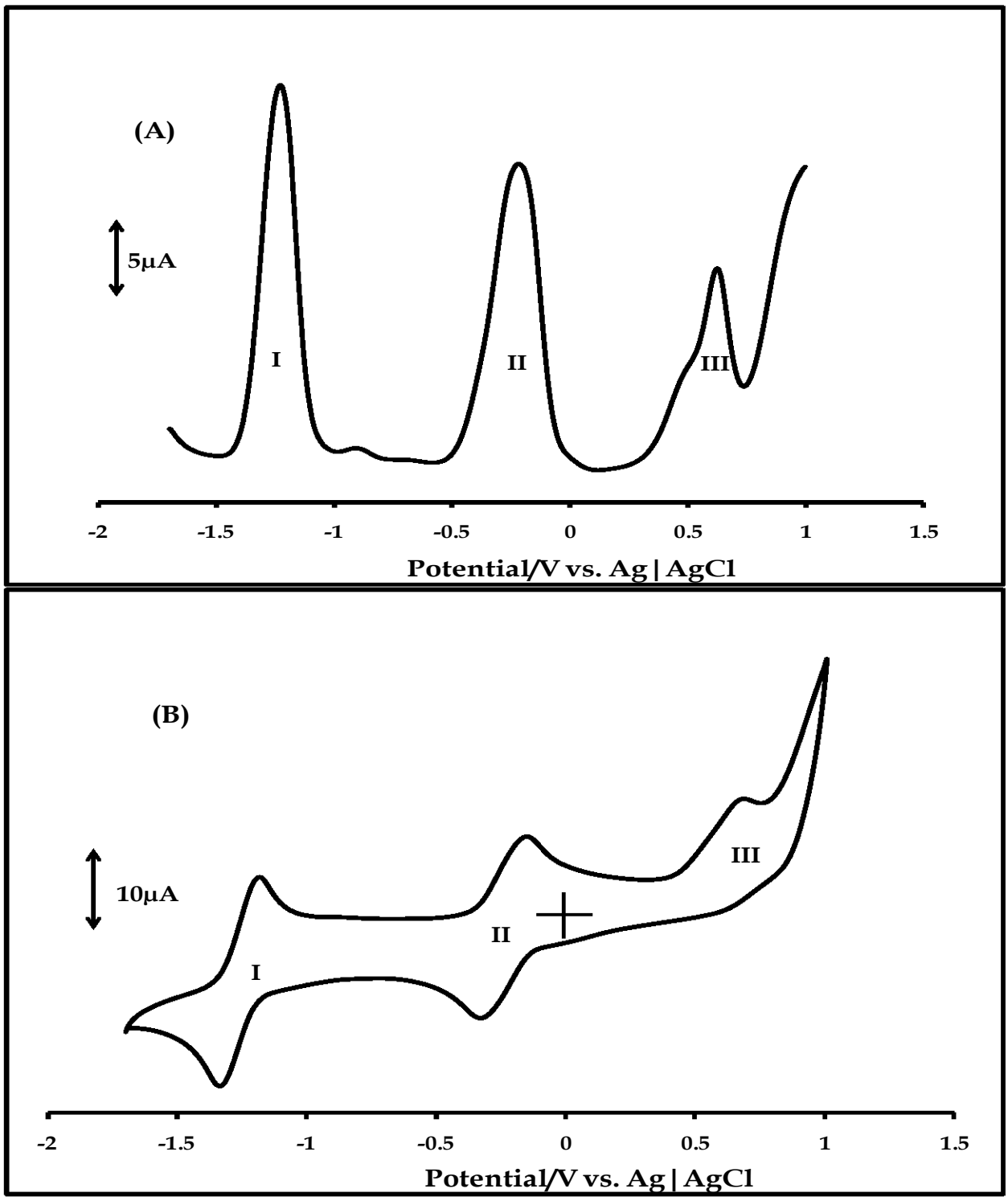

Figure 3.8: (A) Square wave and (B) cyclic voltammetry profiles of 1 × 10^{-3} M of complex **16** in freshly distilled DMF containing 0.1 M $TBABF_4$ supporting electrolyte. Step potential: 5 mV, amplitude: 50 mV, frequency: 10 Hz. Scan rate: 100 mVs^{-1}.

Comparative analysis of the redox properties of complexes **13** and **16** revealed the relevance of substituent position on the electrochemical behaviors of these complexes. Ring-based reduction (Pc^{-2}/Pc^{-3}) occurred at -1.46 V and -1.26 V (vs. Ag|AgCl) in complexes **13** and **16**, respectively (Table 3.2), while metal-based reductions (Co^{II}/Co^{I}) was observed at -0.38 V and -0.24 V in complexes **13** and **16**, respectively (Table 3.2). Metal-based oxidation (Co^{III}/Co^{II}), the only oxidative process in complex **16**, was observed at +0.41 V and +0.64 V (vs. Ag|AgCl) in complexes **13** and **16**, respectively (Table 3.2). These suggest that peripheral substitution **(16**) results in easier reduction than non-peripheral substitution (**13**), while oxidation is easier for non-peripheral derivative (**13**), as shown in Table 3.2. The ease of oxidation in **13** could be attributed to conformational distortion, induced by non-peripheral substitution, and the closeness of the electron-donating substituent to the Pc ring, relative to **16**. The absence of ring oxidation in complex **16** (Fig. 3.8B) underscores the limitation imposed on the complex, with respect to undergoing oxidative processes. These deductions were corroborated by results obtained from spectroelectrochemical studies.

The spectral changes in Fig. 3.9 were obtained during spectroelectrochemical studies involving complex **16**. The spectral transformations observed on the application of potential slightly more negative of process **II** ($E_{1/2}$ = -0.24 V vs. Ag|AgCl, Fig. 3.8B) are shown in Fig. 3.9A. The presence of split Q-band in the starting spectrum (bold solid line) is an indication of aggregation, as result of the relatively high concentration used for controlled potential electrolysis. This was not observed for complex **13** (Fig. 3.7A), due to non-peripheral substitution. The peak at about 628 nm is due to the aggregate, while that at 672 nm is the monomeric peak. The wavelength of the Q-band associated with the monomer is slightly lower than that observed for the complex in Fig. 3.1 (675 nm) (Table 3.1), due to the effects of electrolyte. Upon reduction, at potential more negative than process **II**, a red-shift in Q-band of the monomeric peak (from 672 to 710 nm) (Table 3.3), with increased intensity, was observed. Considerable disaggregation of the complex was also noticed upon reduction, evident from the narrowing of the

absorption bands. Also, there was emergence of a new intense peak at474 nm during

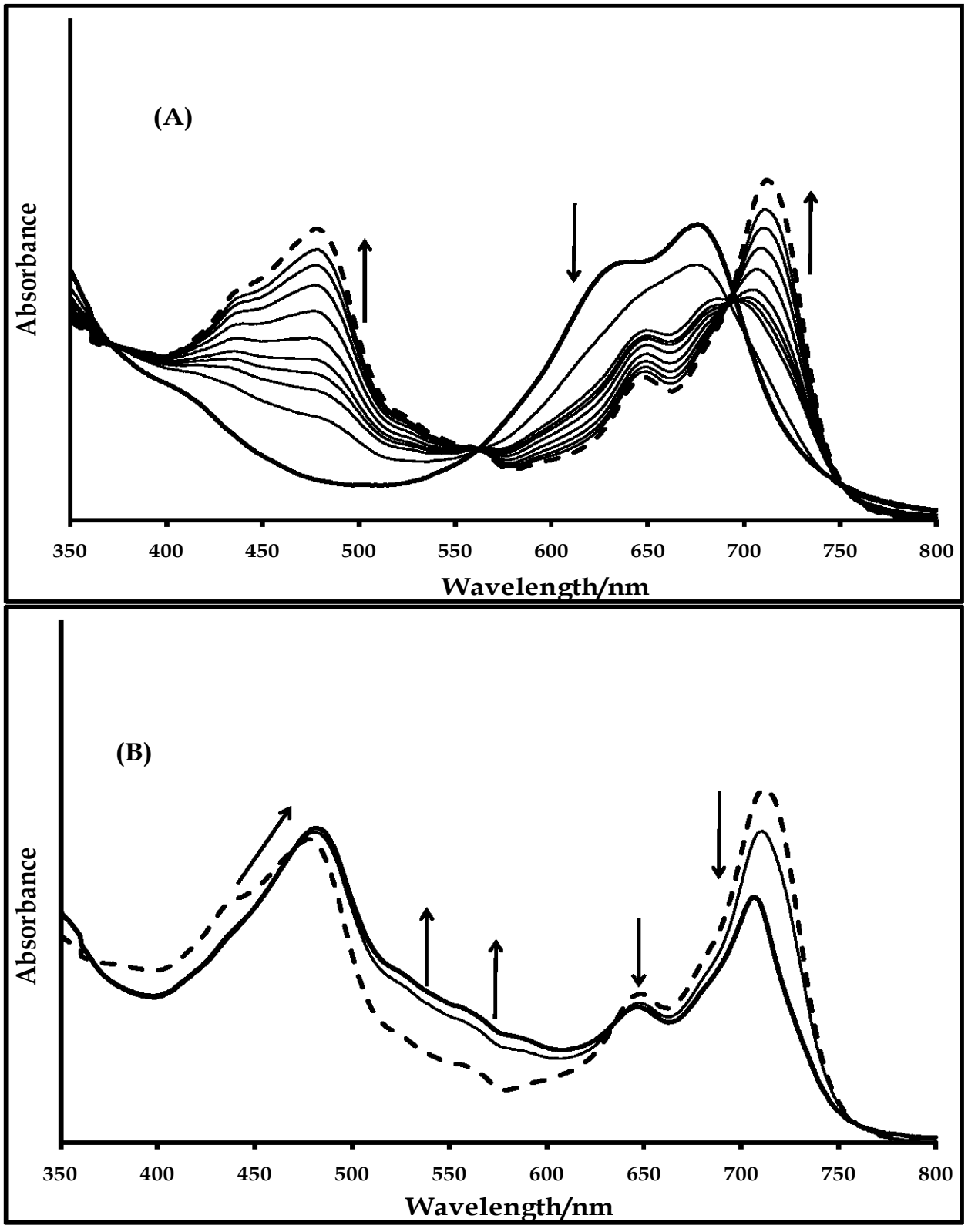

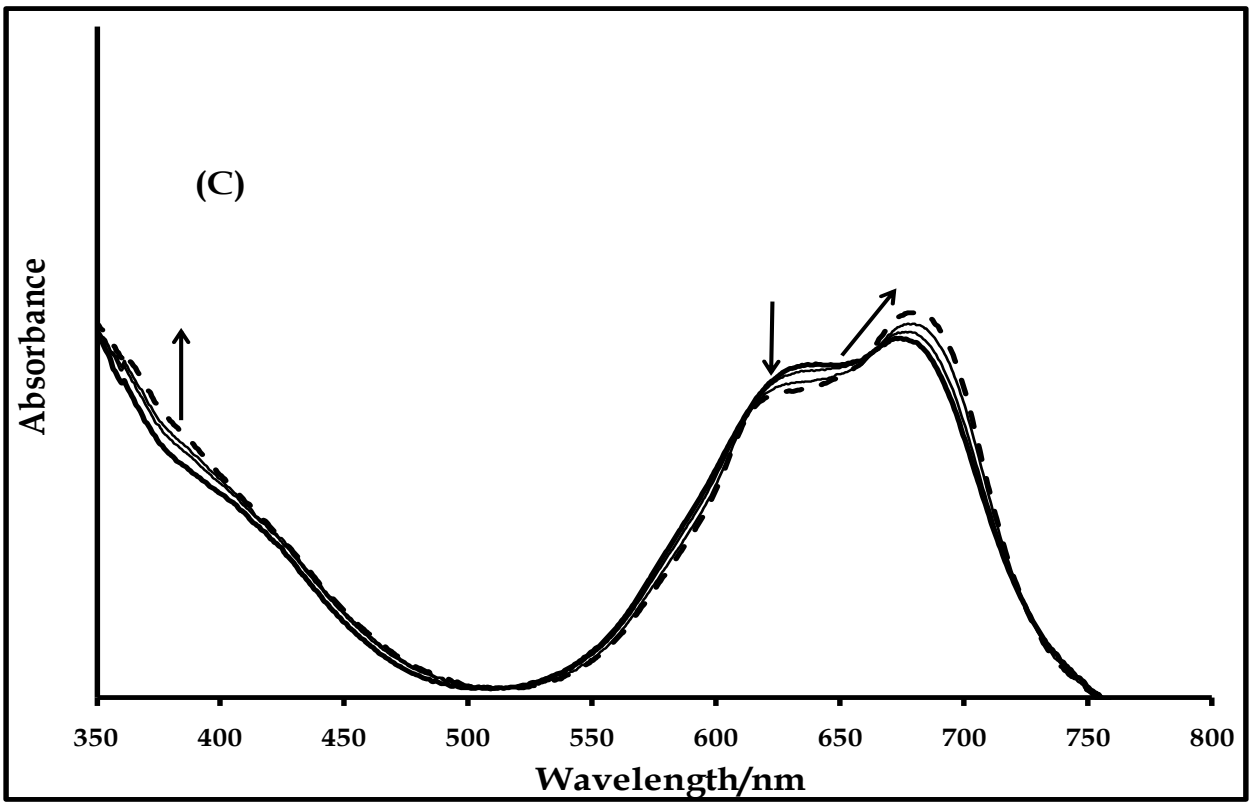

Figure 3.9: UV-Vis spectral changes observed for complex **16** during controlled potential electrolysis at (**A**) -0.3 V (process **II**), (**B**) -1.4 V (process **I**) and (**C**) +0.7 V (process **III**) vs. Ag|AgCl. Electrolyte = DMF containing 0.1 M $TBABF_4$. The final spectrum in (**A**) is the starting spectrum in (**B).**

reduction. New peaks, with an intense signal between 400 and 500 nm, are typical of the formation of $Co^{I}Pc$ species, as explained previously [91]. The shift in Q-band, without decrease in intensity, is a signature of metal-based reduction in MPc complexes. Hence, spectral changes shown in Fig. 3.9A are a confirmation of the reduction of Co^{II} to Co^{I}, supporting the assignment of process **II**, in Fig. 3.8B, to the $Co^{II}Pc^{-2}/Co^{I}Pc^{-2}$ couple. Also clear isobestic points, observed at 556 and 691 nm, indicate that the process is a clean reduction involving two species. However, the first scan does not fall within the isobestic point, due to disaggregation during reduction. About 85% of the original spectrum was regenerated on the application of zero potential, showing some measure of reversibility of the process. The number of electrons transferred was calculated to be approximately 1, using equation 3.1.

Further reduction of the species formed in Fig. 3.9A, at potential more negative of process **I** ($E_{1/2}$ = -1.26 V vs. Ag|AgCl, Fig. 3.8B), resulted in the spectral changes shown in Fig. 3.9B. A decrease in the intensity of the new Q-band (bold dashed line), with shift in position of the band at 474 to 478 nm was noticed. Also, new bands appeared at 555 and 585 nm. Emergence of new bands in the 500 to 600 nm region is characteristic of ring-based reduction and the formation of Pc^{-3} species, as discussed earlier [224]. Hence, the spectral changes observed in Fig. 3.9B confirm the assignment of process **I** (in Fig. 3.8B) to $Co^{I}Pc^{-2}/Co^{I}Pc^{-3}$ couple.

The spectral changes in Fig. 3.9C were obtained on the application of a potential more positive of process **III** ($E_{1/2}$ = +0.64 V vs. Ag|AgCl, Fig. 3.8B). The starting spectrum has a split Q-band, as observed in Fig. 3.9A. Upon oxidation, there was an increase in intensity and shift in position (from 672 to 677 nm) of the monomeric Q-band (Table 3.3). These spectral changes are consistent with the oxidation of Co^{II} to Co^{III} species, thus confirming the assignment of process **III** (in Fig. 3.8B) to $Co^{III}Pc^{-2}/Co^{II}Pc^{-2}$ couple. However, the minimal shift in position and slight change in intensity of the Q-band in Fig. 3.9C underline the difficulty, highlighted previously, with which oxidative processes occurred in complex **16**. This is different from the well-defined spectral changes observed for the corresponding process in complex **13** (Fig. 3.7C), corroborating the deduction that complex **13** is more susceptible to oxidative process than complex **16**.

3.1.3.1.3 Complex 19

Figs. 3.10A and B are, respectively, the square wave and the cyclic voltammograms of 1 x 10^{-3} M of complex **19** in freshly distilled, dried DMF, containing 0.1 M $TBABF_4$ (supporting electrolyte). Like the tetra-substituted derivative (**16**), three redox processes were identified. Process **I** ($E_{1/2}$ = -1.40 V versus Ag|AgCl) is typical of $Co^{I}Pc^{2-}/Co^{I}Pc^{3-}$ couple [226], while process **II** ($E_{1/2}$ = -0.32 V versus Ag|AgCl) is in the potential range for $Co^{II}Pc^{2-}/Co^{I}Pc^{2-}$ couple. These processes are quasi-reversible (for **I**, ΔE = 383 mV and for

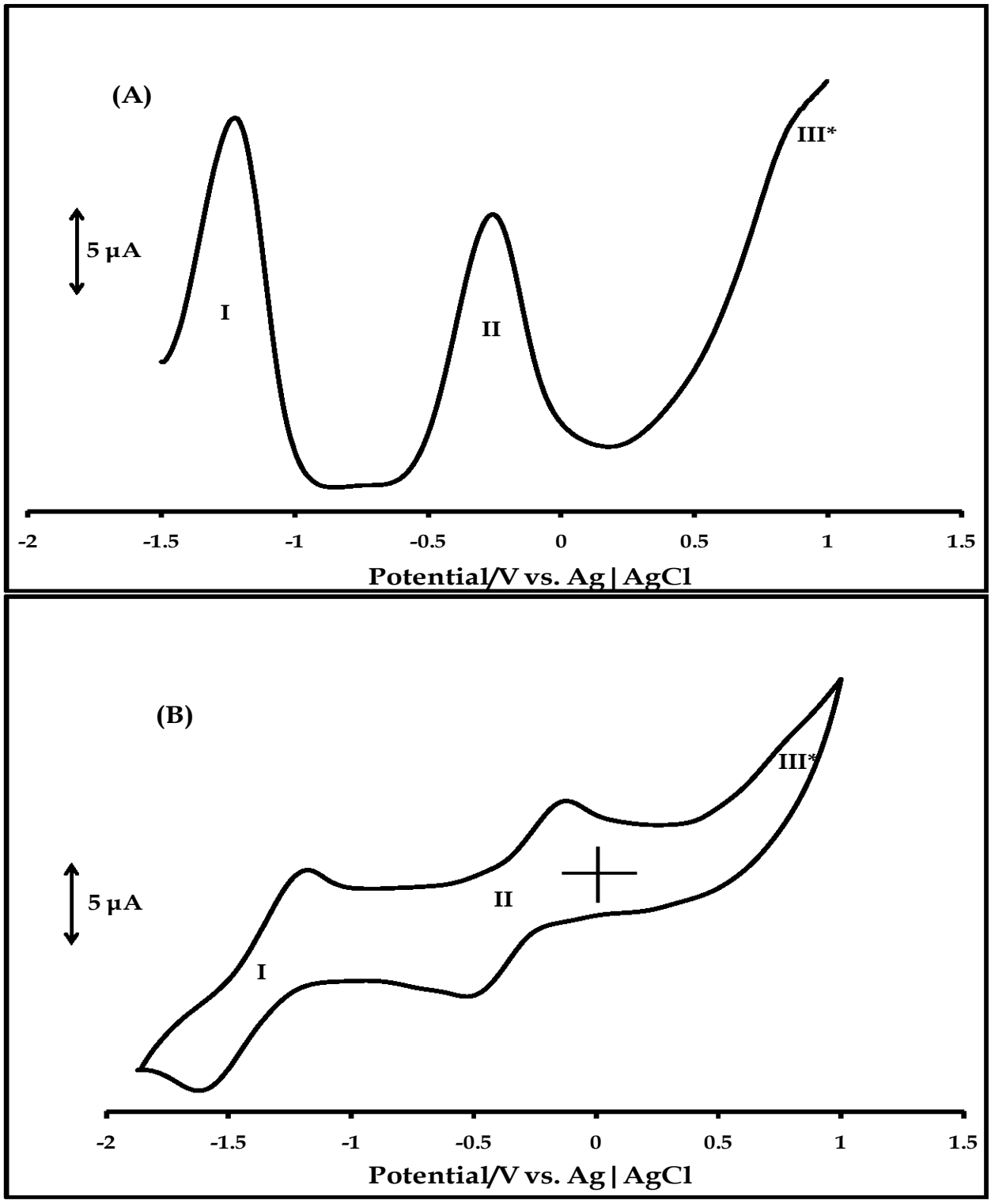

Figure 3.10: (A) Square wave and (B) cyclic voltammetry profiles of 1 × 10^{-3} M of complex **19** in freshly distilled DMF containing 0.1 M $TBABF_4$ supporting electrolyte. Step potential: 5 mV, amplitude: 50 mV, frequency: 10 Hz. Scan rate: 100 mVs^{-1}.

II, ΔE = 312 mV). Process **III*** (E_p = +0.80 V vs. Ag|AgCl) is a weak redox process, assigned to metal oxidation, Co^{III}/Co^{II}. As stated previously, in coordinating solvents [226], this process is expected to occur before ring oxidation. However, the value of the peak potential suggests complication of this process, due to contribution from the oxidation of the ring substituent. Its oxidation potential is more positive, compared to CoPc complexes in general, but is within the range of some arylthio-substituted CoPc derivatives (Table 1.1). Processes **I** and **II** were confirmed by spectroelectrochemistry.

Spectroelectrochemical studies involving complex **19** resulted in the spectral changes shown in Fig. 3.11. Application of potential slightly more negative of process **II** (Fig. 3.10B) resulted in the spectral changes in Fig. 3.11A. The starting spectrum (bold solid line) shows considerable aggregation, as a result of the high concentration used for controlled potential electrolysis. The peaks at 692 nm and 655 nm are associated with monomer and dimer, respectively. A red-shift in the monomeric Q-band (692 nm to 726 nm) (Table 3.3) was observed. Also, there was emergence of a new peak at 492 nm, with increased intensity, characteristic of $Co^{I}Pc$ [91], as discussed previously.

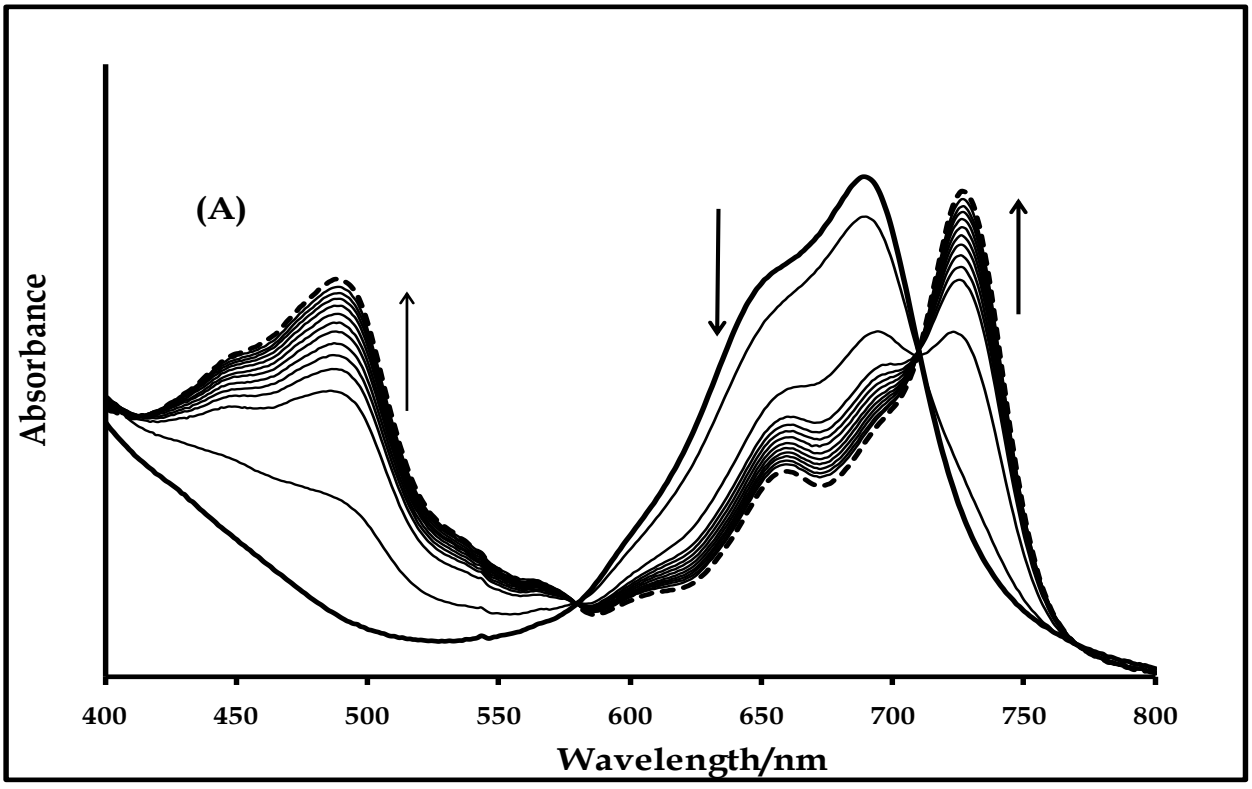

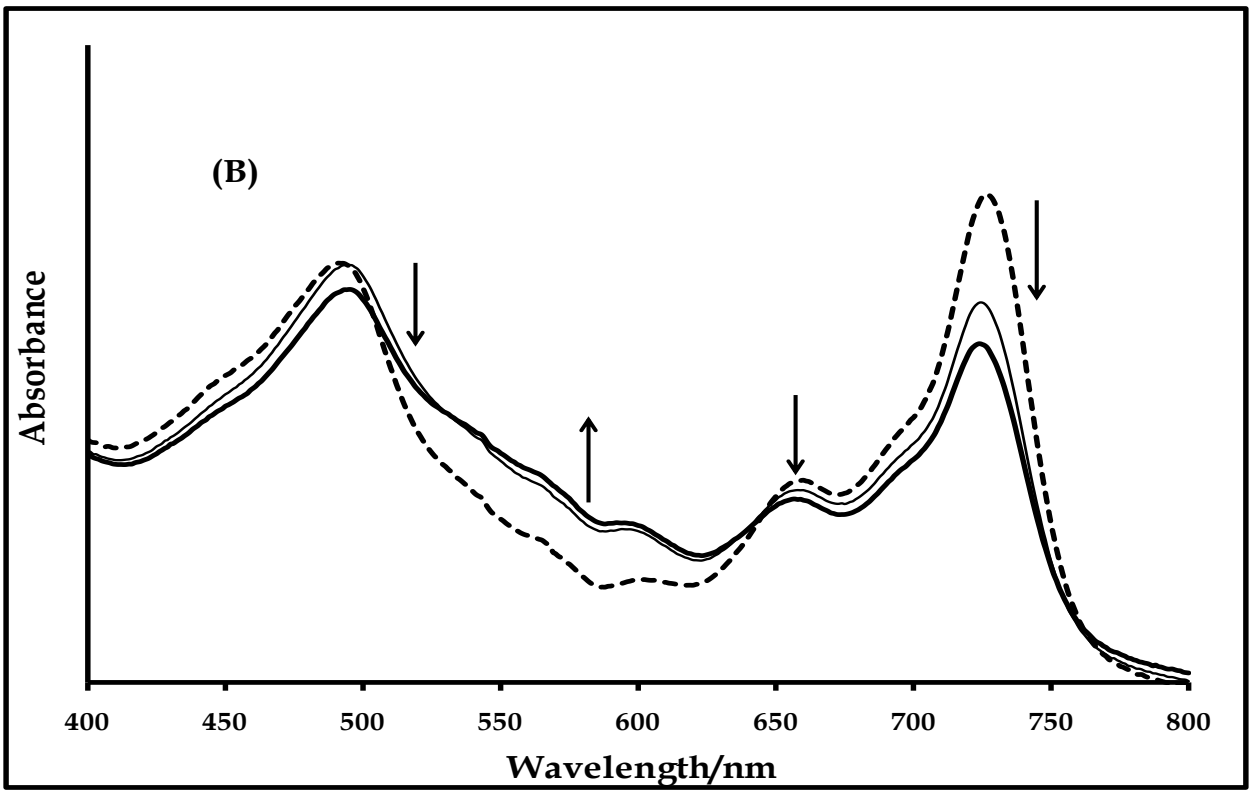

Figure 3.11: UV-Vis spectral changes observed for complex **19** during controlled potential electrolysis at (**A**) -0.40 V (process **II**), (**B**) -1.50 V (process **I**). Electrolyte = DMF containing 0.1 M $TBABF_4$. The final spectrum in (**A**) is the starting spectrum in (**B**).

These spectral transformations are consistent with those obtained for similar processes in complexes **13** and **16**, confirming the assignment of couple **II**, in Fig. 3.10B, to the reduction of $Co^{II}Pc$ to $Co^{I}Pc$. The number of electrons transferred was calculated to be approximately 1, using equation 3.1. Also, distinct isobestic points, at 580 and 710 nm, show that the process is a clear reduction involving two species. The spectral transformations in Fig. 3.11A are as resolved as those observed for the corresponding process in **16** (the peripherally tetra-substituted derivative) (Fig. 3.9A). Further reduction of the species obtained in Fig. 3.11A occurred on the application of potential slightly more negative of process **I**, Fig. 3.11B. The new Q-band at 726 nm decreased in intensity, without a change in position. These spectral changes are similar to the changes observed for the corresponding processes in complexes **13** and **16**, justifying

the assignment of process **I**, in Fig. 3.10B, to ring-based reduction and the formation of $Co^{I}Pc^{3-}$ [224].

3.1.3.1.4 Complex 22

Figs. 3.12A and B, respectively, show the square wave and cyclic voltammetry of 1×10^{-3} M of complex **22** in freshly distilled, dried DMF, containing 0.1 M $TBABF_4$ (supporting electrolyte). Electrochemical properties of complex **22** are not substantially different from that of complex **16**. The major difference was the extent of reversibility of the redox processes. Three distinct redox processes were observed in solution electrochemistry of complex **22**. Like complex **16**, no ring-based oxidation was observed in complex **22**. Although, complex **22** is non-peripherally tetra-substituted, like complex **13**, the electron-withdrawing nature of the phenyl group of the benzylthio substituent favored reduction processes at the expense of oxidation, Table 3.2. Process **III** is an irreversible process, assigned to metal oxidation, $Co^{III}Pc^{-2}/Co^{II}Pc^{-2}$($E_p$ = +0.59 V vs. Ag|AgCl). This process is also less energetically favorable, like the corresponding process in complex **16**, when compared to similar process in complex **13** (E_p = +0.41 V vs. Ag|AgC), Table 3.2. Process **II**, $Co^{II}Pc^{-2}/Co^{I}Pc^{-2}$($E_{1/2}$ = -0.26 V vs. Ag|AgCl), is quasi-reversible, with a cathodic to anodic peak current ratio of near unity, but a peak separation (ΔE = 121 mV) larger than the 90 mV obtained for ferrocene. Process **I**, $Co^{I}Pc^{-2}/Co^{I}Pc^{-3}$ ($E_{1/2}$ = -1.25 V vs. Ag|AgCl), is also quasi-reversible. These processes were also confirmed using spectroelectrochemistry.

Fig. 3.13 shows the spectral transformations obtained during spectroelectrochemical characterization of complex **22**. Application of potentials negative of process **II** ($E_{1/2}$ = -0.26 V vs. Ag|AgCl, Fig. 3.12B) resulted in the spectral changes shown in Fig. 3.13A. The starting spectrum is the same as that shown for complex **22** in Fig. 3.1. The band around 628 nm is associated with vibronic transition but complicated by slight aggregation. The main Q-band at 692 nm was red-shifted upon reduction (692 to 707 nm), without significant decrease in intensity. Also, a new peak, with increase intensity,

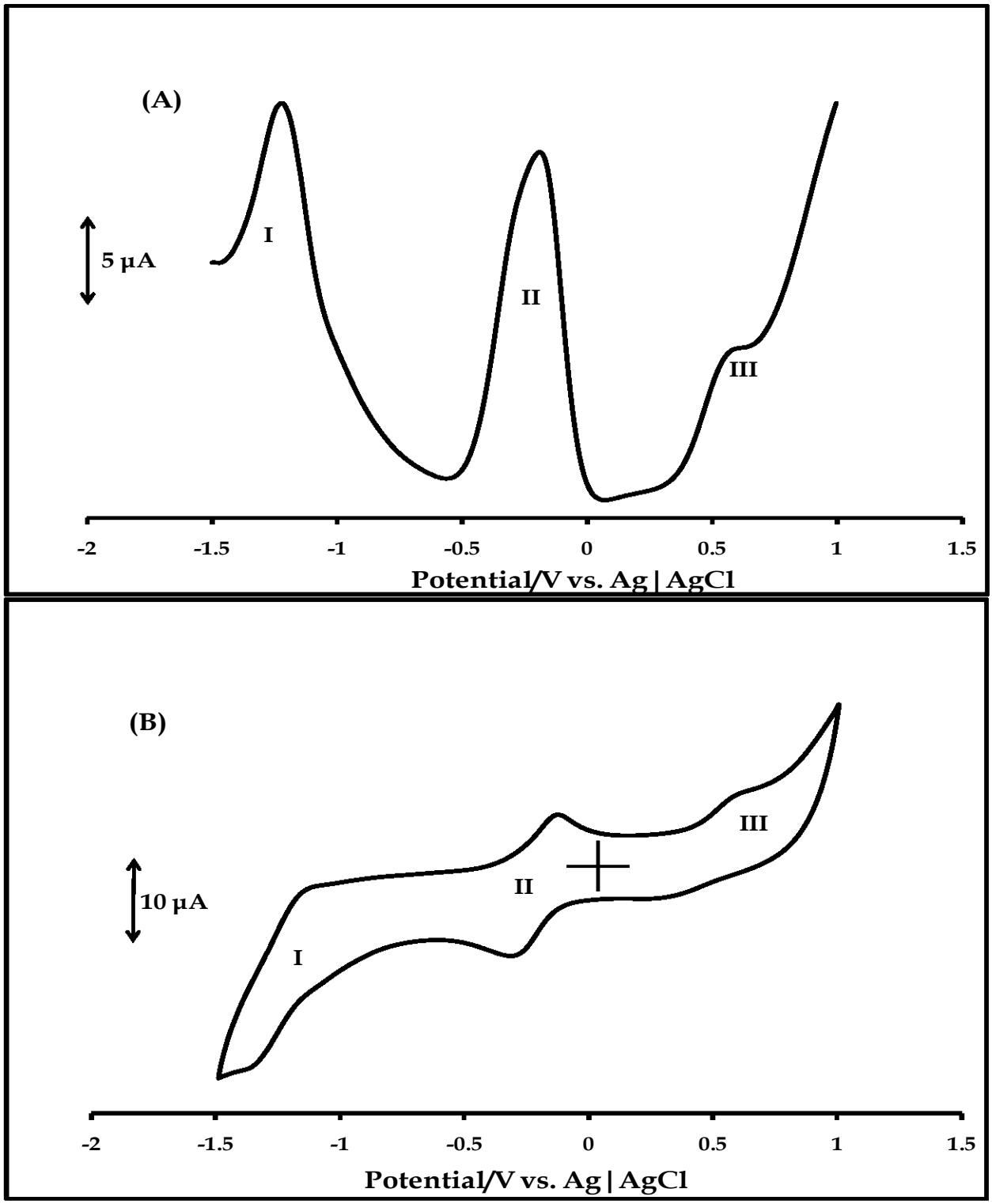

Figure 3.12: (A) Square wave and (B) cyclic voltammetry profiles of 1 × 10^{-3} M of complex **22** in freshly distilled DMF containing 0.1 M $TBABF_4$ supporting electrolyte. Step potential: 5 mV, amplitude: 50 mV, frequency: 10 Hz. Scan rate: 100 mVs^{-1}.

appeared at 473 nm. These spectral changes are typical of the formation of $Co^{I}Pc$ [91], as observed for complexes **13**, **16** and **19**. The shift in Q-band, with the same intensity, agrees with metal-based reduction in MPc. Therefore, the spectral changes in Fig. 3.13A confirm the assignment of process **II** (Fig. 3.12B) to the $Co^{II}Pc^{-2}/Co^{I}Pc^{-2}$ couple. Clear isobestic points, at 572 and 700 nm, show that the process is a clean reduction, involving two species. The number of electrons transferred was determined to be approximately 1, using equation 3.1. Less than 70% of the original spectrum was regenerated on the application of zero potential, showing some measure of reversibility. However, these spectral changes are not as resolved as those observed for the corresponding processes in complexes **13** (Fig. 3.7A), **16** (Fig. 3.9A) and **19** (Fig. 3.11A), justifying the difference in nature of substituent (diethylaminoethanethio in **13**, **16** and **19** versus benzylthio in **22**).

Further reduction of the species obtained in Fig. 3.13A occurred on the application of potentials negative of process **I** ($E_{1/2}$ = -1.39 V vs. Ag|AgCl, Fig. 3.12B), resulting in the spectral changes shown in Fig. 3.13B. There was a decrease in the absorbance of the new Q-band, emergence of a new band between 500 and 600 nm region and shift in the peak at 473 nm to 477 nm. These spectral changes are typical of Pc^{-3} species [224], as remarked previously for the corresponding processes in **13**, **16** and **19**. These confirm the assignment of process **I** (Fig. 3.12B) to the $Co^{I}Pc^{-2}/Co^{I}Pc^{-3}$ couple.

Application of potentials positive of process **III** (E_p = +0.59 V vs. Ag|AgCl, Fig. 3.12B) gave the spectral changes shown in Fig. 3.13C. An increase in absorbance and shift in position of the Q-band (692 to 697 nm) (Table 3.3) of the starting spectrum were observed. Although, these changes are minimal, they are characteristic of the oxidation of Co^{II} to Co^{III}, justifying the assignment of process **III** (Fig. 3.12B) to the $Co^{III}Pc^{-2}/Co^{II}Pc^{-2}$ couple. The minimal spectral changes noticed in Fig. 3.13C is a testimony to the reluctance of the complex, like complex **16**, to undergo oxidative process, as explained previously.

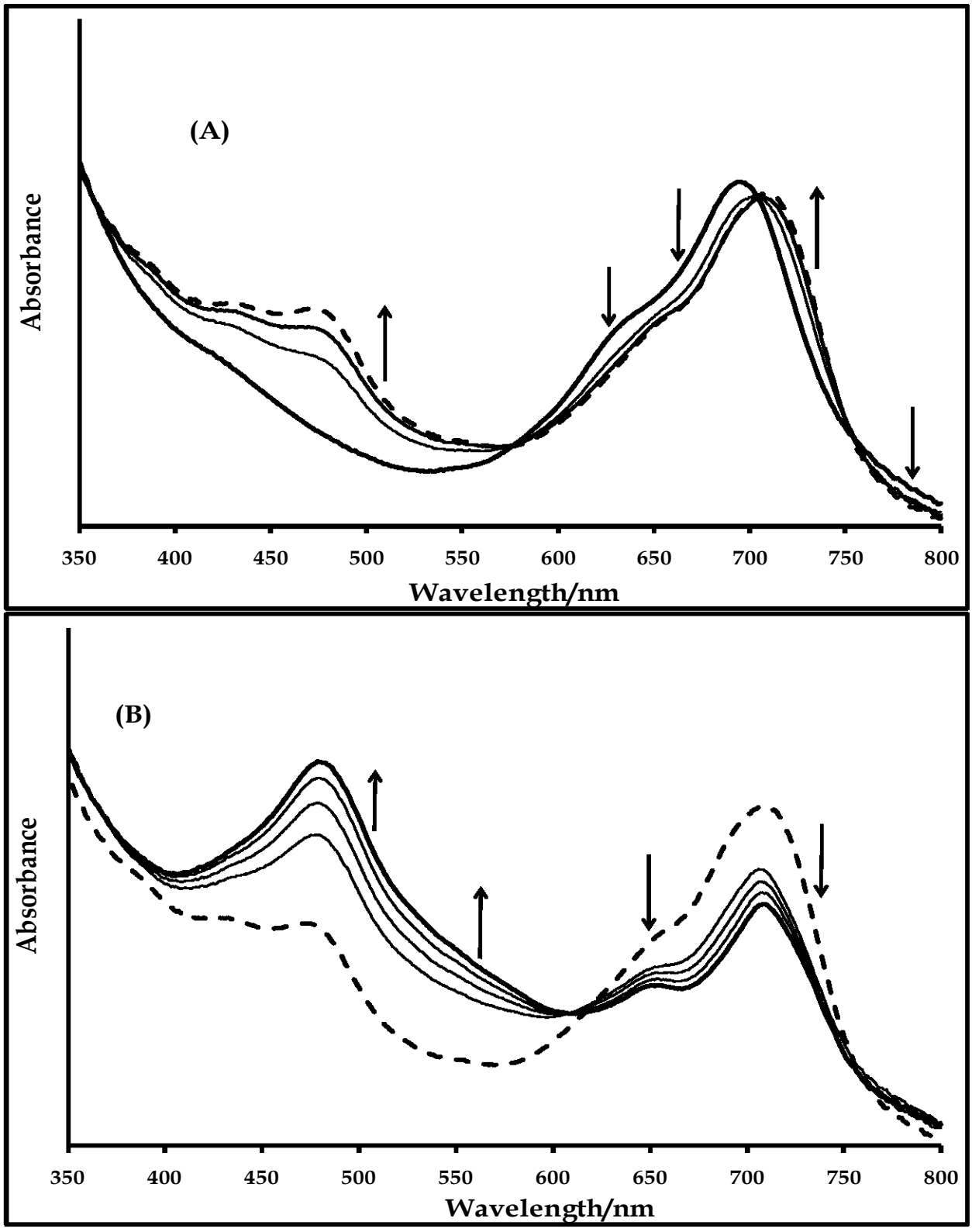
(A)
Absorbance
350
400
450
500
550
600
650
700
750
800
Wavelength/nm
(B)
Absorbance
350
400
450
500
550
600
650
700
750
800
Wavelength/nm

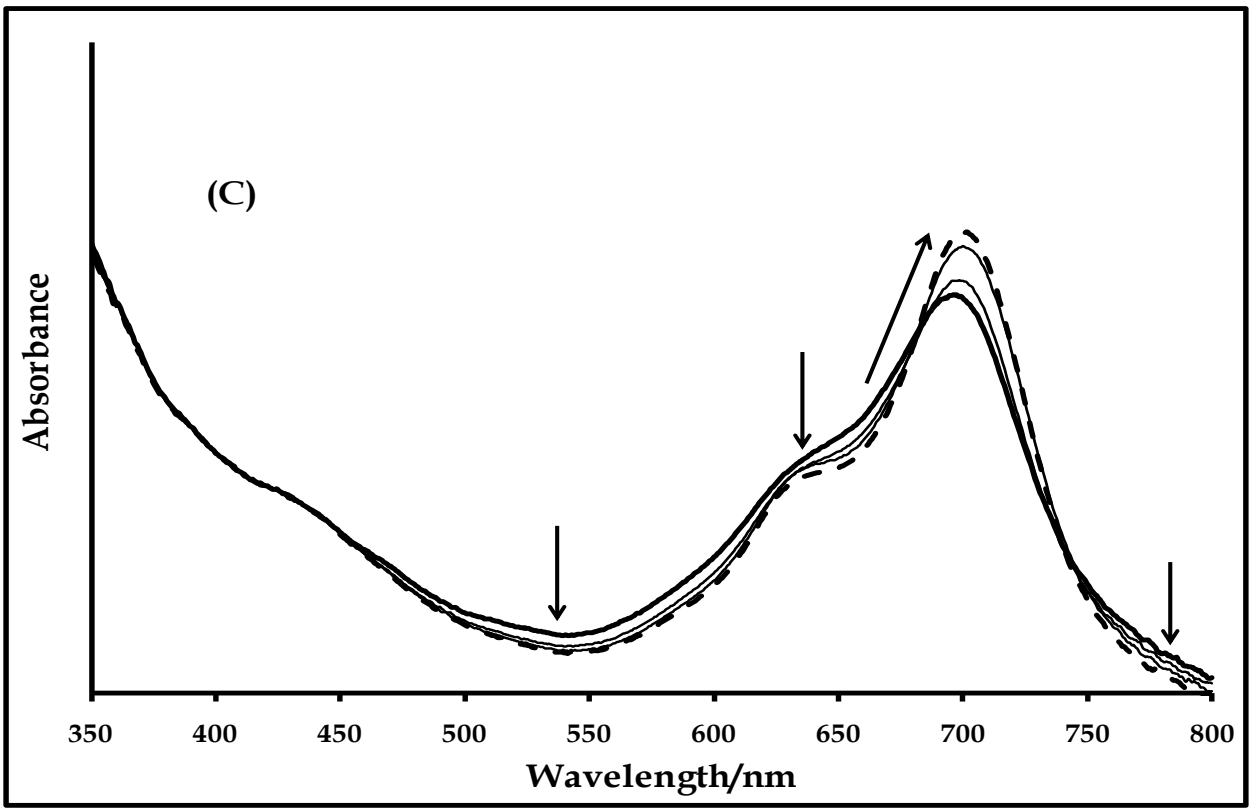

Figure 3.13: UV-Vis spectral changes observed for complex **22** during controlled potential electrolysis at (**A**) -0.35 V (process **II**), (**B**) -1.45 V (process **I**) and (**C**) +0.65 V (process **III**) vs. Ag|AgCl. Electrolyte = DMF containing 0.1 M $TBABF_4$. The final spectrum in (**A**) is the starting spectrum in (**B)**.

3.1.3.2 Manganese phthalocyanine complexes

3.1.3.2.1 Complex 14

The square wave and cyclic voltammetry of 1×10^{-3} M of complex **14**, in freshly distilled, dried DMF, containing 0.1 M $TBABF_4$, as supporting electrolyte, are shown in Figs. 3.14A and B respectively. Three redox processes can be identified. Process **III** (E_p = +0.86 V vs. Ag|AgCl) (Table 3.4) is an irreversible ring-oxidation, assigned to the $Mn^{III}Pc^{-1}/Mn^{III}Pc^{-2}$ couple. The higher peak current, relative to the peak currents of the other redox processes, could be attributed to contribution from the oxidation of the ring substituent, as typical of sulfur containing MPc complexes [95,223].

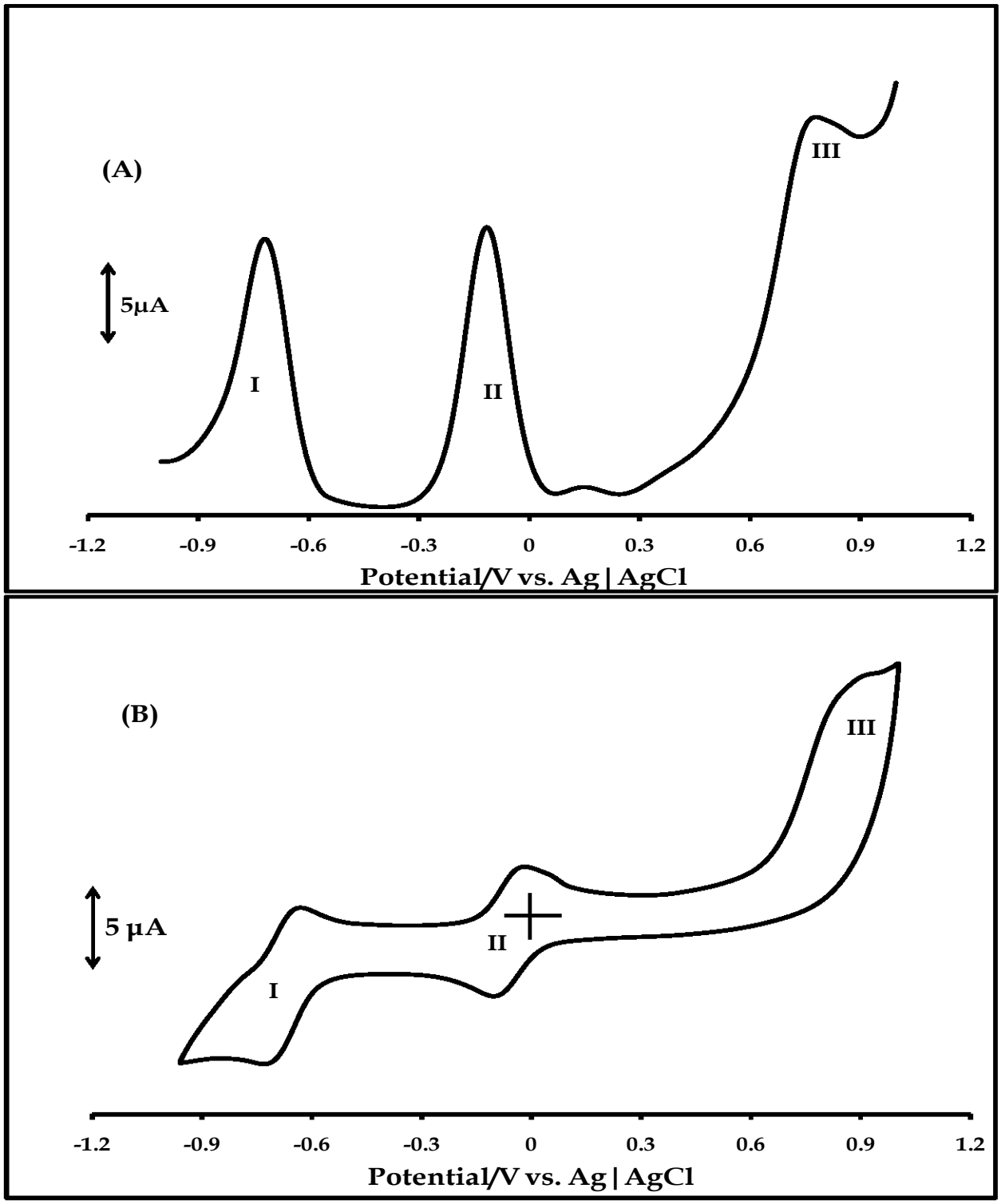

Figure 3.14: (A) Square wave and (B) cyclic voltammetry profiles of 1 × 10^{-3} M of complex **14** in freshly distilled DMF containing 0.1 M $TBABF_4$ supporting electrolyte. Step potential: 5 mV, amplitude: 50 mV, frequency: 10 Hz. Scan rate: 100 mVs^{-1}.

Irreversibility is typical of the oxidation processes in MPc complexes with sulfur-bearing substituents [95,223], as indicated previously. Process **II** ($E_{1/2}$ = -0.04 V vs. Ag|AgCl) (Table 3.4) is reversible, with a cathodic to anodic current ratio of near unity and cathodic to anodic peak separation of 90 mV. It is assigned to metal reduction, $Mn^{III}Pc^{-2}/Mn^{II}Pc^{-2}$. Process **I** ($E_{1/2}$ = -0.68 V vs. Ag|AgCl), Table 3.4, assigned to ring-based reduction ($Mn^{II}Pc^{-2}/Mn^{II}Pc^{-3}$), is also reversible, with a cathodic to anodic current ratio of near unity and a peak separation of 90 mV. The second reduction in MnPc complexes is not well understood. Formation of $Mn^{I}Pc^{-2}$ or $Mn^{II}Pc^{-3}$ has been suggested by different authors. The latter (process **I**) was observed in this work. The above redox assignments were confirmed by spectroelectrochemistry.

Table 3.4: Summary of electrochemical data of MnPc complexes in DMF, in V vs. Ag|AgCl.

Complex	$Mn^{II}Pc^{-2}/Mn^{II}Pc^{-3}$	$Mn^{III}Pc^{-2}/Mn^{II}Pc^{-2}$	$Mn^{III}Pc^{-1}/ Mn^{III}Pc^{-2}$
14	-0.68	-0.04	+0.86
17	-0.78	-0.07	+0.86
20	-0.64	+0.06	+0.90
23	-0.75	-0.04	+1.05

Fig. 3.15 shows the spectral changes observed during spectroelectrochemical investigation of the properties of complex **14**. The spectral changes shown in Fig. 3.15A were obtained on the application of potentials negative of process **II** (Fig. 3.14B). The Q-band (778 nm) of the initial spectrum (bold solid line) is different from that shown in Fig. 3.3 (770 nm) (Table 3.1). As explained previously, this difference is usually associated with the presence of electrolyte used for spectroelectrochemical studies. There was a blue-shift in the Q-band (778 to 713 nm), upon reduction, and a slight decrease in intensity of the charge transfer band around 511 nm. The B band decreased

in intensity as well. The colour of the complex also changed from red to green. A shift in the position of the Q-band, with the same intensity, is characteristic of metal-based electro reduction processes, as highlighted previously for the cobalt derivatives. Specifically, the blue-shift in Q-band (778 to 713 nm in this regard), Table 3.3, is consistent with the reduction of $Mn^{III}Pc^{-2}$ to $Mn^{II}Pc^{-2}$ [91]. These spectral transformations (Fig. 3.15A) confirm the assignment of process **II** in Fig. 3.14B to $Mn^{III}Pc^{-2}/Mn^{II}Pc^{-2}$ couple. The number of electrons transferred was calculated to be approximately 1, using equation 3.1.

The species in Fig. 3.15A was further reduced, by the application of potentials negative of process **I** (Fig. 3.14B), to give the spectral changes shown in Fig. 3.15B. There was a decrease in the intensity of the new peak and increase in the absorption intensity between 400 and 600 nm (531 nm), which are consistent with ring-based redox process in MPc complexes [224,227]. These spectral transformations are a confirmation that process **I** ($E_{1/2}$ = -0.68 V vs. Ag|AgCl, Fig. 3.14B) is due to the $Mn^{II}Pc^{-2}/Mn^{II}Pc^{-3}$ couple and not to the formation of a $M^{I}Pc^{-2}$ species. The number of electrons transferred was estimated to be approximately 1, using equation 3.1.

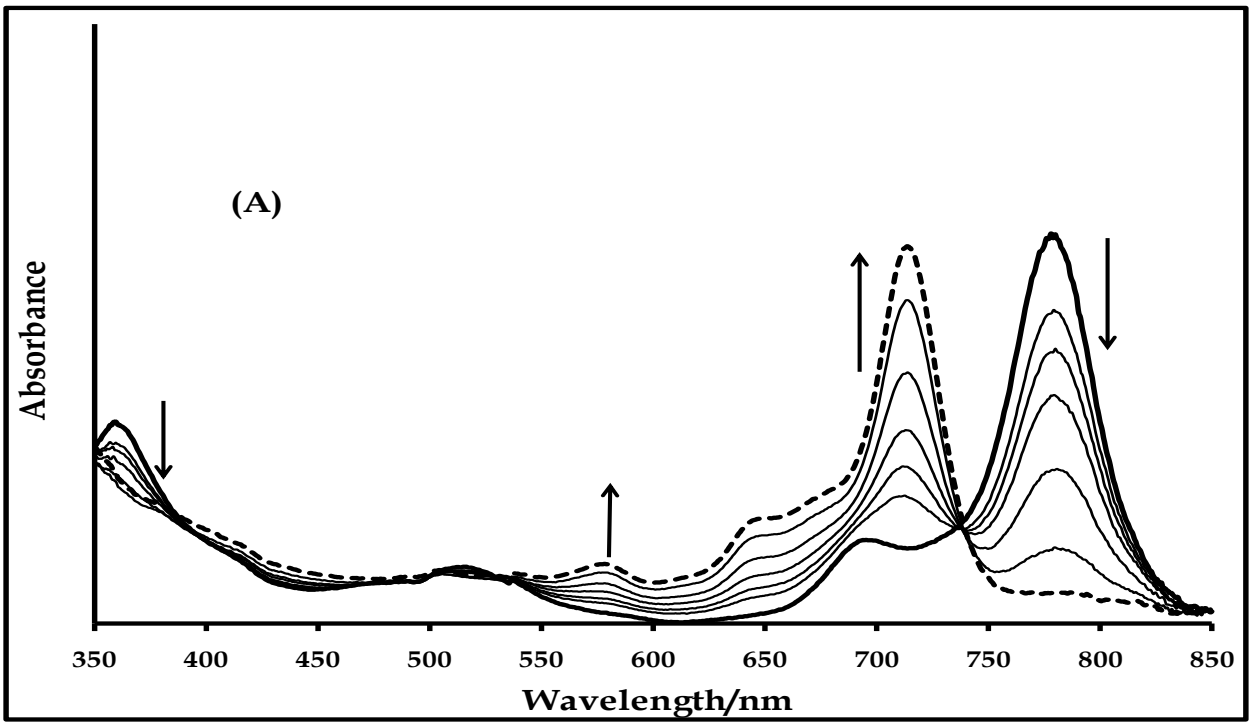

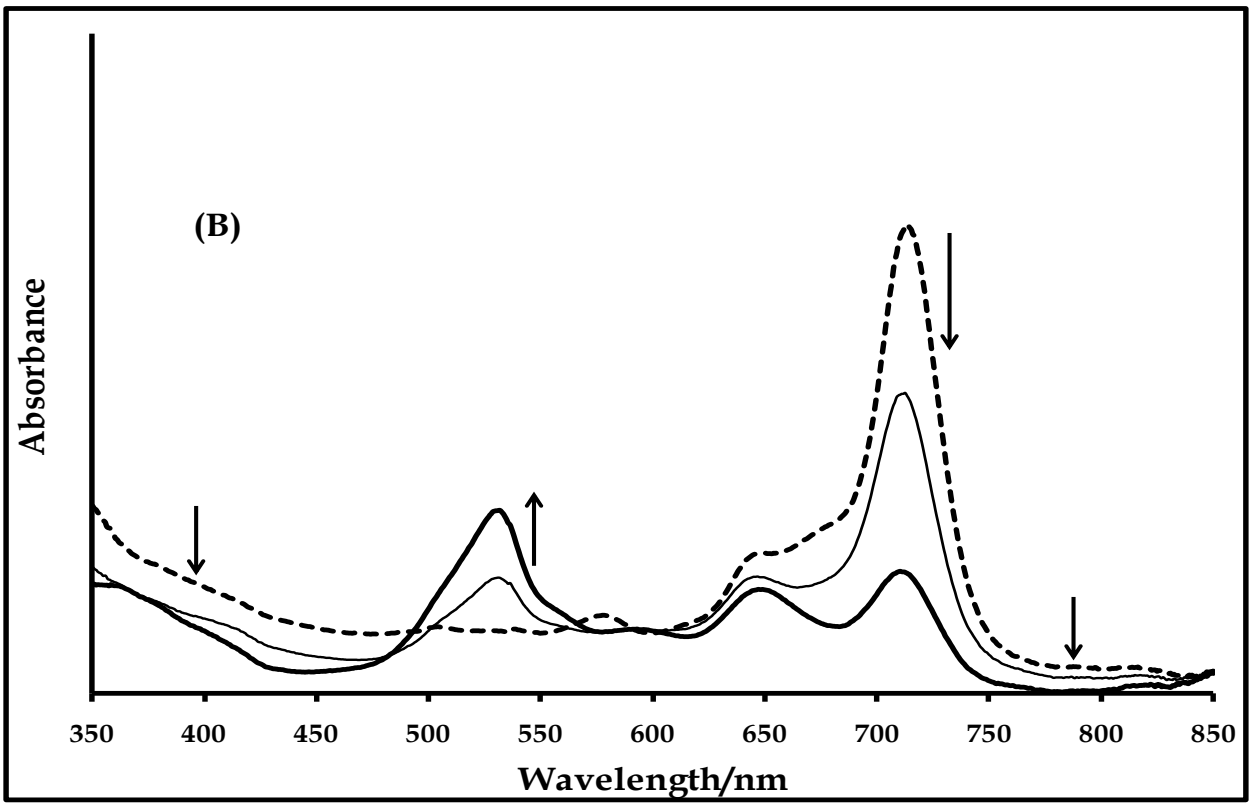

Figure 3.15: UV-Vis spectral changes observed for complex **14** during controlled potential electrolysis at (**a**) -0.10 V (process **II**), (**b**) -0.75 V (process **I**) vs. Ag|AgCl. Electrolyte = DMF containing 0.1 M $TBABF_4$. The final spectrum in (**A**) is the starting spectrum in (**B)**

3.1.3.2.2 Complex 17

Figs. 3.16A and B, respectively, show the square wave and cyclic voltammetry of 1×10^{-3} M of complex **17** in freshly distilled, dried DMF, containing 0.1 M $TBABF_4$, as supporting electrolyte. Fig.3.16B shows three redox processes. Process **III** (E_p = +0.86 V), Table 3.4, is a weak ring-based oxidation, assigned to $Mn^{III}Pc^{-1}/Mn^{III}Pc^{-2}$ couple, in comparison with literature [226]. Process **II** is a quasi-reversible metal reduction process, assigned to $Mn^{III}Pc^{-2}/Mn^{II}Pc^{-2}$ couple ($E_{1/2}$ = -0.07 V vs. Ag|AgCl), Table 3.4, in comparison with literature [226]. Although, process **II** has a cathodic to anodic current ratio of near unity, a peak separation larger than that of ferrocene standard (90 mV), at the same scan rate, was obtained. Process **I** is a quasi-reversible ring reduction, with a

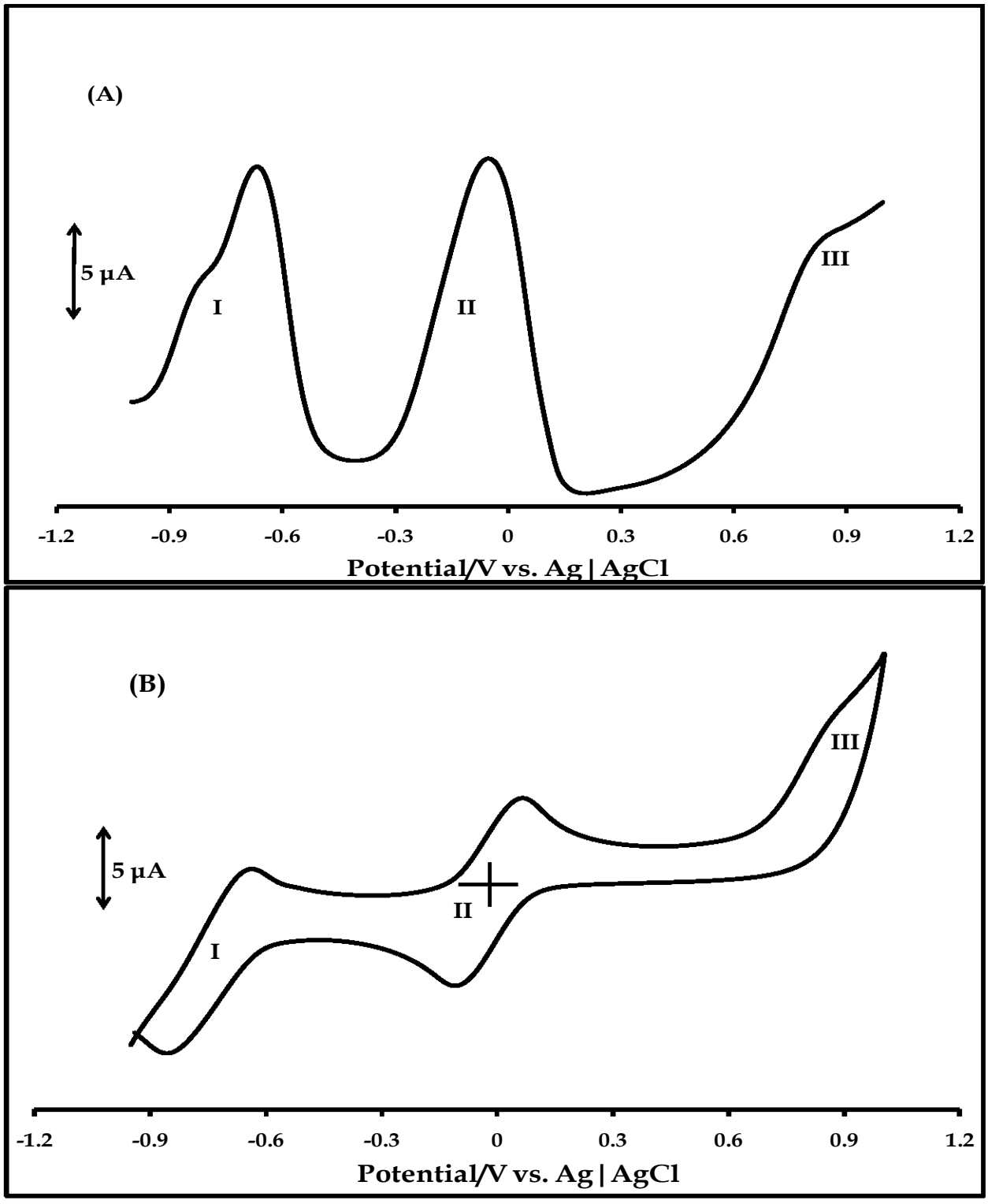

Figure 3.16: (A) Square wave and (B) cyclic voltammetry profiles of 1 × 10^{-3} M of complex **17** in freshly distilled DMF containing 0.1 M $TBABF_4$ supporting electrolyte. Step potential: 5 mV, amplitude: 50 mV, frequency: 10 Hz. Scan rate: 100 mVs^{-1}.

weak anodic component and large peak separation (171 mV). This process is assigned to $Mn^{II}Pc^{-2}/Mn^{II}Pc^{-3}$ couple ($E_{1/2}$ = -0.78 V vs. Ag|AgCl) (Table 3.4). The split observed in process **I** could be due to aggregation. The presence of a weak oxidation signal in **17**, compared to the more defined nature of the corresponding redox process in **14** (the non-peripherally tetra-substituted derivative) (Fig. 3.14B), coupled with a reversible metal and ring-based reduction processes, suggest faster electron transfer processes in complex **14** than in **17**. The differences in electrochemical behaviors of complexes **14** and **17** may be attributed to conformational distortion, resulting from non-peripheral substitution, as explained previously for the cobalt derivatives. This shows the impact of point of substitution on the voltammetry properties of these complexes. These redox assignments were confirmed using spectroelectrochemistry.

Fig. 3.17 shows the spectral changes observed during spectroelectrochemical characterization of complex **17.** The changes in Figs. 3.17A and B were observed on the application of potentials slightly negative of process **II** ($E_{1/2}$ = -0.07 V, Fig. 3.16B), in the presence of oxygen and when de-aerated with nitrogen, respectively. The μ-oxo species (see equation 1.2) was not observed in the first spectrum in Fig. 3.17A, unlike Fig. 3.3. This shows that the ratios of the various MnPc species in solution (shown in introduction, equations 1.1 to 1.4) are dependent on conditions such as the presence of electrolyte, among others. The Q-band (743 nm) (Table 3.3) of the initial spectrum (solid line) was different from that shown in Fig. 3.3 (739 nm) (Table 3.1), due to the presence of the electrolyte used for spectroelectrochemical study, as remarked previously. Upon reduction, a drastic decrease in intensity of the Q-band and collapse of the charge transfer bands between 450 and 550 nm were observed, suggesting the formation of $Mn^{II}Pc^{-2}$ species [91]. The B bands shifted to lower wavelength. However, since spectral transformations occurred in an oxygen-rich environment, a peak due to $Mn^{II}Pc^{-2}$ species was not observed. There was direct conversion of the $Mn^{II}Pc^{-2}$ species to the MnPc μ-oxo complex, evidenced by the emergence of an intense peak at 636 nm. Interestingly,

isobestic points were also observed at 555 and 669 nm, suggesting the presence of two species, the starting $Mn^{III}Pc^{-2}$ and the electro-generated MnPc μ-oxo species.

Fig. 3.17B shows the spectral changes observed in a N_2 de-aerated solution of complex **17** in DMF. The initial spectrum (solid line) is the same as the initial spectrum in Fig. 3.17A. Upon reduction, the Q-band shifted to higher energy (from 743 to 692 nm) (Table 3.3) and the charge transfer bands between 450 and 550 nm collapsed. These spectral transformations are consistent with the reduction of the $Mn^{III}Pc^{-2}$ species and the formation of a $Mn^{II}Pc^{-2}$ species [91], as highlighted earlier for complex **14**. Attempts to prevent the formation of the MnPc μ-oxo species were not completely successful, traces of oxygen in the OTTLE cell resulted in the formation of trace amounts of the MnPc μ-oxo species (at 636 nm in Fig. 3.17B). Interestingly, the intensity of the peak due to the μ-oxo species decreased, while that due to $Mn^{II}Pc^{-2}$ species became dominant, as reduction of $Mn^{III}Pc^{-2}$ species continued (Fig. 3.17B). The presence of diffuse isobestic

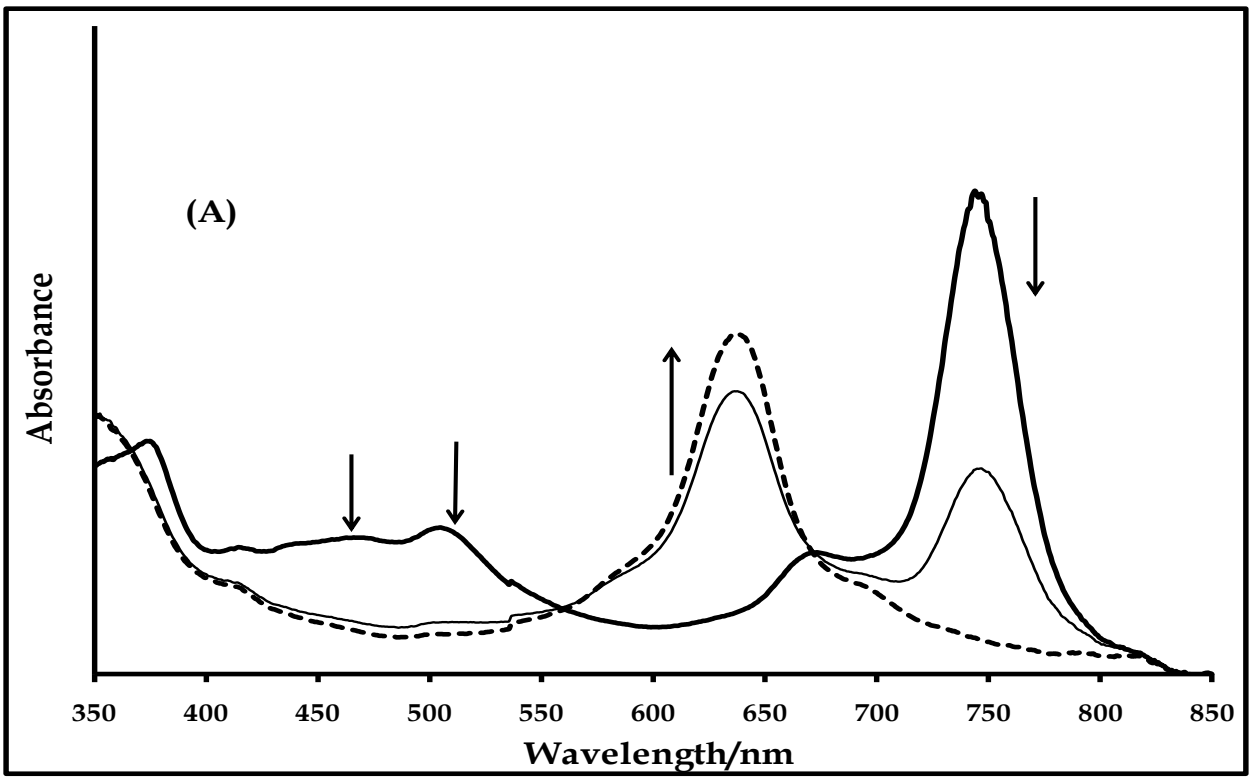

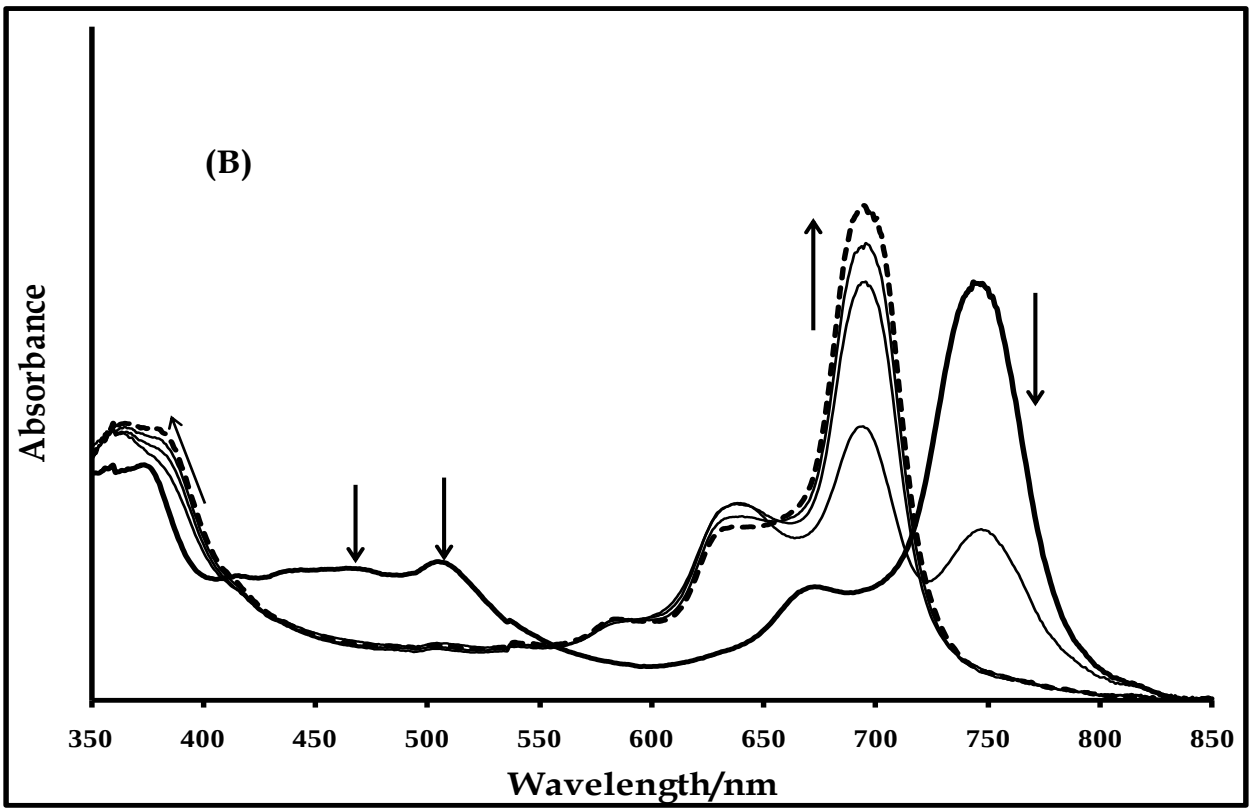

Figure 3.17: UV-Vis spectral changes observed for complex **17** during controlled potential electrolysis at the potential more negative of process **II** (-0.10 V vs. Ag|AgCl) (A) in the presence of oxygen and (B) in N_2 de-aerated solution. Solid line (spectrum before electrolysis) and dashed line (spectrum after electrolysis). Electrolyte = DMF containing 0.1 M $TBABF_4$.

points supports the fact that more than two species are present (the $Mn^{III}Pc^{-2}$, $Mn^{II}Pc^{-2}$ and MnPc μ-oxo species). The complete absence of the $Mn^{II}Pc^{-2}$ species during spectral transformations in Fig. 3.17A, as a result of its direct conversion to the μ-oxo complex, unlike that in Fig. 3.17B, clearly shows the effect of the presence of oxygen on the electronic absorption spectra of MnPc complexes in the visible region, as discussed previously (equations 1.1-1.5). The number of electrons involved cannot be accurately determined, as a result of the contribution of the μ-oxo complex. Further reduction of the $Mn^{II}Pc^{-2}$ species was not successful, due to complications arising from the formation of the MnPc μ-oxo species in Fig. 3.17. But process **I** is assigned to ring-based process, in comparison with complex **14**.

Unlike complex **17**, there was no clear formation of the MnPc μ-oxo species in Fig. 3.15A on reduction of complex **14**. This implies restriction to coplanar association of the rings, via μ-oxo-bridge, in complex **14**, thus preventing the formation of the MnPc μ-oxo complex. This is expected, because of the sterically hindered nature of the non-peripheral position. This shows that the extent of the existence of the μ-oxo complex in MnPc complexes may depend on the position of substituent, in addition to the prevalence of oxygen-rich medium.

3.1.3.2.3 Complex 20

Fig. 3.18 shows the cyclic and square wave (inset) voltammetry of 1×10^{-3} M of complex **20** in freshly distilled, dried DMF, containing 0.1M $TBABF_4$, as supporting electrolyte. Like complexes **14** and **17**, three distinct processes can be identified. Process **III** ($E_{1/2}$ = +0.90 V) (Table 3.4) is an irreversible ring-based oxidation, assigned to $Mn^{III}Pc^{-1}/Mn^{III}Pc^{-2}$ couple. The high peak current suggests a contribution from the oxidation of the ring substituents, as explained previously for complexes **14** (the non-peripherally tetra-substituted derivative) and **17** (the peripherally tetra-substituted derivative). Process **II** ($E_{1/2}$ = +0.06 V versus Ag|AgCl) (Table 3.4) is a reversible metal-based redox process (ΔE = 60 mV), assigned to $Mn^{III}Pc^{-2}/Mn^{II}Pc^{-2}$ couple. Process **I** ($E_{1/2}$ = -0.64 V vs. Ag|AgCl) (Table 3.4) is quasi-reversible (ΔE = 110 mV), it is a ring-based process, attributed to the formation of $Mn^{II}Pc^{-2}/Mn^{II}Pc^{-3}$ couple. The more resolved nature of process **III**, relative to a similar process in complex **17** (the peripherally tetra-substituted derivative) (Fig. 3.16 B), coupled with the reversible nature of process **II,** unlike the irreversibly of the corresponding process in **17**, justify the difference in the number of substituent (tetra- versus octa-substituted). Reversibility of process **II** suggests better electron transfer process in **20** than in **17**. This may be attributed to enhanced electron-releasing tendency, due to the plurality of the sulfur-bearing substituent (Scheme 3.3). Controlled potential electrolysis, discussed below, was employed for confirmation of assigned redox processes.

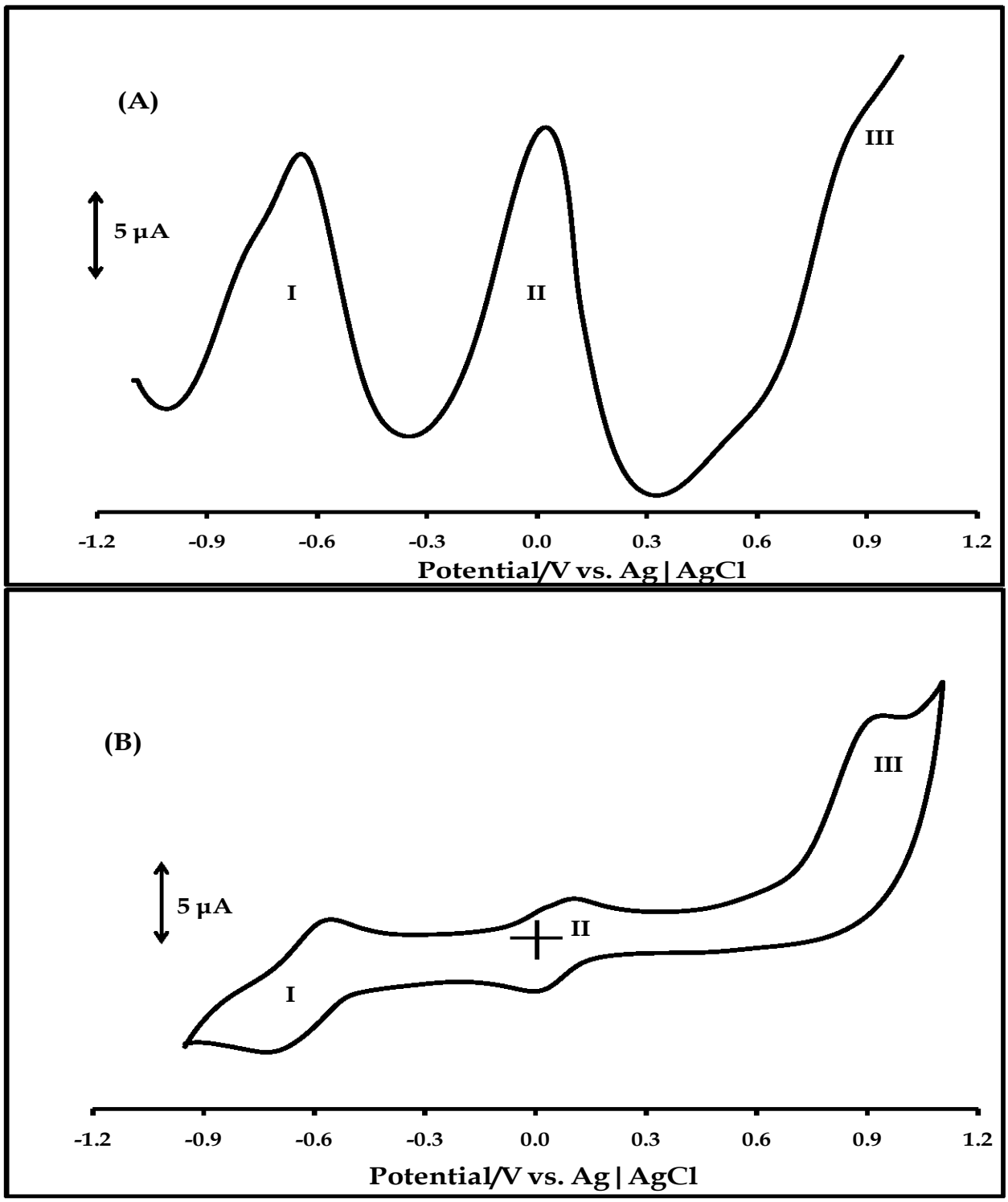

Figure 3.18: (A) Square wave and (B) cyclic voltammetry profiles of 1 × 10^{-3} M of complex **20** in freshly distilled DMF containing 0.1 M $TBABF_4$ supporting electrolyte. Step potential: 5 mV, amplitude: 50 mV, frequency: 10 Hz. Scan rate: 100 mVs^{-1}.

Fig. 3.19 shows the spectral changes observed on the application of potentials negative of couple **II** (+0.06 V versus Ag|AgCl, Fig. 3.18B) (complex **20**). The initial spectrum shows a very pronounced peak at 653 nm, with the main Q-band at 760 nm. The peak at 653 nm is characteristic of MnPc μ-oxo complexes [92]. As reported for complex **17**, the presence of the μ-oxo MnPc species was also investigated by monitoring the spectral transformations of complex **20**, in DMF, in the presence or absence of oxygen. On bubbling nitrogen, the peak at 653 nm decreased in intensity. However, attempts to exclude oxygen completely during spectroelectrochemical studies were unsuccessful. The cyclic and square wave voltammograms reported in Fig. 3.18B were recorded under an atmosphere of nitrogen, hence can be attributed, mainly, to $Mn^{III}Pc$ species.

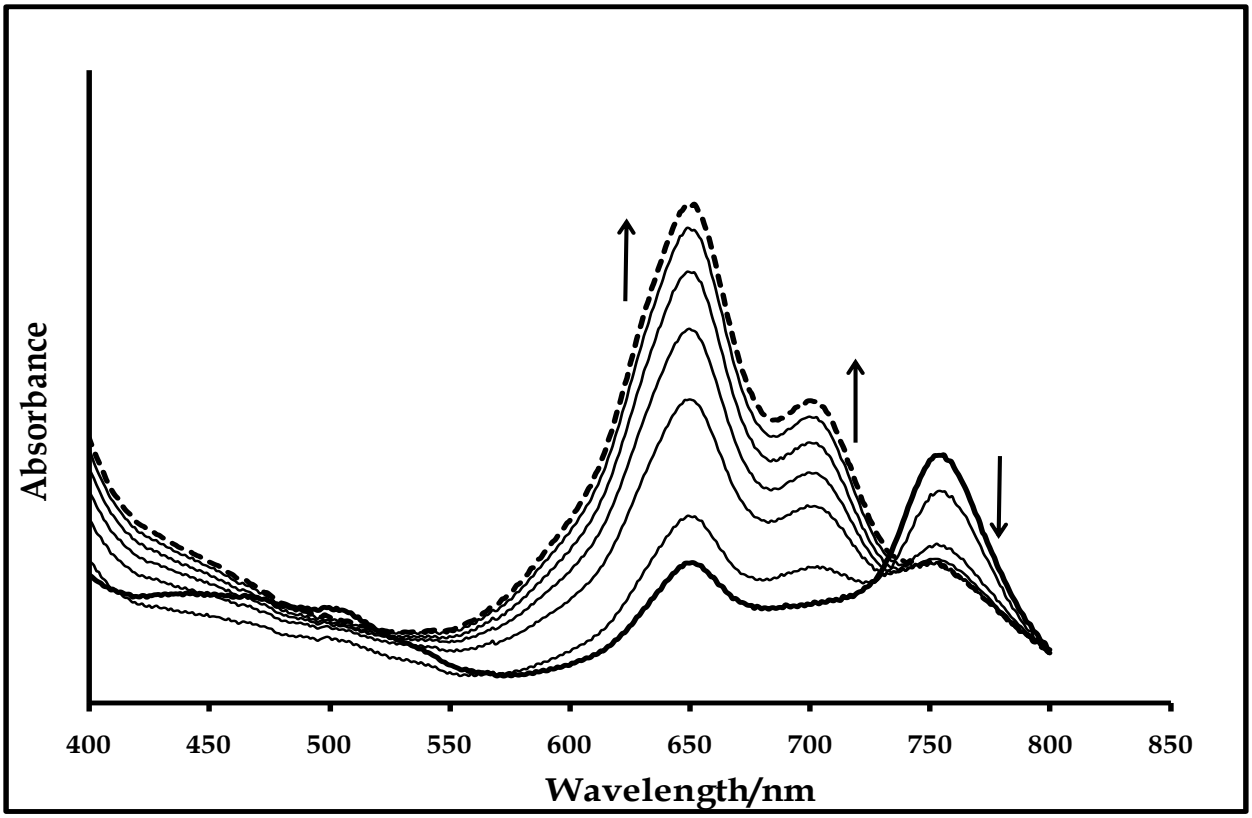

Figure 3.19: UV-Vis spectral changes observed for complex **20** in DMF containing 0.1 M $TBABF_4$ during controlled potential electrolysis at the potential more negative of process **II** (-0.08 V vs. Ag|AgCl). Solid line (spectrum before electrolysis) and dashed line (spectrum after electrolysis).

Upon reduction, at potentials of process **II**, there was a blue shift in Q-band (from 760 to 705 nm) (Table 3.3) and the colour of the complex changed from purple to green. A gradual disappearance of the charge transfer bands in the 500 nm region was also noticed, with diffused isobestic point at 736 nm, confirming the presence of the μ-oxo complex, with the starting $Mn^{III}Pc^{-2}$ species and the electro-generated $Mn^{II}Pc^{-2}$ species. The formation of the latter was accompanied by the formation of more μ-oxo MnPc species.

The persistence of the μ-oxo MnPc species (Fig. 3.19), compared to the substantial decrease in intensity of this species, under a similar condition (N_2-dearated medium) in complex **17** (peripherally tetra-substituted derivative) (Fig. 3.17B), suggests that the presence of this phenomenon may be influenced by the number of substituent, in addition to the point of substitution on the Pc ligand and concentration of oxygen in the medium. The blue shift in Q-band is associated with the reduction of $Mn^{III}Pc^{-2}$ to $Mn^{II}Pc^{-2}$ [91], as explained previously. These spectral changes thus confirmed that redox couple **II** in Fig. 3.18B is due to the reduction of $Mn^{III}Pc^{-2}$ to $Mn^{II}Pc^{-2}$**.** The number of electrons transferred can not be accurately estimated, due to complications arising from the μ-oxo MnPc species. However, this assignment is consistent with those reported for other thio-derivatised MnPc complexes (Table 1.2). The origin of process **I** (Fig. 3.18B) can not be confirmed by spectroelectrochemistry, due to the complicated nature of the spectral changes in Fig. 3.19, but the assignment of CV data agrees substantially with the electrochemical data of other thio-substituted MnPc complexes (Table 1.2).

3.1.3.2.4 Complex 23

The square wave and cyclic voltammetry of 1×10^{-3} M of complex **23**, in freshly distilled, dried DMF, containing $TBABF_4$ (supporting electrolyte), are shown in Fig. 3.20A and B. Two well-resolved redox processes (**I** and **II**) and one weak irreversible oxidation (**III***) process were observed. Process **I** ($E_{1/2}$ = -0.75 V versus Ag|AgCl), Table 3.4, may be assigned to ring reduction and $Mn^{II}Pc^{-2}/Mn^{II}Pc^{-3}$ couple [226], while process **II**

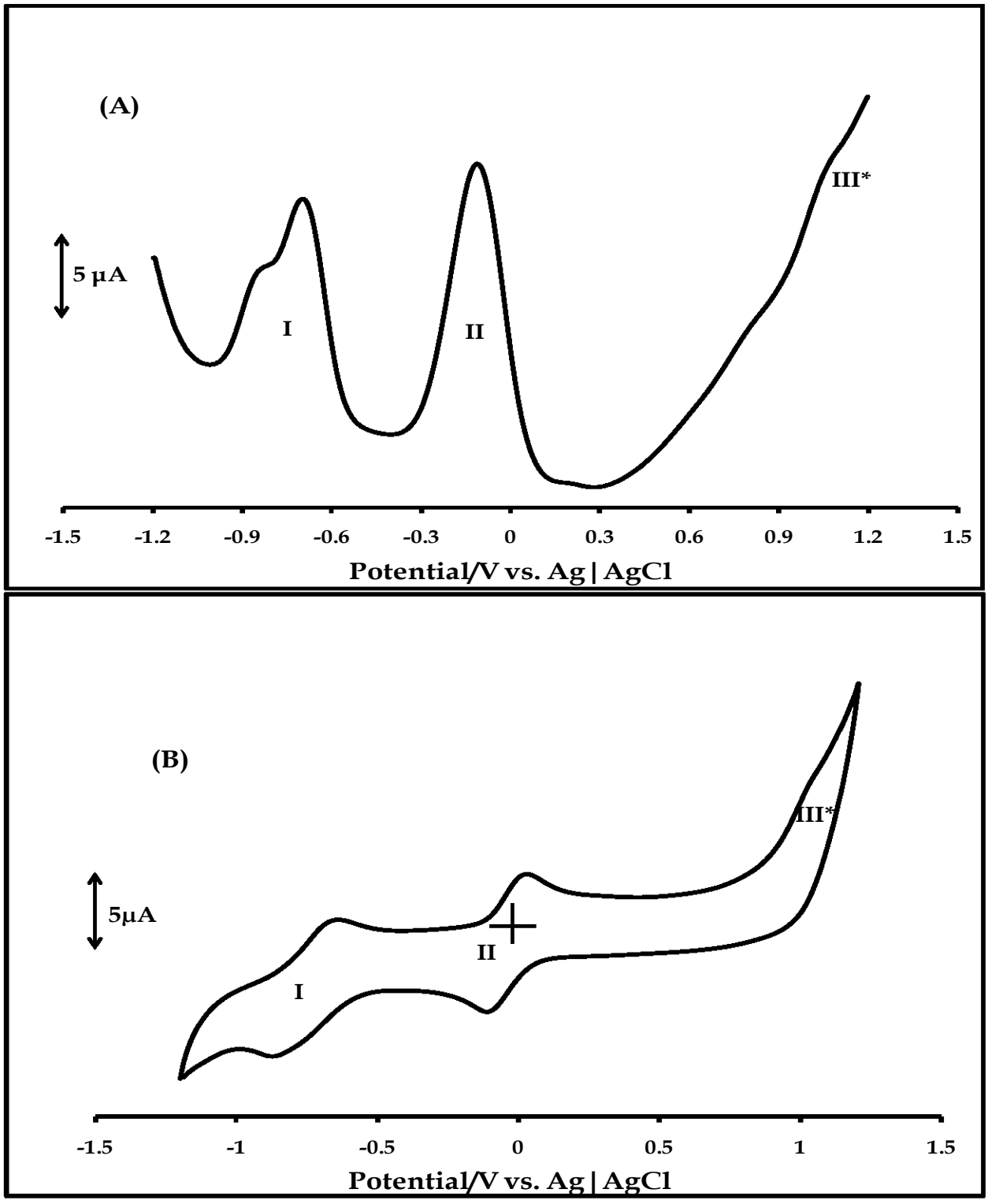

Figure 3.20: (A) Square wave and (B) cyclic voltammetry profiles of 1 × 10^{-3} M of complex **23** in freshly distilled DMF containing 0.1 M $TBABF_4$ supporting electrolyte. Step potential: 5 mV, amplitude: 50 mV, frequency: 10 Hz. Scan rate: 100 mVs^{-1}.

($E_{1/2}$ = -0.04 V versus Ag | AgCl), Table 3.4, can be attributed to a metal-based reduction, $Mn^{III}Pc^{-2}/Mn^{II}Pc^{-2}$, in comparison with literature [94]. Processes **I** (ΔE = 171 mV) and **II** (ΔE = 73 mV) are quasi-reversible and reversible, respectively. The split observed in process **I** may be attributed to aggregation [226]. Process **III*** (Ep = +1.05 V versus Ag | AgCl) (Table 3.4) is a weak irreversible process, assigned to ring oxidation ($Mn^{III}Pc^{-1}/Mn^{III}Pc^{-2}$), in comparison with literature [226]. These assignments were confirmed using controlled potential electrolysis.

Controlled potential electrolysis involving complex **23** resulted in the spectral changes shown in Fig. 3.21. On the application of potentials slightly negative of process **II** (Fig. 3.20B), the spectral transformations in Fig. 3.21A were observed. The initial spectrum is the same as that observed for the complex in Fig. 3.3 (Q-band: 768 nm), Table 3.1. There was a blue shift in Q-band (768 to 710 nm) (Fig. 3.21A) and collapse of the charge transfer band (509 nm) upon reduction. These spectral changes are consistent with a

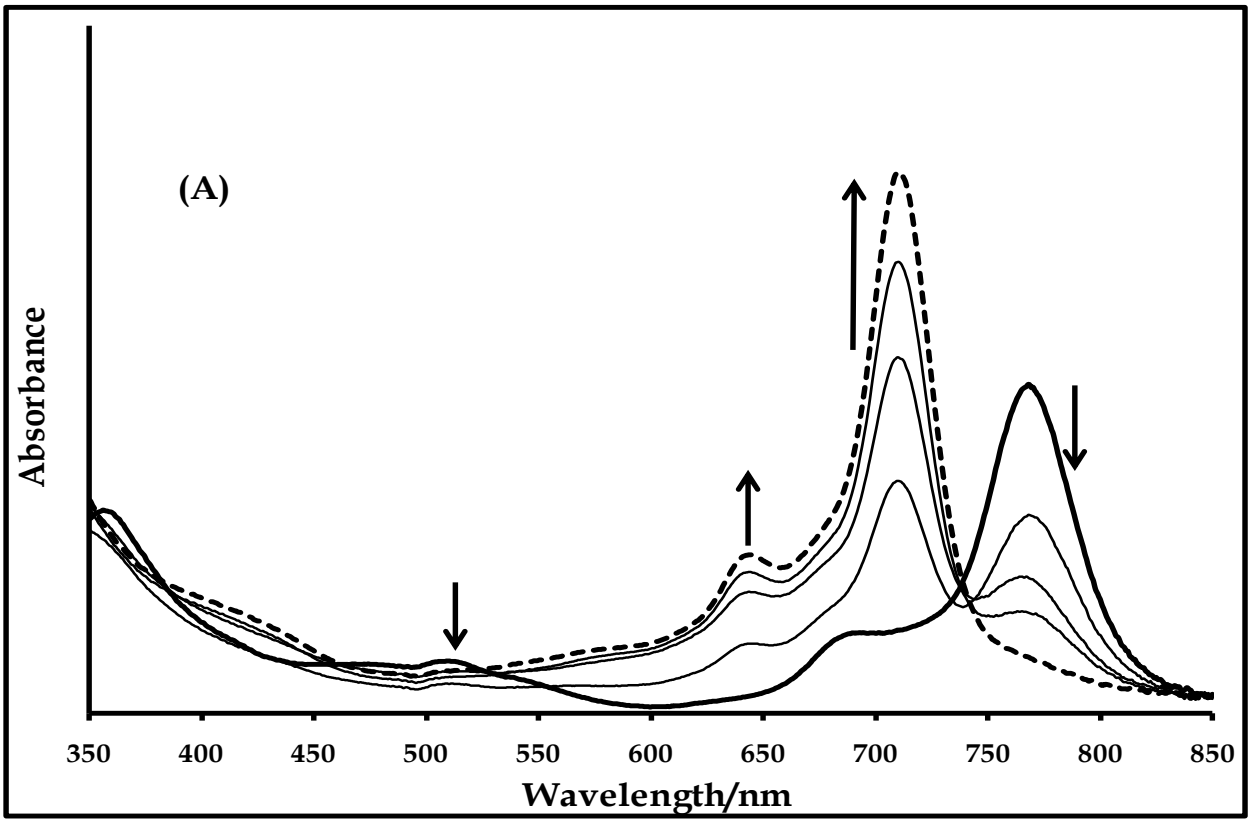

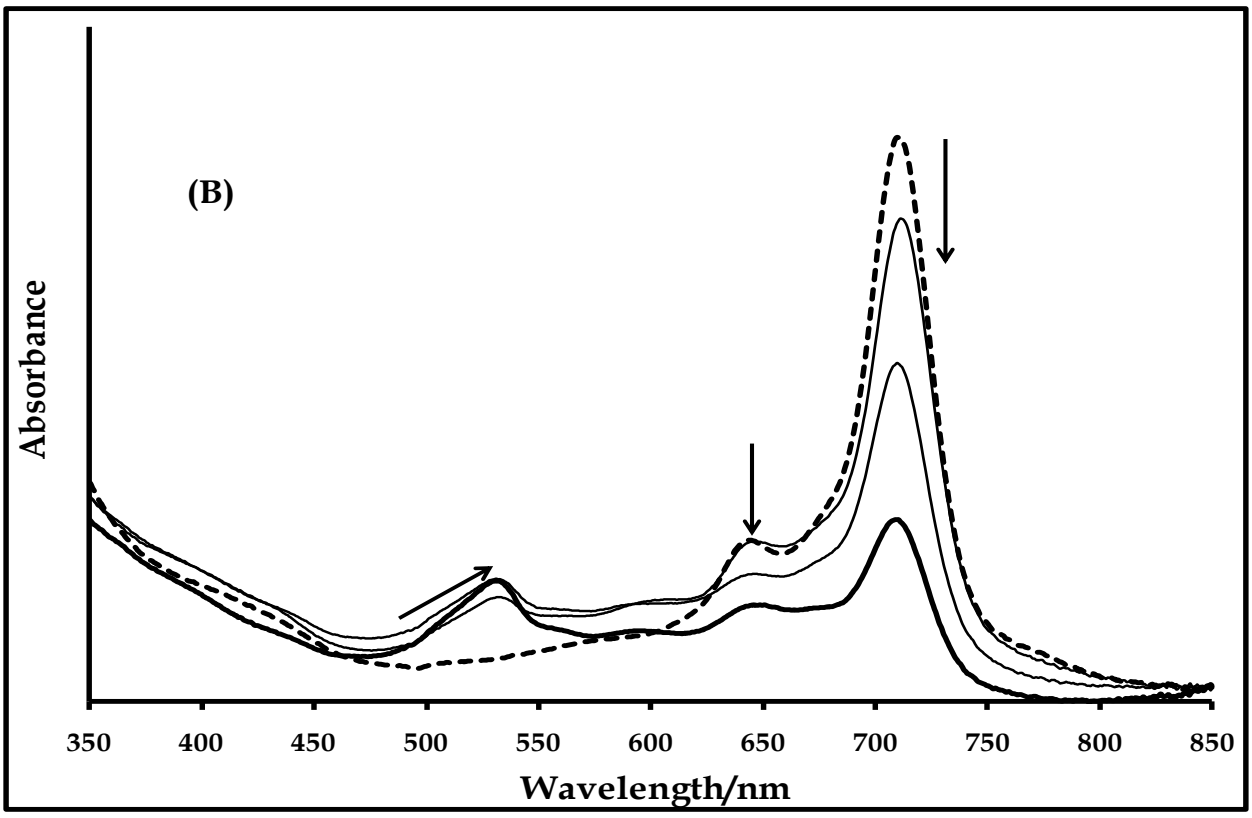

Figure 3.21: UV-Vis spectral changes observed for complex **23** during controlled potential electrolysis at (**A**) -0.1 V (process **II**), (**B**) -0.85 V (process **I**) vs. Ag|AgCl. Electrolyte = DMF containing 0.1 M $TBABF_4$. The final spectrum in (**A**) is the starting spectrum in (**B)**.

metal-based reduction (Mn^{III} to Mn^{II}) in MnPc complexes [91], as remarked previously, supporting the assignment of process **II** to $Mn^{III}Pc^{-2}/Mn^{II}Pc^{-2}$ couple. The number of electrons transferred was estimated to be approximately 1, using equation 3.1. The spectral changes in Fig. 3.21B were obtained on the application of potentials slightly negative of process **I**. There was further reduction of the species generated in Fig. 3.21A, resulting in a decrease in intensity of the Q-band and the emergence of a new band around 530 nm. This indicates reduction of Pc^{-2} to Pc^{-3} [61], justifying the assignment of process **I** to the $Mn^{II}Pc^{-2}/Mn^{II}Pc^{-3}$ couple. The number of electrons transferred was evaluated to be 1 using equation 3.1.

For all the complexes (**14**, **17**, **20** and **23**), confirmation of process **III** was complicated by degradation of the complexes, on the application of potentials slightly positive of this

process. This is consistent with the behavior of thio-substituted MPc complex [225], as remarked earlier for the CoPc derivatives. Nonetheless, assignment of this process agrees closely with the values reported previously for other MnPc complexes [84,95].

3.1.3.3 Iron phthalocyanine complexes

3.1.3.3.1 Complex 15

Figs. 3.22A and B show the square wave and cyclic voltammetry of 1×10^{-3} M of complex **15** in freshly distilled, dried DMF, containing 0.1 M $TBABF_4$, as the supporting electrolyte. Four redox processes were identified and assigned, in comparison with literature for FePc complexes, Table 1.3. Process **I** is a quasi-reversible (ΔE = 171 mV) ring-based reduction, assigned to the $Fe^{I}Pc^{-2}/Fe^{I}Pc^{-3}$ couple ($E_{1/2}$ = -1.14 V vs. Ag|AgCl), Table 3.5. Process **II** is also a quasi-reversible (ΔE = 121 mV) redox process, assigned as a metal-based reduction, $Fe^{II}Pc^{-2}/Fe^{I}Pc^{-2}$, ($E_{1/2}$ = -0.49 V vs. Ag|AgCl) [74], Table 3.5. Process **III** is a metal-based oxidation, associated with $Fe^{III}Pc^{-2}/Fe^{II}Pc^{-2}$ species ($E_{1/2}$ = +0.29 V vs. Ag|AgCl) [81], Table 3.5. This process is also quasi-reversible (with a weak cathodic component). Process **IV** is an irreversible ring-based oxidation, assigned to the $Fe^{III}Pc^{-1}/Fe^{III}Pc^{-2}$ couple (Ep = +0.93 V vs. Ag|AgCl) [81], Table 3.5. These redox assignments were not confirmed by spectroelectrochemistry, due to the complicated nature of the UV-Vis spectra of these complexes in DMF. Nonetheless, they are consistent with those reported previously for thio-substituted FePc complexes (Table 1.3).

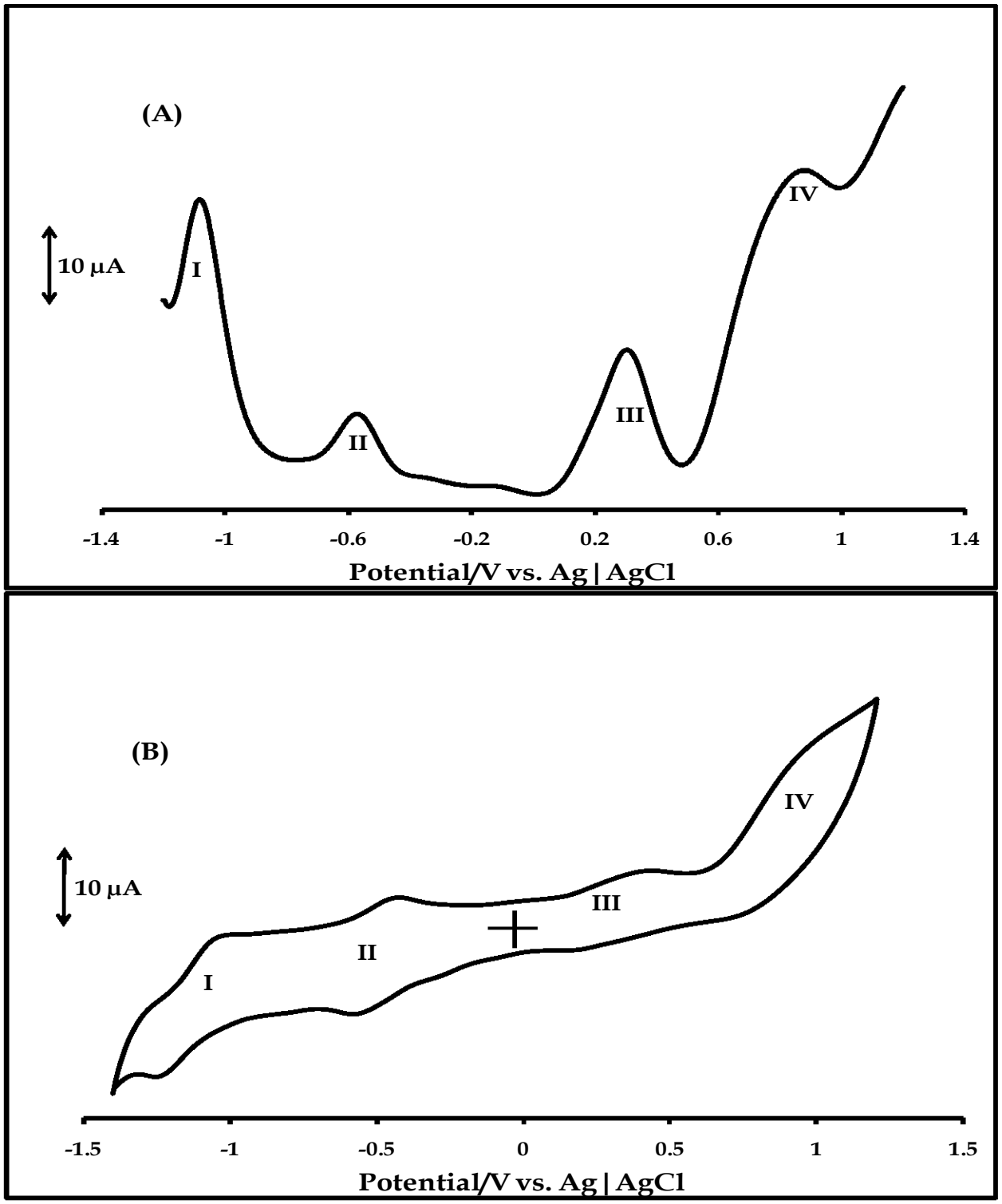

Figure 3.22: (A) Square wave and (B) cyclic voltammetry profiles of 1 × 10^{-3} M of complex **15** in freshly distilled DMF containing 0.1 M $TBABF_4$ supporting electrolyte. Step potential: 5 mV, amplitude: 50 mV, frequency: 10 Hz. Scan rate: 100 mVs^{-1}.

Table 3.5: Summary of electrochemical data of FePc complexes in DMF, values in Volt vs. Ag|AgCl.

Complex	$Fe^{I}Pc^{-2}/Fe^{I}Pc^{-3}$	$Fe^{II}Pc^{-2}/Fe^{I}Pc^{-2}$	$Fe^{III}Pc^{-2}/Fe^{II}Pc^{-2}$	$Fe^{III}Pc^{-1}/Fe^{III}Pc^{-2}$
15	-1.14	-0.49	+0.29	+0.93
18	-1.03	-0.43	+0.33	+0.97
21	-0.96	-0.35	+0.26	+0.87
24	-1.11	-0.64	+0.22	_

3.1.3.3.2 Complex 18

Figs. 3.23A and B show the square wave and cyclic voltammetry of 1 × 10^{-3} M of complex **18** in freshly distilled, dried DMF, containing 0.1 M $TBABF_4$, as supporting electrolyte. Four redox processes can be identified. Process **I** is a quasi-reversible (with anodic to cathodic peak difference, Δ*E*, larger than 90 mV obtained for ferrocene standard) ring-based redox process, assigned to the $Fe^{I}Pc^{-2}/Fe^{I}Pc^{-3}$ couple ($E_{1/2}$ = -1.03 V vs. Ag|AgCl) (Table 3.5), in comparison with literature (Table 1.3). Processes **II** is a metal-based redox process, associated with the $Fe^{II}Pc^{-2}/Fe^{I}Pc^{-2}$ couple ($E_{1/2}$ = -0.43 V vs. Ag|AgCl) [74], Table 3.5. Its cathodic to anodic current ratio is near unity, but quasi-reversible (Δ*E* > 90 mV obtained for ferrocene standard). Process **III** shows a weak cathodic component, thus quasi-reversible. It is assigned to metal-based oxidation and the $Fe^{III}Pc^{-2}/Fe^{II}Pc^{-2}$ couple ($E_{1/2}$ = +0.33 V vs. Ag|AgCl) (Table 3.5). Process **IV** is an irreversible ring-based oxidation, attributed to the $Fe^{III}Pc^{-1}/Fe^{III}Pc^{-2}$ couple (E_p = +0.97 V vs. Ag|AgCl) (Table 3.5).

It is important to mention the influence of point of substitution (non-peripheral, **15**, versus peripheral, **18**) on the electrochemical properties of these complexes (Table 3.5). Like the cobalt analogues, non-peripheral substitution favored oxidation, while peripheral substitution made reduction occurred much more readily.

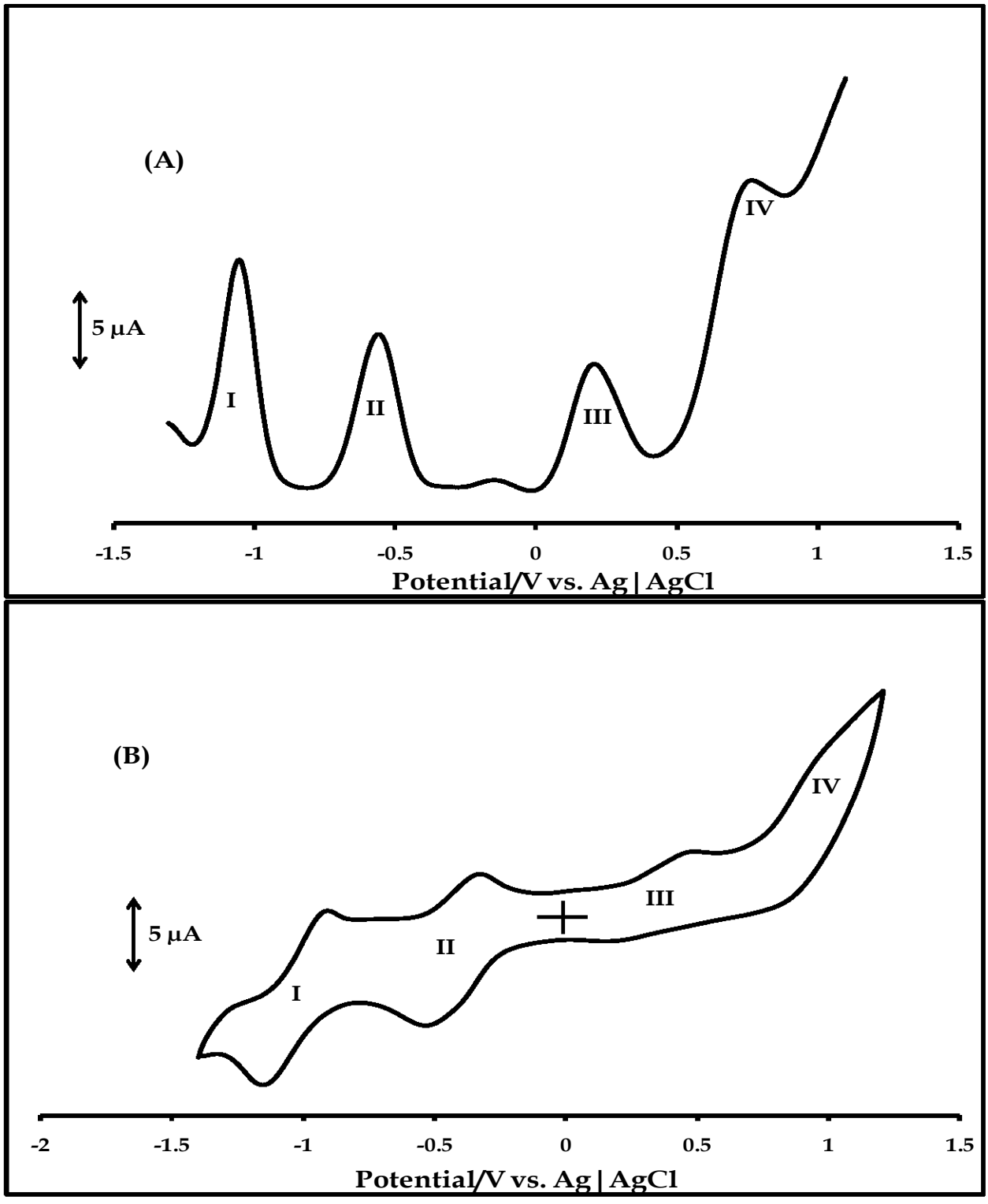

Figure 3.23: (A) Square wave and (B) cyclic voltammetry profiles of 1 × 10^{-3} M of complex **18** in freshly distilled DMF containing 0.1 M $TBABF_4$ supporting electrolyte. Step potential: 5 mV, amplitude: 50 mV, frequency: 10 Hz. Scan rate: 100 mVs^{-1}.

As discussed for complex **15**, the complicated nature of the spectra of complex **18** in DMF made spectroelectrochemical investigation of these redox assignments difficult, but they are consistent with the electrochemical data of other thio-derivatised FePc complexes (Table 1.3).

3.1.3.3.3 Complex 21

The square wave and cyclic voltammetry of 1 x 10^{-3} M of complex **21** in freshly distilled, dried DMF, containing 0.1 M $TBABF_4$, as the supporting electrolyte, are shown in Figs. 3.24A and B, respectively. Although, the UV-Vis spectra in DMF (Fig. 3.5C) showed complicated behavior, the square wave and cyclic voltammetry peaks are well resolved, as shown in Fig. 3.24. The cyclic voltammogram will be dominated by $Fe^{II}Pc$ species, since the spectrum of the complex shows this species to be dominant. Four distinct processes were observed. Process **I** ($E_{1/2}$ = -0.96 V versus Ag|AgCl) is assigned to ring reduction, $Fe^{I}Pc^{-2}/Fe^{I}Pc^{-3}$, Table 3.5. This process is quasi-reversible, with cathodic to anodic current ratio of almost unity, but peak separation, ΔE, of 120 mV, compared to 90 mV for ferrocene at the same scan rate (100 mV). Process **II** ($E_{1/2}$ = -0.35 V versus Ag|AgCl) (Table 3.5) is assigned to metal reduction, $Fe^{II}Pc^{-2}/Fe^{I}Pc^{-2}$. This process is reversible with ΔE = 90 mV, and cathodic to anodic current ratio close to unity. Process **III** ($E_{1/2}$ = +0.26 V versus Ag|AgCl), Table 3.5, is assigned to metal oxidation, $Fe^{III}Pc^{-2}/Fe^{II}Pc^{-2}$, in comparison with other thio-substituted FePc complexes [74], Table 1.3. Process **III** is quasi reversible, with a weak cathodic component. Process **I** (E_p = +0.87 V versus Ag|AgCl), Table 3.5, is assigned to ring oxidation, $Fe^{III}Pc^{-1}/Fe^{III}Pc^{-2}$. This process is irreversible, as typical of thio-substituted MPc complexes [95,223].

The reversible nature of process **II** (Fig. 3.24B), coupled with the less positive oxidation potentials of processes **III** and **IV** (Table 3.5), relative to those of the corresponding processes in complex **18** (the peripherally tetra-substituted derivative) (Fig. 3.23B), are evidence of enhanced electron-donating tendency, associated with the plurality of the

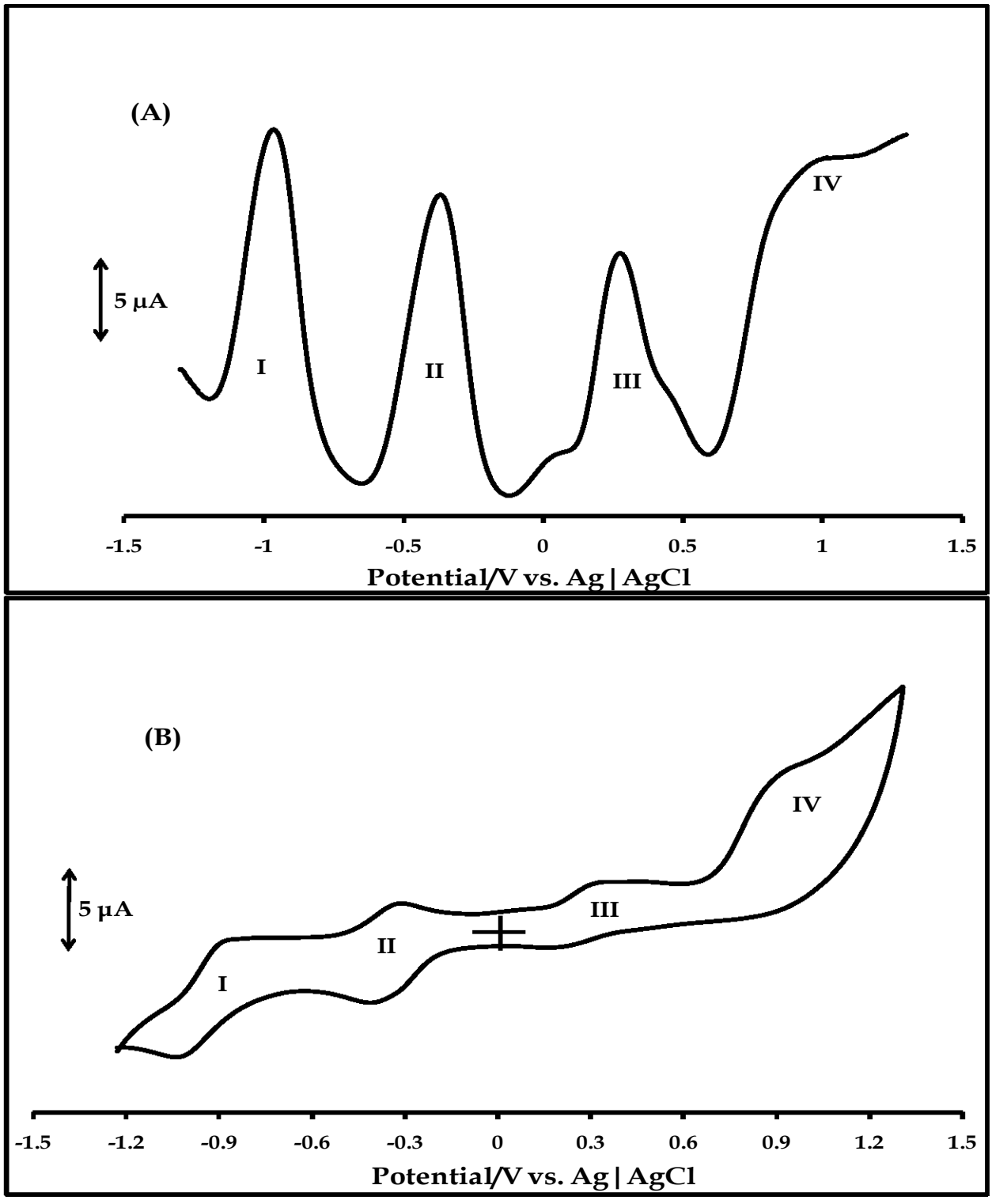

Figure 3.24: (A) Square wave and (B) cyclic voltammetry profiles of 1×10^{-3} M of complex **21** in freshly distilled DMF containing 0.1 M $TBABF_4$ supporting electrolyte. Step potential: 5 mV, amplitude: 50 mV, frequency: 10 Hz. Scan rate: 100 mVs^{-1}.

electron-releasing substituent in complex **21** (the octa-substituted derivative) (Scheme 3.3). Like complexes **15** and **18**, spectroelectrochemical studies were not successful for the confirmation of assigned redox processes. However, the assignments were based on the well-known electrochemistry of FePc complexes, in comparison with other thio-substituted FePc complexes (Table 1.3).

3.1.3.3.4 Complex 24

Fig. 3.25A and B are the square wave and cyclic voltammetry of 1×10^{-3} M of complex **24** in freshly distilled, dried DMF containing $TBABF_4$, as the supporting electrolyte. Three redox processes can be observed. Process **I** ($E_{1/2}$ = -1.11 V versus Ag|AgCl), Table 3.5, is reversible (ΔE = 70 mV), in terms of cathodic to anodic peak separation, but the peak current ratio deviates from unity. This process is assigned to ring reduction and the $Fe^{I}Pc^{-2}/Fe^{I}Pc^{-3}$ couple [100]. Process **II** ($E_{1/2}$ = -0.64 V versus Ag|AgCl), Table 3.5, is also reversible (ΔE = 50 mV), it is attributed to metal-based reduction ($Fe^{II}Pc^{-2}/Fe^{I}Pc^{-2}$) [226]. Process **III** ($E_{1/2}$ = +0.22 V versus Ag|AgCl) is a quasi-reversible (ΔE = 131 mV) metal-based oxidation, assigned to the $Fe^{III}Pc^{-2}/Fe^{II}Pc^{-2}$ couple, Table 3.5. No ring-based oxidation was observed in complex **24**, unlike complexes **15**, **18** and **21**, justifying the difference in the nature of substituent {diethylaminoethanethio (**15**, **18** and **21**) versus benzylthio (**24**)}. Process **II** was confirmed by spectroelectrochemistry.

Fig. 3.26 shows the spectral changes observed on the application of potentials slightly negative of process **II**. The first part involves shift in position of the Q-band (672 to 676 nm), with a new band at 550 nm, Fig. 3.26A. The second part (Fig. 3.26B) shows intensification of the 550 nm band and formation of a pink solution. Reduction of $Fe^{II}Pc$ to $Fe^{I}Pc$ is known to show no Q band, but gives a pink solution, due to absorption in the 500 nm region [91]. The pink colour of the solution has been attributed to disturbance of the π-π* spectrum of the Pc by Fe^{I} [91,228]. Hence, spectral changes in Figs. 3.26A and B confirm the assignment of process **II** to the $Fe^{II}Pc^{-2}/Fe^{I}Pc^{-2}$ couple.

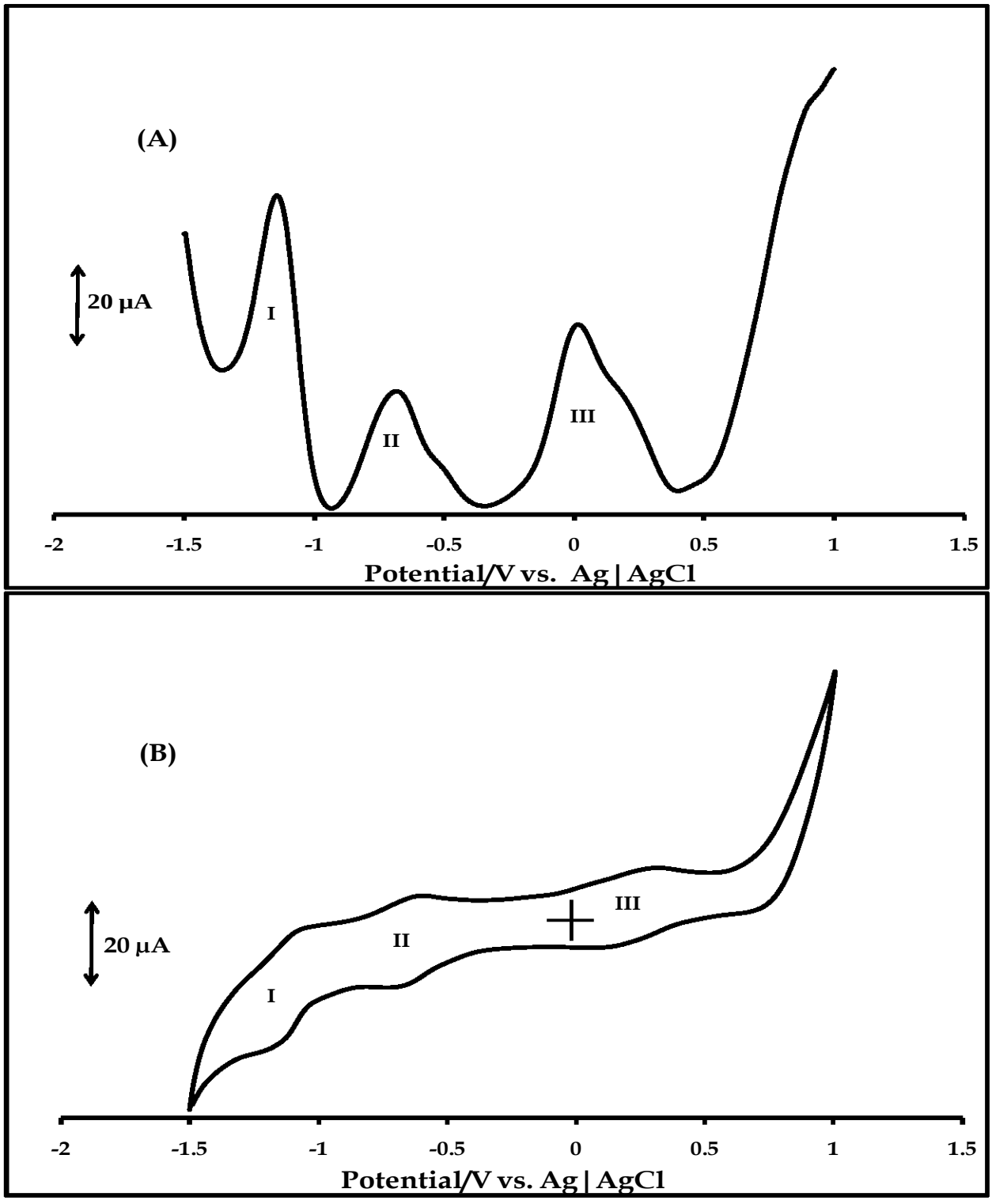

Figure 3.25: (A) Square wave and (B) cyclic voltammetry profiles of 1 × 10^{-3} M of complex **24** in freshly distilled DMF containing 0.1 M $TBABF_4$ supporting electrolyte. Step potential: 5 mV, amplitude: 50 mV, frequency: 10 Hz. Scan rate: 100 mVs^{-1}.

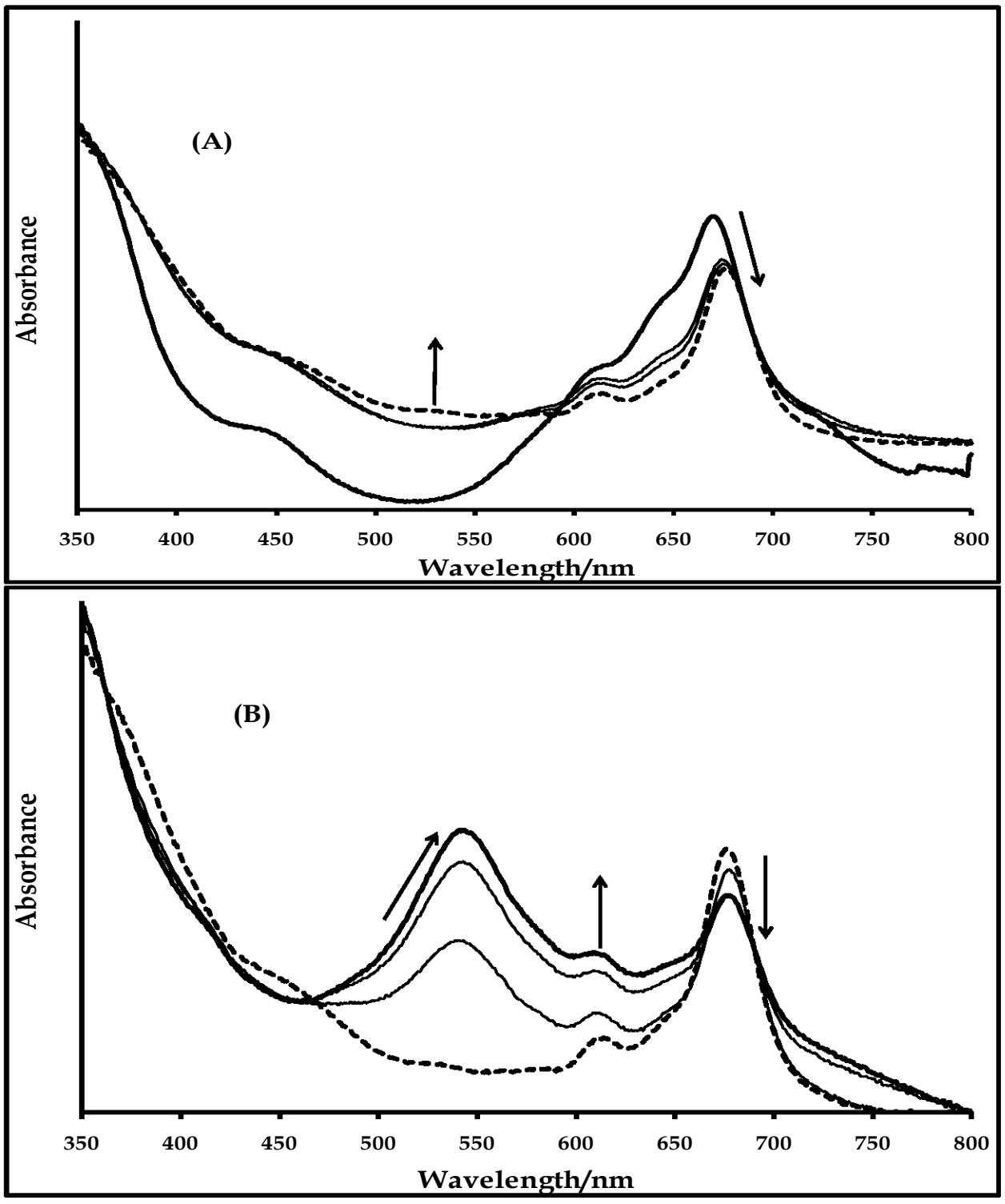

Figure 3.26: UV-Vis spectral changes observed for complex **24** during controlled potential electrolysis at ~ - 1.0 V vs. Ag|AgCl (process **II**), (A) initial changes and (B) final changes. Electrolyte = DMF containing 0.1 M $TBABF_4$. The final spectrum in (**A**) is the starting spectrum in (**B)**.

3.2 Nanomaterials

Acid functionalization of single walled carbon nanotubes and the formation of SWCNT-**18** nano-composite are shown in Scheme 3.5. Functionalization of SWCNTs may occur at the side walls, defect sites or open ends of the tube. In this work, functionalization is expected to take place at the open ends of the tubes, considering the possibility of cutting and opening the tubes, due to the conditions (the use of mixture of concentrated HNO_3 and H_2SO_4) employed for purification (Scheme 3.5).

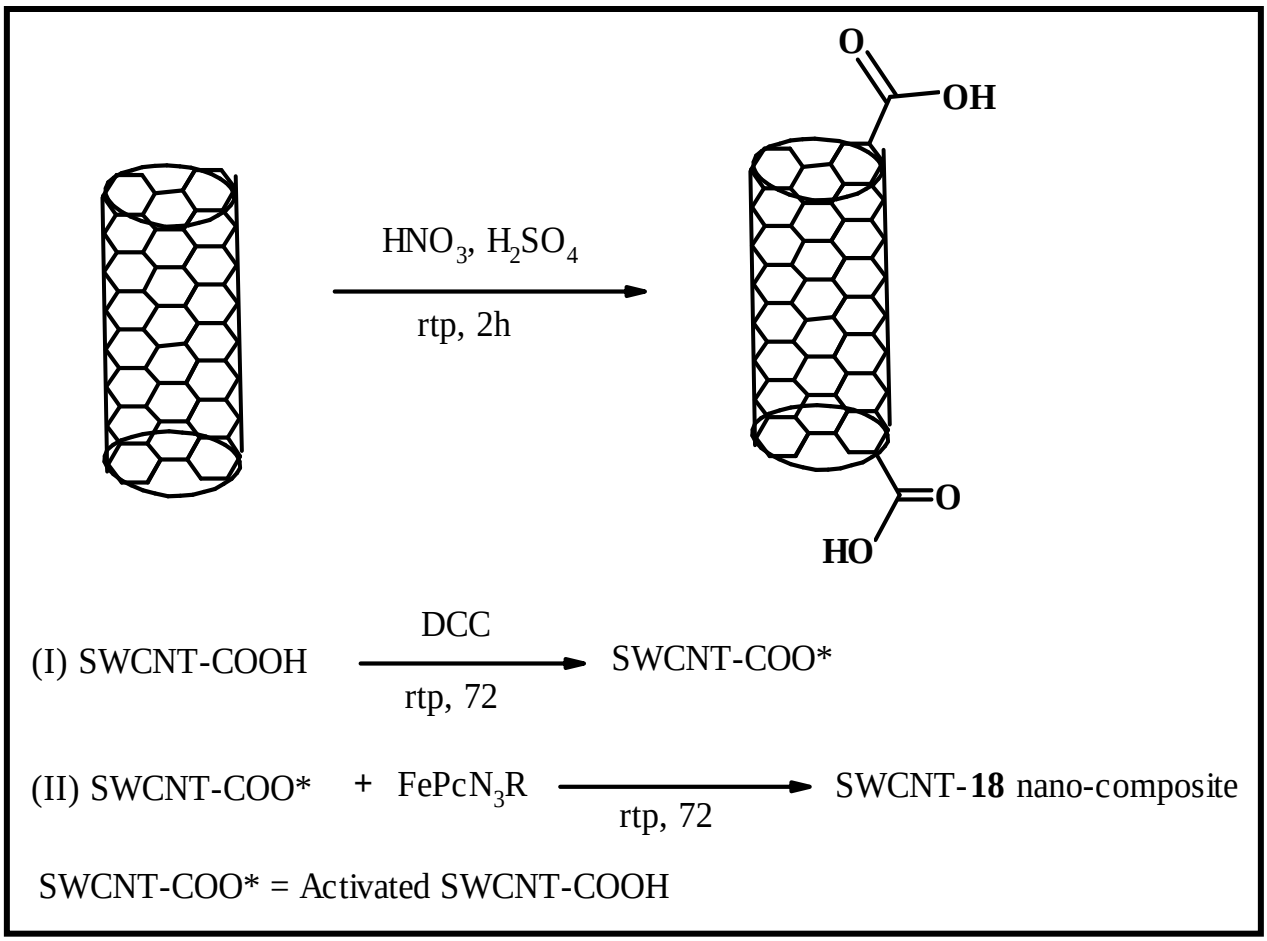

Scheme 3.5: Formation of SWCNT-COOH and SWCNT-**18** nano-composite

3.2.1 IR Spectral Properties

Infrared spectroscopy was used to investigate the molecular make-up of the nano-composite, relative that of its individual units. IR spectrum of SWCNT-COOH (Fig. 3.27A) shows a broad peak, characteristic of O-H stretch of COOH, near 3300 cm^{-1}, while bands at 1702 and 1228 cm^{-1} are attributed to C═O and C-O stretches of COOH, respectively. For complex **18** (Fig. 3.27B), bands at 2968 and 1600 cm^{-1} are attributed to aliphatic C-H and aromatic C═C stretches, respectively. Peaks at 1460 and 1393 cm^{-1} are signatures of CH_2 and CH_3 deformations, while bands at 822 and 746 cm^{-1} can be associated with aromatic C-H bends, for **18**. For the mixture of complex **18** and SWCNT-COOH (Fig. 3.27C), bands at 2970 and 1460 cm^{-1} are associated with aliphatic C-H stretch and CH_2 or CH_3 bend, respectively, which are features of complex **18** component of the mixture. The band at 1708 cm^{-1} is characteristic of C═O stretch of COOH in the SWCNT-COOH component of the mixture. IR spectrum of the nano-composite (SWCNT-**18**) (Fig. 3.27D) shows bands that suggest successful fabrication of the composite. A peak at 3327 cm^{-1} can be ascribed to O-H stretch (from the free COOH of SWCNT-COOH). A broad peak, characteristic of O-H stretch of COOH, was not observed in Fig. 3.27D, due to likely overlap with aliphatic C-H stretch. The strong band at 1625 cm^{-1} is characteristic of C═O stretch of amide, confirming the formation of the nano-composite. C═O stretch of free COOH in SWCNT-COOH was observed at 1702 cm^{-1} (Fig. 3.27A). The difference in position of C=O stretch can be attributed to resonance effect, which weakens the C═O stretch of amides and conjugated carbonyls; hence appears at lower frequency than normal C═O stretch. The rest of the bands can be associated with SWCNT or complex **18**.

The amide bond in the nanocomposite is expected to be coordinate covalent in nature, because ethyl is not a good leaving group. Enhanced electrophilicity of the carboxyl group of SWCNT-COOH, in the presence of DCC (Scheme 3.5), facilitated nucleophilic attack by the nitrogen atom of the tertiary amine functionality of

complex **18** (Scheme 3.2). Formation of an amide bond between tertiary amines and acids has been reported in a patent on the synthesis of carbon acid amides [229]. Formation of the amide bond was initiated and promoted by the activation of the acids, using suitable activating agents, such as the coupling agent (DCC) used in this work.

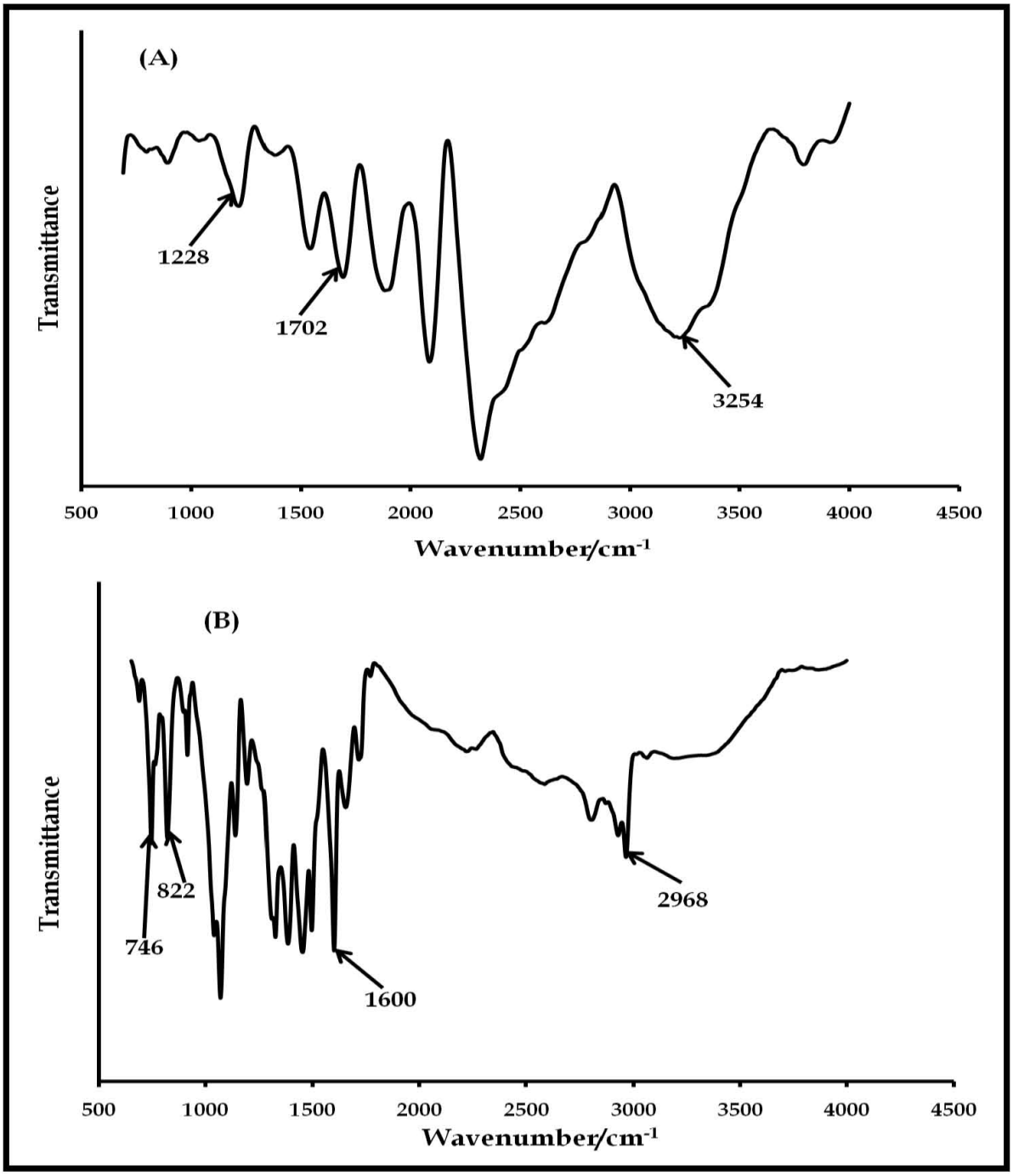

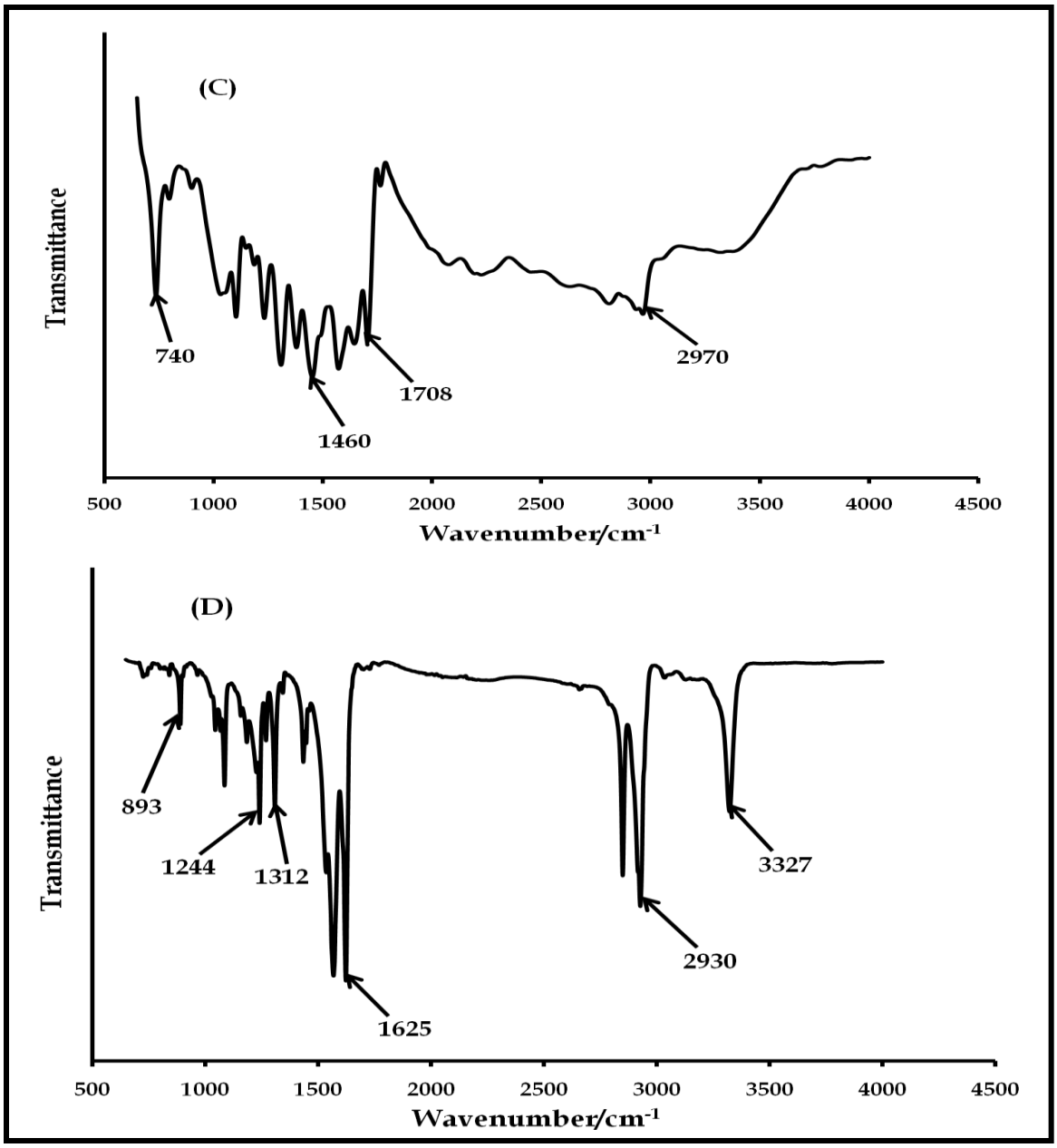

Figure 3.27: IR spectra of (A) SWCNT-COOH, (B) complex **18**, (C) mixture of SWCNT-COOH and complex **18** and (D) SWCNT-**18** composite

3.2.2 XRD Spectral Properties

The structural properties of the nano-composite, relative to that of its constituent units (SWCNT-COOH and complex **18**), were investigated using X-ray diffraction.

Changes in nature and positions of X-ray diffraction (XRD) peaks are reflective of changes in structural features of the sample under consideration. Figs. 3.28A-D show the XRD spectra of SWCNT-COOH, complex **18**, mixture of SWCNT-COOH and complex **18**, and SWCNT-**18** nano-composite, respectively. In Fig. 3.28A (SWCNT-COOH), the broad (2θ = 20.4° and 25.9°) and sharp (2θ = 44.4° and 51.8°) peaks are indicative of the amorphous and crystalline natures of the SWCNT-COOH, respectively. Using the International Center for Diffraction Data (ICDD) database, the peak at 2θ = 25.9° (approximately 26°) can be ascribed to (002) d-spacing of the SWCNT-COOH [194,230], while peaks at 2θ = 44.4° and 51.8° are characteristic of (100) [194] and (200) [230] reflections of carbon of the SWCNT-COOH, respectively. The peak at 2θ = 24.1° was the only pronounced peak on the XRD spectrum of **18** (Fig. 3.28B). This peak is close to the (002) reflection of carbon [230]. Importantly, the broad nature of this peak underlines the substantial amorphous nature of complex **18**. XRD spectrum of the mixture of SWCNT-COOH and complex **18** (Fig. 3.28C) was dominated by peaks characteristic of the structural properties of the SWCNT-COOH component. As discussed above, peaks at approximately 26°, 44.4° and 51.7° are signatures of (002), (100) and (200) reflections of carbon of the SWCNT-COOH, respectively [194,230]. The peak near 26° overlaps that of complex **18**. XRD spectrum of the nano-composite (Fig. 3.28D) was significantly different from that obtained for the individual components or ordinary mixture of the units of the nano-composite. There was complete disappearance of reflections {(002), (100) and (200)} originating from planes within the SWCNT-COOH. Also, peaks associated with reflections from planes within complex **18** have completely disappeared. These observations suggest successful fabrication of the nano-composite. The XRD spectrum in Fig. 3.28D was analyzed using ICDD database. Miller indices (hkl) for the observed peaks (110) (7.6°), (220) (15.3°), (310) (17.2°), (400) (21.8°), (330) (22.3°) and (321) (28.7°) suggest that reflections from planes within the composite are different from those within its constituent units (SWCNT-COOH and complex **18**), confirming the formation of the composite. Importantly, intensities of some of the peaks on the XRD spectrum of the

nano-composite were relatively higher than the intensities of the peaks on the XRD spectrum of any of its constituent units. This suggests that reflecting planes within the composite pass through areas of higher electron densities, compared to that within its constituent units. This is expected, since electron density of the composite is a re-enforcement of that of its individual components.

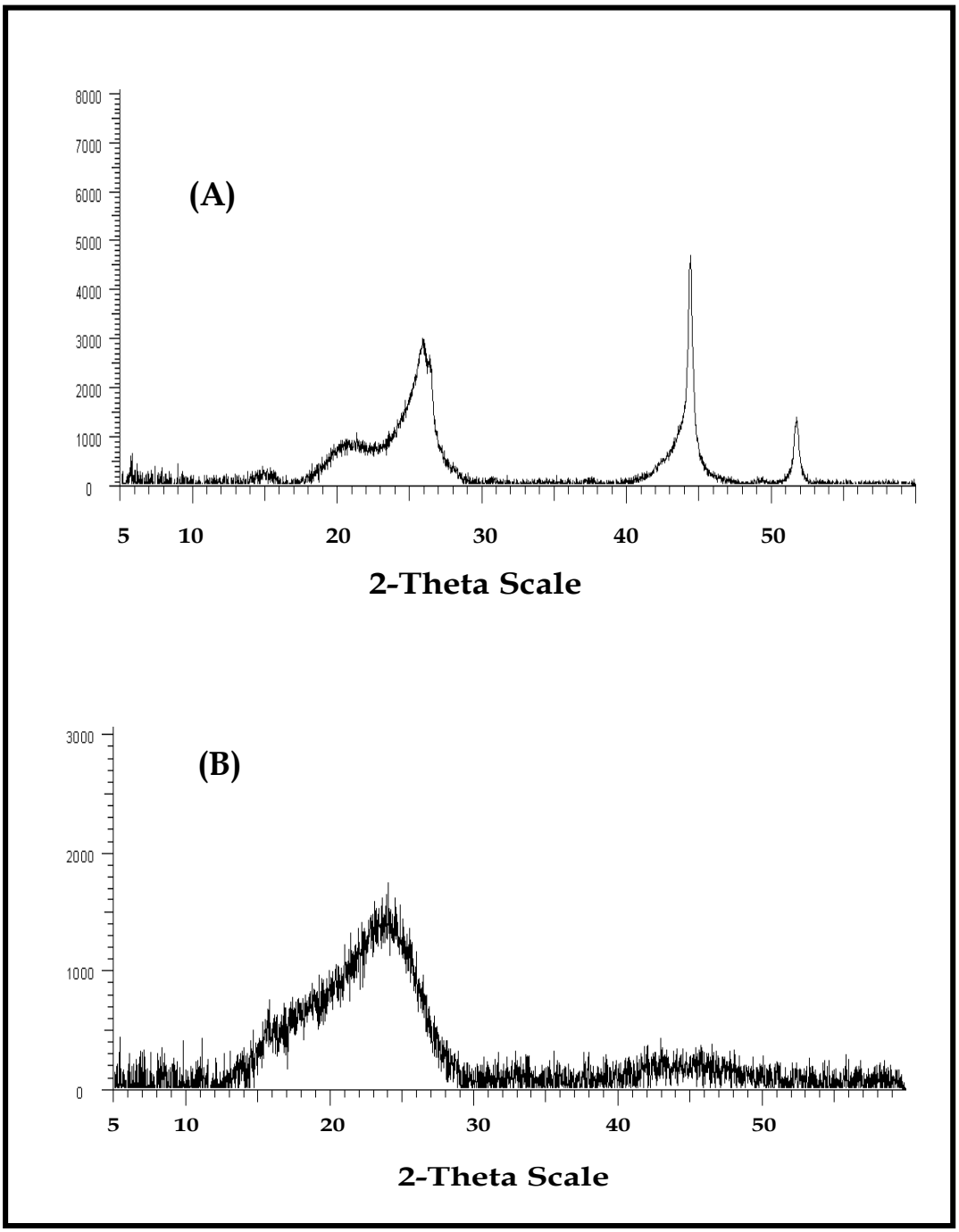

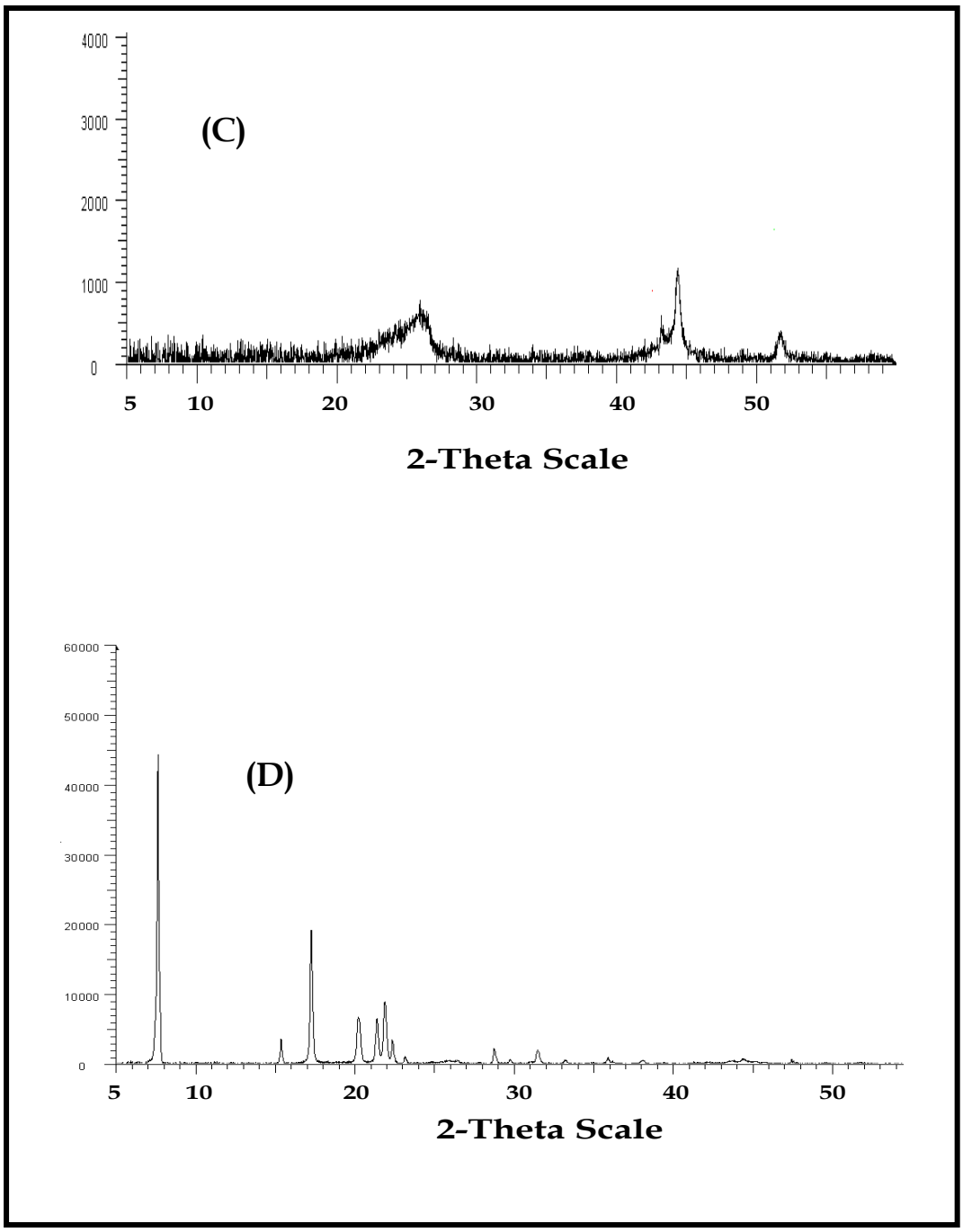

Figure 3.28: XRD spectra of (A) SWCNT-COOH, (B) complex **18**, (C) mixture of SWCNT-COOH and complex **18**, and (D) SWCNT-**18** nano-composite

3.2.3 Microscopic Properties

TEM technique offered a microscopic view of the nano-composite. Fig. 3.29A shows the TEM image of SWCNT-COOH. Importantly, the image of the nano-composite

(Fig. 3.29B) is distinctly different from that shown in Fig. 3.29A. Fig. 3.29B shows a nano-composite, with complex **18** attached continuously to the carbon nanotubes. Possible schematic representations of the nano-composite are shown in Fig. 3.30.

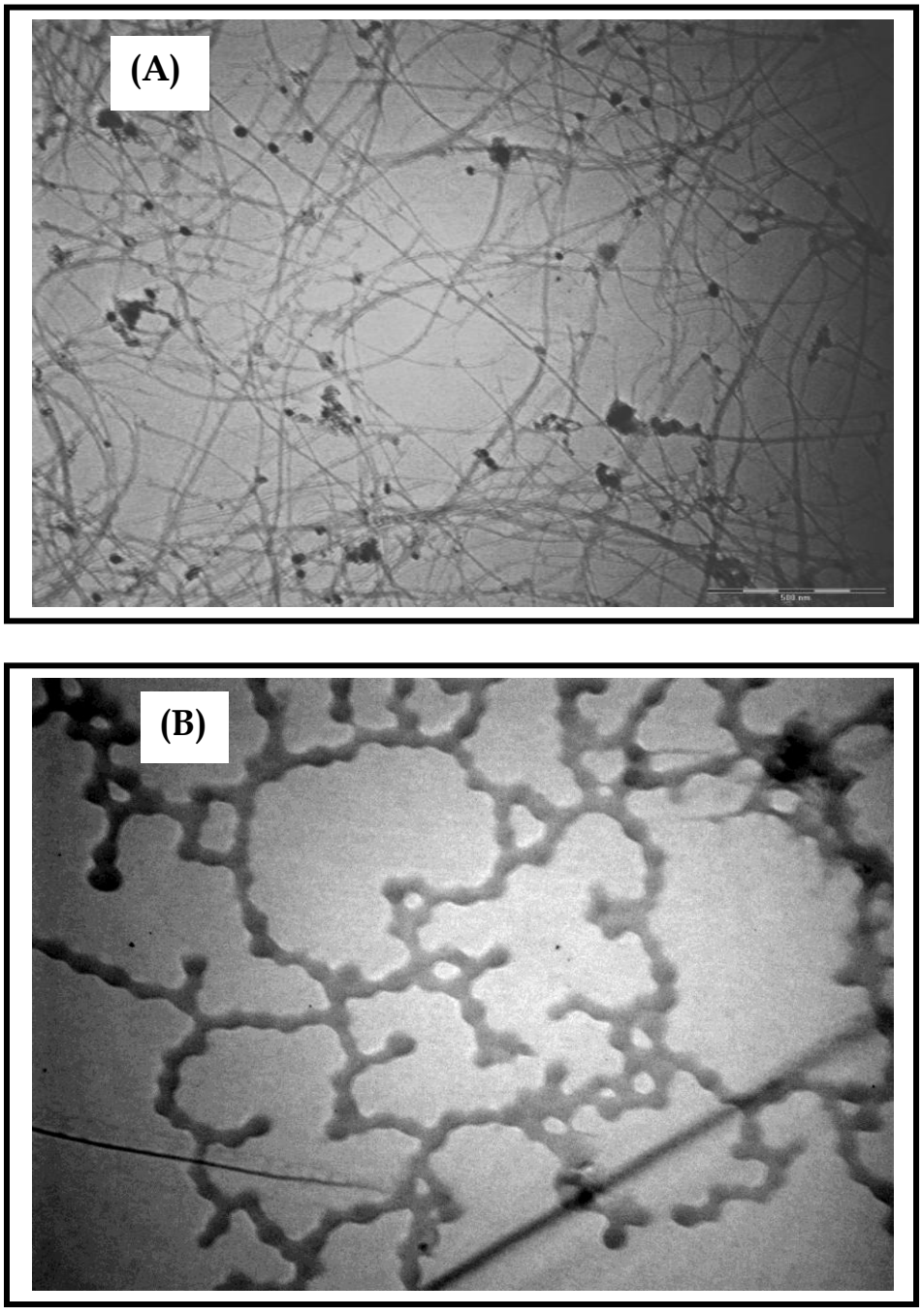

Figure **3.29**: TEM images of (A) SWCNT-COOH (× 10000) and (B) SWCNT-**18** nano-composite (× 80000).

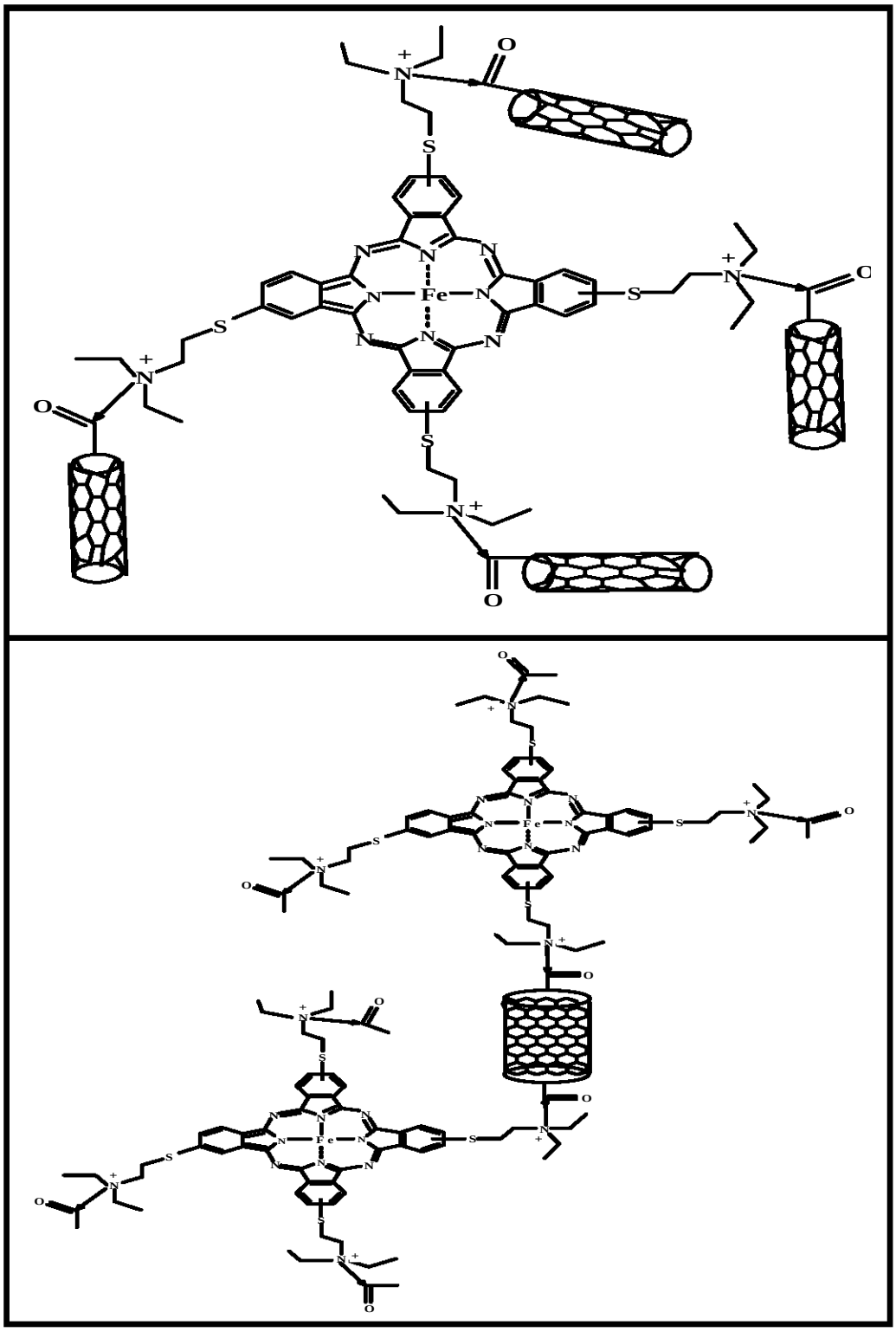

Figure 3.30: Possible schematic representations of SWCNT-**18** nano-composite

CHAPTER 4

SURFACE PROPERTIES OF MODIFIED ELECTRODES

4.1 Metallophthalocyanine self-assembled monolayer (SAM) on gold electrodes

SAM-modified gold electrodes were designed by immersing the bare gold disc electrode in DMF solution of desired MPc complex, for 24 hr in each case. Tetra-substituted derivatives of the complexes (**13**-**15, 18** and **22**-**24**) were employed for SAM formation. Formation of SAM was facilitated by coordination of the sulfur group (using its lone pairs of electrons) to gold, with the C-S bond intact after SAM formation, as reported previously [145], using electrochemical methods, which showed MPcs with different substituents, but same central metal, gave different SAM behavior [145]. Also, the existence of C-S bond after SAM formation has been confirmed, using in-situ surface enhanced raman spectroscopy (SERS), for SAMs of anthraquinone derivatives, formed on gold electrode [231]. The molecular configuration of the anthraquinone derivatives is similar to that of the MPc complexes studied in this work. The effects of the molecular identity and position of substituent, as well as the nature of central metal, on the surface properties of the adsorbed MPc complexes were investigated. The surface properties of **18**-SAM**-**modified gold electrode were also studied, with respect to those of the SAM of the nano-composite, SWCNT-**18**-SAM, in order to investigate the effects of the presence of SWCNT on such properties.

4.1.1 Inhibition of gold surface oxidation

Fig. 4.1 shows the oxidation (at +0.37 V vs. Ag|AgCl) and reduction (gold oxide stripping peak) (at around 0.02 V vs. Ag|AgCl) of bare gold surface in 0.1 M KOH. There was appreciable passivation of this redox process on (**13**-**15**)-SAM-modified gold electrodes (Fig. 4.1A). Complexes **13**, **14** and **15** are non-peripherally tetra-substituted diethylaminoethanethio-derivatised Co, Mn and FePc complexes, respectively (Scheme 3.1). Gold oxidation was considerably inhibited, with a drastic decrease in intensity of the gold oxide stripping peak, Fig. 4.1A. This suggests that the electrolyte was no longer accessible to the bare gold surface, confirming SAM formation. However, there was

gradual desorption of the SAMs during repetitive scanning, suggesting the unstable nature of the SAMs at alkaline pH.

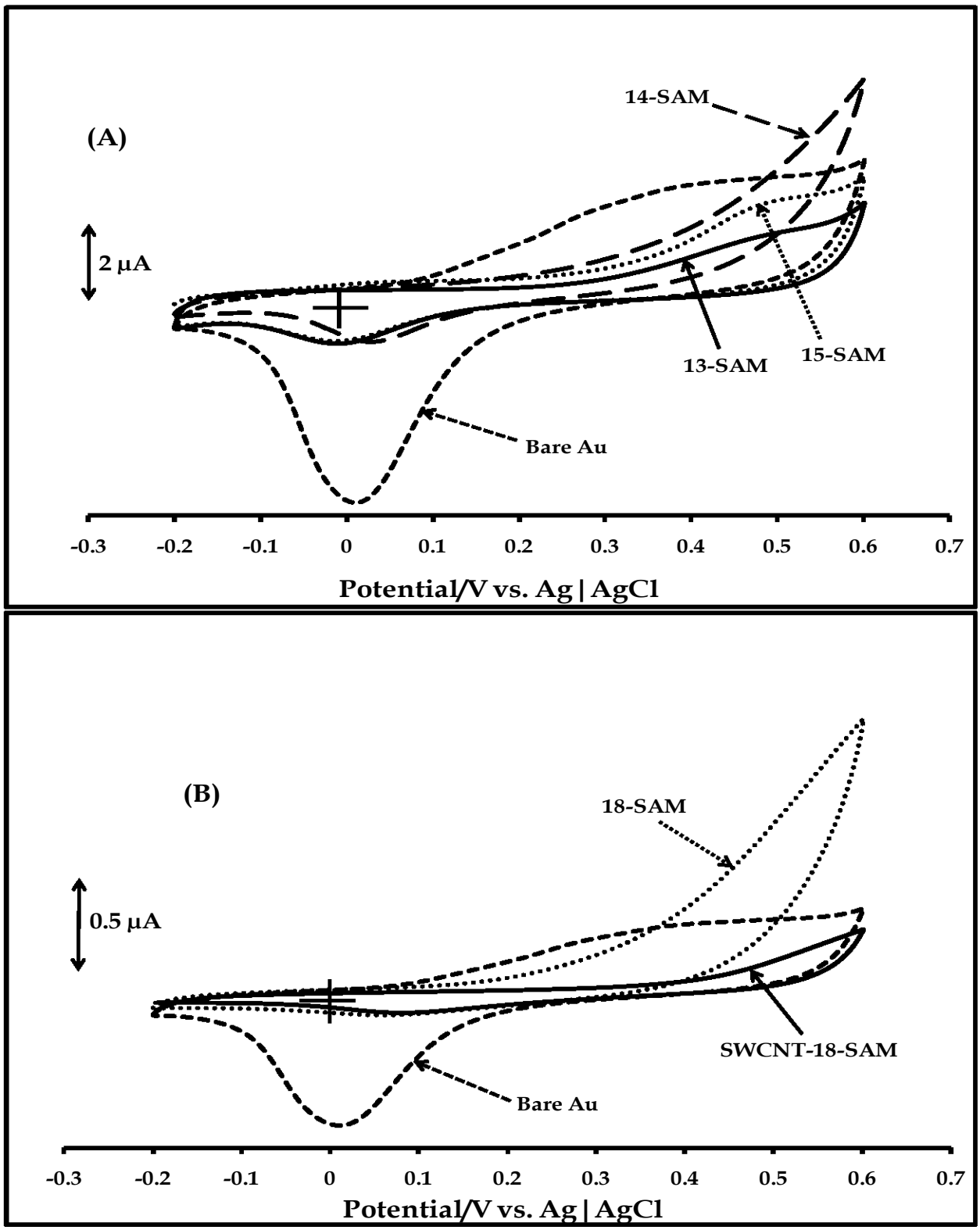

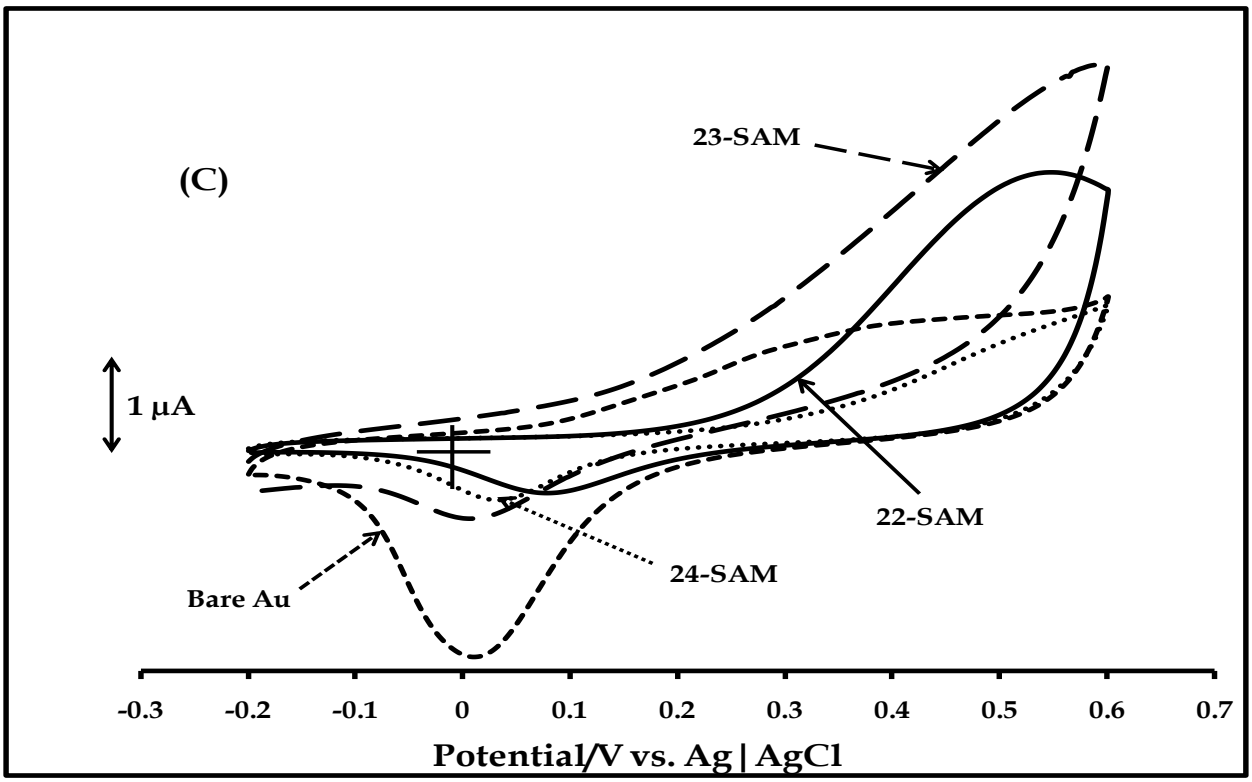

Figure 4.1: Cyclic voltammetry profiles of bare and (A) (**13**-**15**)-SAM, (B) **18**-SAM and SWCNT-**18**-SAM and (C) (**22**-**24**)-SAM-modified gold electrodes in 0.1 M KOH solution. Scan rate: 25 mV s^{-1}.

Gold oxidation and reduction of gold oxide were also inhibited on **18-**SAM and SWCNT-**18**-SAM-modified gold electrodes (Fig. 4.1B). Complex **18** is the peripheral derivatives (Scheme 3.2) of complex **15**. Inhibition of this process was also observed on the SAMs of complexes **22**-**24** (Fig. 4.1C), confirming SAM formation. Complexes **22**-**24** (Scheme 3.4) are bezylthio-derivatised analogues of complexes **13**-**15**.

The extent of inhibition of this process on the SAM-modified gold electrodes was evaluated by estimating the ion barrier factor, Γ_{ibf}, (equation 4.1) [136] for each SAM.

$$\Gamma_{ibf} = 1 - \frac{Q_{SAM}}{Q_{Bare}} \qquad 4.1$$

where Q_{SAM} and Q_{Bare} (1.82×10^{-5} C) are the total charges under the reduction peak (gold oxide stripping peak) on the SAM-modified and bare gold electrodes, respectively (Fig 4.1). The closer to 1 the value of Γ_{ibf}, the more closely packed the SAM of interest. The

values obtained for **13-, 14-** and **15**-SAMs are 0.88, 0.83 and 0.87, respectively. For **18**-SAM, the value obtained is 0.90, while a value of 0.82 is obtained for SWCNT-**18**-SAM. For **22**-, **23**- and **24**-SAMs, 0.82, 0.76 and 0.79 are obtained, respectively (Table 4.1).

Table 4.1: Ion barrier factors of SAM modified gold electrodes in 0.1 M KOH solution.

Electrode	Γ_{ibf}
13-SAM	0.88 ± 0.02
14-SAM	0.83 ± 0.02
15-SAM	0.87 ± 0.02
18-SAM	0.90 ± 0.01
SWCNT-**18**-SAM	0.82 ± 0.01
22-SAM	0.82 ± 0.03
23-SAM	0.76 ± 0.02
24-SAM	0.79 ± 0.01

The values of Γ_{ibf} clearly show the effect of the type and position of substituent on the surface properties of these SAMs. The SAM of the peripherally tetra-substituted complex (**18-**SAM) has Γ_{ibf} of ~1, which suggests that this SAM is close to being defect-free, unlike the SAMs of the non-peripheral complexes (**13-15**). Values of Γ_{ibf} obtained for the SAMs of complexes **13-15** show the presence of defects. Although, the value of Γ_{ibf} for **18**-SAM is not significantly higher than that of **15**-SAM, direct comparison of **15**- and **18**-SAM suggests that peripherally substituted thio-derivatised MPc complexes may form more closely packed SAMs than their non-peripheral derivatives. The higher value of Γ_{ibf} for **18**-SAM, relative to that of SWCNT-**18**-SAM, can be attributed to the

densely packed, crystalline nature of **18**-SAM, as typical of SAMs of alkanethiols [232] and alkylthio-derivatised MPc complexes. The presence of SWCNT in the SAM of the nano-composite (SWCNT-**18**) may affect this behavior, thus the lower value of Γ_{ibf} for this SAM. Also, values of Γ_{ibf} for the SAMs of complexes **22-24** suggest that these SAMs have more defects than those of complexes **13-15**, despite the fact that the complexes (**13-15** and **22-24**) are non-peripherally substituted. This observation may be attributed to the tendency of alkylthio substituents (in the SAMs of **13-15**) to assume a more closely packed nature, compared to benzylthio substituents. Although, there was interference from the redox activities of the SAMs of complexes **22-24** (especially **22**-SAM), the observed cathodic peaks on these SAMs were primarily due to reduction of gold oxide, justifying the presence of defects. In a more closely packed SAMs, with Γ_{ibf} of ~1 [137,145], like that of complex **18**, Fig. 4.1B, the peak associated with gold oxide reduction is less pronounced, because the SAMs are close to being defect-free.

4.1.2 Inhibition of underpotential deposition of copper

Cyclic voltammetry profiles of bare and SAM-modified gold electrodes in 1×10^{-3} M $CuSO_4$, containing 0.5 M H_2SO_4, are shown in Fig. 4.2. Underpotential deposition (UPD) of Cu, the broad peak around +0.07 V versus Ag|AgCl in the negative-going scan, and stripping of deposited Cu (at +0.12 versus Ag|AgCl) in the return scan, were observed on the bare gold electrode. These processes were substantially inhibited on the SAM-modified gold electrodes. However, redox activities of the SAMs were very pronounced in this electrolyte, with metal-based redox processes ($M^{III/II}$) of the adsorbed MPc complexes being observed. The nature of central metal in the adsorbed complexes has significant effect on the observed redox processes.

Metal-based processes were observed at $E_{1/2}$ = +0.18 V, E_p = +0.06 V and E_p = +0.16 V versus Ag|AgCl on **13**-, **14**- and **15**-SAM-modified gold electrodes, respectively (Fig. 4.2A), Table 4.2. For **18**-SAM-modified gold electrode, the redox process at $E_{1/2}$ = +0.17 V versus Ag|AgCl (Fig. 4.2B) can also be attributed to metal-based process. Fe^{III}/Fe^{II} redox process (E_p= +0.17 V vs. Ag|AgCl), Table 4.2, was also noticed on SWCNT-**18**-

SAM-modified gold (Fig. 4.2B). Metal-based redox processes were also observed on **22**-SAM ($E_{1/2}$ = +0.20 V versus Ag|AgCl), **23**-SAM (E_p = +0.06 V versus Ag|AgCl) and **24**-SAM ($E_{1/2}$ = +0.16 V versus Ag|AgCl) (Fig. 4.2D), Table 4.2. These values are slightly different from those obtained in pH 4 buffer (to be discussed later), due to the difference in nature of electrolyte.

Table 4.2: Values of $E_{1/2}$ or E_p in Volts versus Ag|AgCl for metal-based redox processes of the SAM-modified gold electrodes in 1 × 10^{-3} M $CuSO_4$/0.5 M H_2SO_4 and pH 4 buffer solutions.

Electrode	M^{III}/M^{II}	[a]$E_{1/2}$ or E_p	[b]$E_{1/2}$ or E_p
13-SAM	Co^{III}/Co^{II}	+0.18 ± 0.01	+0.05 ± 0.01
14-SAM	Mn^{III}/Mn^{II}	+0.06 ± 0.01	-0.21 ± 0.01
15-SAM	Fe^{III}/Fe^{II}	+0.16 ± 0.01	+0.12 ± 0.01
18-SAM	Fe^{III}/Fe^{II}	+0.17 ± 0.01	+0.22 ± 0.01
SWCNT-**18**-SAM	Fe^{III}/Fe^{II}	+0.17 ± 0.01	+0.18 ± 0.01
22-SAM	Co^{III}/Co^{II}	+0.20 ± 0.01	+0.17 ± 0.01
23-SAM	Mn^{III}/Mn^{II}	+0.06 ± 0.01	+0.02 ± 0.001
24-SAM	Fe^{III}/Fe^{II}	+0.16 ± 0.01	+0.16 ± 0.01

[a]Values in 1 × 10^{-3} M $CuSO_4$/0.5 M H_2SO_4 solution.

[b]Values in pH 4 buffer solution.

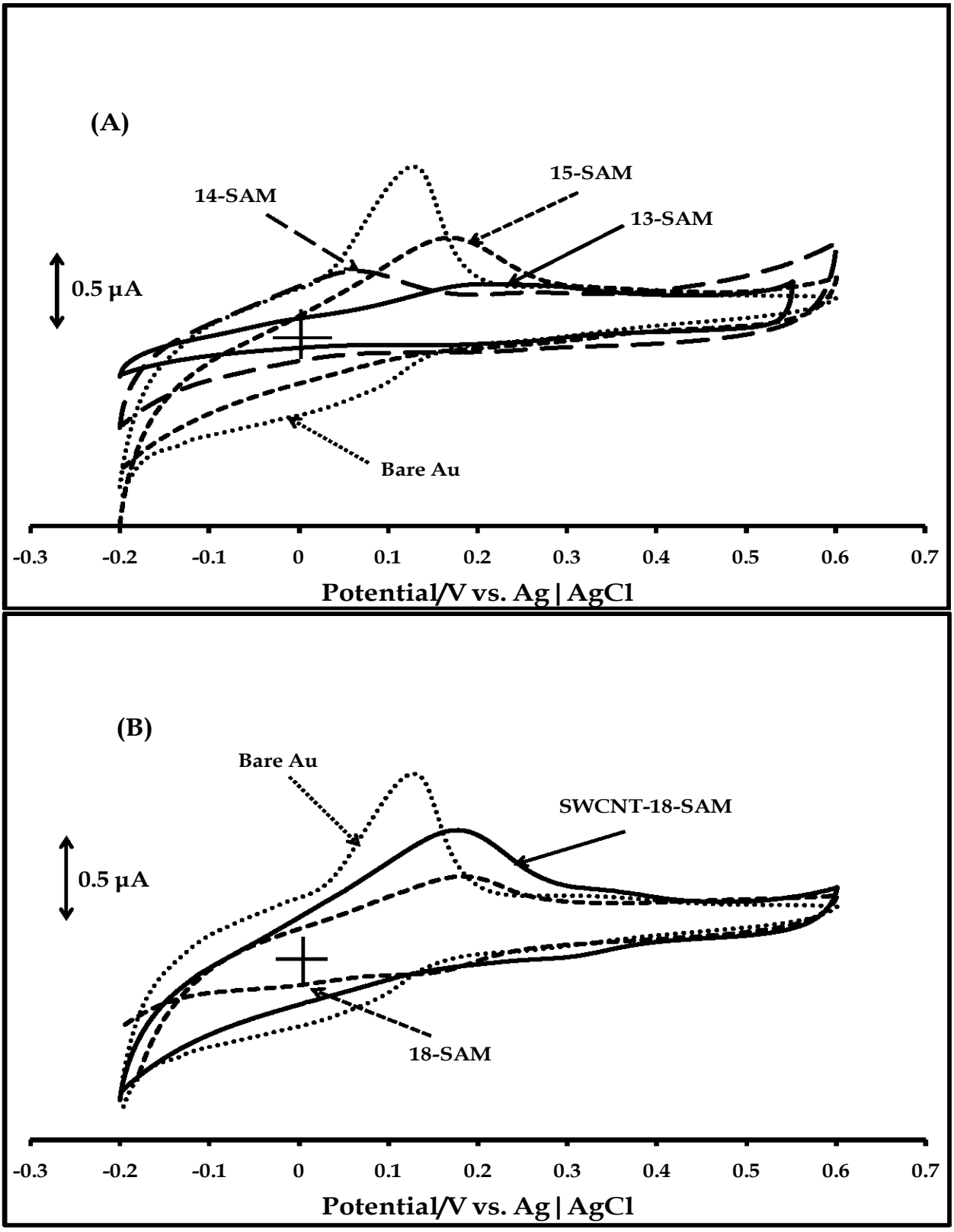
(A)
15-SAM
14-SAM
13-SAM
0.5 µA
Bare Au
-0.3
-0.2
-0.1
0
0.1
0.2
0.3
0.4
0.5
0.6
0.7
Potential/V vs. Ag | AgCl
(B)
Bare Au
SWCNT-18-SAM
0.5 µA
18-SAM
-0.3
-0.2
-0.1
0
0.1
0.2
0.3
0.4
0.5
0.6
0.7
Potential/V vs. Ag | AgCl

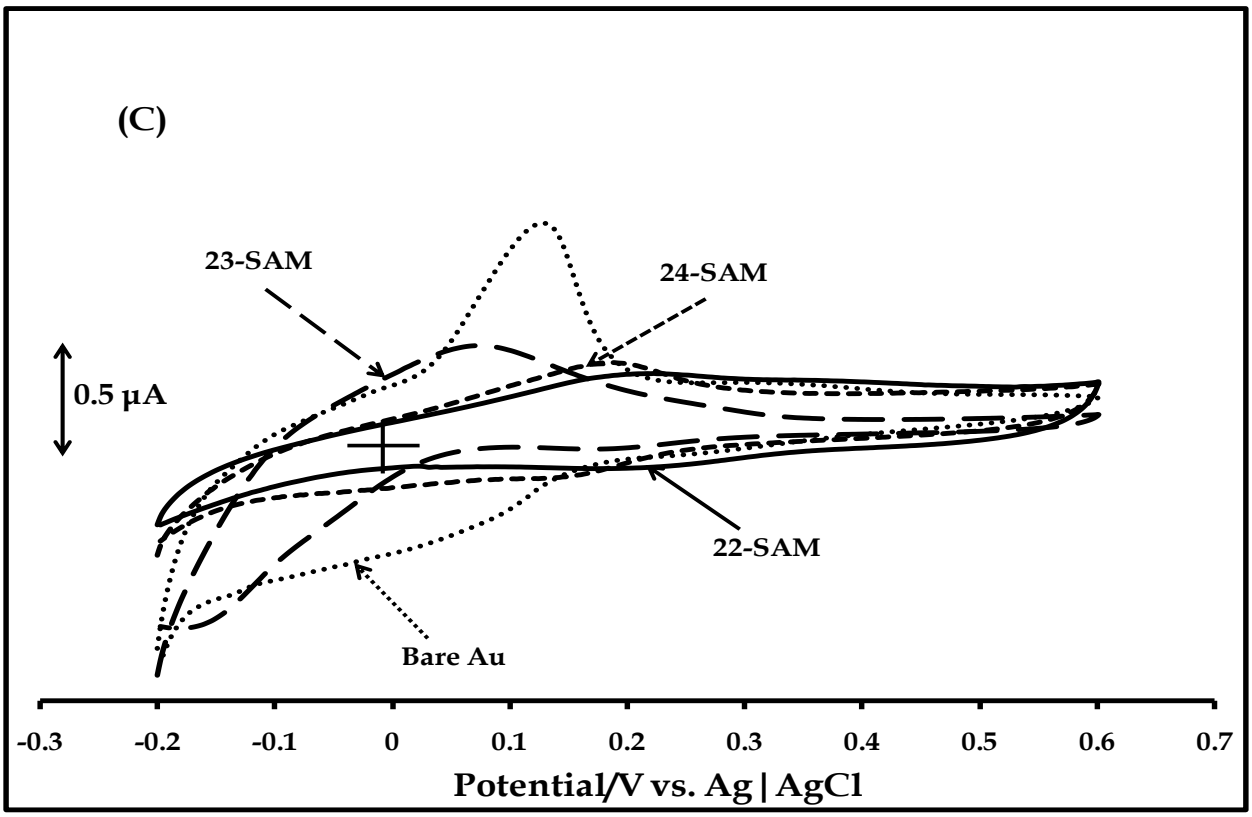

Figure 4.2: Cyclic voltammetry profiles of bare and SAM-modified gold electrodes in 1 × 10^{-3} M $CuSO_4$ containing 0.5 M H_2SO_4. Scan rate: 25 mV s^{-1}.

4.1.3 Inhibition of faradaic processes involving soluble redox species

Fig. 4.3 shows the cyclic voltammograms obtained for the bare electrode and the SAM-modified gold electrodes in 1 × 10^{-3} M ferrous ammonium sulphate $(Fe(NH_4)(SO_4)_2$, containing 1 × 10^{-3} M perchloric acid ($HClO_4$). The clearly resolved quasi-reversible redox process ($[Fe(H_2O)_6]^{3+}/[Fe(H_2O)_6]^{2+}$) on the bare gold electrode was inhibited on the SAM-modified gold electrodes. Inhibition of this process suggests isolation of the gold surface from the electrolyte, confirming SAM formation. The extent of inhibition reflects the position of substituent on the Pc ligand of the adsorbed MPc complexes, but the molecular nature of the substituent has insignificant effect on this blocking behavior.

The clearly resolved quasi-reversible redox process ($[Fe(H_2O)_6]^{3+}/[Fe(H_2O)_6]^{2+}$) on the bare gold electrode is almost completely inhibited on **15**- and **13**-SAM-modified gold

electrodes (Fig. 4.3A), while the cathodic branch of the Fe^{III}/Fe^{II} redox process (poorly resolved) shifts to more negative potential, with decreased intensity, on **14**-SAM-modified gold electrode (Fig. 4.3A). Inhibition of this process on the SAM-modified gold electrodes suggests isolation of the gold surface from the electrolyte, confirming SAM formation. Blocking of this process was most pronounced on **18**-SAM-modified gold electrode (Fig. 4.3B), confirming the influence of the position of substituent. This is consistent with the trend observed for the inhibition of gold oxidation on these SAMs (Figure 4.1A and B). However, on SWCNT-**18**-SAM-modified gold electrode (Fig. 4.3B), this process ($[Fe(H_2O)_6]^{3+}/[Fe(H_2O)_6]^{2+}$) is observed, but less resolved than that on bare gold electrode. Since the value of Γ_{ibf} obtained for this SAM (0.82) (Table 4.1) suggests minimal defects, the residual voltammetry wave of the Fe^{3+}/Fe^{2+} redox couple, observed on this SAM, may be attributed to better electron transport within SWCNT-**18**-SAM, relative to **18**-SAM. This was confirmed using EIS, discussed shortly. Interestingly, XRD spectrum of the nano-composite (Fig. 3.28D) suggests that this composite (SWCNT-**18)** has higher electron density than complex **18**.

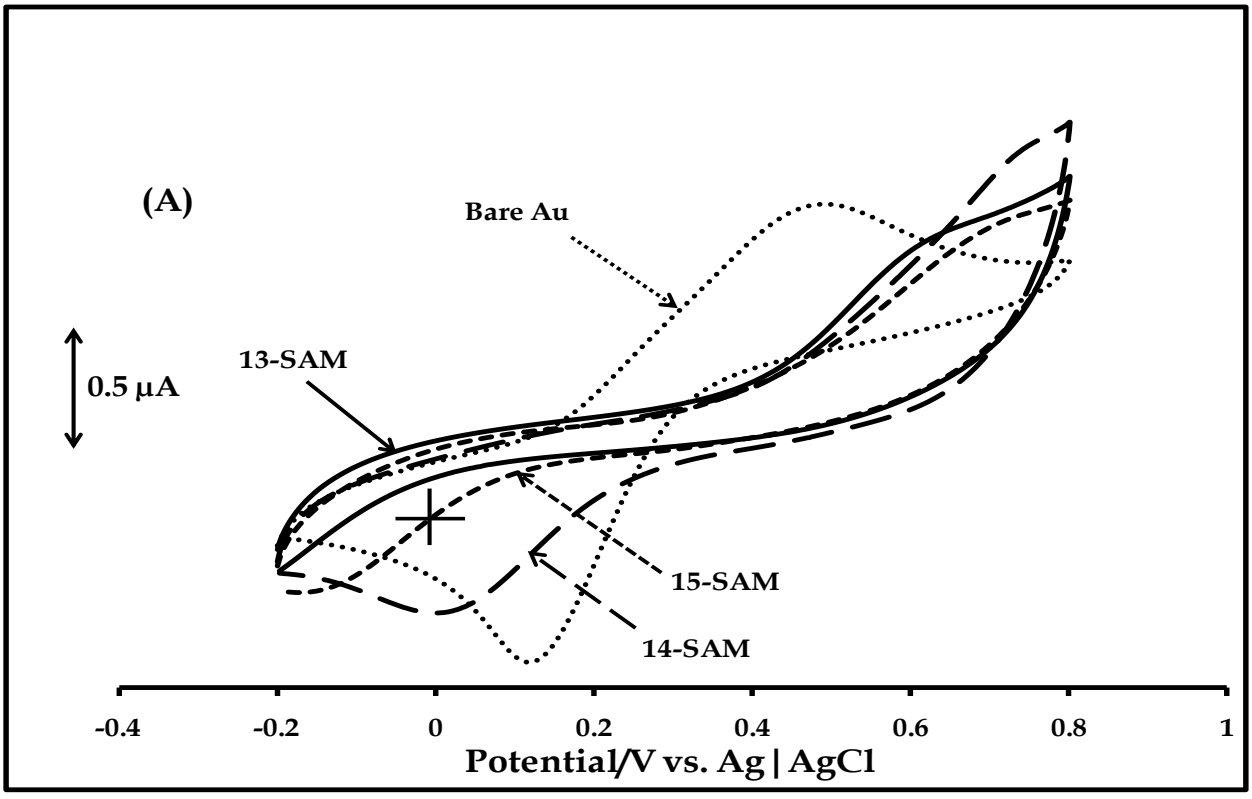

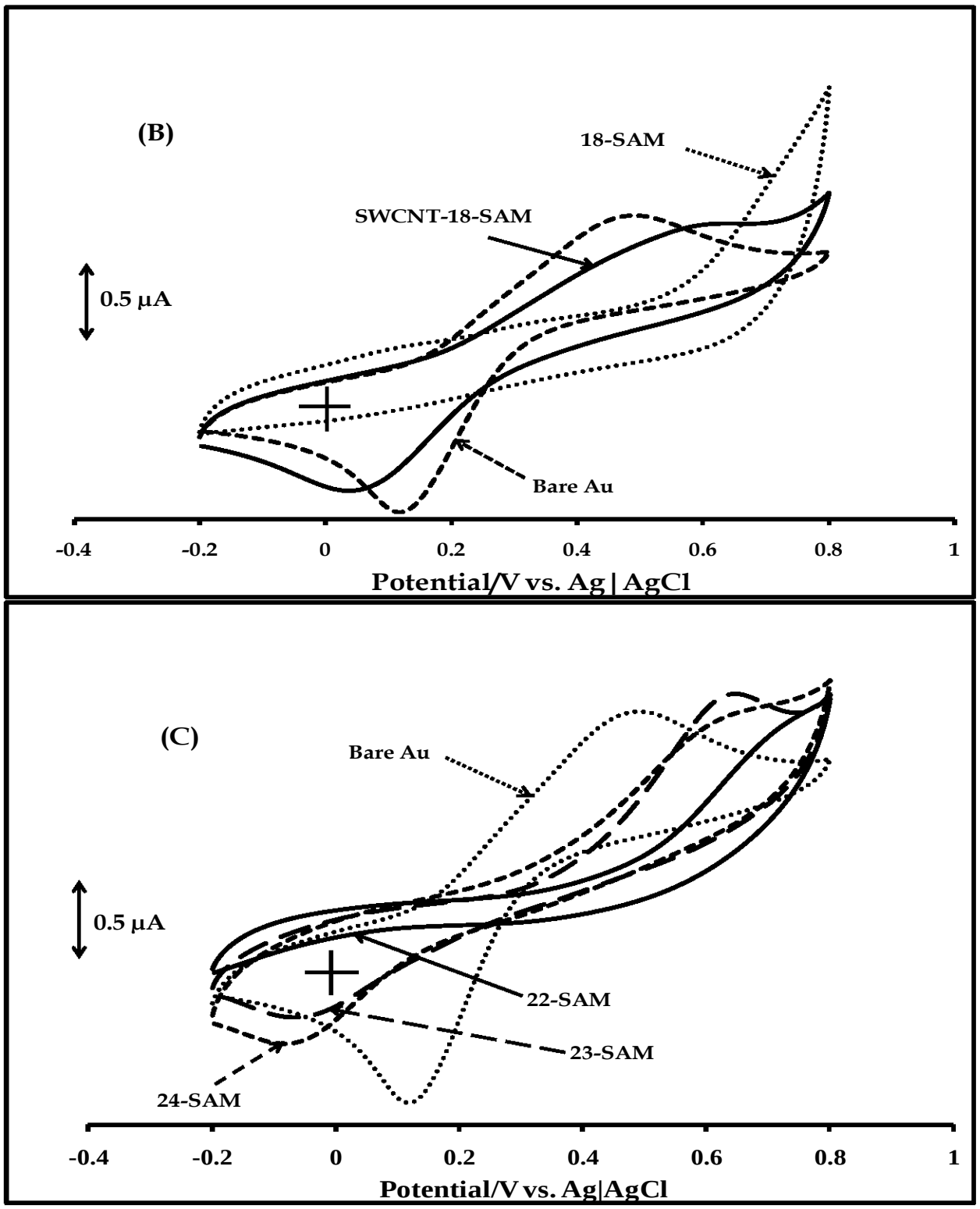

Figure 4.3: Cyclic voltammetry profiles of bare and SAM-modified gold electrodes in 1 × 10^{-3} M $Fe(NH_4)(SO4)_2$ solution containing 1 × 10^{-3} M $HClO_4$. Scan rate: 25 mV s^{-1}.

Inhibition of the $[Fe(H_2O)_6]^{3+}/[Fe(H_2O)_6]^{2+}$ redox process may also be explained in terms of electrostatic repulsion of the cationic Fe^{III} and Fe^{II} ions in solution. The four pedant amines of the complexes (**13-15** and **18**) are tertiary (Schemes 3.1 and 3.2), hence susceptible to protonation in $HClO_4$, resulting in appreciably positively charged electrode surface.

On **22**-SAM-modified gold electrodes, the $[Fe(H_2O)_6]^{3+}/[Fe(H_2O)_6]^{2+}$ redox process was completely inhibited, but its cathodic and anodic branches were slightly observable on **23**- and **24**-SAM-modified gold electrodes (Fig. 4.3C).

The cyclic voltammetry behaviors of these SAMs were also investigated in 1×10^{-3} M solution of $[Fe(CN)_6]^{3-}$ containing 0.1 M KCl, as supporting electrolyte (Fig. 4.4). Unlike the $[Fe(H_2O)_6]^{3+}/[Fe(H_2O)_6]^{2+}$ redox process in Fig. 4.3, the $[Fe(CN)_6]^{3-/4-}$ redox couple was insignificantly inhibited on the SAM-modified gold electrodes (Fig. 4.4). Similar behavior has been reported previously for adsorbed cobalt tetra-amino phthalocyanine films on vitreous carbon electrode [233] and MnPc on gold electrode [137]. This behavior has been variously explained, as discussed previously. For instance, lack of inhibition may be interpreted in terms of the fast nature of electron transfer for this process. Absence of pronounced inhibition of this process on the SAMs of complexes **13-15**, **18** and SWCNT-**18** (Figs. 4.4A and B) may also be interpreted in terms of enhanced surface concentration of $[Fe(CN)_6]^{3-}$ and $[Fe(CN)_6]^{4-}$ ions on the electrode, due to electrostatic attraction of these anionic species, assuming the amine groups of the adsorbed complexes are positively charged in the unbuffered KCl electrolyte. Observation of this process on the SAM-modified Au electrodes can also be evaluated within the context of the electrocatalytic properties of the SAMs. The oxidation potential of the $[Fe(CN)_6]^{3-/4-}$ redox process ($E_{1/2}$ = +0.1 V versus Ag|AgCl) is within the range of metal-based processes of the adsorbed complexes.

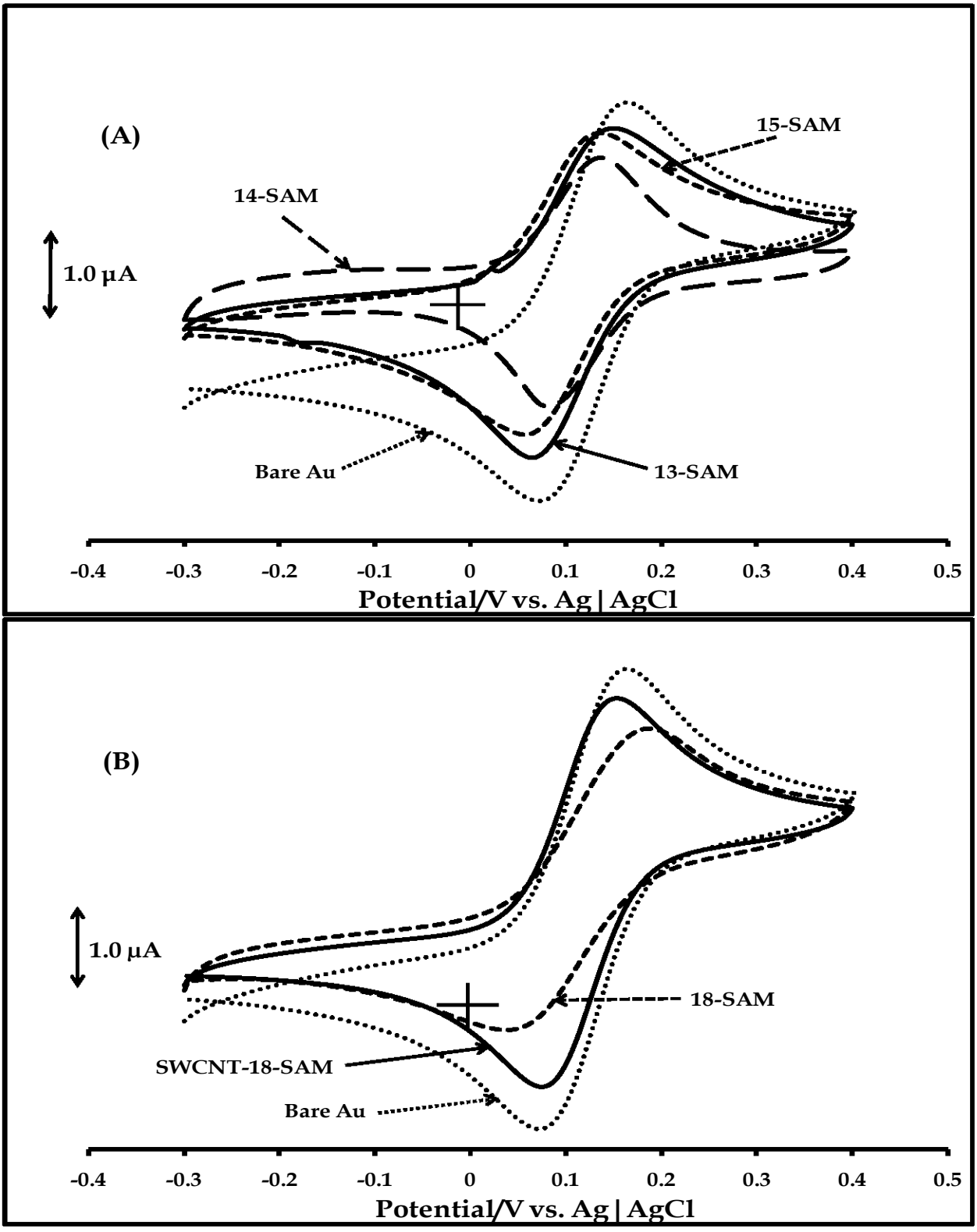
(A)
15-SAM
14-SAM
1.0 µA
Bare Au
13-SAM
-0.4
-0.3
-0.2
-0.1
0
0.1
0.2
0.3
0.4
0.5
Potential/V vs. Ag | AgCl
(B)
1.0 µA
18-SAM
SWCNT-18-SAM
Bare Au
-0.4
-0.3
-0.2
-0.1
0
0.1
0.2
0.3
0.4
0.5
Potential/V vs. Ag | AgCl

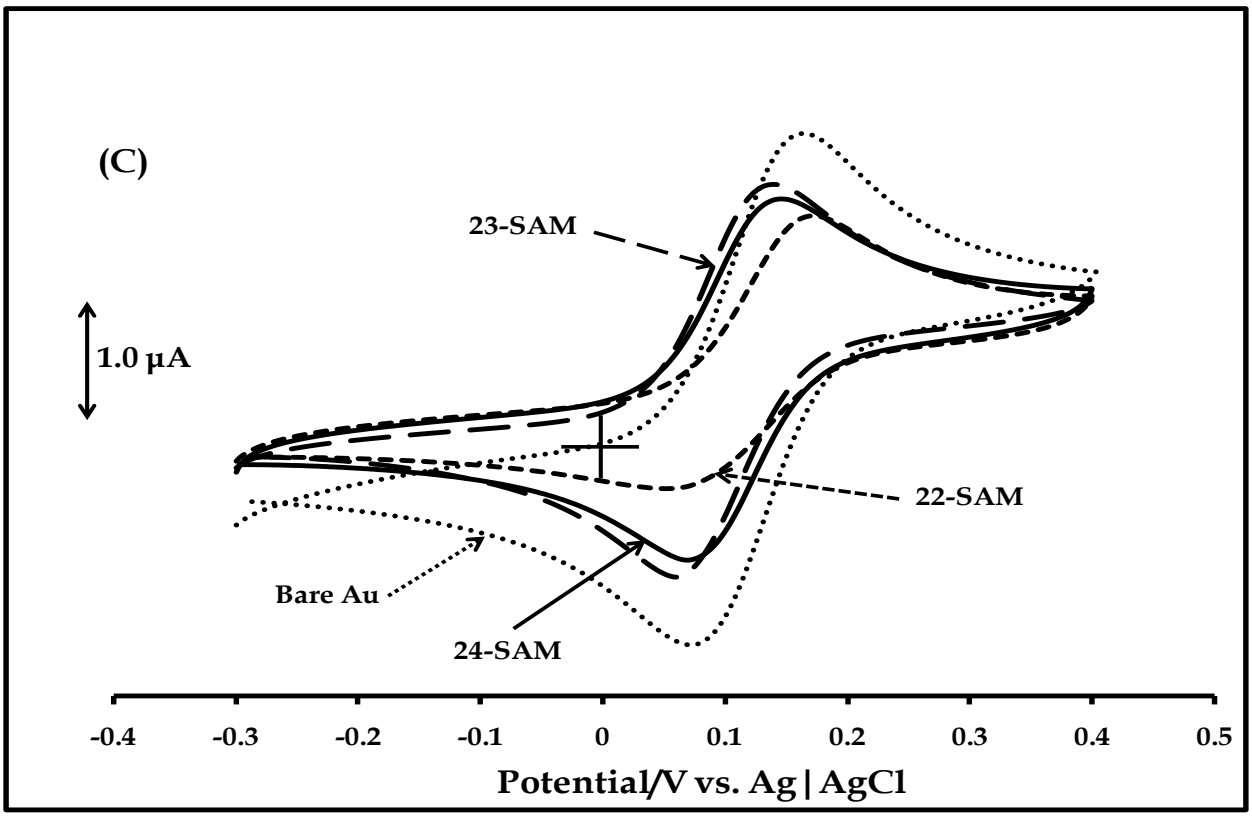

Figure 4.4: Cyclic voltammetry profiles of bare and (A) (**13**-**15**)-SAM, (B) **18**-SAM and SWCNT-**18**-SAM and (C) (**22**-**24**)-SAM-modified gold electrodes in 1 × 10^{-3} M solution of $[Fe(CN)_6]^{3-}$ containing 0.1 M KCl supporting electrolyte. Scan rate: 25 mVs^{-1}.

Nonetheless, SAM formation is demonstrated by differences in the values of peak splitting (ΔE) and current intensities for this process on the SAM-modified gold electrodes, compared to that on bare gold electrode (83 mV) (Fig. 4.4). The values of ΔE are 72 mV, 57 mV and 80 mV on **13**-, **14**- and **15**-SAM-modified gold electrodes, respectively (Fig. 4.4A). On **18**-SAM and SWCNT-**18**-SAM-modified gold electrodes (Fig. 4.4B), ΔE values are 130 mV and 70 mV, respectively, while on **22**-, **23**- and **24**-SAM-modified gold electrodes (Fig. 4.4C), 117 mV, 73 mV and 67 mV, respectively, are obtained for ΔE. The differences in ΔE and current intensities for the $[Fe(CN)_6]^{3-/4-}$ redox couple on the SAM- modified gold electrodes, relative to that on bare gold electrode, may be associated with the effect of electron tunneling the SAMs.

Although, values of ΔE cannot be adequately interpreted in terms of any specific trend, the type of metal centre, position and nature of the substituent in the adsorbed MPc

complexes are relevant. Importantly, ΔE for the $[Fe(CN)_6]^{3-/4-}$ redox couple on SWCNT-**18**-SAM-modified gold electrode (70 mV), relative to that on **18**-SAM (130 mV) (Fig. 4.4B) is of particular interest. It shows enhanced electron transfer process, due to the presence of SWCNT, as remarked previously. This was investigated by electrochemical impedance spectroscopy (EIS), using the $[Fe(CN)_6]^{3-/4-}$ redox process as probe. Generally, in this work, EIS was used to provide an in-depth understanding of the dynamics of electron transport within the SAMs studied.

4.1.4 Impedimentary properties

4.1.4.1 (13-15)-SAM-modified gold electrodes

Impedimentary properties of the SAM modified gold electrodes are closely related to the electrical nature of the SAM/electrode interfaces. Fig. 4.5 shows the fitted impedance data (Nyquist plots) of bare, **13**-, **14**- and **15**-SAM-modified gold electrodes in 1×10^{-3} M solution of $[Fe(CN)_6]^{3-}$, containing 0.1 M KCl, as supporting electrolyte. The impedance spectrum of the bare gold electrode shows a semi-circle, characteristic of charge transfer-limited impedance, in the high- frequency region, and a straight line, associated with a purely diffusion-limited reaction, in the low-frequency limit. The suitable equivalent circuit representative of this behavior is shown in Fig. 4.6A, where R_S is the resistance of the electrolyte solution between the reference and the working electrodes, R_{CT} is the charge transfer resistance, Z_W is mass-transfer or Warburg impedance and C_{dl} is the double-layer capacitance, that mimics the capacitance of the electrochemical double layer of the cell. The values of these quantities and their percentage errors are shown in Table 4.3.

Impedance spectra of **13**-SAM and **14**-SAM modified gold electrodes (Fig. 4.5) completely exhibit a diffusion-limited behaviour, eliminating contribution from charge transfer-mediated impedance. The most suitable equivalent circuit, representative of the physical electrochemistry of these cells, is shown in Fig. 4.6C; the circuit components

have the same meanings as defined previously. The fitted experimental impedance data for **13**- and **14**-SAMs are also indicated in Table 4.3.

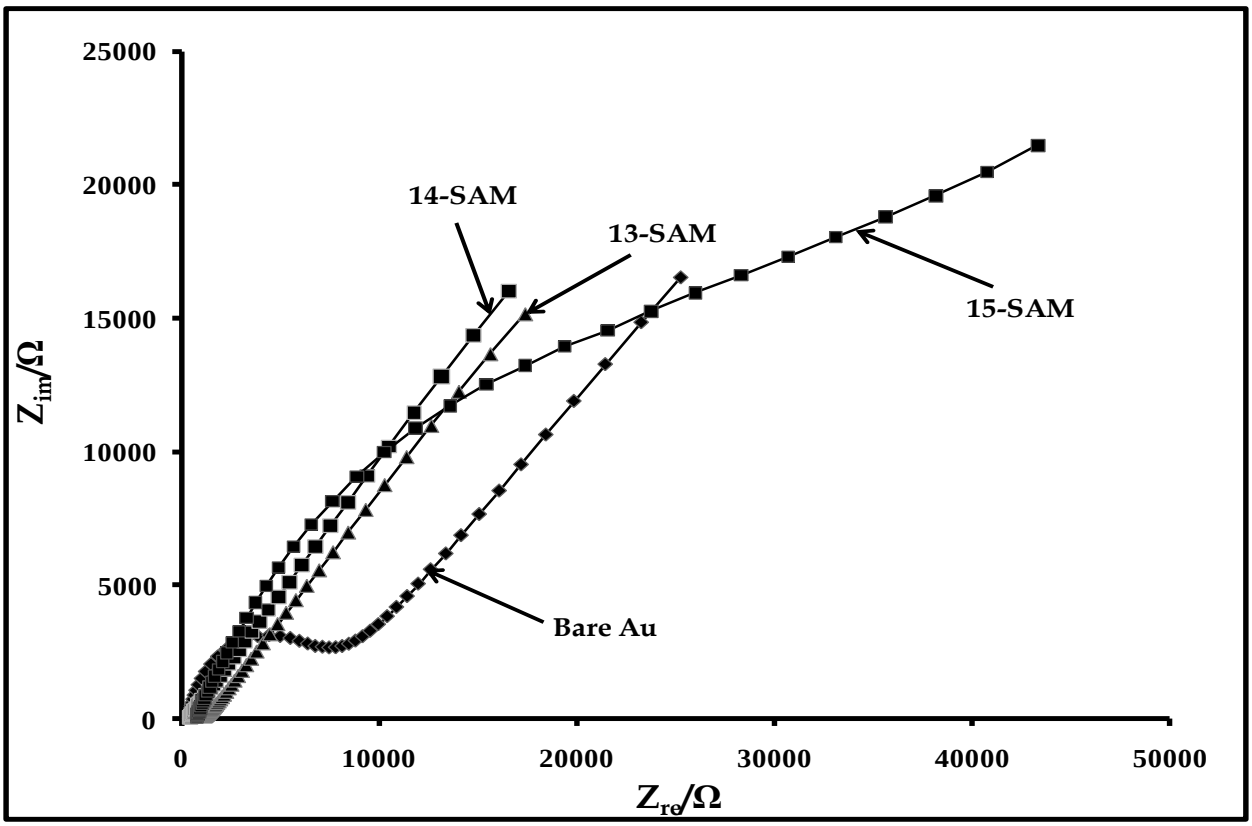

Figure 4.5: Impedance spectra obtained for bare and (**13**-**15**)-SAM-modified gold electrodes in 1 × 10^{-3} M solution of $[Fe(CN)_6]^{3-}$ containing 0.1 M KCl as the supporting electrolyte. Applied potential = 0.10 V versus Ag | AgCl.

The impedance spectrum of **15**-SAM-modified gold electrode (Fig. 4.5) has a feature of charge transfer-limited behaviour and negligible diffusion-controlled nature. However, a huge error resulted when the experimental impedance data was fitted using the circuit in Fig. 4.6A. A better fit was obtained when the data was interpreted using the circuit in Fig. 4.6B, eliminating contribution from diffusion-limited impedance, where R_S, R_{CT} are as defined previously. The third component is the so called constant phase element (CPE). The impedance spectrum of **15**-SAM-modified gold electrode is not semicircular, but has the shape of an arc; hence the inclusion of C_{dl} as a circuit element resulted in non-linearity in the equivalent circuit proposed. Wu and co-workers [234,235]

described this model-depended non-linearity as intrinsic. As observed in this work, they suggested that the substitution of C_{dl} with a distributed circuit element, like CPE, will give a better fit and reduce errors associated with non-linearity of the proposed circuit.

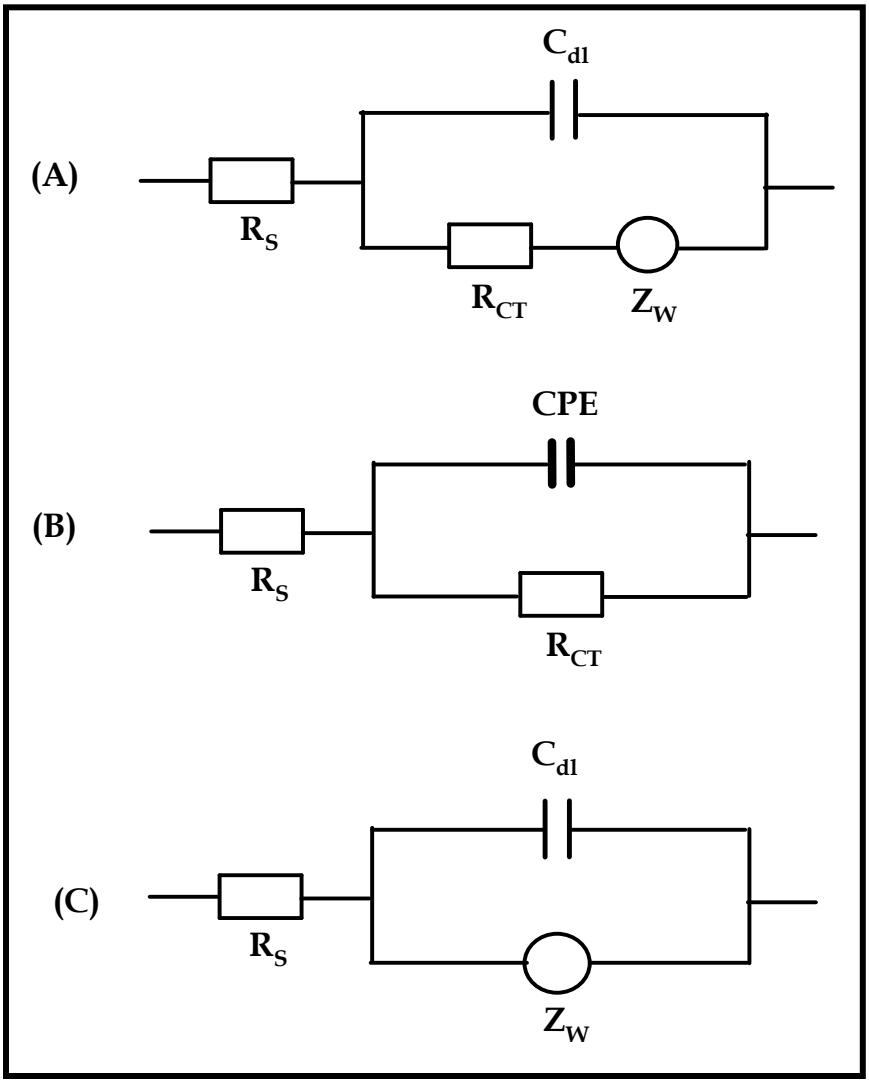

Figure 4.6: (A) Suggested equivalent circuits for the impedance spectral of bare, **18**-, SWCNT-**18**, (**22**-**24**)-SAM-modified gold electrodes, (B) equivalent circuit for **15**-SAM-modified gold electrode and (C) equivalent circuit for **13**- and **14**-SAM-modified gold electrodes.

Table 4.3: Summary of impedance data obtained for bare and SAM-modified gold electrodes at applied potential of 0.1 V versus Ag|AgCl.

Electrode	R_S (KΩ)	R_{CT} (KΩ)	C_{dl} (μF)	Z_W (Ω s$^{-1/2}$) (× 10^{-5})	f (Hz)	Phase angle (°)	n
Bare Au	0.45 ± 0.01	5.92 ± 0.15	0.18 ± 0.01	4.8 ± 0.01	500	56	0.58
13-SAM	0.55 ± 0.01	_	0.48 ± 0.03	6.02 ± 0.03	13	39	0.72
14-SAM	0.44 ± 0.01	_	0.52 ± 0.02	5.54 ± 0.01	2	37	0.67
15-SAM[a]	0.69 ± 0.01	6.08 ± 0.21	0.01 ± 0.001	_	16	49	0.68
18-SAM	0.81 ± 0.02	6.10 ± 0.30	0.56 ± 0.02	4.30 ± 0.20	100	46	0.80
SWCNT-**18**-SAM	0.47 ± 0.01	0.62 ± 0.02	0.14 ± 0.01	5.74 ± 0.10	2512	24	0.60
22-SAM	0.71 ± 0.03	18.8 ± 0.70	0.13 ± 0.01	3.77 ± 0.3	398	61	0.85
23-SAM	0.51 ± 0.01	1.66 ± 0.10	0.32 ± 0.01	4.75 ± 0.1	501	36	0.78
24-SAM	0.38 ± 0.01	0.71 ± 0.02	0.43 ± 0.01	5.49 ± 0.1	501	32	0.81

[a]Value of C_{dl} estimated from CPE using equation 4.2.

CPE is an empirical representation of deviation of the double-layer capacitance from ideal behavior. It is characteristic of impedance behavior of the double-layer capacitance at solid electrodes [148]. This behavior depends mainly on the state of the electrode's surface, like its roughness and degree of polycrystallinity, and most importantly, on anion adsorption [148]. In the present work, the non-ideal capacitive nature of **15**-SAM/electrode interface may be associated with adsorption of $[Fe(CN_6)]^{3-}$ anion, with the physical nature of the SAM influencing the kinetic of adsorption. This position is supported by reports that almost ideal capacitive behavior was observed at a deliberately roughened Pt surface [148]. The conclusion was that anion adsorption, rather than the nature of the electrode surface is central to non-ideal capacitive behavior, as a

result of the frequency-dependent adsorption pseudo-capacitive nature, associated with anion chemisorptions and associated kinetics of the process. The impedance data for this SAM is indicated in Table 4.3. The true capacitance, *C*, was estimated from the value of CPE using equation 4.2 [236].

$$C = \mathrm{Q}^{O}(\omega_{max})^{n-1} \qquad 4.2$$

where *C* is the true capacitance, Q^o is the CPE, ω_{max} is the frequency corresponding to the maximum value of impedance.

Differences in the values of impedance parameters for (**13**-**15**)-SAM-modified gold electrodes suggest that the conducting pathways of the SAMs are closely associated with the central metal of the phthalocyanine complexes constituting the SAMs. **15**-SAM-modified gold electrode, with higher R_{CT} (6.08 KΩ) than that of the bare gold electrode, significantly inhibited electron transfer in the $[Fe(CN)_6]^{3-/4-}$ redox couple. This is consistent with the relatively high value of ΔE (80 mV) obtained for the $[Fe(CN)_6]^{3-/4-}$ redox process on this electrode (Fig. 4.4A). Expectedly, the resistance of the electrolyte solution (R_S) does not show any significant variation (0.44 – 0.69 KΩ, Table 4.1) for the bare and SAM-modified gold electrodes.

Further evaluation of the impedimentary properties of (**13**-**15**)-SAMs was carried out, using Bode plots (phase angle versus log *f*), derived from the impedance spectra in Fig. 4.5. The Phase angle and frequency of the peak due to the bare gold electrode (Fig. 4.7) are 55.7° and 500 Hz, respectively. In the presence of SAMs, the phase peak shifted to different values of frequencies and phase angles (between 2 and 16 Hz, with phase angles between 36.7 and 49.3°, Table 4.3), indicating SAM formation. The shift in phase peak to lower frequency shows that electron transfer rate decreases as a result of electrode modification. This was observed more clearly for **15**-SAM in Fig. 4.7, but poorly resolved for **13**- and **14**-SAMs, Fig. 4.7, which is consistent with the diffusion-controlled nature of their impedance behavior.

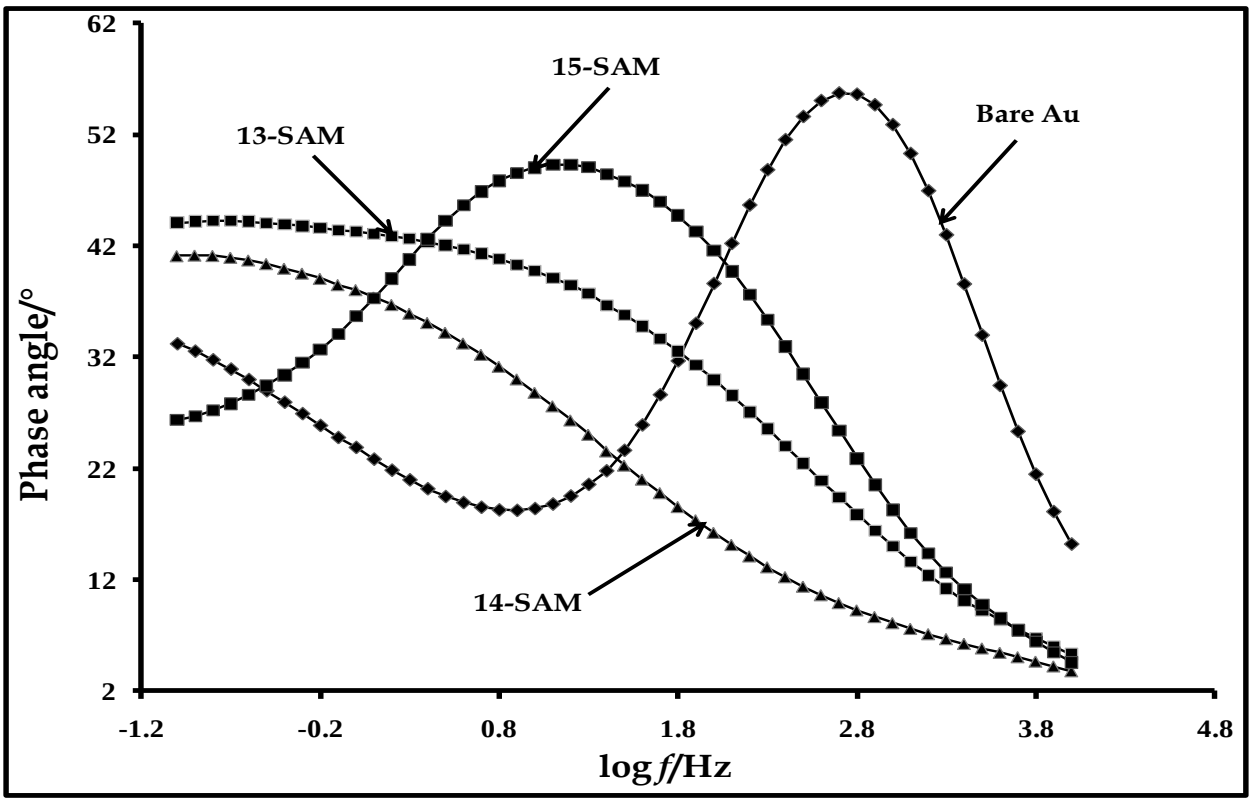

Figure 4.7: Bode plots (phase angle versus log *f*) obtained for bare and (**13**-**15**)-SAM-modified gold electrodes in 1 × 10^{-3} M solution of $[Fe(CN)_6]^{3-}$ containing 0.1 M KCl as the supporting electrolyte. Applied potential = 0.10 V versus Ag | AgCl.

4.1.4.2 18-SAM and SWCNT-18-SAM-modified gold electrodes

Comparative analysis of electron transport within **18**-SAM and SWCNT-**18**-SAM-modified gold electrodes was also conducted using EIS. This technique offers better understanding of the relevance of the SWCNT unit of the SWCNT-**18**-SAM in electron transport. Fig. 4.8 shows the fitted impedance spectra of **18**-SAM and SWCNT-**18**-SAM-modified gold electrodes in 1 × 10^{-3} M solution of $[Fe(CN)_6]^{3-}$, containing 0.1 M KCl (supporting electrolyte). Like the bare gold electrode in Fig. 4.5, all the impedance spectra in Fig. 4.8 shows semi-circular behavior, characteristic of charge transfer-limited impedance, in the high- frequency region, and a linear portion, associated with a purely diffusion-controlled phenomenon, in the low-frequency region. This impedance behavior can also be explained using the circuit in Fig. 4.6A, as discussed previously for the impedance spectrum of bare gold

electrode. The values obtained for the circuit parameters are shown in Table 4.3. R_S is within narrow range (0.47 to 0.81 KΩ). This is not suprising, since electrode modification does not significantly affect this parameter. Also, Z_W (impedance associated with diffusion of analyte to the electrode surface) are, expectedly, not significantly affected by electrode modification. Each of the electrodes has 'n' value less than 1. This is consistent with the non-ideal capacitive nature of the electrodes. Values of C_{dl} are also a reflection of the conducting nature of the SAM film; SWCNT-**18**-SAM-modified gold electrode has lower value of capacitance (0.14 μF) than **18**-SAM (0.56 μF). Values of charge transfer resistance, R_{CT}, were the most informative of the electrical conductivity of the electrodes. SWCNT-**18**-SAM-modified gold electrode has the lowest charge transfer resistance. R_{CT} for **18**-SAM-modified gold electrode (6.10 KΩ) was ten folds that for SWCNT-**18**-SAM-modified gold electrode, 0.62 KΩ.

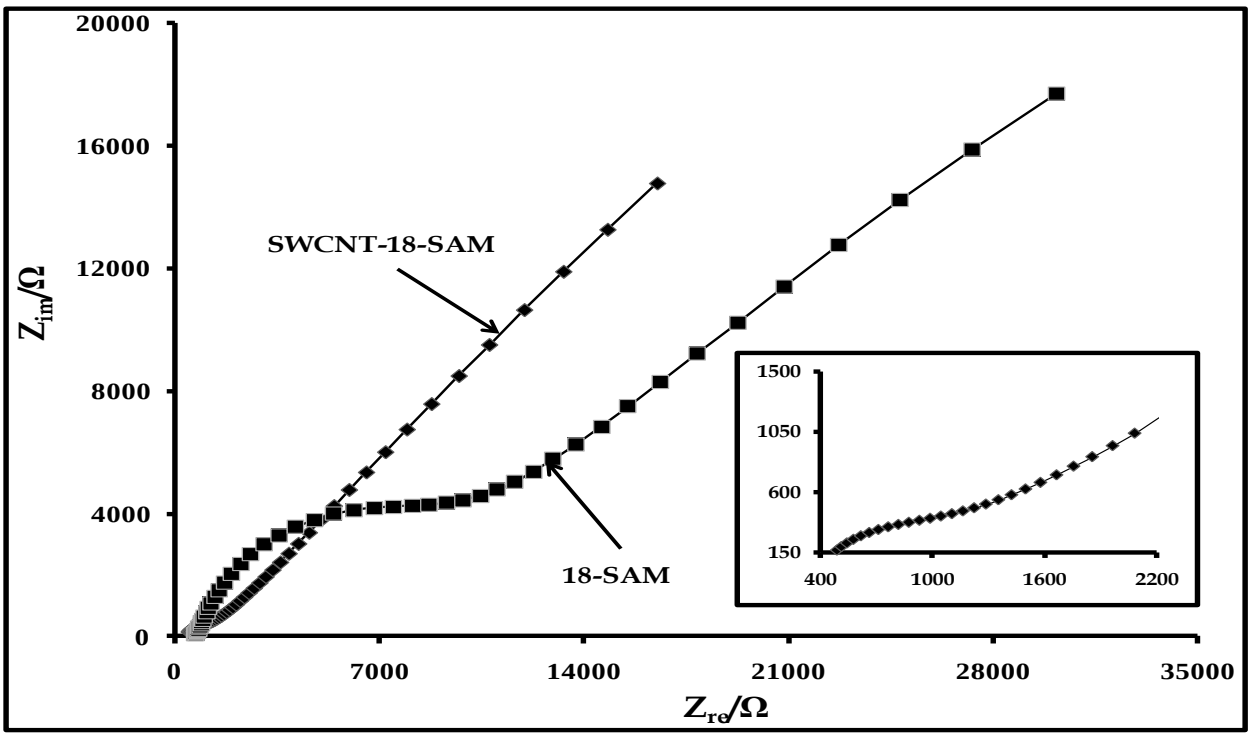

Figure 4.8: Impedance spectra obtained for **18**-SAM and SWCNT-**18**-SAM-modified gold electrodes in 1 × 10^{-3} M solution of $[Fe(CN)_6]^{3-}$ containing 0.1 M KCl as supporting electrolyte. Applied potential = 0.10 V versus Ag|AgCl. Inset: enlarged semicircular portion of the impedance spectrum of SWCNT-**18**-SAM.

The values of R_{CT} are consistent with the values of ΔE for the$[Fe(CN)_6]^{3-/4-}$ redox couple on these SAMs (130 mV and 70 mV on **18**-SAM and SWCNT-**18**-SAM, respectively) (Fig. 4.4B). High electrical conductivity of SWCNT, coupled with enhanced electron density of the nano-composite, may have facilitated better electron transport in the SWCNT-**18**-SAM, resulting in lower R_{CT}.

The Bode plots derived from the impedance spectra in Fig. 4.8 are shown in Fig. 4.9. A shift in the phase peak, relative to that of bare gold electrode, was also observed in the presence of **18**-SAM (46° and 100 Hz) and SWCNT-**18**-SAM (23.8° and 2512 Hz), Table 4.3, suggesting a different nature of electrode/electrolyte interfaces (Fig. 4.9). Also, positions of phase peaks are consistent with the cyclic voltammograms in Fig. 4.4B, corroborating the explanation thereof. A phase peak at 2512 Hz for SWCNT-**18**-

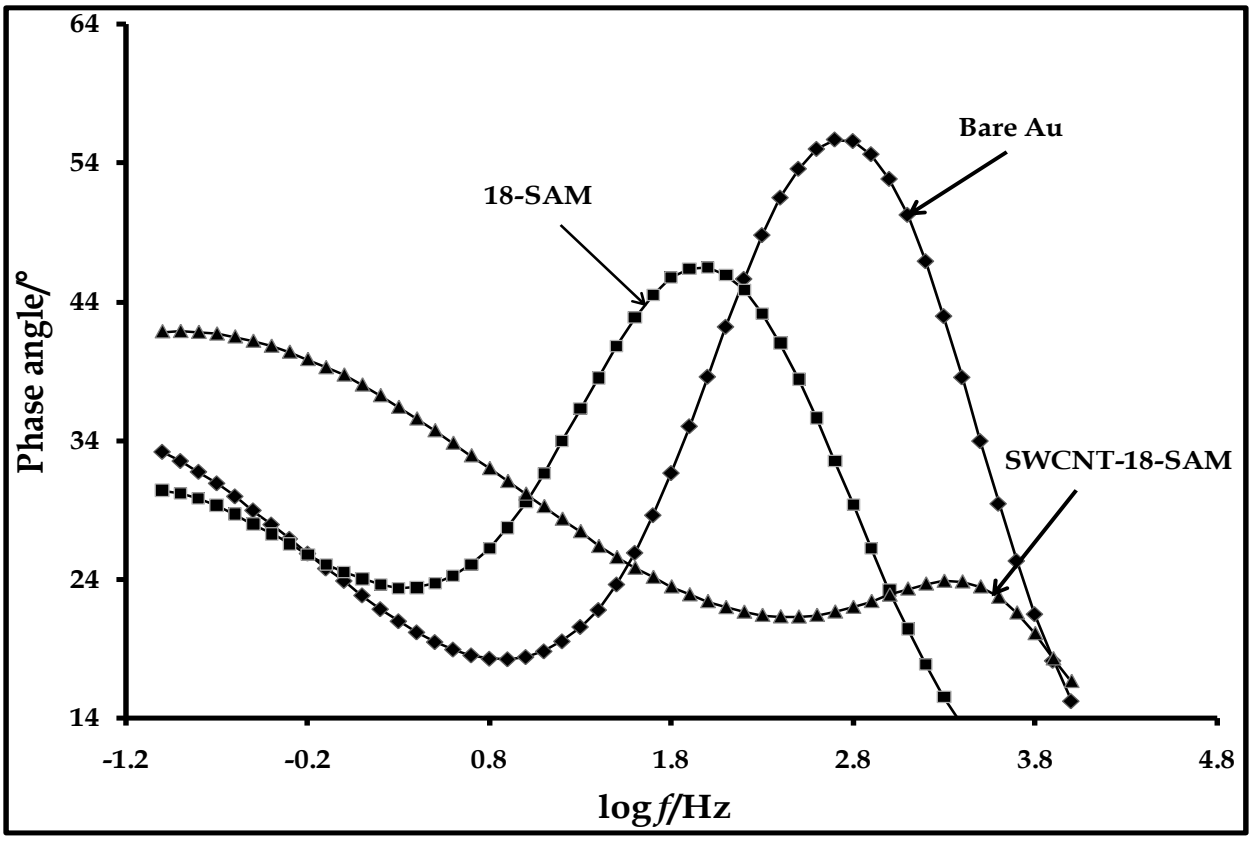

Figure 4.9: Bode plots (phase angle versus log *f*) obtained for bare, **18**-SAM and SWCNT-**18**-SAM-modified gold electrodes in 1 × 10^{-3} M solution of $[Fe(CN)_6]^{3-}$ containing 0.1 M KCl as supporting electrolyte. Applied potential = 0.10 V versus Ag|AgCl.

SAM-modified gold electrode is higher than that on bare gold electrode (500 Hz) or **18**-SAM-modified gold electrode (100 Hz); suggesting that electron transport in the SWCNT-**18**-SAM was the best, with the Fe^{III}/Fe^{II} redox process having the highest rate constant on this SAM. This agrees perfectly with the peak splitting, ΔE, (70 mV) (Fig. 4.4B) observed for this process on SWCNT-**18-**SAM-modified gold electrode, relative to that on the bare (83 mV) or **18**-SAM-modified (130 mV) gold electrode.

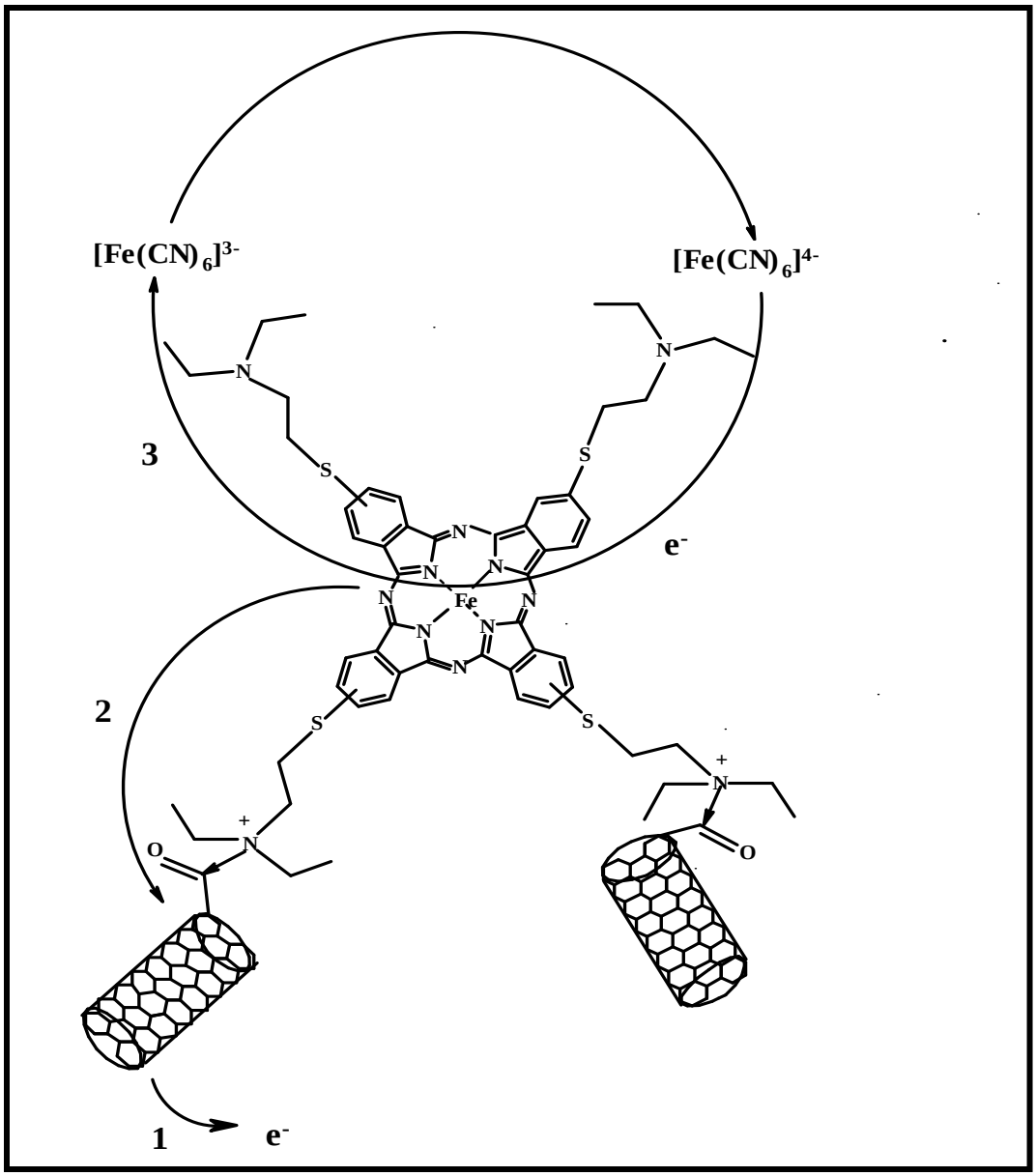

Scheme 4.1: Hypothetical model illustrating electron transport mechanism within SWCNT-**18-**SAM.

Based on the impact of SWCNT on electron transport, evidenced from the values of R_{CT} (0.62 KΩ) and phase peak (2512 Hz) for SWCNT-**18**-SAM, the mechanism in Scheme 4.1 is proposed, to illustrate electron transport within the SWCNT-**18**-SAM-modified gold electrode. Process (1) represents tunneling of electrons from the SCWNT to gold electrode (the latter not shown), facilitating electron transport from the central metal of complex **18** (process (2)), resulting in the oxidation of $Fe^{II}Pc$ to $Fe^{III}Pc$. Process (3) illustrates heterogeneous electron transfer involving the metal center of complex **18** and the reversible $[Fe(CN)_6]^{3-/4-}$ redox process. Electrocatalytic property of this SAM, towards the oxidation of carbofuran (one of the analytes of interest), discussed later in this work, can also be explained using this hypothetical model.

4.1.4.3 (22-24)-SAM-modified gold electrodes

The fitted impedance spectra of (**22-24**)-SAM-modified gold electrodes (Fig. 4.10)

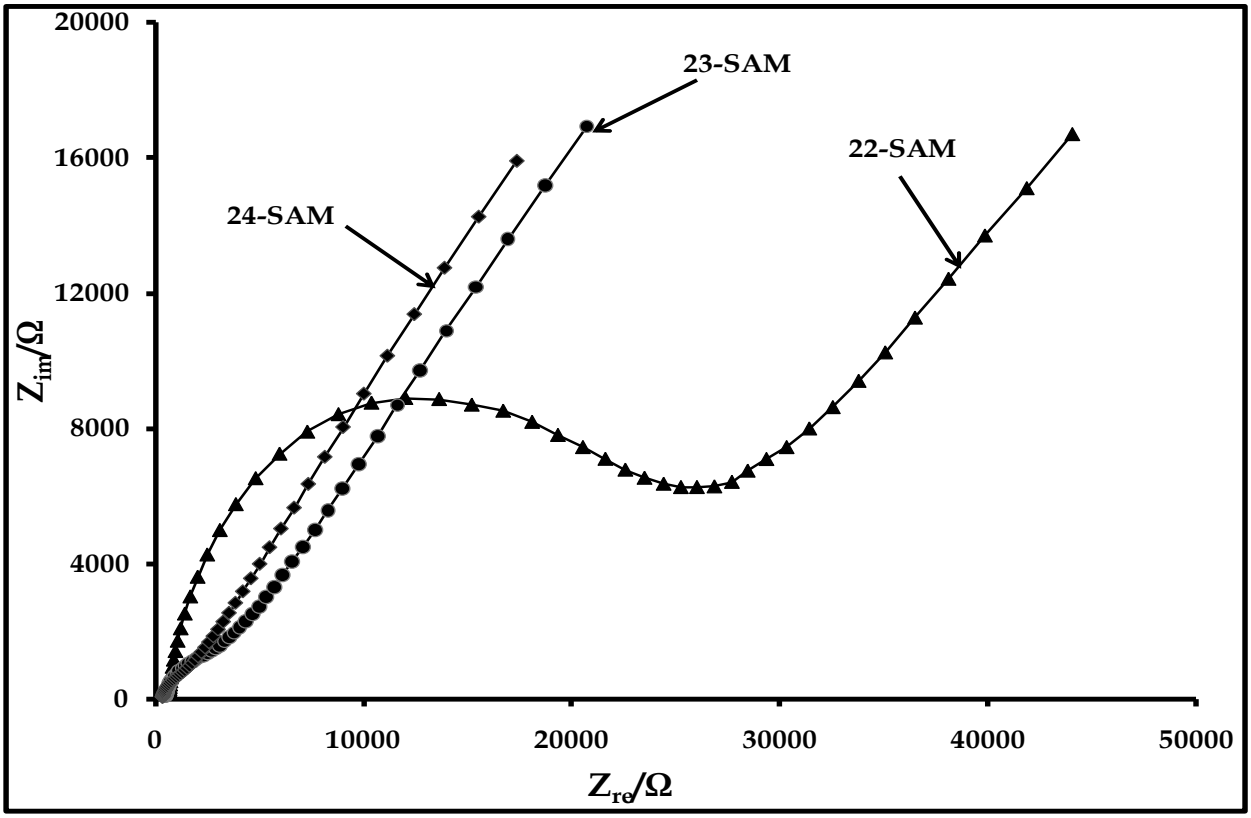

Figure 4.10: Impedance spectra obtained for (**22-24**)-SAM-modified gold electrodes in 1 × 10^{-3} M solution of $[Fe(CN)_6]^{3-}$ containing 0.1 M KCl as the supporting electrolyte. Applied potential = 0.10 V versus Ag|AgCl.

also exhibit the same nature as those of bare (Fig. 4.5), **18**-SAM and SWCNT-**18**-SAM-modified gold electrodes (Fig. 4.8) (i.e. charge transfer limited and diffusion mediate impedance characteristics). Thus, the circuit in Fig. 4.6A is also suitable for the interpretation of this impedance behavior. The values of the circuit components are indicated in Table 4.3. Importantly, values of R_{CT} (18.78 KΩ for **22**-SAM, 1.66 KΩ for **23**-SAM and 0.71 KΩ for **24**-SAM) aggree substantially with those of ΔE for the $[Fe(CN)_6]^{3-/4-}$ redox process on these SAMs (117 mV, 73 mV and 67 mV on **22**-, **23**- and **24**-SAM-modified gold electrodes, respectively) (Fig. 4.4C), while R_S are, expectedly, within narrow range (0.38-0.71 KΩ). Also, values of n (0.85 for **22**-SAM, 0.78 for **23**-SAM and 0.81 for **24**-SAM) justify the non-ideal capacitive nature of these electrodes.

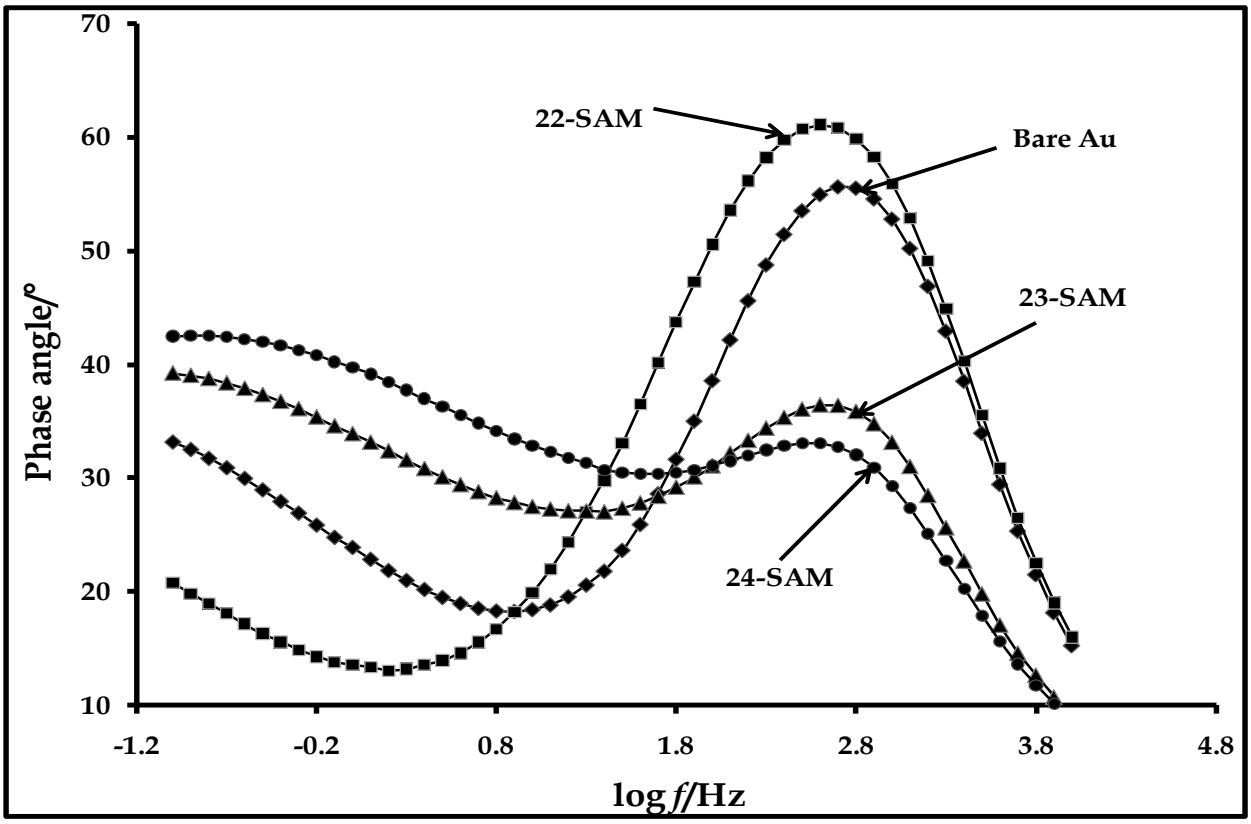

Figure 4.11: Bode plots (phase angle versus log *f*) obtained for bare and (**22**-**24**)-SAM-modified gold electrodes in 1 × 10^{-3} M solution of $[Fe(CN)_6]^{3-}$ containing 0.1 M KCl as the supporting electrolyte. Applied potential = 0.10 V versus Ag | AgCl.

A shift in the phase peaks, relative to that of the bare gold electrode, was also noticed in the Bode plots (Fig. 4.11) derived from the impedance spectra of (**22**-**24**)-SAM- modified gold electrodes(Fig. 4.10) (61°, 398 Hz for **22**-SAM, 36°, 501 Hz for **23**-SAM and 32°, 501 Hz for **24**-SAM), justifying electrode modification. The observed phase peaks in Fig. 4.11 are also consistent with the values of ΔE (117 mV, 73 mV and 67 mV on **22**-, **23**- and **24**-SAM-modified gold electrodes) and R_{CT} (18.78 KΩ for **22**-SAM, 1.66 KΩ for **23**-SAM and 0.71 KΩ for **24**-SAM) obtained for the $[Fe(CN)_6]^{3-/4-}$ redox process on these SAMs. Finally, it is important to mention that, for each of the bare and SAM modified gold electrodes, the value of phase angle is less than the 90° expected for an ideal capacitive behavior. This is consistent with the non-ideal capacitive nature of these electrodes.

4.1.5 Metal-based redox properties

Metal-based redox processes of the SAM-modified gold electrodes were characterized in pH 4 buffer solution (Fig. 4.12). This pH was used since the best voltammetry response of the insecticide, carbofuran (one of the analytes of interest), was obtained at this value. Also, SAMs of all the complexes were appreciably stable at this pH.

In Fig. 4.12B, a well-defined Mn^{III}/Mn^{II} redox wave can be identified on **14**-SAM-modified gold electrode, at -0.21 V versus Ag|AgCl, Table 4.4. Co^{III}/Co^{II} and Fe^{III}/Fe^{II} redox processes on **13**-SAM (inset in Fig. 4.12 A) and **15**-SAM (inset in Fig. 4.12C), respectively, are poorly resolved. The difficulty in observing these processes as adsorbed species is not surprising, such behavior has been reported before for SAMs of iron phthalocyanine complex [75] and cobalt porphyrin complexes [237,238], limiting their uses in the calculation of surface coverages and the prediction of orientations of these complexes on electrodes. Enhanced resolution of the Co^{III}/Co^{II} and Fe^{III}/Fe^{II} redox waves can be achieved by repetitive cycling of the SAM-modified gold electrodes in coordinating solvents (DMF or pyridine), containing electrolytes such as $TBABF_4$ or tetrabutylammonium percholate (TBAP). In this work, **13**- and **15**-SAM-modified gold

Table 4.4: Electrochemical data of SAM-modified gold electrode, $E_{1/2}$ or E_p in Volts vs. Ag|AgCl in pH 4 buffer solution.

Electrode	M^{III}/M^{II}	$E_{1/2}$ or E_p	Γ_{SAM} (mol cm^{-2})
13-SAM[a]	Co^{III}/Co^{II}	+0.05 ± 0.01	1.20 ± 0.14 × 10^{-10}
14-SAM	Mn^{III}/Mn^{II}	-0.21 ± 0.01	2.69 ± 0.11 × 10^{-10}
15-SAM[a]	Fe^{III}/Fe^{II}	+0.12 ± 0.01	1.02 ± 0.17 × 10^{-10}
18-SAM	Fe^{III}/Fe^{II}	+0.22 ± 0.01	1.09 ± 0.03 × 10^{-10}
SWCNT-**18**-SAM	Fe^{III}/Fe^{II}	+0.18 ± 0.01	1.30 ± 0.03 × 10^{-10}
22-SAM	Co^{III}/Co^{II}	+0.17 ± 0.01	3.90 ± 0.08 × 10^{-11}
23-SAM	Mn^{III}/Mn^{II}	+0.02 ± 0.001	1.30 ± 0.03 × 10^{-10}
24-SAM	Fe^{III}/Fe^{II}	+0.16 ± 0.01	7.50 ± 0.19 × 10^{-11}

[a]Values of E_p and Γ_{SAM} recorded after repetitive cycling of SAM in DMF/$TBABF_4$.

electrodes were further characterized in pH 4 buffer solution, after repetitive cycling (10 cycles) in DMF containing 0.1 M $TBABF_4$, resulting in better resolution of the Co^{III}/Co^{II} (Fig. 4.12A) and Fe^{III}/Fe^{II} (Fig. 4.12C) redox processes. An irreversible Co^{III}/Co^{II} redox process was observed at less positive potential (~ +0.05 V versus Ag|AgCl), relative to that of the poorly-resolved reversible species (inset in Fig. 4.12A) (+0.13 V versus Ag|AgCl), while the Fe^{III}/Fe^{II} redox wave appeared at ~ +0.12 V versus Ag|AgCl (the same as that of the poorly-resolved species, +0.11 V versus Ag|AgCl) Table 4.4. DMF coordinates strongly to Co^{III}, stabilizing Co^{III}Pc species in CoPc complexes [226]. Hence, enhanced resolution of Co^{III}/Co^{II} redox wave in Fig. 4.12A may be attributed to this phenomenon. Enhanced stability of Fe^{III}Pc/Fe^{II}Pc redox couple, on coordination of Fe^{III}Pc species to perchlorate ion, has also been reported [226]. Therefore, better resolution

of Fe^{III}/Fe^{II} redox process, observed in Fig. 4.12C, may be interpreted in terms of coordination of $Fe^{III}Pc$ species to fluoroborate ion.

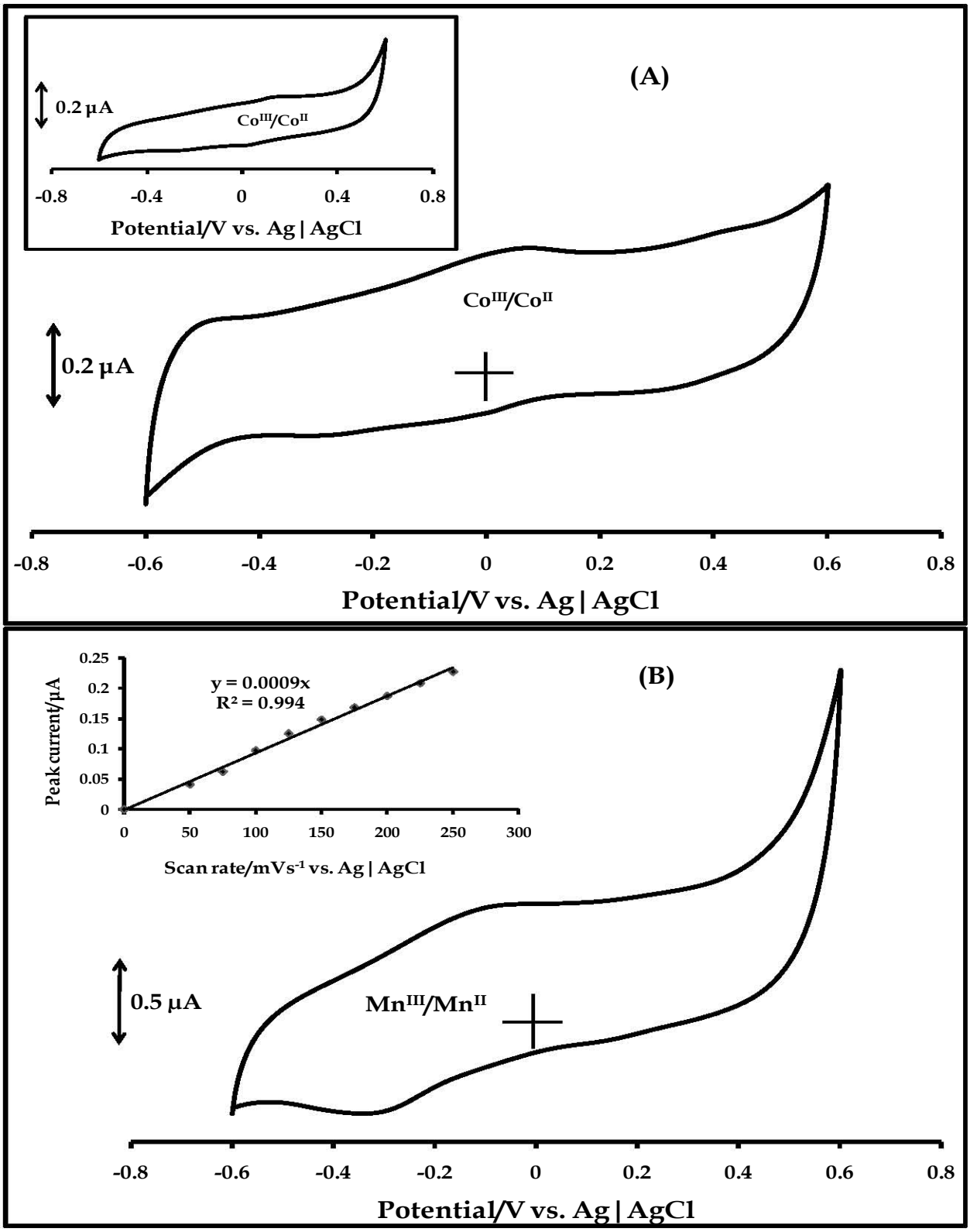

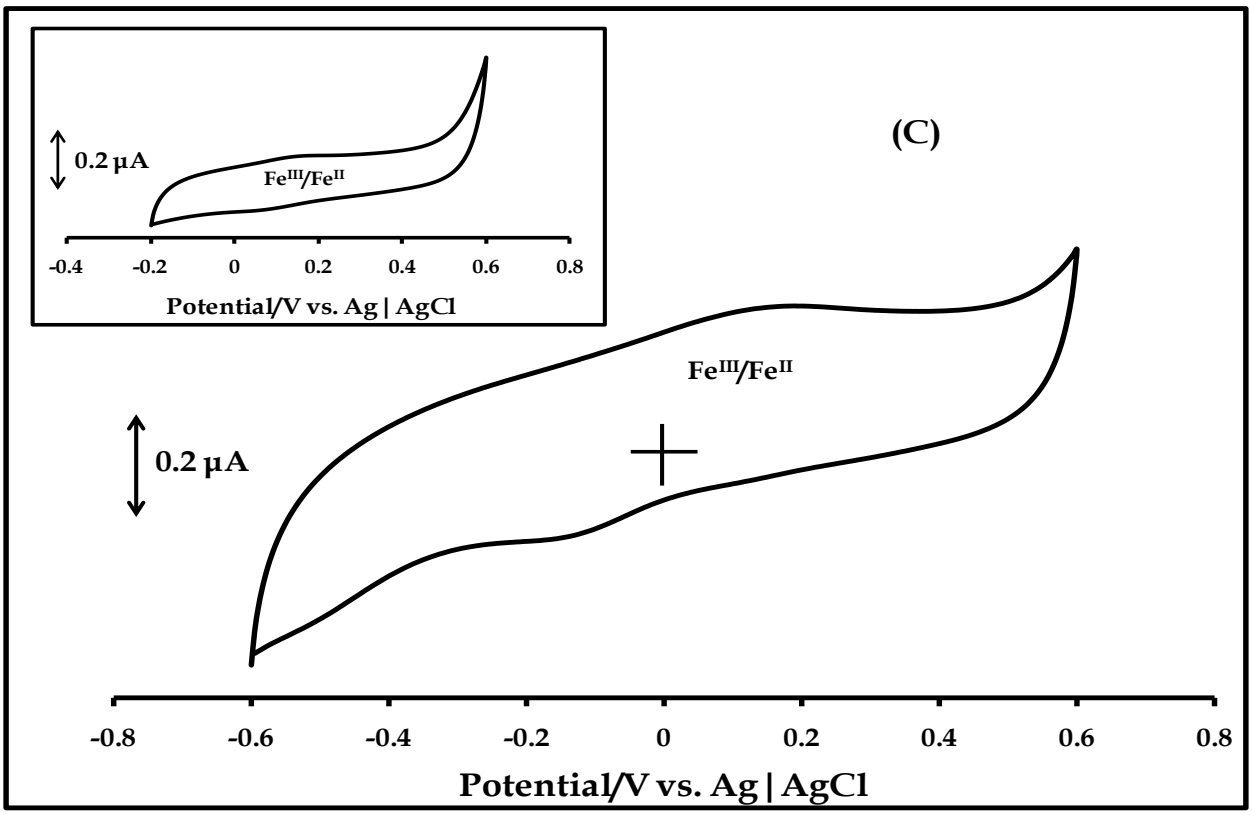

Figure 4.12: Cyclic voltammetry profiles of (A) **13**-SAM, (B) **14**-SAM (inset: plot of peak current versus scan rate) and (C) **15**-SAM-modified gold electrodes in pH 4 buffer solution. Scan rate: 50 mVs^{-1}. Insets in (A) and (C) are the cyclic voltammograms before repetitive scanning in DMF/$TBABF_4$ solution.

The linear dependence of peak current (anodic) on scan rate (Fig. 4.12B, inset) for **14**-SAM (representative of **13**- and **15**-SAMs) confirmed surface confinement of the complex on gold electrode.

Fig. 4.13A shows the cyclic voltammetry profile of **18**-SAM-modified gold electrode in pH 4 buffer solution. The redox process at $E_{1/2}$ = +0.22 V versus Ag|AgCl is attributed to Fe^{III}/Fe^{II} species (Table 4.4). The cyclic voltammetry trace in Fig. 4.13B shows the Fe^{III}/Fe^{II} redox process (on SWCNT-**18**-SAM-modified gold electrode) at $E_{1/2}$ = +0.18 V versus Ag|AgCl (Table 4.4). Interestingly, anodic to cathodic peak differences of the Fe^{III}/Fe^{II} redox process are 147 and 34 mV on **18**-SAM and SWCNT-**18**-SAM-modified gold electrode respectively, supporting the claim that electron transport may be enhanced in the presence of SWCNT. Also, this process is better resolved on SWCNT-

18-SAM modified gold electrode than on **18-**SAM film. Fig. 4.13C shows the cyclic voltammetry traces of SWCNT-**18**-SAM-modified gold electrode in pH 4 buffer at different scan rates (50 - 450 mVs^{-1}).

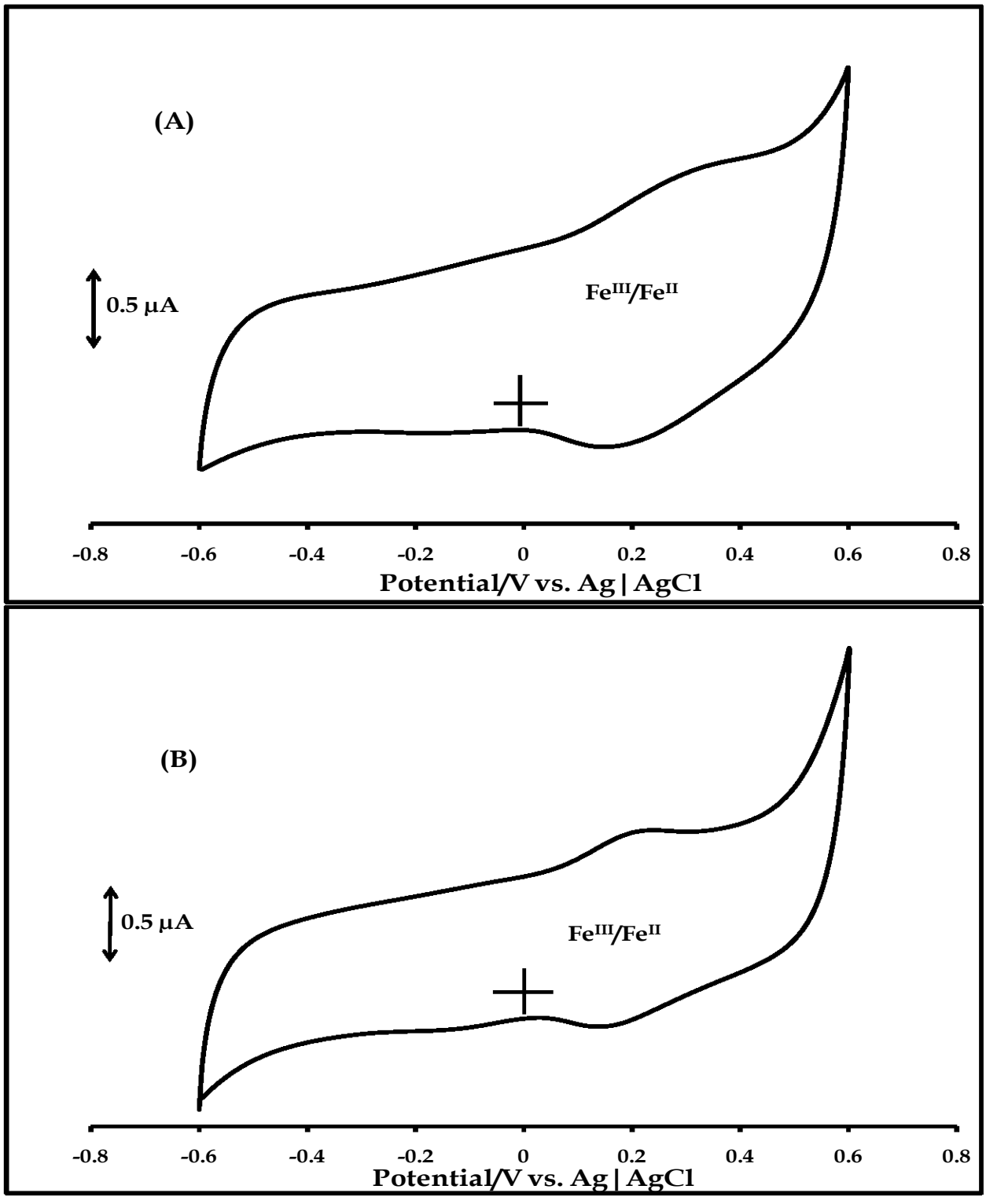

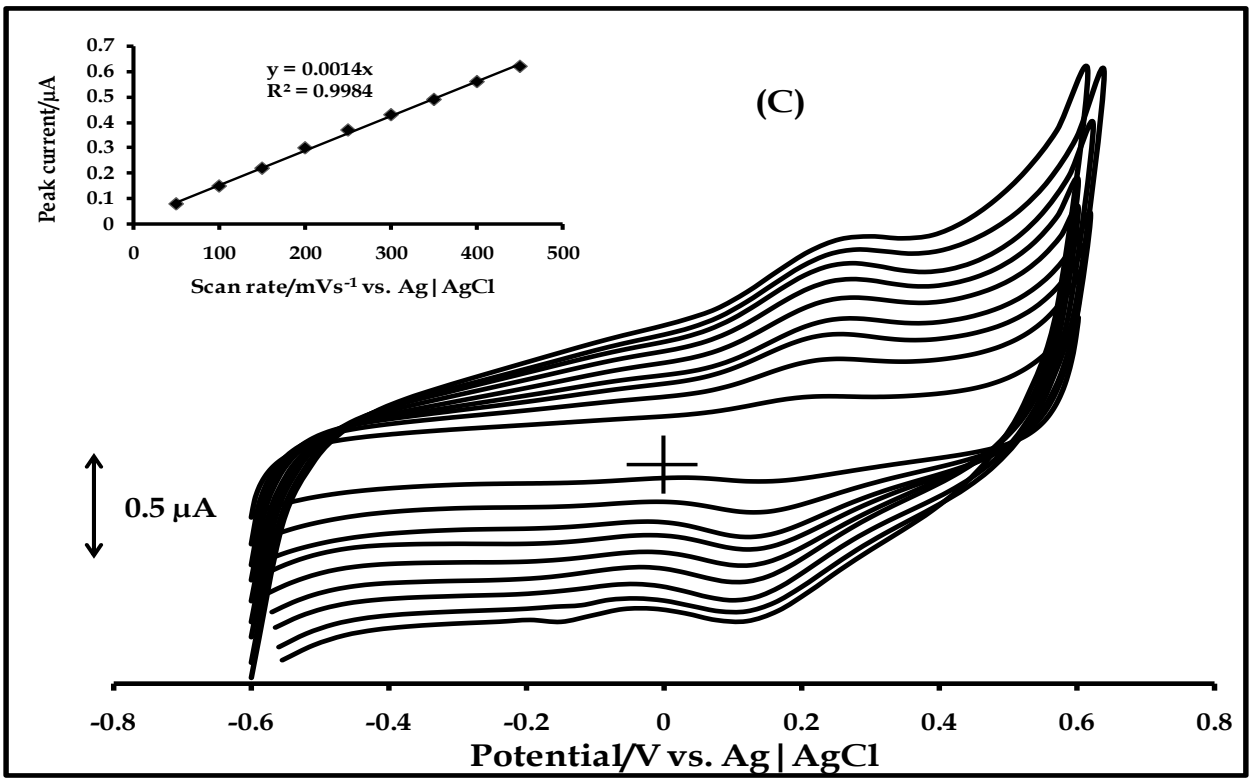

Figure 4.13: Cyclic voltammetry profiles of (A) **18**-SAM, (B) SWCNT-**18**-SAM (Scan rate: 50 mVs^{-1}), and (C) SWCNT-**18**-SAM-modified electrode at different scan rates (50-450 mVs^{-1}), in pH 4 buffer solution. Inset in (C) is the plot of peak current versus scan rate.

The inset in Fig. 4.13C shows the plot of anodic peak current versus scan rate (representative of **18**-SAM). The linear dependence of peak current on scan rate suggests surface-confinement of the SWCNT-**18** species on the electrode.

Fig. 4.14 shows the cyclic voltammetry profiles of **22**-, **23**- and **24**-SAM-modified gold electrodes in pH 4 buffer solution. The Co^{III}/Co^{II} redox process (Ep = +0.17 V versus Ag|AgCl) (Table 4.4), observed on **22**-SAM-modified gold electrode (Fig. 4.14A), was poorly resolved, like that observed on **13**-SAM (inset in Fig. 4.12A). Unlike **13**-SAM modified gold electrode (Fig. 4.12A), resolution of the Co^{III}/Co^{II} redox wave did not improve on **22**-SAM-modified gold electrode, after repeated voltammetry scanning in DMF/$TBABF_4$ solution. For the SAM of the corresponding peripherally tetra-substituted derivative [137], the Co^{III}/Co^{II} process of the adsorbed complex was observed at +0.32 V versus Ag|AgCl in pH 4 buffer, Table 1.4, which suggests that this process is

more energetically feasible on **22**-SAM-modified gold electrode. This observation may be attributed to non-peripheral substitution in complex **22**. A well-resolved metal-based process ($E_{1/2}$ = +0.02 V versus Ag|AgCl) (Table 4.4), attributed to Mn^{III}/Mn^{II} species, was observed on **23**-SAM-modified gold electrode (Fig. 4.14B). This process was observed at $E_{1/2}$ = -0.04 V versus Ag|AgCl in DMF/$TBABF_4$ solution of complex **23** (Fig. 3.20B) (Table 3.4). On the SAM of the peripherally tetra-substituted derivative of complex **23** [137], Mn^{IV}/Mn^{III} process was observed at +0.27 V, while in this work, there was no evidence of this process, Mn^{III}/Mn^{II} process was observed at +0.02 V, instead of the Mn^{IV}/Mn^{III} redox couple. The redox process observed on **24**-SAM-modified gold electrode in Fig. 4.14C ($E_{1/2}$ = +0.16 V versus Ag|AgCl), Table 4.4, is attributed to Fe^{III}/Fe^{II} species. In DMF/$TBABF_4$ solution of complex **24**, this process was observed at $E_{1/2}$ = +0.22 V versus Ag|AgCl (Fig. 3.25B) (Table 3.5). Apart from the differences in media (aqueous and DMF) and electrolytes (pH 4 buffer and $TBABF_4$), one of the major

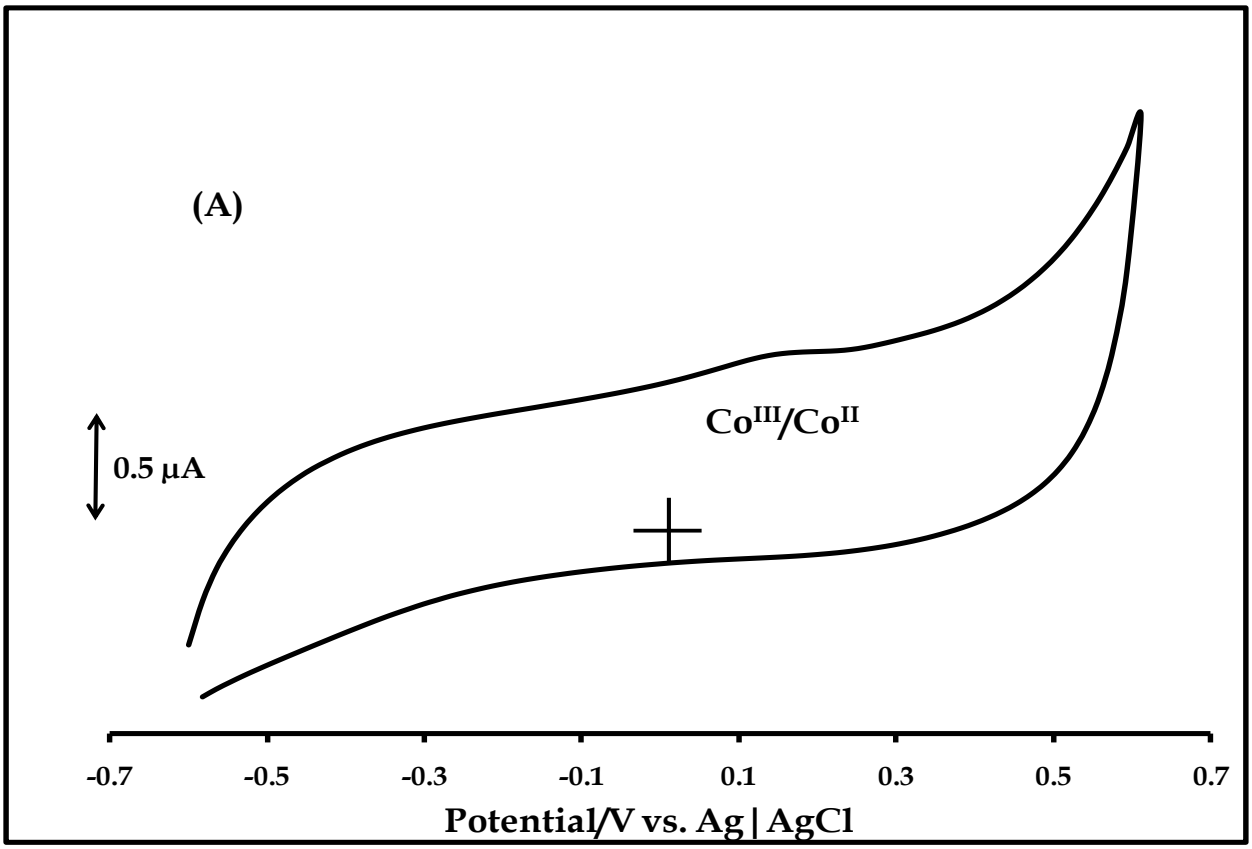

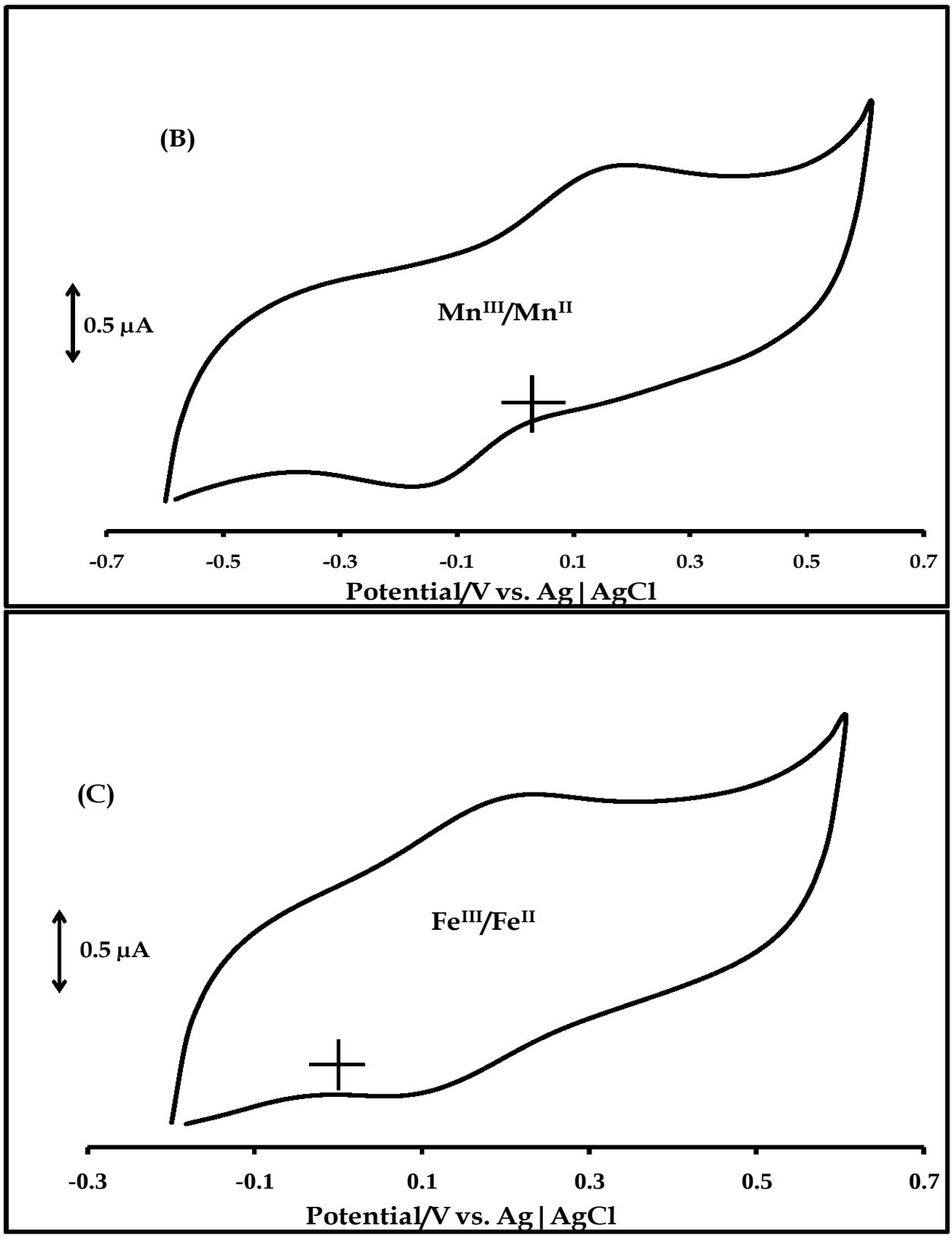
(B)
0.5 µA
Mn^{III}/Mn^{II}
-0.7
-0.5
-0.3
-0.1
0.1
0.3
0.5
0.7
Potential/V vs. Ag | AgCl
(C)
0.5 µA
Fe^{III}/Fe^{II}
-0.3
-0.1
0.1
0.3
0.5
0.7
Potential/V vs. Ag | AgCl

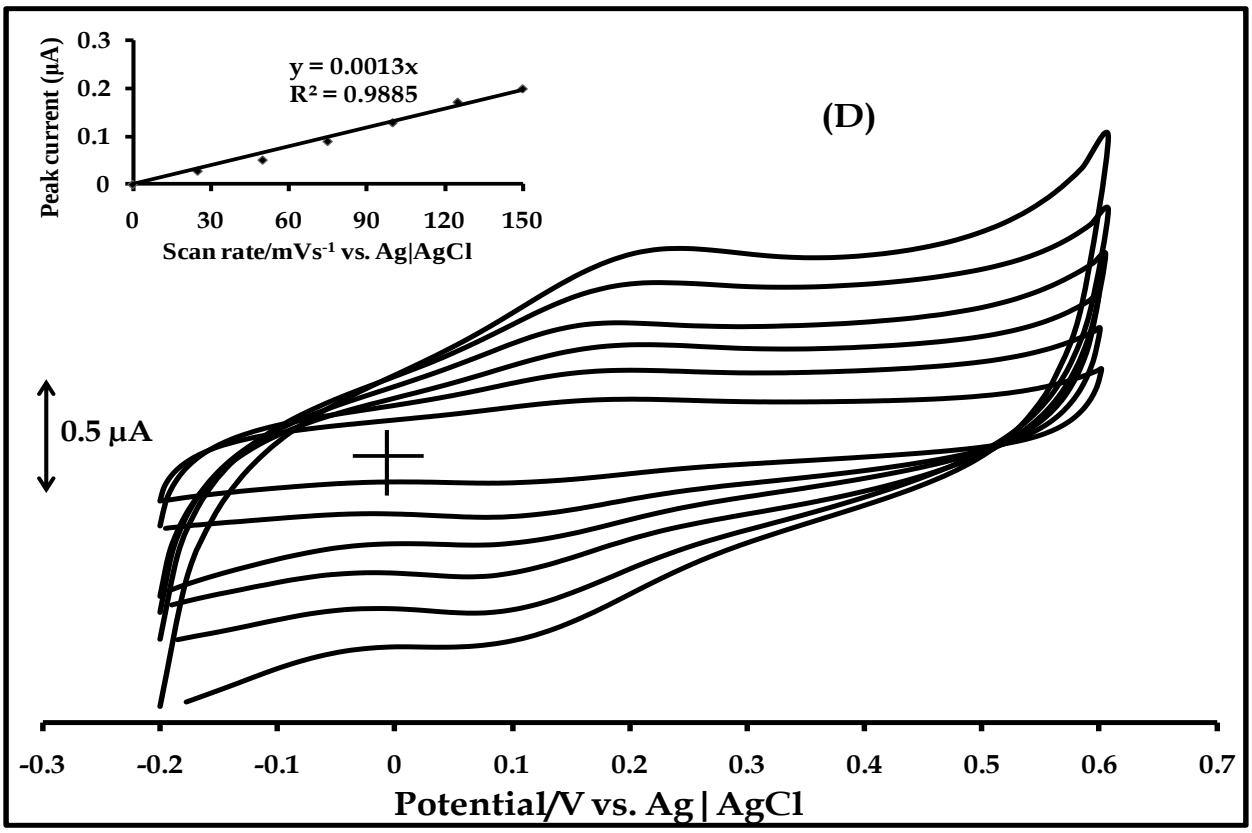

Figure 4.14: Cyclic voltammetry profiles of (A) **22**-SAM, (B) **23**-SAM, (C) **24**-SAM-modified gold electrodes in pH 4 buffer solution, scan rate: 175 mVs^{-1} and (D) **24**-SAM-modified gold electrode at different scan rate (25-150 mVs^{-1}). Inset in (D) is the plot of peak current versus scan rate.

properties of chemically modified electrodes is that the formal potential of the surface-bound redox center is close to that of the solution derivative [239]. This was the trend observed in the electrochemical data of all the adsorbed complexes (**13-15**, **18**, **22** and **23**), relative to those of their solution species. Fig. 4.14D shows the cyclic voltammetry profiles of **24**-SAM-modified gold electrode in pH 4 buffer at different scan rates (25-175 mVs^{-1}). The linear relationship between peak current (anodic) and scan rate (inset in Fig. 4.14D), representative of the SAMs of complexes **22** and **23**, suggests surface confinement of the species on gold electrode. For all the SAM-modified gold electrodes, the observed metal-based redox processes have peak separations, ΔE, larger than that expected for surface confined species (value close to zero). Such observation has been reported for Co^{3+}/Co^{2+} couple (ΔE > 150 mV) in cobalt porphyrins in low pH solutions

[240], like the pH used in this work. It was attributed to the slow kinetics of the couple at low pH.

4.1.6 Surface coverage

Surface coverage for each SAM was estimated from the relevant redox processes in Figs. 4.12 (A-C), 4.13 (A and B) and 4.14 (A-C), using equation 4.3.

$$\Gamma_{MPc-SAM} = \frac{Q}{nFA} \qquad 4.3$$

where Q is the background corrected charge of the anodic peak in each of the figures, A is the real surface area of the gold electrode, n is the number of electrons transferred (which is 1) and F is Faraday's constant. The real surface area of the electrode was estimated using Randles-Sevcik equation [239] (equation 4.4). $[Fe(CN)_6]^{3-}$ was used as the redox active species because it has a known diffusion coefficient.

$$I_{pa} = (2.69 \times 10^5) n^{3/2} D^{1/2} v^{1/2} AC \qquad 4.4$$

where n is the number of electrons transferred (which is 1), D is the diffusion coefficient of the redox active species (7.6×10^{-6} cm^2 s^{-1}) [239], A is the geometric surface area (0.020 cm^2), v is the scan rate (0.05 V s^{-1}) and C is the bulk concentration of $[Fe(CN)_6]^{3-}$ (0.01 M). Roughness factor of the electrode was calculated to be 1.05 (ratio of I_{pa} (exptal)/I_{pa} (theor)), where I_{pa} (exptal) and I_{pa} (theor) are the experimental current and current calculated using equation 4.4, respectively. The geometrical area was used in the estimation of I_{pa} (theor). The product of roughness factor and theoretical surface area gives the real surface area (0.021 cm^2).

The values of surface coverage obtained are 1.20×10^{-10}, 2.69×10^{-10} and 1.02×10^{-10} mol cm^{-2} for **13**-SAM**, 14-**SAM and **15**-SAM-modified gold electrodes, respectively (Table 4.4). Values of Γ_{SAM} reported for **13-** and **15**-SAM-modified gold electrodes were recorded after repetitive cyclic voltammetry scanning of these electrodes in DMF/$TBABF_4$ solution. Generally, surface coverage of approximately 1×10^{-10} mol cm^{-2}

has been reported for monolayer of metalloporphyrin and metallophthalocyanine complexes lying flat on a substrate [137,241,242], Γ_{SAM} for **13**-SAM and **15**-SAM-modified gold electrodes are consistent with this value. For **14**-SAM modified-gold electrode, the value of surface coverage suggests a different orientation of the complex on gold, compared to the flat orientation suggested for **13**- and **15**-SAMs. It has been reported that a perpendicular orientation is expected for cobalt *meso*-tetrakis (4-pyridyl) porphyrin adsorbed on a gold surface, with a surface coverage of 3.3×10^{-10} mol cm^{-2} [243]. Hence, high value of surface coverage obtained for **14**-SAM may indicate a perpendicular orientation of the SAM on gold surface. This may be attributed to the presence of acetate axial ligand, which distorts flat orientation of the SAM on the substrate.

All the SAMs were substantially stable in buffer of pH range 1-7, but desorbed at alkaline pH. Metal-based processes were not observed at alkaline pH, due to desorption of the SAMs at this pH. This is consistent with previous report for octabutylthiol substituted FePc complex [75]. Stability of these SAMs (**13**-**15**) (at pH 1-7) may be interpreted in terms of their densely packed crystalline nature, derived from the bulky diethylaminoethanethio substituent. This nature has been reported for SAMs of n-alkyl thiol formed on gold electrode [232]. Density and degree of crystallinity of the SAMs were directly proportional to the length of alkyl chain.

For **18**-SAM and SWCNT-**18**-SAM-modified gold electrodes, the values of Γ_{SAM} are 1.09×10^{-10} and 1.30×10^{-10} mol cm^{-2}, respectively (Table 4.4). The value of Γ_{SAM} for **18-**SAM is consistent with that expected for a monolayer of MPc-SAM (1×10^{-10} mol cm^{-2}) lying flat on the electrode surface [137,241,242], as mentioned previously. The relatively higher value of Γ_{SAM} for SWCNT-**18**-SAM modified gold electrode can be attributed to the attachment of SWCNT (Fig. 3.29B).

Values of Γ_{SAM} for **22**-SAM, **23**-SAM and **24**-SAM-modified gold electrodes are 3.9×10^{-11}, 1.3×10^{-10} and 7.50×10^{-11} mol cm^{-2}, respectively (Table 4.4). The surface coverage

obtained for **22**-SAM-modified gold electrode is a rough estimate, due to the poorly-resolved nature of the Co^{III}/Co^{II} redox process on this electrode (Fig. 4.14A). The relatively higher value of Γ_{SAM} for **23**-SAM-modified gold electrodes, with respect to those of **22**- and **24**-SAM-modified gold electrodes, confirms the relevance of the acetate axial ligand, as indicated previously for **14**-SAM-modified gold electrode. The lower values of Γ_{SAM} obtained for complexes **22**-**24**, relative to those of complexes **13**-**15**, are consistent with the trend observed in the blocking properties of these SAMs (Fig. 4.1). Like alkanethiols and other alkylthio-substituted MPc complexes, the diethylaminoethanethio-substituted complexes (**13**-**15**) have the tendency to form more compact SAM than their arylthio-substituted analogues (**22**-**24**), thus the relatively higher values of Γ_{SAM}.

4.1.7 Microscopic properties

Microscopic nature of the SAMs was investigated using scanning electron microscopy (SEM). For microscopic investigation, SAMs were formed on gold-coated glasses. Fig. 4.15 shows the SEM images of (A) bare, (B) **18**-SAM (representative of the SAMs of the other complexes) and (C) SWCNT-**18**-SAM-modified gold-coated glasses. Fig. 4.15A shows a rough gold-coated surface, while the self-assembled nature of complex **18** can

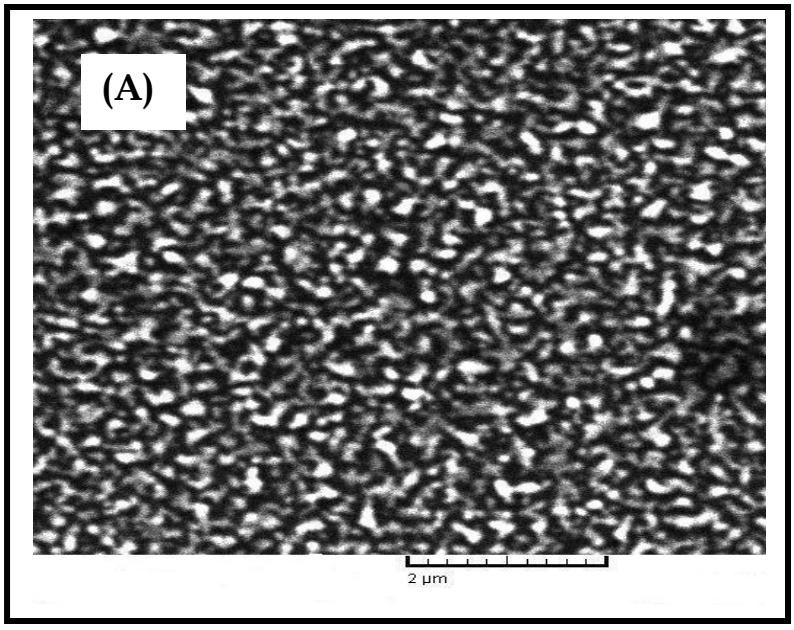

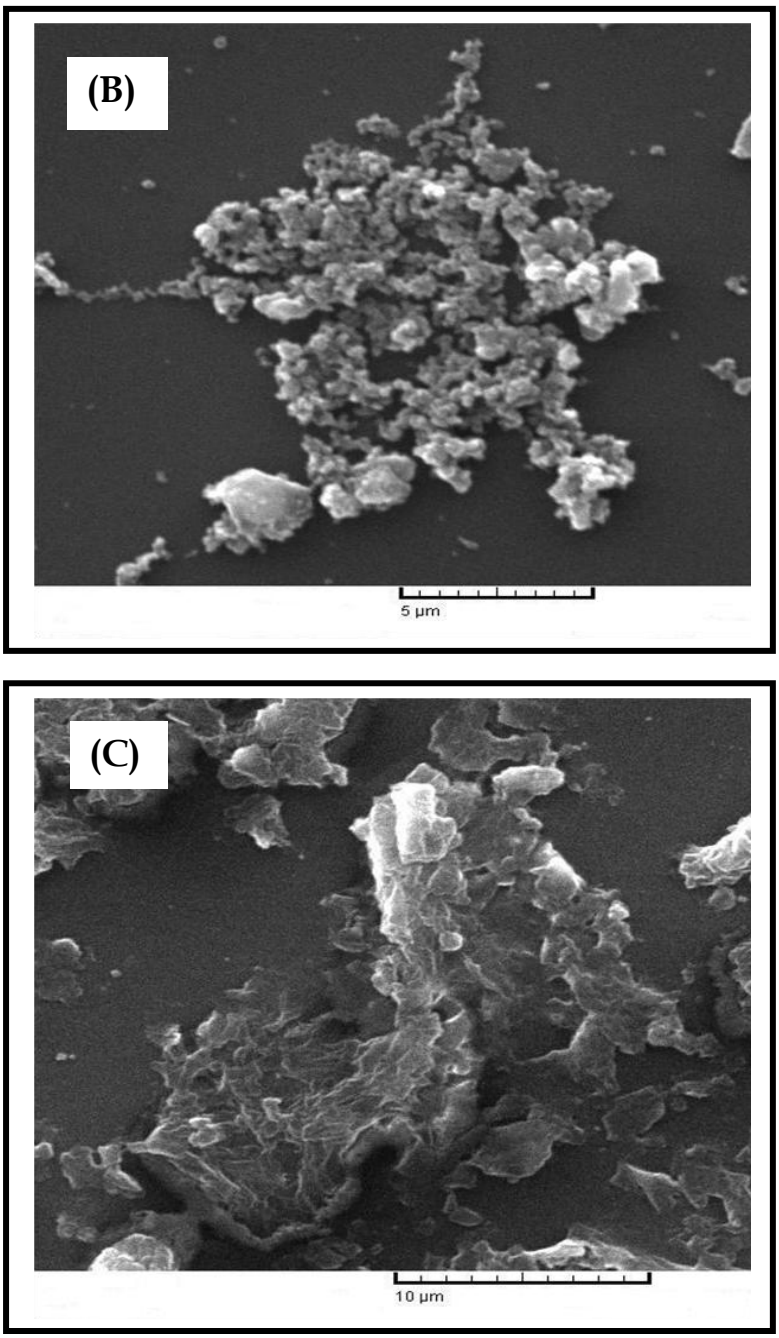

Figure 4.15: SEM images of (A) bare, (B) **18**-SAM and (C) SWCNT-**18**-SAM-modified gold-coated glasses.

be observed in Fig. 4.15B. SEM image of SWCNT-**18-**SAM (Fig. 4.15C) shows a different morphology from that of **18**-SAM. The difference in morphology can be attributed to the presence of SWCNT in the nano-composite.

4.2 Metallophthalocyanine-modified glassy carbon electrodes

Manganese complexes (**14**, **17** and **20**) were employed for the design of MnPc-modified glassy carbon electrodes. The motivation for the use of MnPc complexes was informed by the relatively limited examples of electrocatalytic MnPc systems, despite having electrocatalytic properties comparable to those of their Co and Fe analogues. Complexes **14** and **17** were used to investigate the influence of point of substitution on the surface properties and mechanism of formation of films of these complexes on glassy carbon electrode. The use of complex **20** (the octa-substituted derivative of **17**) was necessitated by the quest to investigate the effect of the plurality of the substituent (diethylaminoethanethio) on the surface properties of the resulting MPc film, relative to that of **17**.

4.2.1 Electropolymerization/Electrodeposition

Fig. 4.16A shows the evolution of cyclic voltammetry profiles obtained during repetitive cyclic voltammetry scanning (fifteen cycles) of bare GCE in 10^{-3} M of complex **17** in freshly distilled, dried DMF, containing 0.1 M $TBABF_4$. The best voltammetry responses of bendiocarb (one of the analytes of interest) on the MPc- modified GCEs was obtained with the films formed from fifteen voltammetry cycles. Hence the use of this number of voltammetry scans for film formation. An increase in current intensities and changes in peak positions of the anodic peaks of couples **I** and **II** indicate changing nature of the electrode surface and film formation. The emergence of a new cathodic peak around -0.62 V vs. Ag|AgCl (Fig. 4.16A) suggests that film formation was facilitated by electropolymerization. Electropolymerization of MPc complexes is aided by the formation of radicals from substituents containing oxidizable groups, such as sulphur and nitrogen [132]. In the present work, oxidation involving the tertiary amine group of the diethylaminoethanethio substituent will promote electropolymerization. After modification, the electrode was rinsed in DMF, dried in a slow stream of argon and characterized. The modified electrode is designated poly-**17**-GCE.

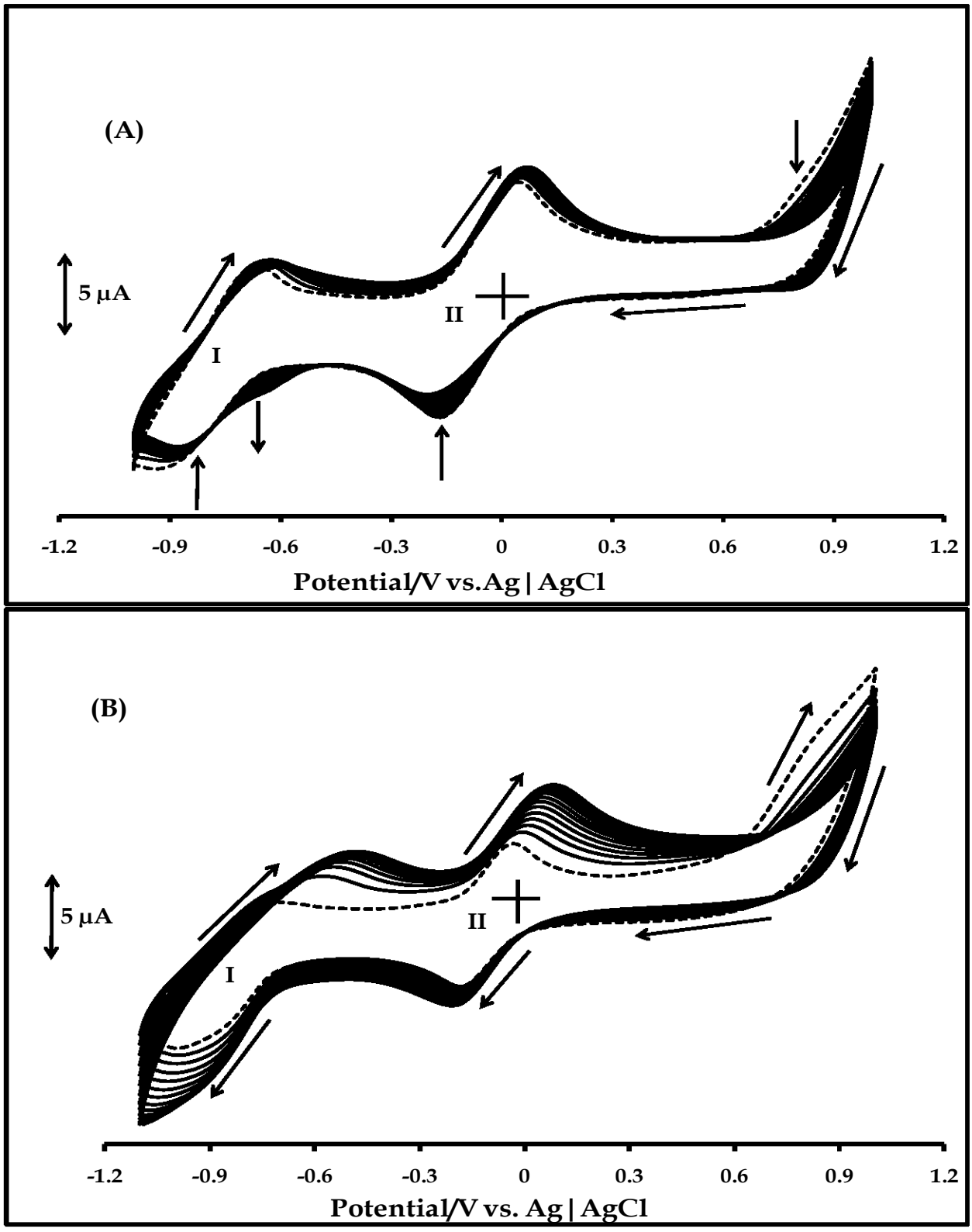
(A)
5 µA
I
II
-1.2
-0.9
-0.6
-0.3
0
0.3
0.6
0.9
1.2
Potential/V vs.Ag | AgCl
(B)
5 µA
I
II
-1.2
-0.9
-0.6
-0.3
0
0.3
0.6
0.9
1.2
Potential/V vs. Ag | AgCl

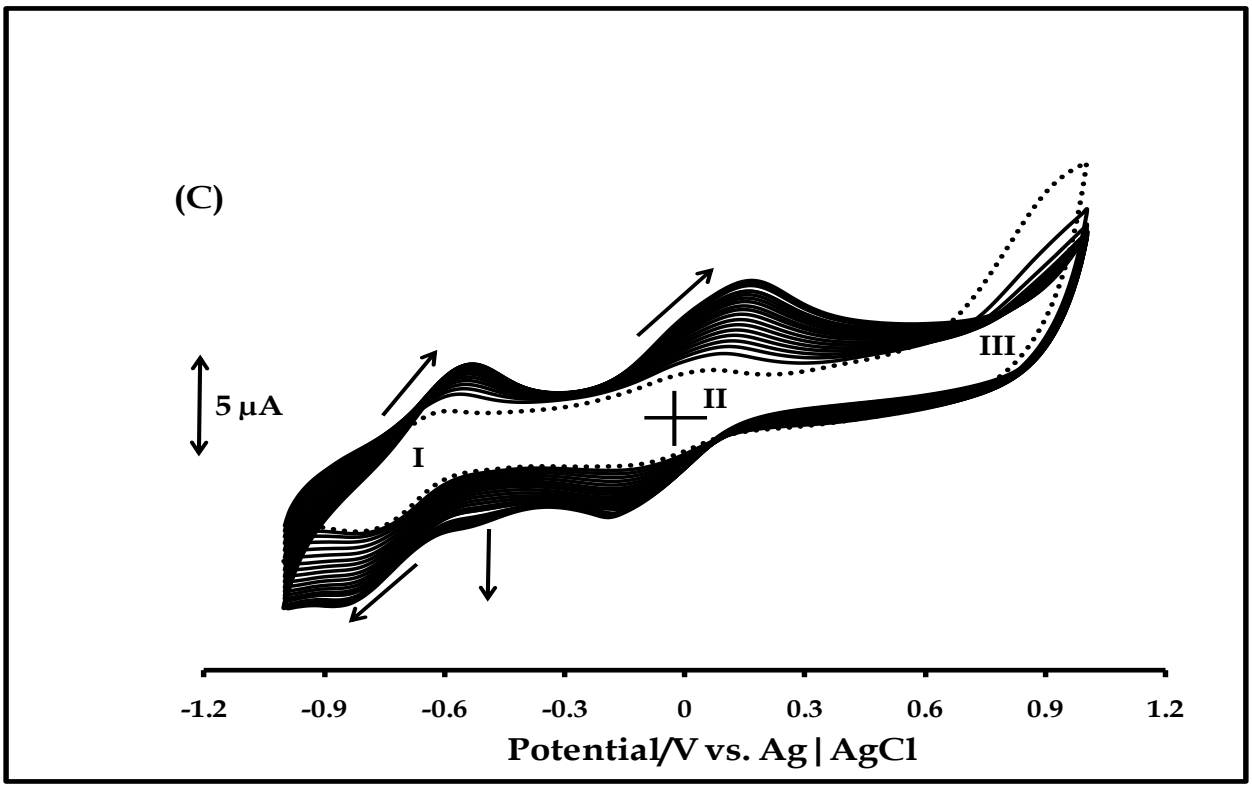

Figure 4.16: Evolution of cyclic voltammetry profiles during repetitive scanning (15 cycles) of bare GCE in 1×10^{-3} M of (A) complex **17**, (B) complex **14** and (C) complex **20** (20 cycles) in freshly distilled DMF containing 0.1 M $TBABF_4$. Scan rate: 100 mVs^{-1}. Dashed line = First scan.

Film formation from complex **14** was achieved as described above for complex **17**, using the same number of voltammetry cycles (fifteen). Fig. 4.16B shows the evolution of cyclic voltammetry profiles during film formation. However, unlike the case with complex **17**, no new peak was observed for complex **14** during cyclic voltammetry scanning, hence electropolymerization is ruled out and electrodeposition is suggested. Electrodeposition is characterized by increasing current intensities and changing positions of both the anodic and cathodic components of couples **I** and **II** during successive voltammetry cycles, without formation of new peaks. For both complexes, wave **II** is due to $Mn^{III}Pc^{-2}/Mn^{II}Pc^{-2}$ couple, and **I** to $Mn^{II}Pc^{-2}/Mn^{II}Pc^{-3}$, in comparison with literature [67]. The formation of radicals, from the oxidation of the substituents of complex **14**, is expected, as discussed for complex **17**. However, film formation via

electropolymerization may have been discouraged by the absence of end to end coupling (necessary for polymer formation) of the macrocycles, due to steric hindrance, resulting from non-peripheral substitution (Scheme 3.1). The above scenario suggests certain degree of morphological differences in the films of these complexes. This was investigated using atomic force microscopy (AFM), discussed later in this work. The modified electrode in Fig. 4.16B is represented as electrodep-**14**-GCE.

Fig. 4.16C shows the evolution of cyclic voltammograms obtained during repetitive scanning (20 cycles) of 1 x 10^{-3} M of complex **20** in freshly distilled, dried DMF, containing 0.1 M $TBABF_4$. The optimum current response of bentazon (detected on this electrode) was obtained from the polymer formed from twenty voltammetry cycles; hence the use of this number of voltammetry scans for polymer formation. Electropolymerization was justified by the emergence of new peak at ~-0.5 V, the shift in peak potentials and increase in peak currents of both the cathodic and anodic components of the couples labeled **I** and **II** in Fig. 4.16C. The peak potentials of the anodic components shift from ~+0.02 to ~+0.14 V (for couple **II**) and ~-0.65 to ~-0.56 V (for couple **I**) while that of the cathodic components shift from ~-0.08 to ~-0.17 V (for couple **II**) and ~-0.77 to ~-0.83 V (for couple **I**). The shift to more positive potentials, for the anodic components, and more negative potentials, for the cathodic components, with increase in scan number, is a proof of an increase in the electrical resistance of the polymeric film, and overpotential is needed to overcome this resistance [244]. The resulting polymer is designated poly-**20**-GCE.

4.2.2 Surface voltammetry properties

Cyclic voltammetry was used for characterization of the films on GCE. Fig. 4.17A shows the cyclic voltammetry profile of poly-**17**-GCE in pH 4 buffer solution. The best current response of the insecticide, bendiocarb (the analyte detected on this electrode), discussed later, was obtained at this pH value, hence its use for voltammetry characterization of modified electrodes (poly-**17**-GCE and electrodep-**14**-GCE). The

existence of redox processes, labeled **I** ($E_{1/2}$ = -0.72 V vs. Ag|AgCl), **II** ($E_{1/2}$ = -0.32 V vs. Ag|AgCl), **III** (E_p = +0.52 V vs. Ag|AgCl) and **IV** ($E_{1/2}$ = +0.77 V vs. Ag|AgCl), Table 4.5, confirms the presence of the polymeric film of complex **17** on poly-**17**-GCE. Processes **I**, **II**, **III** and **IV** are assigned to $Mn^{II}Pc^{-2}/Mn^{II}Pc^{-3}$, $Mn^{III}Pc^{-2}/Mn^{II}Pc^{-2}$, $Mn^{IV}Pc^{-2}/Mn^{III}Pc^{-2}$ and $Mn^{IV}Pc^{-1}/Mn^{IV}Pc^{-2}$ couples respectively, in comparison with literature [67,76,90,95] (Table 4.5). Proof of the existence of $Mn^{IV}Pc^{-2}/Mn^{III}Pc^{-2}$ redox process, as an adsorbed species [245], is provided later.

Fig. 4.17B shows the cyclic voltammogram of electrodep-**14**-GCE in pH 4 buffer. Like the film of the peripheral analogue (complex **17**) discussed above, the occurrence of redox processes, designated **I** ($E_{1/2}$ = -0.71 V vs. Ag|AgCl), **II** ($E_{1/2}$ = -0.29 V vs. Ag|AgCl), **III** (E_p = +0.40 V vs. Ag|AgCl) and **IV** (E_p = +0.74 V vs. Ag|AgCl) (Table 4.5) confirms the presence of the film on the electrode surface. The half-wave and peak potentials of the observed redox processes are marginally different from those of the peripheral derivative. The closeness in electrochemical properties suggests similarity in

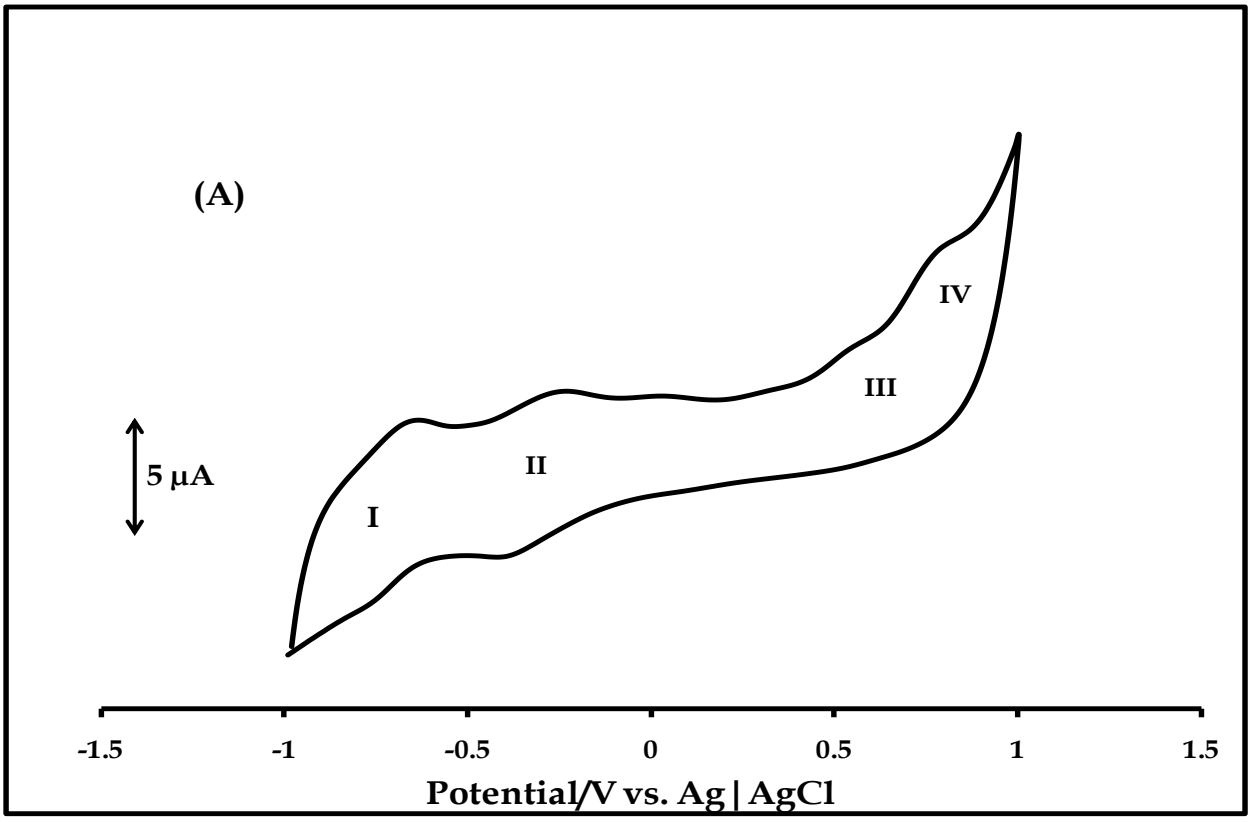

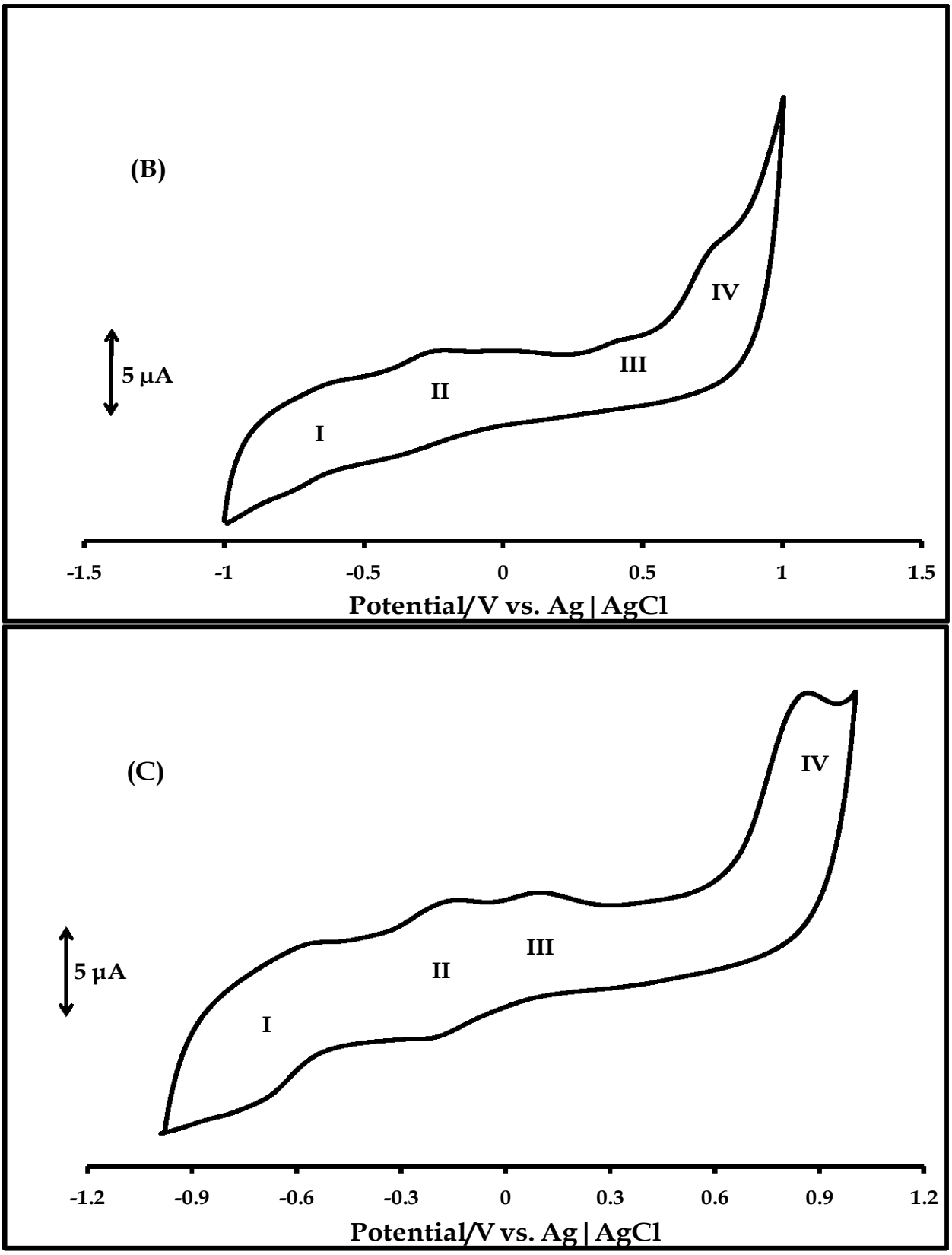
(B)
5 µA
I
II
III
IV
-1.5
-1
-0.5
0
0.5
1
1.5
Potential/V vs. Ag|AgCl
(C)
5 µA
I
II
III
IV
-1.2
-0.9
-0.6
-0.3
0
0.3
0.6
0.9
1.2
Potential/V vs. Ag|AgCl

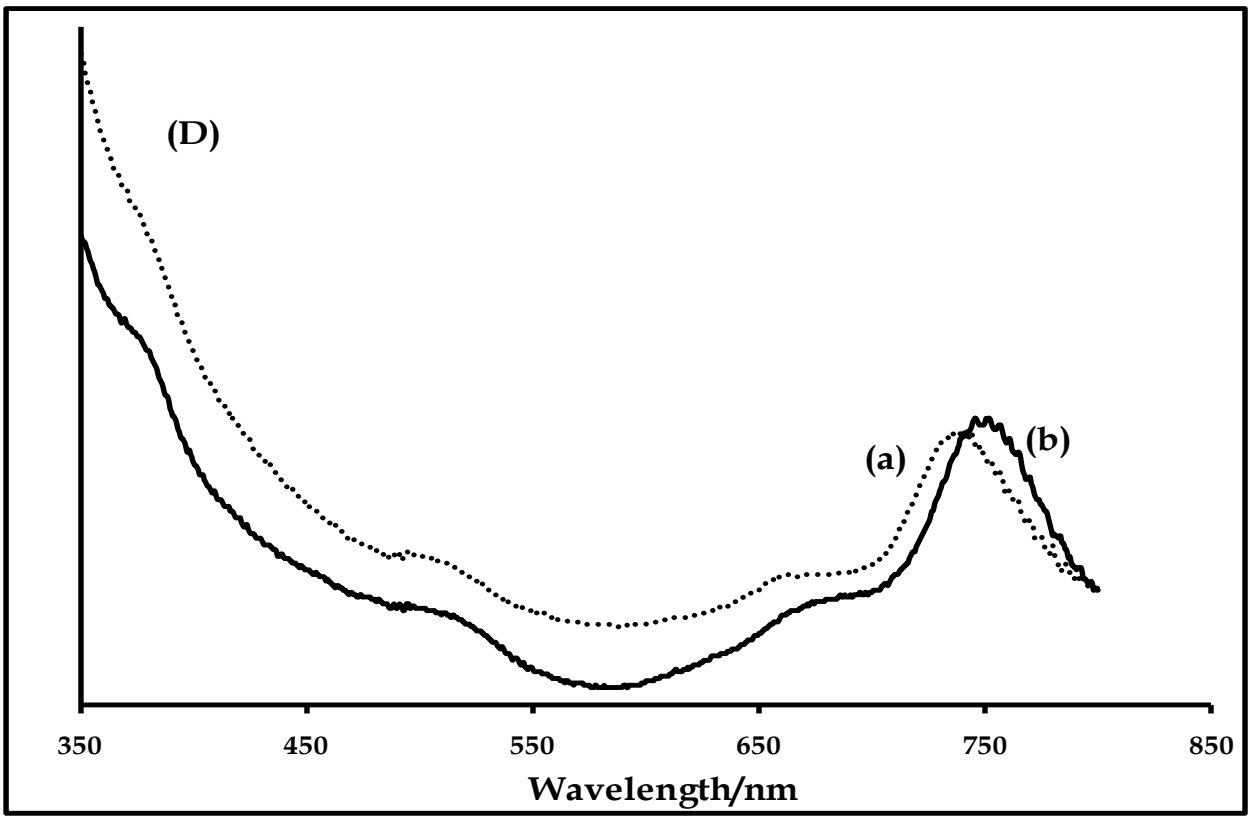

Figure 4.17: Cyclic voltammetry profiles of (A) poly-**17**-GCE, (B) electrodep-**14**-GCE in pH 4 buffer solution and (C) poly-**20**-GCE in pH 5 buffer solution. Scan rate: 100 mVs^{-1}. (D) UV-Vis spectral changes of poly-**17** on ITO, on application of potentials of process **III** in pH 4 buffer, (a) before and (b) after.

the conducting backbone of these films. This is expected, since the conducting pathway of each film is a combination of the π-systems of the individual macrocycles, which is the same for both films.

The cyclic voltammetry response of poly-**20**-GCE in 0.1 M phosphate buffer solution (pH 5) is shown in Fig. 4.17C. This pH gave the best current response of the herbicide, bentazon (the analyte detected on this electrode), hence it relevance. Observation of the redox processes (**I**-**IV**) on poly-**20**-GCE confirms the presence of the polymer. These processes are more resolved than those observed on poly-**17**-GCE (the polymeric film of the tetra-substituted derivative of complex **20**) (Fig. 4.17A). This observation can be

attributed to enhanced electron-donating nature, due the number of the electron-releasing substituent. Processes **I** ($E_{1/2}$ = -0.62 V), **II** ($E_{1/2}$ = -0.18 V), **III** (E_p = +0.08 V)

Table 4.5: Electrochemical data of MnPc-modified glassy carbon electrodes, potential in Volts versus Ag | AgCl.

Electrode	$Mn^{II}Pc^{-2}/Mn^{II}Pc^{-3}$	$Mn^{III}Pc^{-2}/Mn^{II}Pc^{-2}$	$Mn^{IV}Pc^{-2}/Mn^{III}Pc^{-2}$	$Mn^{IV}Pc^{-1}/Mn^{IV}Pc^{-2}$	[a]Γ_{MPc}/mol cm^{-2} ($\times 10^{-10}$)	Medium
Electrod-**14**	-0.71	-0.29	+0.40	+0.74	2.68	pH 4
Poly-**17**	-0.72	-0.32	+0.52	+0.77	3.49	pH 4
Poly-**20**	-0.62	-0.18	+0.08	+0.80	5.63	pH 5

[a]Value calculated using the charge under the anodic peak of the $Mn^{III}Pc^{-2}/Mn^{II}Pc^{-2}$ redox couple on the respective MnPc-modified glassy carbon electrode.

and **IV** (E_p = +0.80 V), on poly-**20**-GCE (Table 4.5), are assigned to $Mn^{II}Pc^{-2}/Mn^{II}Pc^{-3}$, $Mn^{III}Pc^{-2}/Mn^{II}Pc^{-2}$, $Mn^{IV}Pc^{-2}/Mn^{III}Pc^{-2}$ and $Mn^{IV}Pc^{-1}/Mn^{IV}Pc^{-2}$ couples, respectively. Process **III** is more energetically feasible on poly-**20**-GCE than on electrodep-**14**-GCE or poly-**17**-GCE (Table 4.5), justifying enhanced electron-donating nature of the substituent. Like complex **17**, process **III** is not observed in solution of complex **20** (Fig. 3.18B), but may be observed as adsorbed species, as reported previously for NiPc [245]. It is important to mention that the $Mn^{IV}Pc^{-2}/Mn^{III}Pc^{-2}$ couples was also not observed on **14**-SAM (Fig. 4.12B), unlike the case with its electrodeposited film (electrodep-**14**-GCE) (Fig. 4.17B). This suggests that electrochemical properties of MPc-based films may be influenced by method of formation, among other factors.

The assignment of $Mn^{IV}Pc^{-2}/Mn^{III}Pc^{-2}$ couple on each film was confirmed by spectroelectrochemistry on complex **17** (representative of **14** and **20**). Complexes **17** (representative of **20**) and **14** were electropolymerized and electrodeposited on ITO, respectively. The shift in position of Q band to higher wavelength, on the application of

potential of process **III**, confirms metal oxidation ($Mn^{III}Pc$ to $Mn^{IV}Pc$). Fig. 4.17D shows the change in Q-band position (from 735 to 748 nm) observed for complex **17** (representative of complexes **14** and **20**). $Mn^{IV}Pc^{-2}/Mn^{III}Pc^{-2}$ couple was not observed in solution (Fig. 3.14B for complex **14**, Fig. 3.17B for complex **17** and Fig. 3.18B for complex **20**). It has been reported before for some MPc complexes, such as NiPc, that metal-based redox processes, not observed in solution, can be observed in the solid state [245].

4.2.3 Surface coverage

The value of surface coverage (Table 4.5) for each MnPc-modified GCE was calculated using equation 4.3. The real surface area (0.071 cm^2) of the glassy carbon electrode was calculated using equation 4.4, as discussed previously for gold electrode. Γ_{MPc} was estimated by using the value of Q (the background-corrected charge) for the anodic peak of couple **II** in the cyclic voltammogram of interest in Fig. 4.17. Values of surface coverage obtained are 2.68×10^{-10}, 3.49×10^{-10} and 5.63×10^{-10} mol cm^{-2} for electrodep-**14**-GCE, poly-**17**-GCE and poly-**20**-GCE, respectively, Table 4.5. This suggests a multilayer coverage, since each of these values is higher than that expected for a monolayer of phthalocyanine molecules lying flat or vertically oriented on the electrode surface [241,242]. Also, perpendicular orientation of these complexes is envisaged on GCE, as discussed previously for **14**-SAM on gold electrode [243] (Table 4.4). This further reiterates the relevance of the acetate axial ligand (present in all the MnPc complexes) on the orientation of these complexes on a given substrate.

4.2.4 Microscopic properties

Surface characteristics of electrodeposited film of complex **14** and electropolymerized film of complex **17** (representative of complex **20**) were further probed, using AFM in the non-contact mode in air. AFM has proven to be an invaluable technique in probing the structure and reactivity of surfaces. In addition to investigating morphological changes, AFM gives information on the extent of coverage, by estimating the difference

in the height of the surface before and after modification [246]. In the present study, ITO-coated glass was used as the solid substrate for recording AFM images.

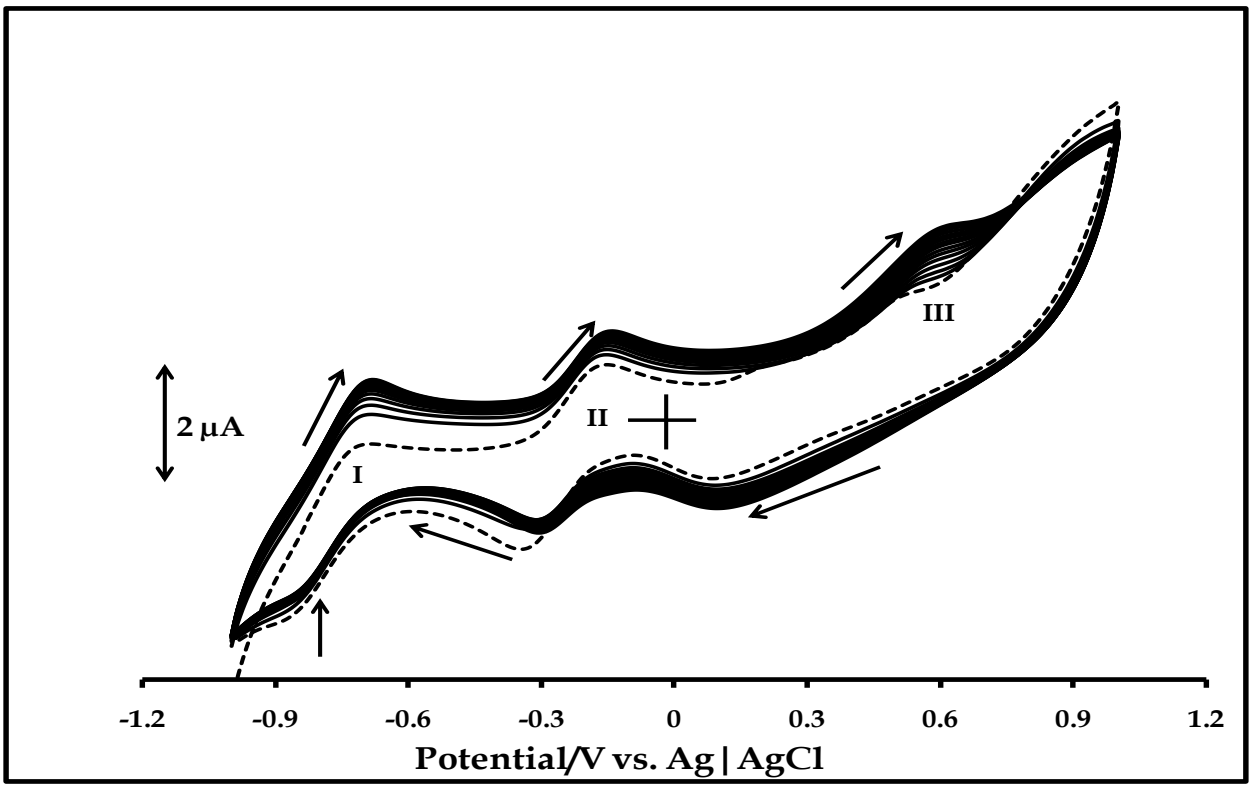

Figure 4.18: Evolution of cyclic voltammetry profiles during repetitive scanning (15 cycles) of ITO coated glass in 1 × 10^{-3} M of complex **14** in freshly distilled DMF containing 0.1 M $TBABF_4$. Scan rate: 100 mVs^{-1}. Dashed line = First scan.

Fig. 4.18 shows the evolution of the cyclic voltammetry profiles of bare ITO-coated glass in 1 x 10^{-3} M of complex **14** in freshly distilled, dried DMF, containing 0.1 M $TBABF_4$, as supporting electrolyte. Formation of the film was evident from increase in current intensities of the anodic components of couples **I**, **II** and **III**, due to electrodeposition. The shift in positions of the anodic components of couples **II** and **III** (the latter couple is not observed clearly in Fig. 4.16B) is also a confirmation of film formation. For complex **17**, cyclic voltammograms showing the formation of a polymer, similar to that observed on GCE, were also recorded. Morphological characteristics of the films on ITO gave understanding of their likely nature on glassy carbon electrode. Figs. 4.19A, B, and C are the AFM images of bare ITO-coated glass, films of poly-**17**-ITO and electrodep-**14**-

ITO, respectively. The bare ITO-coated glass shows a very rough surface, normally referred to as granular morphology [247].

The film formed from complex **17** (Fig. 4.19B) shows a compact surface, with a thickness of 0.026 µm (difference between thickness after film formation and thickness of bare ITO-coated glass). The mean roughness of the film is about 1.10 nm compared to 0.21 nm for the bare ITO coated glass. These observations are a confirmation of the presence of the film on the glass. The compact nature of the film on glass is representative of its likely morphology on glassy carbon electrode. Morphological features may play a role in the diffusion of analytes within the film. This is discussed in chapter 5 of this work. Films formed from complex **14** (Fig. 4.19C) are strikingly different from that of complex **17**. The film thickness is about 0.003 µm with a mean roughness of 0.50 nm. Fig. 4.19C shows a relatively porous film, compared to the one in Fig. 4.19B. The porous nature of the film of **14**, compared to the compact nature of the film of **17**, may be attributed to the fact that the latter is a polymer while the former is electrodeposited. The above observations demonstrate the relevance of point of substitution on the mechanism of formation and morphological features of these MnPc-based molecular films. Effects of the surface nature of the film on current response and kinetic of electro-oxidation of the

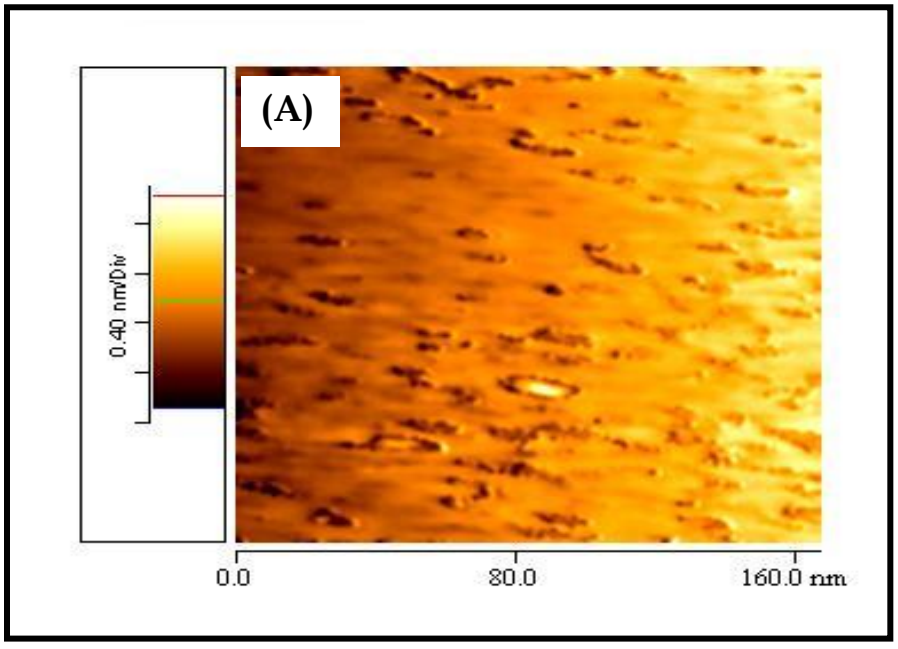

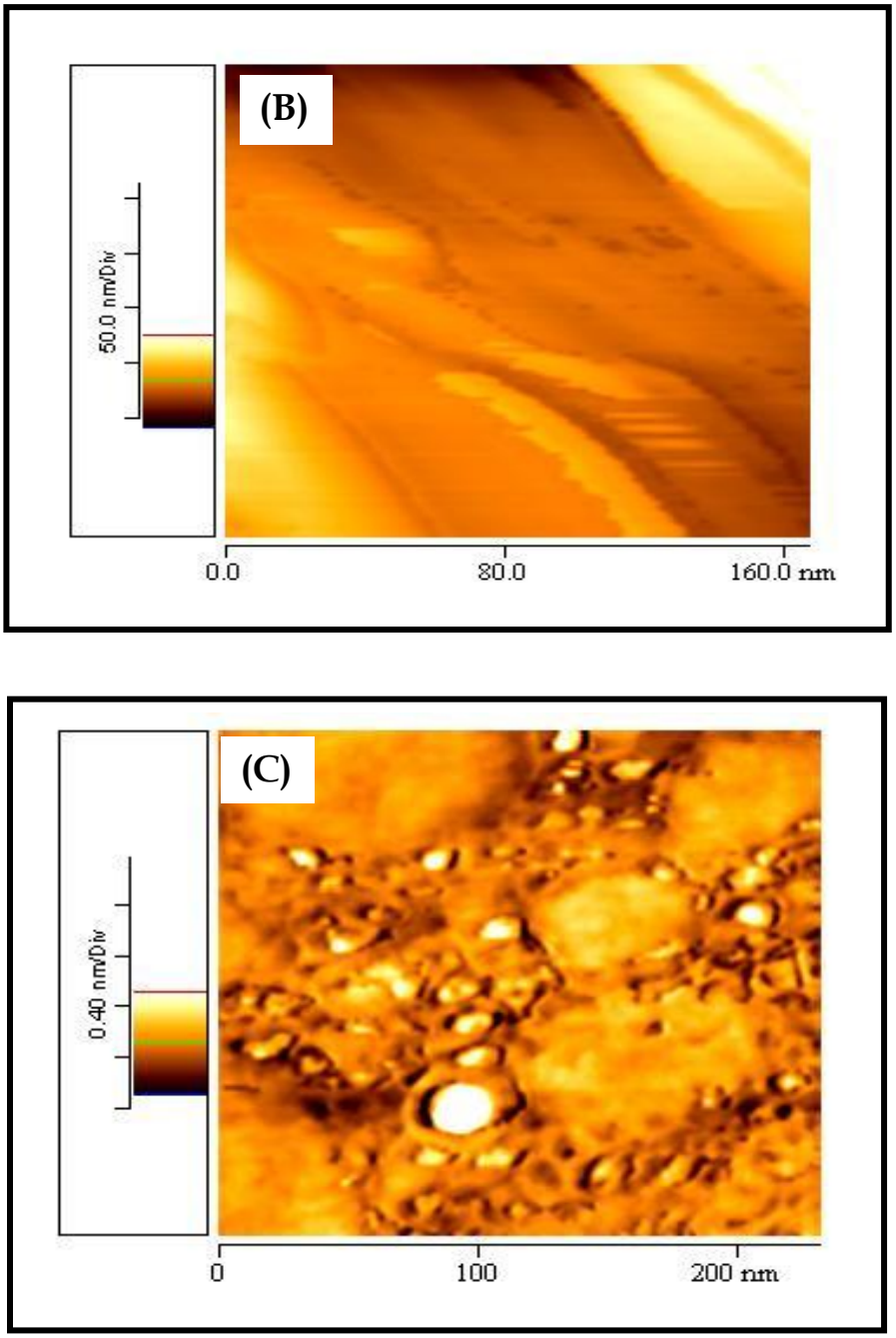

Figure 4.19: AFM images of (A) bare ITO glass, (B) poly-**17**-ITO and (C) electrodep-**14**-ITO

insecticide, bendiocarb (the analyte detected on electrodep-**14**-GCE and poly-**17**-GCE), are explained in chapter 5 of this work.

CHAPTER 5

ELECTROCATALYSIS OF PESTICIDES

5.1 Carbofuran

5.1.1 Voltammetry response

Electrocatalytic oxidation of the insecticide, carbofuran, was carried out on the MPc-SAM-modified gold electrodes. Carbofuran is not electroactive, but prior to electrocatalysis, carbofuran was hydrolyzed in alkaline medium (0.5 M NaOH), for 0.5 h (the time that gave the optimum current response of the insecticide), to generate the electroactive phenolic species (Scheme 5.1). The pH of the resulting solution was adjusted to 4 on addition of acetic acid. The best current signal of carbofuran was obtained at pH 4, thus all voltammetry measurements involving this insecticide were done at this pH. SAMs of all the complexes were also stable at this pH.

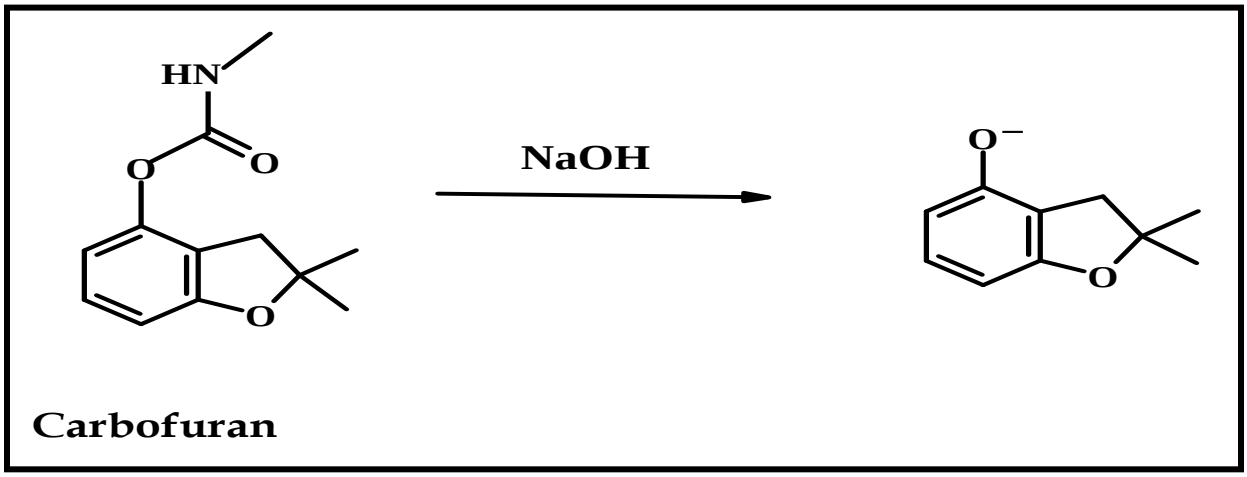

Scheme 5.1: Alkaline hydrolysis of carbofuran

Voltammetry responses of 200 µM hydrolyzed solution of carbofuran on bare and (**13**-**15**)-SAM-modified gold electrodes are shown in Fig. 5.1. Irreversible oxidation of the insecticide was observed on the bare (0.67 V, 0.74 µA) and SAM-modified gold electrodes. In Fig. 5.1, the voltammetry signals of the insecticide on **13**-SAM- (0.42 V, 1.62 µA), **14**-SAM- (0.48 V, 1.88 µA) and **15**-SAM- (0.40 V, 1.12 µA) modified gold electrodes (Table 5.1) are individually better than that on bare gold electrode, justifying the electrocatalytic influence of the SAMs on the oxidation of carbofuran. Although, oxidation of the insecticide was most energetically feasible (least positive oxidation

potential) on **15**-SAM-modified gold electrode, the lowest current response was observed on this SAM, while the current response on **14**-SAM was the best.

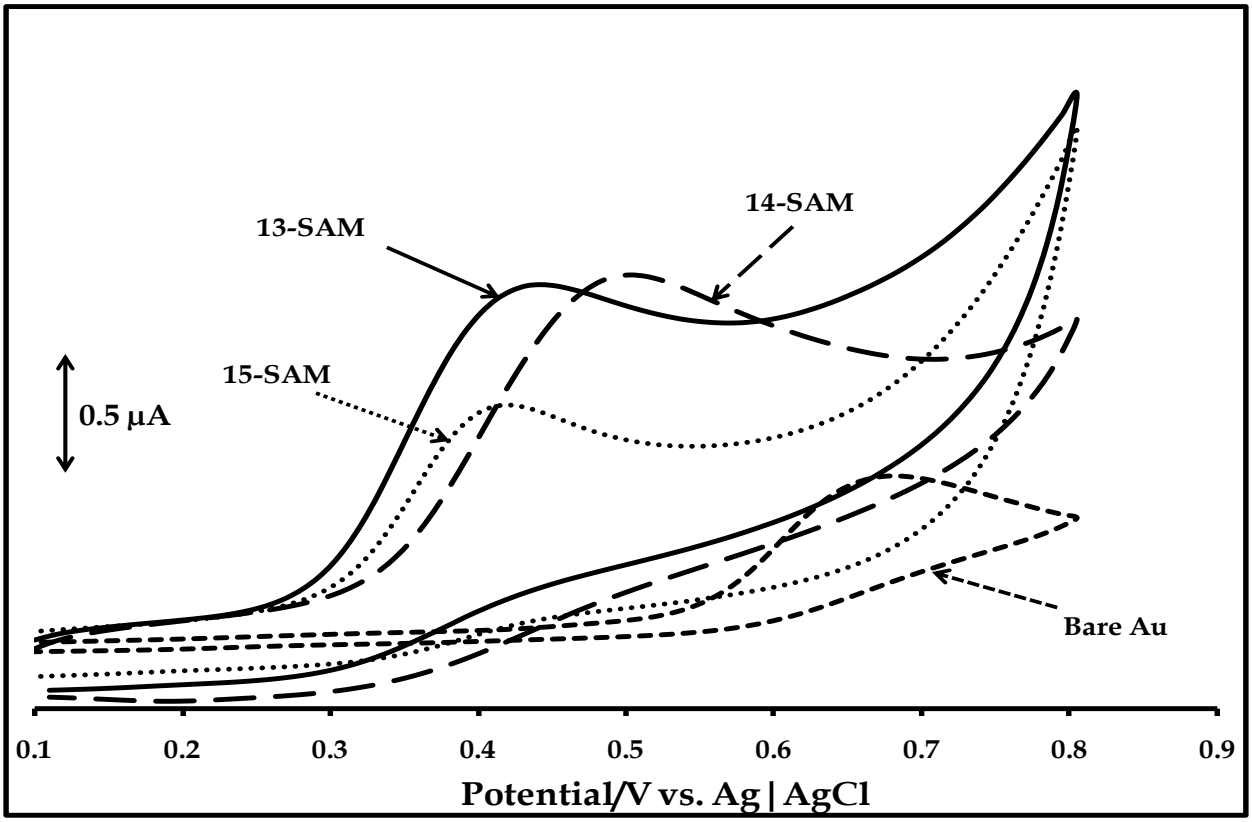

Figure 5.1: Voltammetry responses of 200 µM hydrolyzed solution of carbofuran, at pH 4, on bare and (**13**-**15**)-SAM-modified gold electrodes. Scan rate: 100 mVs^{-1}.

Metal-based processes of the adsorbed complexes (M^{III}/M^{II}), in pH 4 buffer alone, were observed at $E_{1/2}$ = +0.13, -0.21 V and +0.11 on **13**-SAM, **14**-SAM and **15**-SAM-modified gold electrodes, respectively (Tables 4.4 and 5.1), suggesting the involvement of these processes in electrocatalysis of the insecticide. This is discussed shortly.

Fig. 5.2 shows the responses of the insecticide on (**22**-**24**)-SAM-modified gold electrodes. Electrocatalysis of the oxidation of carbofuran is evident in Fig. 5.2, better voltammetry responses of the insecticide were recorded on these SAMs (0.51 V, 1.22 µA on **22**-SAM), (0.44 V, 1.81 µA on **23**-SAM) and (0.37 V, 1.40 µA on **24**-SAM) (Table 5.1), relative to that

Table 5.1: Summary of electrochemical data for the oxidation of carbofuran on SAM-modified Au electrodes. E_p in Volts versus Ag|AgCl, pH 4.

Electrode	E_p (V)	I_p (µA)	M^{III}/M^{II}
Bare Au	+0.67	0.74	
13-SAM	+0.42	1.62	+0.05
14-SAM	+0.48	1.88	-0.21
15-SAM	+0.40	1.12	+0.12
22-SAM	+0.51	1.22	+0.17
23-SAM	+0.44	1.81	+0.02
24-SAM	+0.37	1.40	+0.16
18-SAM	+0.53	0.95	+0.22
SWCNT-**18-**SAM	+0.44	2.07	+0.18

observed on bare gold electrode. Like the SAMs of complexes **13-15**, oxidation potentials of carbofuran on (**22-24**)-SAMs suggest the involvement of metal-based redox processes of the adsorbed complexes, Table 5.1, in catalysis, since the catalytic peaks of carbofuran are in the stability range of the M^{III}/M^{II} couples. In Fig. 5.2, the highest current response was observed on **23**-SAM-modified gold electrode, while the oxidation of the insecticide was most energetically feasible on **24**-SAM-modified gold electrode, Table 5.1. It is important to mention that, in both Figs. 5.1 and 5.2, the highest current signal of carbofuran was observed on the SAM of MnPc complex, in each case (complexes **14** and **23)** (Table 5.1). This suggests that, in terms of current response, MnPc complexes, rather than their Co or Fe derivatives, may be desirable, as electrocatalysts for this insecticide. However, the current signal on **14**-SAM (1.88 µA) is marginally better than that on **23**-SAM (1.81 µA) modified gold electrodes, justifying the difference in nature of substituent {diethylaminoethanethio (**14**) versus benzylthio (**23**)}. The marginal difference in current response may be attributed to relatively better

coverage of the gold surface by **14**-SAM (Γ_{ibf} of 0.83, Table 4.1), compared to **23**-SAM (Γ_{ibf} of 0.76, Table 4.1).

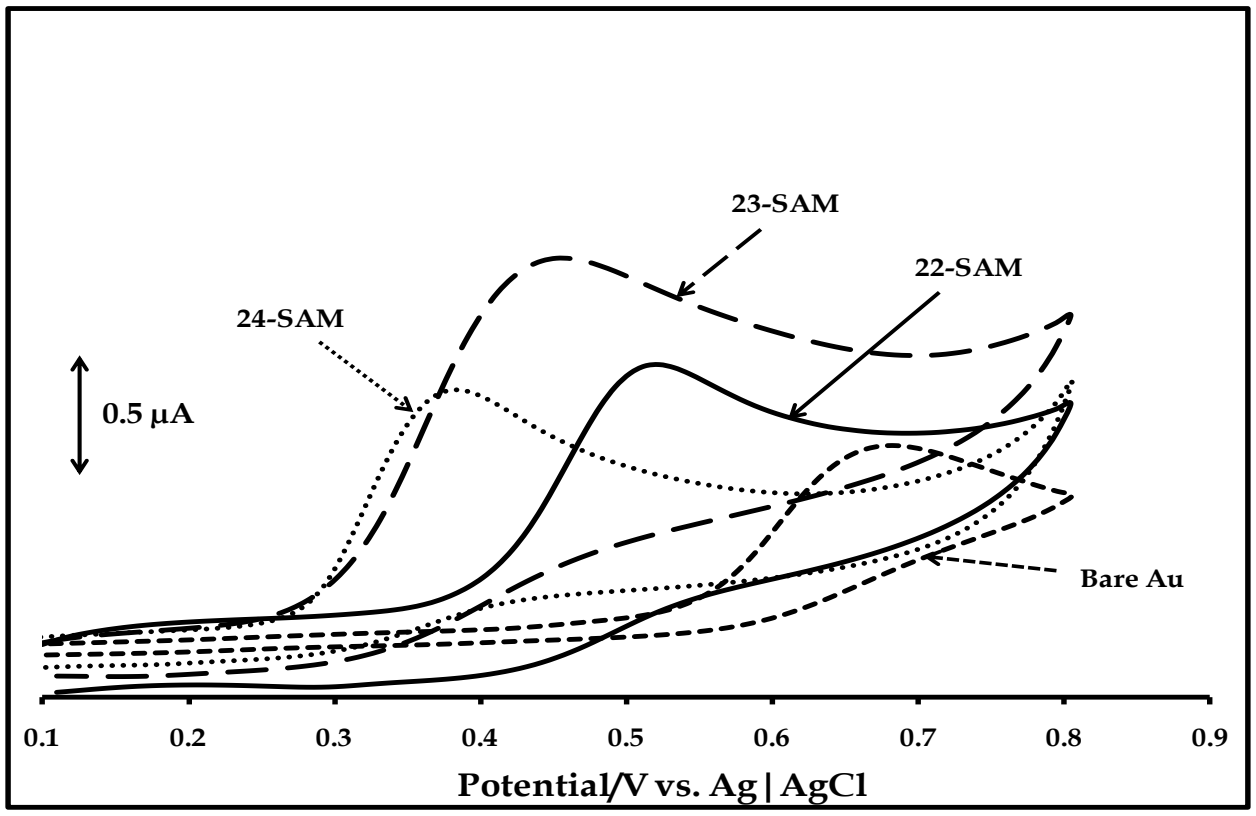

Figure 5.2: Voltammetry responses of 200 µM hydrolyzed solution of carbofuran, at pH 4, on bare and (**22**-**24**)-SAM-modified gold electrodes. Scan rate: 100 mVs^{-1}.

Electrocatalysis of carbofuran on the SAMs of the FePc complexes (**15** and **24**) (Fig. 5.1 and 5.2) was evaluated, within the context of the oxidation potential of the insecticide. Oxidation of carbofuran was more energetically feasible on each of these SAMs (0.40 V and 0.37 V on **15**- and **24**-SAMs, respectively), compared to the SAM of the corresponding Co or MnPc complex (Table 5.1). This was the motivation for the use of FePc complex in the fabrication of the nano-composite (SWCNT-**18**) discussed previously, in a bid to enhance the voltammetry response of the insecticide. In terms of the most favourable oxidation potential of the insecticide, complex **24** was the best of all the catalysts studied, but the molecular nature of its substituent (absence of the required functionality, necessary for integrating MPc with SWCNTs) was a limitation in the

quest to fabricating a SWCNT-FePc nano-composite. However, the choice of complex **18** (peripherally diethylaminoethanethio-substituted FePc, Scheme 3.2), over complex **15** (the non-peripheral derivative of complex **18**), was informed by the consideration for the effect of steric hindrance on successful integration of SWCNT with the desired FePc complex. Electrocatalytic oxidation of carbofuran was investigated on the SAM of the resulting nano-composite (SWCNT-**18**-SAM-modified gold electrode). Voltammetry signal of carbofuran was also recorded on **18**-SAM-modified gold electrode, in order to evaluate the contribution of the SWCNT unit to the electrocatalytic influence of the nano-composite.

Fig. 5.3 shows the cyclic voltammetry responses of carbofuran (200 μM) on **18**-SAM and SWCNT-**18**-SAM-modified gold electrodes. The current response of carbofuran on SWCNT-**18**-SAM-modified gold electrode (2.07 μA, 0.44 V) is better than the best (0.48 V, 1.88 μA on **14**-SAM-modified gold electrode, Table 5.1) on the MPc-SAM-modified gold electrodes. This can be attributed to high electrical conductivity of SWCNT in the SWCNT-**18**-SAM. This suggests that enhanced electrocatalytic surface can be created for this insecticide, by integrating the electrocatalytic properties of appropriate MPc complex with the outstanding electronic properties of SWCNT. The response of the insecticide on **18**-SAM-modified gold electrode (0.95 μA, 0.53 V) is better than that on bare gold electrode (0.74 μA, 0.67 V) (Table 5.1), but with SWCNT, there is a huge improvement, as highlighted above. Oxidation potential of carbofuran on SWCNT-**18**-SAM or **18**-SAM-modified gold electrode (+0.44 V versus Ag|AgCl) suggests the involvement of Fe^{III}/Fe^{II} redox couple in catalysis. This process is observed on SWCNT-**18**-SAM-modified gold electrode in pH 4 buffer solution ($E_{1/2}$ = +0.18 V versus Ag|AgCl) (Tables 4.4 and 5.1).

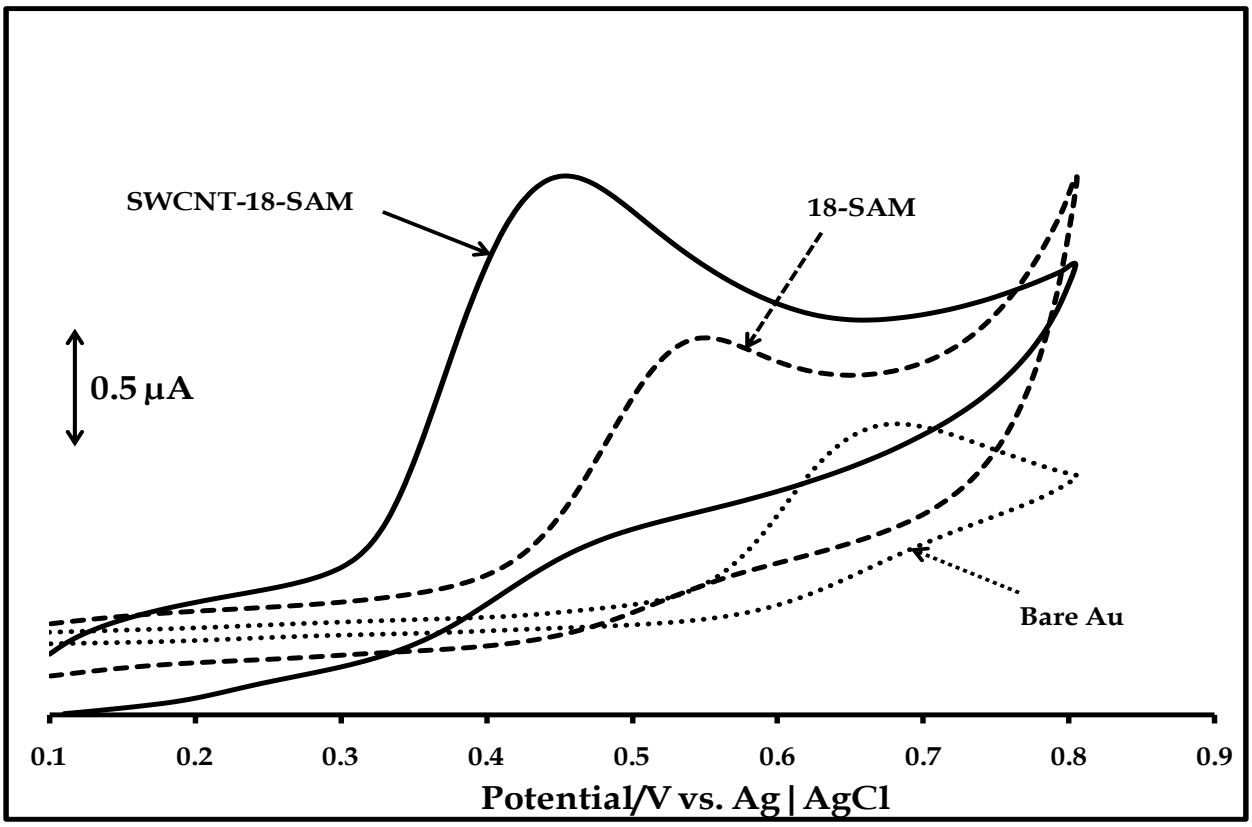

Figure 5.3: Voltammetry responses of 200 µM hydrolyzed solution of carbofuran, at pH 4, on bare, **18**-SAM and SWCNT-**18**-SAM-modified gold electrodes. Scan rate: 100 mVs^{-1}.

5.1.2 Mechanism and kinetics of electrocatalysis

The mechanism of electrocatalytic oxidation of carbofuran was elucidated using rotating disc electrode (RDE) voltammetry. Mechanistic parameters (Tafel slope and electron transfer coefficient) were estimated from Tafel plots, derived from relevant RDE voltammograms. A Tafel plot is a plot of overpotential, η, versus log I_k. I_k is the kinetic current corrected for mass transport $\{I_k = (I \times I_L)/(I_L - I)\}$, while overpotential, η, is the difference between the applied potential, E, and the equilibrium potential, E^o). I is the current taken from the foot of the relevant RDE voltammetric wave, while I_L is the limiting current. However, the value of E^o can not be reliably determined on a RDE voltammogram, hence, η is taken as potential in this case. I_k is linearly related to overpotential by the Tafel equation (equation 5.1).

$\eta = a + b \log I_k$ 5.1

where a is the Tafel constant, relating the exchange current density (I_o) and b is the Tafel slope [248] (equation 5.2).

$b = 2.3RT/\alpha n_a F$ 5.2

where n_a is the number of electrons involved in the rate-determining step and α is the electron transfer coefficient, also known as the symmetry factor.

Fig. 5.4A shows the rotating disc electrode voltammograms for the oxidation of 200 µM hydrolyzed solution of carbofuran (pH 4) on **13**-**15**-SAM (at 1600 rotations per minute).

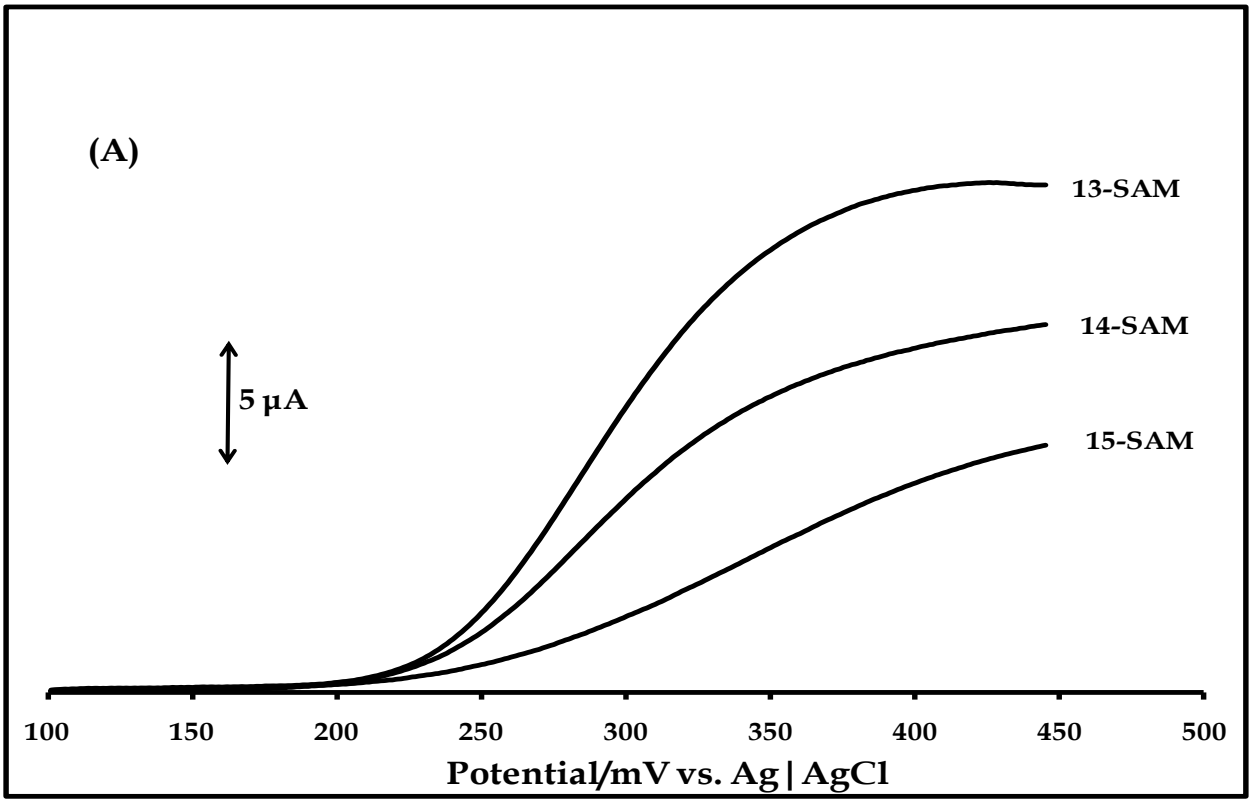

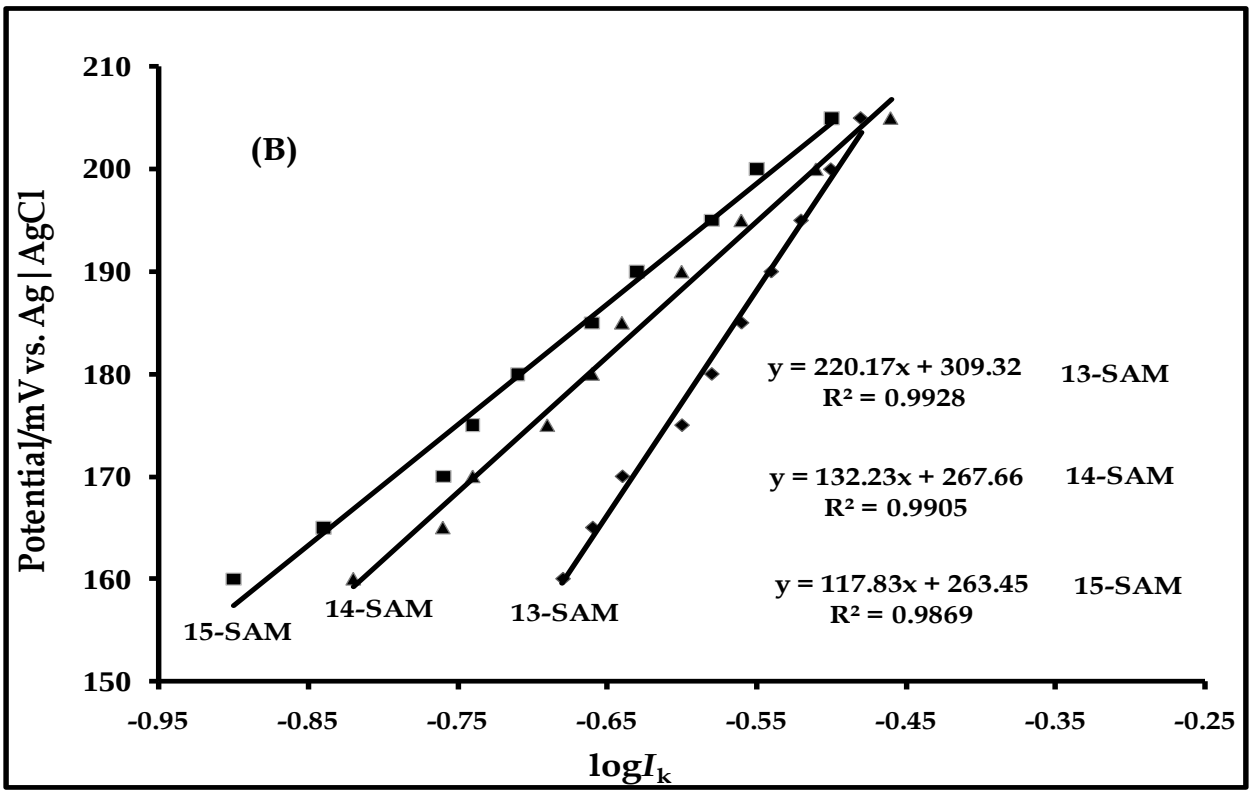

Figure 5.4: (A) RDE voltammograms (at 1600 rpm) for the oxidation of 200 µM solution of carbofuran (pH 4) on (**13-15)**-SAM-modified gold electrodes, scan rate: 20 mVs^{-1}. (B) Tafel plots derived from the RDE voltammograms in (A).

Table 5.2: Mechanistic data for the oxidation of carbofuran (pH 4) on SAM-modified gold electrodes.

Electrode	Tafel slope/ $mVdecade^{-1}$	α
13-SAM	220	0.27
14-SAM	132	0.45
15-SAM	117	0.50
22-SAM	108	0.55
23-SAM	64	0.90
24-SAM	99	0.60
SWCNT-**18**-SAM	70	0.84

The Tafel plots obtained from these voltammograms are shown in Fig. 5.4B. Tafel slopes of 220, 132 and 117 mV/decade (Table 5.2) were obtained for the oxidation of carbofuran on **13**-SAM, **14**-SAM and **15**-SAM-modified gold electrodes, respectively. The corresponding values of α were 0.27, 0.45 and 0.50 (Table 5.2).

The RDE voltammogram (at 1000 rotations per minute) in Fig. 5.5A was obtained for the oxidation of 200 μM hydrolyzed solution of carbofuran on SWCNT-**18**-SAM-modified gold electrode, while Fig. 5.5B is the corresponding Tafel plot. A Tafel slope of 70 mV/decade, with α value of 0.84 (Table 5.2), was obtained for the oxidation of carbofuran on this electrode.

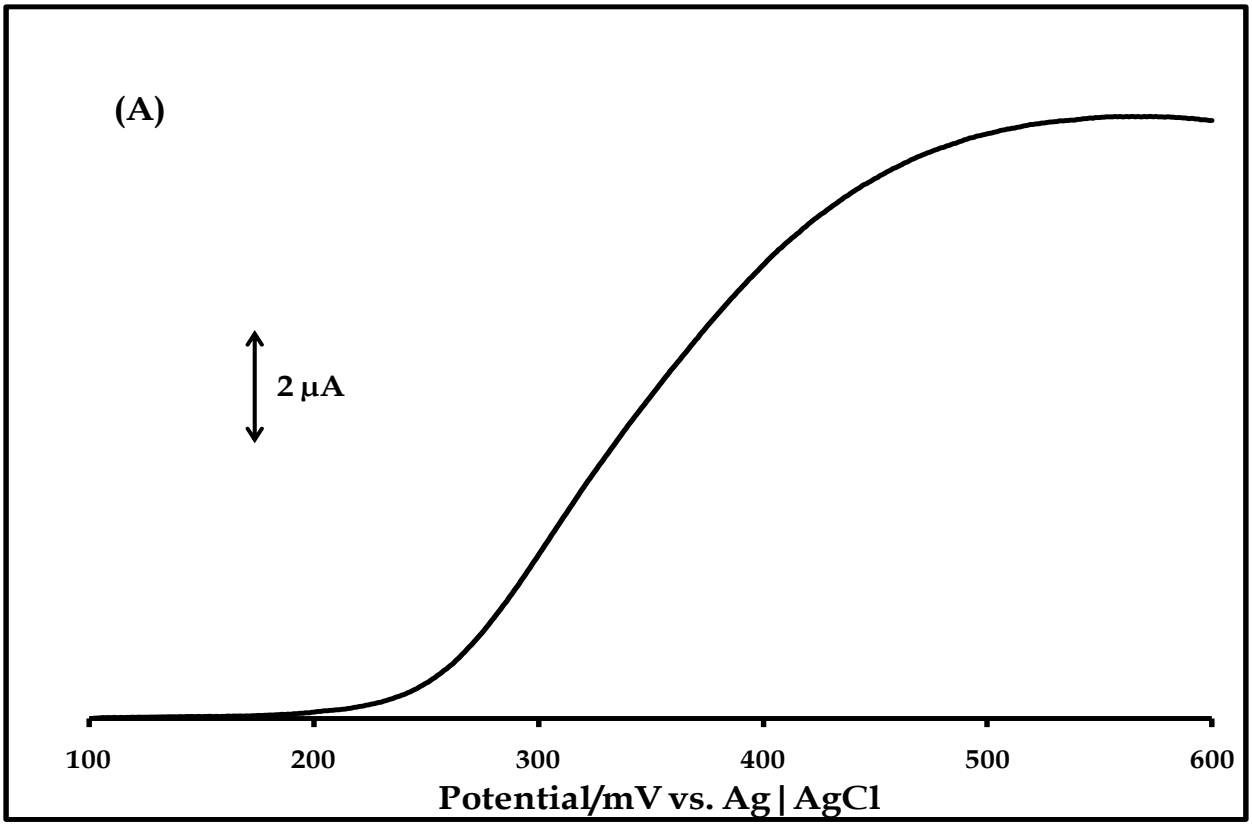

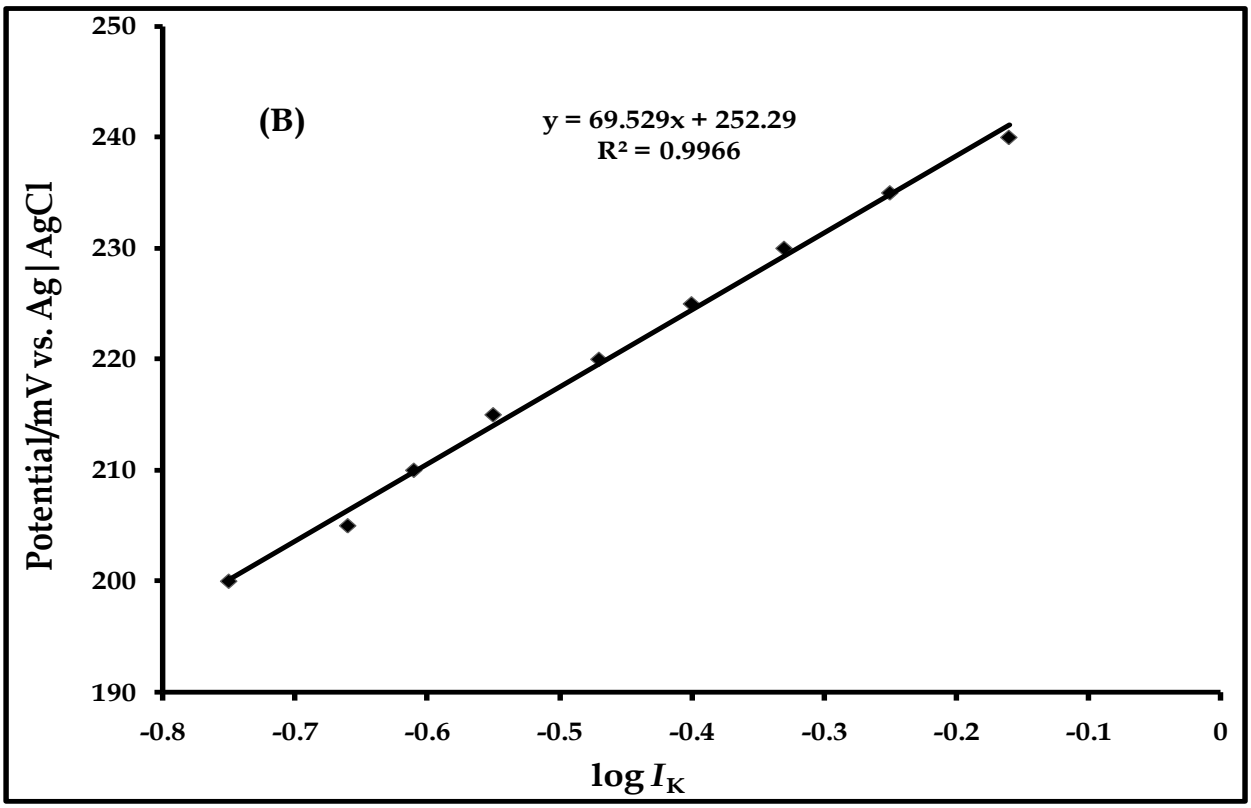

Figure 5.5: (A) RDE voltammograms (at 1000 rpm) for the oxidation of 200 µM solution of carbofuran (pH 4) on SWCNT-**18**-SAM-modified gold electrodes. Scan rate: 20 mVs^{-1}. (B) Tafel plot derived from the RDE voltammogram in (A).

Fig. 5.6 A and B are, respectively, the RDE voltammograms and the Tafel plots for the oxidation of 500 µM hydrolyzed solution of carbofuran on (**22**-**24**)-SAM-modified gold electrodes. Tafel slopes of, approximately, 108, 64 and 99 mV/decade (Table 5.2) were obtained for the oxidation of 500 µM hydrolyzed solution of carbofuran on **22**-, **23**- and **24**-SAM-modified gold electrodes, respectively, with corresponding α values of 0.55, 0.90 and 0.60.

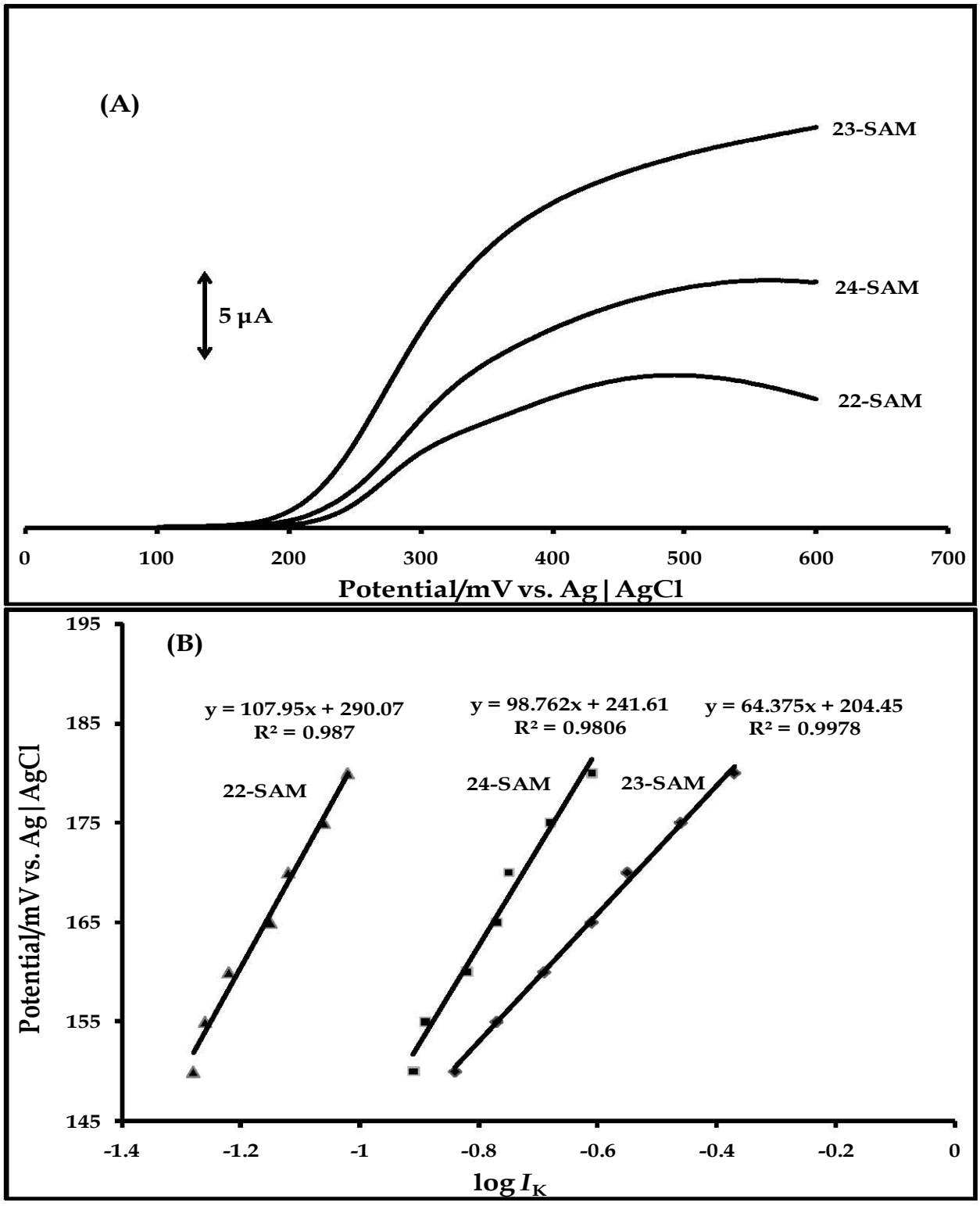

Figure 5.6: (A) RDE voltammograms (at 300 rpm) for the oxidation of 500 µM solution of carbofuran (pH 4) on (**22-24**)-SAM-modified gold electrodes. Scan rate: 20 mVs^{-1}. (B) Tafel plot derived from the RDE voltammogram in (A).

The value of α is closely related to the geometry of the intersection region of the free energy curves of reactant and product in a redox reaction [248]. In the absence of actual measurements, α is usually approximated as 0.5, but in most systems, its value lies between 0.3 and 0.7 [248]. In this work, the values of α obtained for the oxidation of carbofuran on the SAM-modified gold electrodes (Table 5.2) are substantially consistent with this range.

Tafel slope is diagnostic of the mechanism of catalysis. A value less than or equal to 120 mVdecade^{-1} suggests absence of analyte-catalyst interaction, while a Tafel slope higher than 120 mVdecade^{-1} is indicative of the presence of an analyte-catalyst intermediate. Specifically, a Tafel slope close to 118 mV/decade indicates that the transfer of the first one electron is rate determining, while a value close to 59 mV/decade suggests that a fast first electron transfer is followed by a slow chemical step [249]. Tafel slopes obtained for the oxidation of carbofuran on **15**-SAM, SWCNT-**18**-SAM and (**22**-**24**)-SAM-modified gold electrodes are within the range 60-120 mV/decade (Table 5.2). Importantly, oxidation potentials of carbofuran on the SAM-modified gold electrodes (Table 5.2) are within the stability range of metal-based redox processes of the adsorbed complexes ($M^{III/II}$) (Tables 4.4 and 5.1), thus the involvement of these redox processes in catalysis. The mechanism below (equations 5.3 and 5.4) is suggested for the oxidation of carbofuran on these electrodes.

$$M^{II}Pc \longrightarrow M^{III}Pc + e^- \qquad 5.3$$

$$M^{III}Pc + \mathbf{R}O^- \longrightarrow M^{II}Pc + \mathbf{R}O\cdot \qquad 5.4$$

Oxidation of carbofuran on SWCNT-**18**-SAM-modified gold electrode is expected to follow the mechanism hypothesized for electron transport within this SAM (Scheme 4.1). This implies the mediatory role of the surface-bound Fe^{III}/Fe^{II} redox couple (equation 5.4 in the suggested mechanism) in the oxidation of carbofuran, on SWCNT-**18**-SAM modified gold electrode, will be preceded by tunneling of electrons through the SWCNT unit of the SAM (step 1 in Scheme 4.1).

Tafel slopes obtained for the oxidation of carbofuran on **13**- and **14**-SAM-modified gold electrodes are higher than 120 mV/decade, suggesting the involvement of analyte-catalyst intermediate in the oxidation of carbofuran on these SAMs. High Tafel slopes have been reported for the electrocatalytic oxidation and trace detection of amitrole using a Nafion/lead-ruthenium oxide pyrochlore chemically modified electrode (239mV/decade) [250]. Also, oxidation of glucose in alkaline solution, on a RuO_2-carbon paste composite electrode [251], and oxidation of β-cyanoethyl ether on a platinum electrode, in a solution of sulphuric acid [252], have been reported with high values of Tafel slope (~240 mV/decade). This observation was interpreted in terms of strong substrate-catalyst interaction, resulting in the formation of substrate-catalyst-intermediate. A strong analyte-catalyst interaction is thus envisaged on **13**-SAM-modified gold electrode, but weak interactions on **14**-SAM-modified gold electrode, the latter with a smaller Tafel slope. Inner sphere mechanism is thus proposed (equations 5.5 – 5.7) for the electrocatalysis of carbofuran on **13**-SAM-modified electrode (representative of that on **14**-SAM). The Co^{III}/Co^{II} species, observed on **13**-SAM-modified gold electrode, in pH 4 buffer solution ($E_{1/2}$ = +0.05 V versus Ag|AgCl, Tables 4.4 and 5.1), is implicated in catalysis.

$$Co^{II}Pc \longrightarrow Co^{III}Pc + e^- \qquad 5.5$$

$$Co^{III}Pc + \mathbf{R}O^- \longrightarrow [Co^{III}Pc\text{-}\mathbf{R}O]^{2+} \qquad 5.6$$

$$[Co^{III}Pc\text{-}\mathbf{R}O]^{2+} \longrightarrow Co^{II}Pc + \mathbf{R}O^{\cdot} \qquad 5.7$$

The standard heterogeneous rate constant, k_o, for the oxidation of carbofuran was also evaluated on **23**-SAM-modified gold electrode (one the SAMs of the MnPc complexes with the highest current response of carbofuran, Table 5.1). Fig. 5.7A shows the RDE voltammograms obtained for the oxidation of 500 µM hydrolyzed solution of carbofuran on **23**-SAM-modified gold electrode, at different rotation speeds (200-500 rpm). Inset is the plot of mass transport limiting current (I_L) (obtained at 0.6 V versus Ag|AgCl) versus square root of rotation speed ($\omega^{1/2}$) in rad s^{-1}. I_L is linearly related to

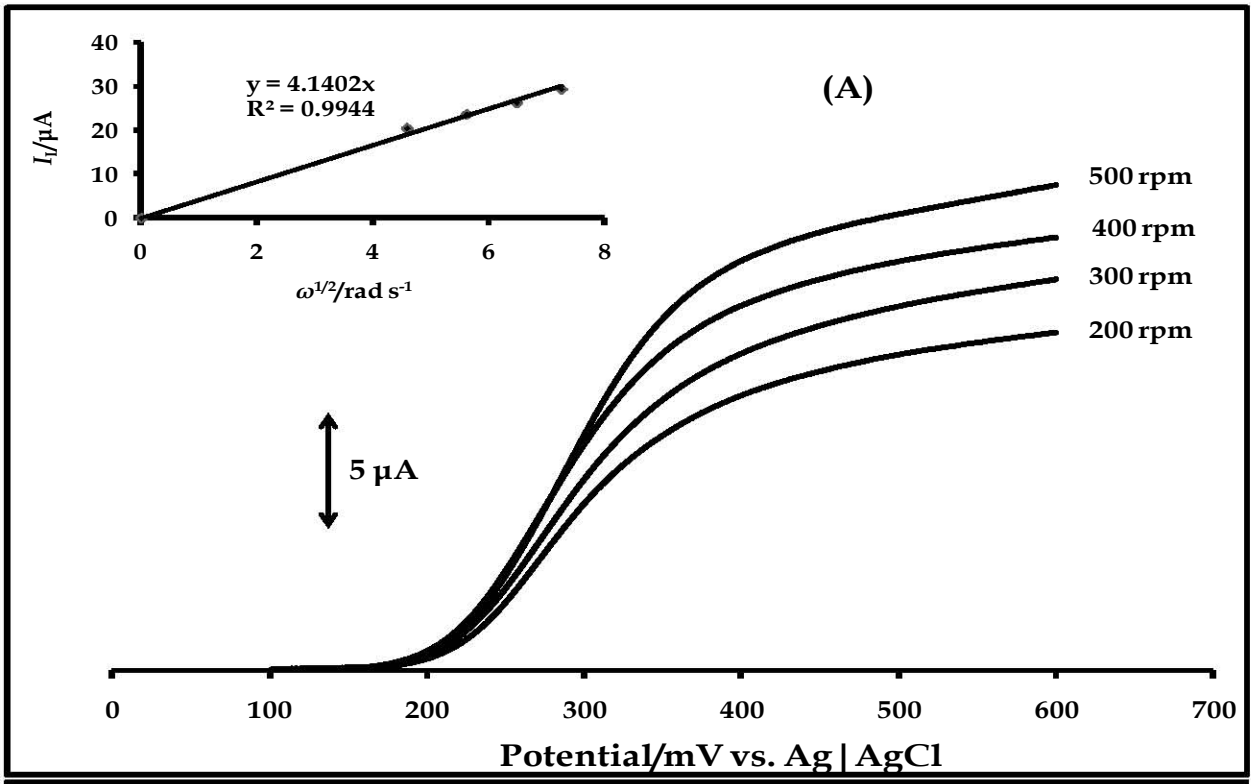
(A)
y = 4.1402x
R² = 0.9944
I_l/µA
$\omega^{1/2}$/rad s^{-1}
500 rpm
400 rpm
300 rpm
200 rpm
5 µA
Potential/mV vs. Ag | AgCl

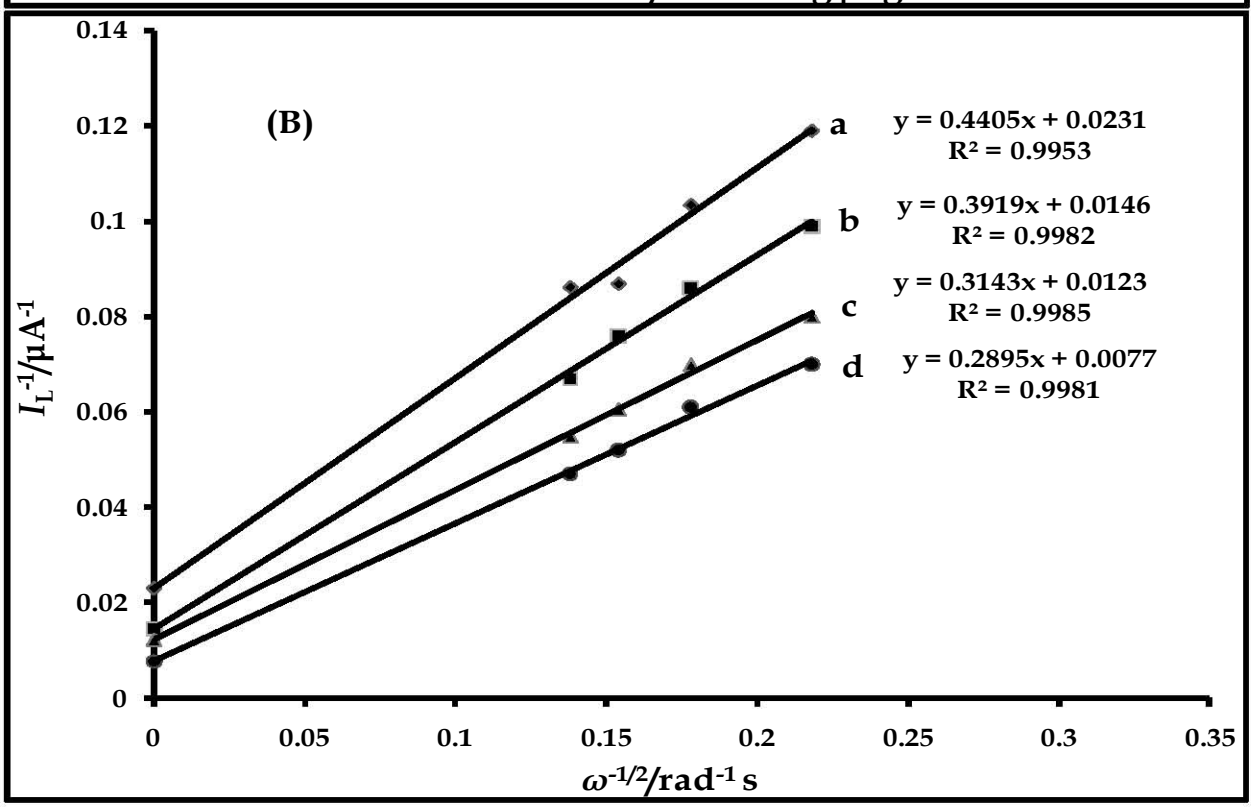
(B)
a
y = 0.4405x + 0.0231
R² = 0.9953
b
y = 0.3919x + 0.0146
R² = 0.9982
c
y = 0.3143x + 0.0123
R² = 0.9985
d
y = 0.2895x + 0.0077
R² = 0.9981
I_L^{-1}/µA^{-1}
$\omega^{-1/2}$/rad^{-1} s

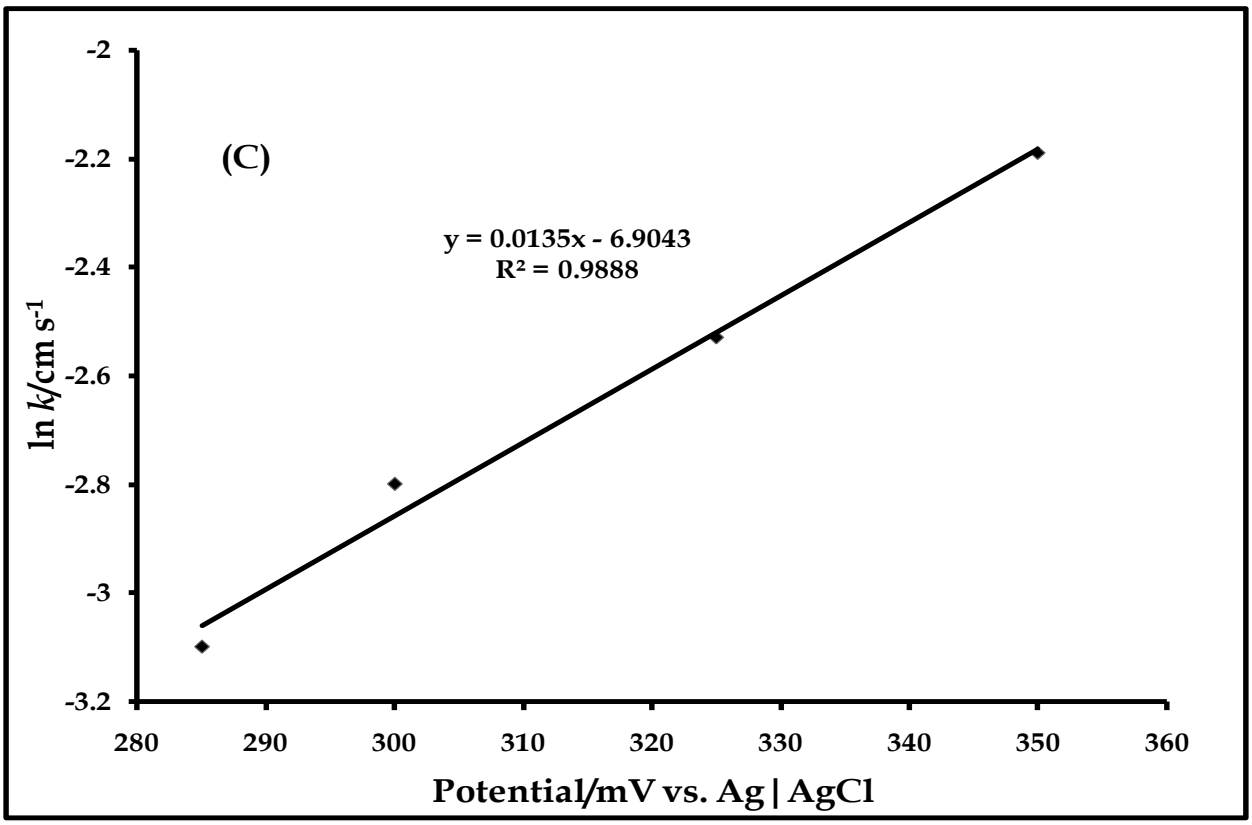

Figure 5.7: (A) RDE voltammograms for the oxidation of 500 µM hydrolyzed solution of carbofuran (200-500 rpm) on **23**-SAM (inset: Levich plot), (B) Koutecky-Levich plots for the oxidation of carbofuran at different potential: (a) 285, (b) 300, (c) 325 and (d) 350 mV versus Ag | AgCl and (C) Plot of ln *k* versus potential.

$\omega^{1/2}$, with zero intercept, suggesting diffusion-controlled mass transport, predicated by the Levich equation (equation 5.8) [152].

$$I_L = 0.62nFAD^{2/3}\upsilon^{-1/6}\omega^{1/2}C \qquad 5.8$$

$$\frac{1}{I} = \frac{1}{I_K} + \frac{1}{I_L} \qquad 5.9$$

where n is the number of electrons transferred during the oxidation of carbofuran, which is 1, while A (0.021 cm^2) is the real surface area calculated previously. C, υ and D are the concentration (5.0 × 10^{-4} M or 5 × 10^{-7} mol cm^{-3}), kinematic viscosity and diffusion coefficient (in cm^2 s^{-1}) of carbofuran, respectively. The measured current (I) is defined by the Koutecky-Levich equation (equation 5.9) [153], which takes into account the

mixed diffusion-kinetic regimes at intermediate potentials (first term) and mass transport limiting currents at high overpotentials (second term). The first term in equation 5.9 denotes the kinetic current (I_k), which is the current in the absence of mass transport effect (equation 5.10)

$$I_k = nFAkC \qquad 5.10$$

Equation 5.9 predicts a linear dependence of $1/I$ on $\omega^{-1/2}$, with $1/I_k$ as intercept. Fig. 5.7B shows the plots of $1/I$ versus $\omega^{-1/2}$ for the oxidation of carbofuran on **23**-SAM-modified gold electrode, at different rotation rates (200-500), for each potential, (285, 300, 325 and 350 mV) (a-d). Value of I_k, for each potential, was evaluated from the intercept ($1/I_k$) of the corresponding plot of $1/I$ versus $\omega^{-1/2}$, and the heterogeneous rate constant, k, calculated, using equation 5.10. An increase in the value of k, with increase in potential, was observed. Using the Botler-Volmer expression for k (equation 5.11) [248], the standard heterogeneous rate constant, k_o, was evaluated.

$$\ln k = \ln k_o + \frac{nF(-\alpha)}{RT}\eta \qquad 5.11$$

A plot of ln k versus η (potential in this case) is linear (Fig. 5.7C), with ln k_o as intercept (-6.90). The value of k_o (1.01×10^{-3} cm s^{-1}) was obtained from ln k_o. This value is fairly high, justifying the high current response of carbofuran on this electrode (**23**-SAM-modified gold electrode).

5.1.3 Sensitivity and selectivity studies

Sensitivity and selectivity studies were carried out with the most sensitive of the SAMs studied (SWCNT-**18**-SAM, Table 5.1). Sensitivity of the SWCNT-**18-**SAM-modified gold electrode towards carbofuran was investigated using different concentrations of the analyte (50-500 µM). Current response of carbofuran is linearly related to concentration (Fig. 5.8) within the range studied. The regression equation of the linear plot is shown in equation 5.12, with $R^2 = 0.9996$

$$I_p = 0.011[\text{carbofuran}] \pm 0.003 \qquad 5.12$$

The sensitivity of the electrode was 0.011 µA/µM (0.52 A mol^{-1} L cm^{-2}) (slope of the plot/area of the electrode), with detection limit of 0.82 µM (8.2 × 10^{-7} mol/L), determined using 3δ criterion [253] (where δ is the standard deviation of the blank). This value is close to that (5.0 × 10^{-8} mol/L) reported [200] for detection of carbofuran at a disposable heated screen-printed carbon electrode, using differential pulse voltammetry (DPV). The lower value of detection limit associated with the latter can be atributed to the more sensitive nature of DPV, relative to cyclic voltammetry.

The mixed solution method [254], using diazinon, chlorpyrifos and dichlorvos as interferents, was used to investigate the selectivity of the electrode for carbofuran. These interferents are organophosphate pesticides, normally employed for the same purpose as carbofuran, thus the possibility of their presence in the same environmental samples as carbofuran. Interestingly, mechanism of their pesticidal actions and toxicities are closely related to that of carbofuran (inhibition of cholinestarase activity).

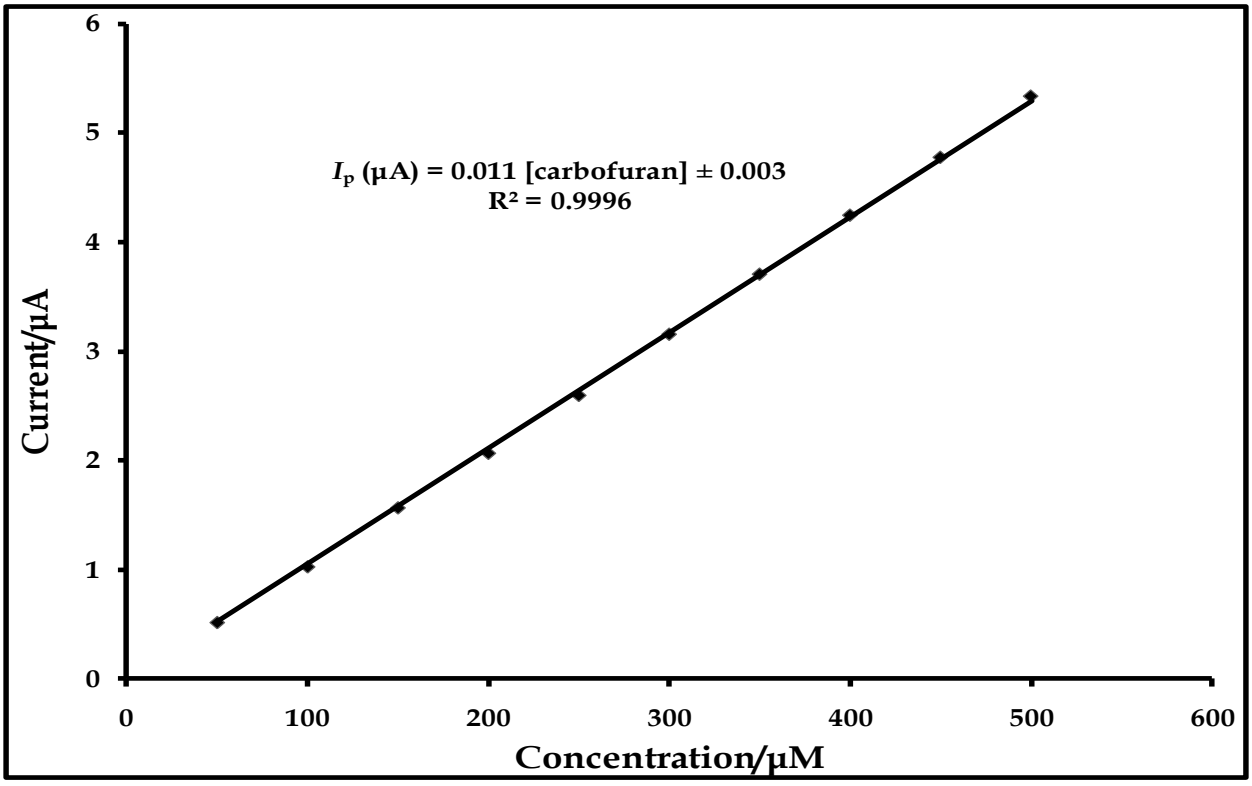

Figure 5.8: Calibration curve of carbofuran on SWCNT-**18**-SAM modified gold electrode

The concentration of carbofuran (200 µM) was kept constant, while that of each interferent varied (100-300 µM). Values of amperometric selectivity coefficients (K_{amp}) (Table 5.3), a measure of the degree of interference, were determined, using equation 5.13.

$$K_{amp} = \left(\frac{I_{mixture}}{I_{carbofuran}} - 1\right)\frac{[carbofuran]}{[interferent]} \qquad 5.13$$

where $I_{mixture}$ and $I_{carbofuran}$ are the background corrected current responses of carbofuran in the presence and absence of interferent, respectively. K_{amp} value in order of magnitude higher than 10^{-3} denotes strong interference, while value close to 10^{-3} indicates weak interference. A value less than 10^{-3} suggests no interference. Table 5.3 shows the values of K_{amp}, obtained for different concentrations of interferents.

Table 5.3: Values of amperometric coefficient for SWCNT-**18**-SAM-modified gold electrode with respect to 200 µM carbofuran

Interferent	Diazinon			Chlorpyrifos			Dichlorvos		
Concentration (µM)	100	200	300	100	200	300	100	200	300
K_{amp} ($\times 10^{-2}$)	0.048	0.097	0.12	0.11	0.19	18	0.11	7.4	8.6

At concentration less than or equal to that of carbofuran, diazinon did not interfere with the response of the electrode, while the selectivity of the electrode for carbofuran was weakly affected by the presence of chlorpyrifos, within this concentration range. At higher concentration than that of carbofuran, diazinon showed very weak interference, while chlorpyrifos interfered strongly. Dichlorvos interfered weakly with the selectivity of the electrode at concentration lower than that of carbofuran, but at higher or same concentration as carbofuran, the electrode lost its selectivity for carbofuran.

The difference in the degree of interference may be associated with the molecular features of the interferents. Dichlorvos and chlorpyrifos are halogenated organophosphate pesticides, thus may undergo electrochemical reduction at the carbon

atoms bearing the halogens. The carbon atom of the vinyl group, containing the two chloro groups, is the possible electroactive position in dichlorvos [255], while the carbon atoms, bearing the chloro groups, in the heterocyclic ring, are the likely electroactive points in chlorpyrifos. Diazinon does not posses the above structural features, thus the insignificant degree of interference observed in the presence of this insecticide. This suggests that the electrode is highly selective for carbofuran in the presence of electro-inactive interferent and at relatively low concentration of electroactive interferent.

5.1.4 Stability test

The stability of the SAM-modified gold electrodes was investigated by repetitive cycling of the electrodes in hydrolyzed solutions of carbofuran. Oxidation potential of the insecticide shifted to more positive values, with corresponding decrease in current signal on the bare and SAM-modified gold electrodes, during repeated cyclic voltammetry scans (10 cycles). This behavior is depicted in Fig. 5.9A, on **24**-SAM-modified gold electrode (the SAM with the least positive oxidation potential of carbofuran, Table 5.1) (representative of other SAMs) in 600 µM hydrolyzed solution of

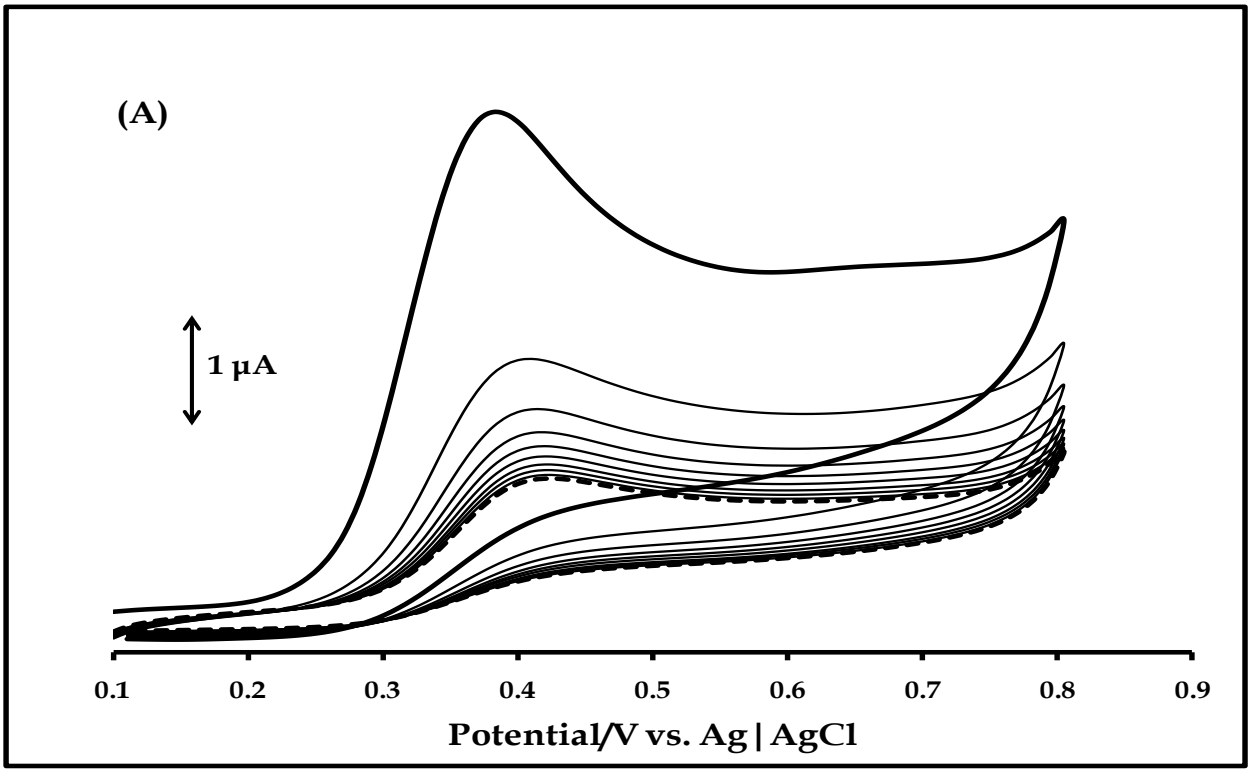

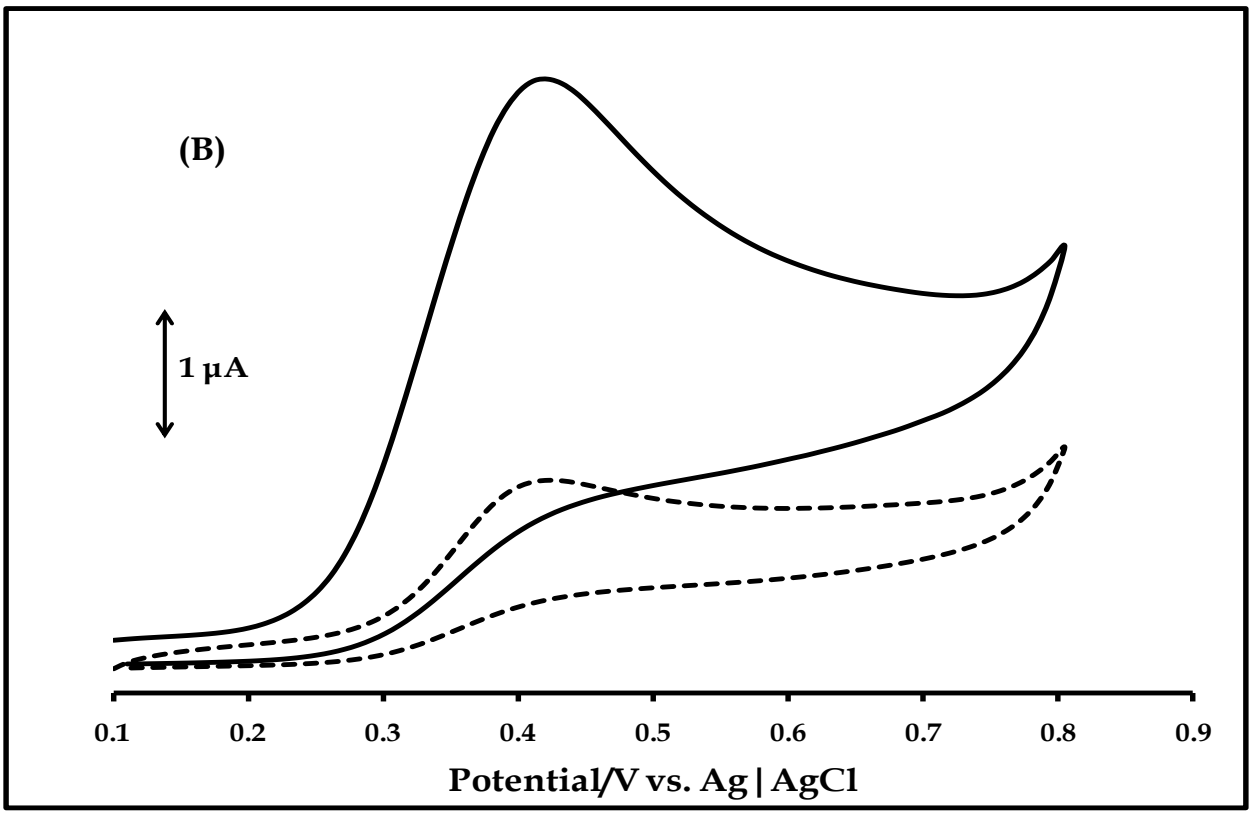

Figure 5.9: Cyclic voltammetry profiles obtained during (A) repetitive cycling (10 cycles) of **24**-SAM-modified gold electrode in 600 µM hydrolyzed solution of carbofuran (pH 4) (first scan = solid line, last scan = dashed line) and (B) after rinsing the electrode in excess acetone (solid line).

carbofuran (pH 4). In Fig. 5.9A, the oxidation potential of carbofuran shifts from +0.37 V (first scan = solid line) to +0.41 V versus Ag|AgCl (last scan = dashed line), with a corresponding decay in current response (from 4.33 to 1.03 µA) (76% decrease in current response). These observations can be attributed to passivation of the electrode, due to deposition of polyphenylene oxide (formed from the polymerization of the oxidation products of phenolic species). Interestingly, the severity of this occurrence was curtailed on the SAM-modified gold electrodes, relative to that on bare gold electrode. In Fig. 5.9B, 95% (4.11 µA) (solid line) of the original current signal (4.33 µA, Fig. 5.9A) of the insecticide was regenerated, at +0.41 V, on rinsing the electrode in excess acetone. This suggests that the SAM was significantly stable after voltammetry measurements, hence suitable for reproducible quantitative measurement of carbofuran. However,

regeneration of the voltammetry signal of the insecticide was associated with slight increase in oxidation potential (+0.37 to +0.41 V versus Ag|AgCl), as highlighted previously.

5.2 Bendiocarb

5.2.1 Catalysis of electro-oxidation

Like carbofuran, bendiocarb is also not electroactive, but its electroactive phenolic derivative (2,3-isopropylidenedioxyphenoxide) was formed on alkaline (0.5 M NaOH) hydrolysis (Scheme 5.2). Acetic acid was added to adjust the pH to 4 (the pH that gave the best voltammetry response of bendiocarb). Electrocatalysis of oxidation of this carbamate insecticide was studied on MnPc-modified glassy carbon electrodes (electrodep-**14**-GCE and poly-**17**-GCE).

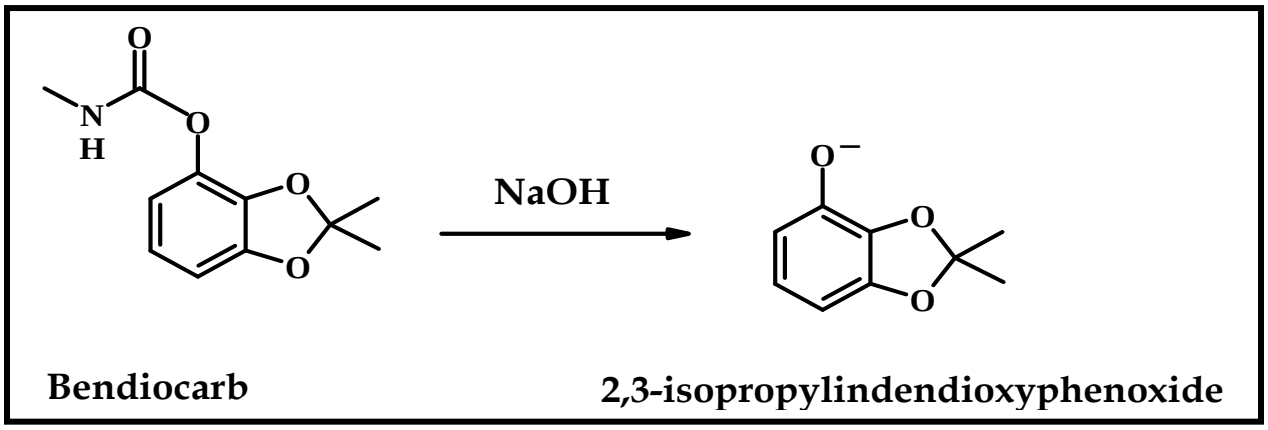

Scheme 5.2: Alkaline hydrolysis of bendiocarb

Fig. 5.10 shows the cyclic voltammograms of 100 μM hydrolyzed solution of bendiocarb (pH 4) on bare GCE, electrodep-**14**-GCE and poly-**17**-GCE. An irreversible oxidation peak was observed for bendiocarb on the bare (0.74 μA at 0.56 V vs. Ag|AgCl) and MnPc-film-modified GCEs. The best response, in terms of current signal and overpotential (1.64 μA at 0.44 V vs. Ag|AgCl), was observed on electrodep-**14**-GCE, while the signal on poly-**17**-GCE was 1.05 μA at 0.52 V vs. Ag|AgCl. Most importantly,

electrocatalysis of oxidation of bendiocarb on each of the modified electrodes is obvious, by virtue of less positive oxidation potential and better current response than that observed on the bare electrode. Two peaks are observed for the oxidation of bendiocarb on electrodep-**14**-GCE, but not clearly defined for poly-**17**-GCE. The second peak near 0.65 V is weaker for complex **17**; this could be attributed to MPc-based redox process (peak **IV** in Figs. 4.17A and B).

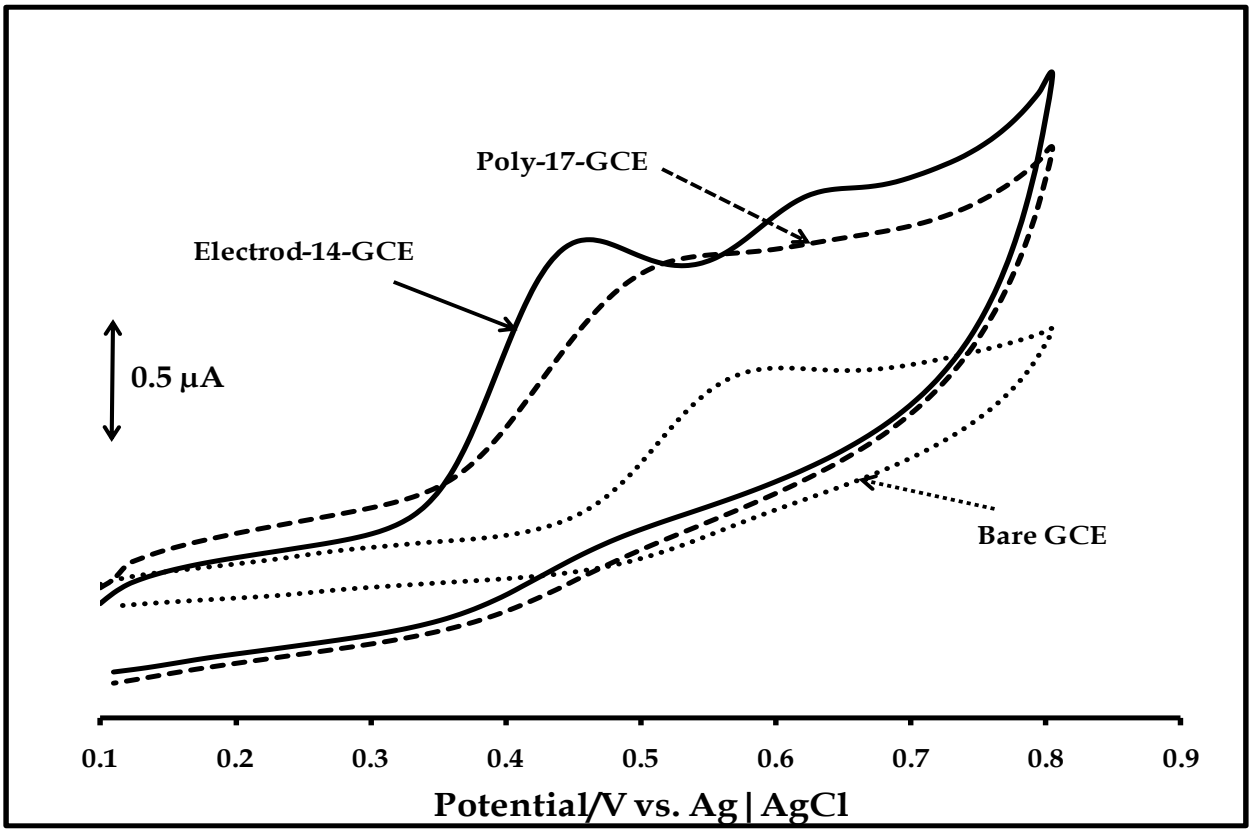

Figure 5.10: Cyclic voltammetry profiles of 100 µM hydrolyzed solution of bendiocarb (pH 4) on bare GCE, electrode-**14**-GCE and poly-**17**-GCE. Scan rate: 100 mVs^{-1}.

Responses of bendiocarb on the MnPc-film-modified GCEs may be related to the morphology of the films. AFM images in Fig. 4.19 show that non-peripheral (complex **14**) substitution gives rise to appreciably porous film. This may have impacted positively on diffusion of bendiocarb and percolation of charged species within the film, thus resulting in better current response on electrodeposited film of complex **14**.

Electrochemical impedance spectroscopy (EIS) was used to further interpret the responses of bendiocarb on the bare and MnPc-film-modified glassy carbon electrodes.

Fig. 5.11A shows the impedance spectra (Nyquist plots) obtained for the bare and MnPc-film-modified GCEs, at an applied potential of 0.50 V vs. Ag|AgCl, using 100 µM hydrolyzed solution of bendiocarb as redox probe. Each of the impedance spectra in Fig. 5.11A is like an arc, and not a complete semi-circle. Hence, the suitability of an equivalent circuit, with CPE (constant phase element) substituted for C_{dl} (Fig. 4.6B), for fitting the impedance data. The circuit parameters are as defined previously. Values obtained for various parameters are indicated in Table 5.4, with their estimated percentage errors. Values of charge transfer resistances are reflective of the nature of the films.

Table 5.4: Summary of EIS (at applied potential of 0.50 V vs. Ag|AgCl) and cyclic voltammetry data for the oxidation of bendiocarb on bare MnPc-modified GCE.

Electrode	R_S (KΩ)	R_{CT} (KΩ)	CPE (µF) (× 10^{-3})	Phase angle (°)	f (Hz)	n	E_p, V vs. Ag|AgCl[a]
Bare GCE	6.51 ± 0.22	288 ± 17	1.62 ± 0.07	62	5.01	0.65	0.56 (0.74 µA)
electrodep-**14**-GCE	7.39 ± 0.37	61 ± 5	4.42 ± 0.36	50	1.26	0.61	0.44 (1.64 µA)
poly-**17**-GCE	3.67 ± 0.13	158 ± 16	8.56 ± 0.50	49	2.51	0.67	0.52 (1.05 µA)

[a]Values in brackets are catalytic currents of the oxidation of bendiocarb

The highest charge transfer resistance (288 KΩ) was obtained on the bare electrode, justifying the lowest current response of bendiocarb (0.74 µA) on this electrode. Charge transfer resistances of bendiocarb on electrodep-**14**-GCE and poly-**17**-GCE films are 61 and 158 KΩ, respectively, indicative of the current responses of bendiocarb on these films (Table 5.4). Also, values of R_{CT} are closely related to the morphology of the films.

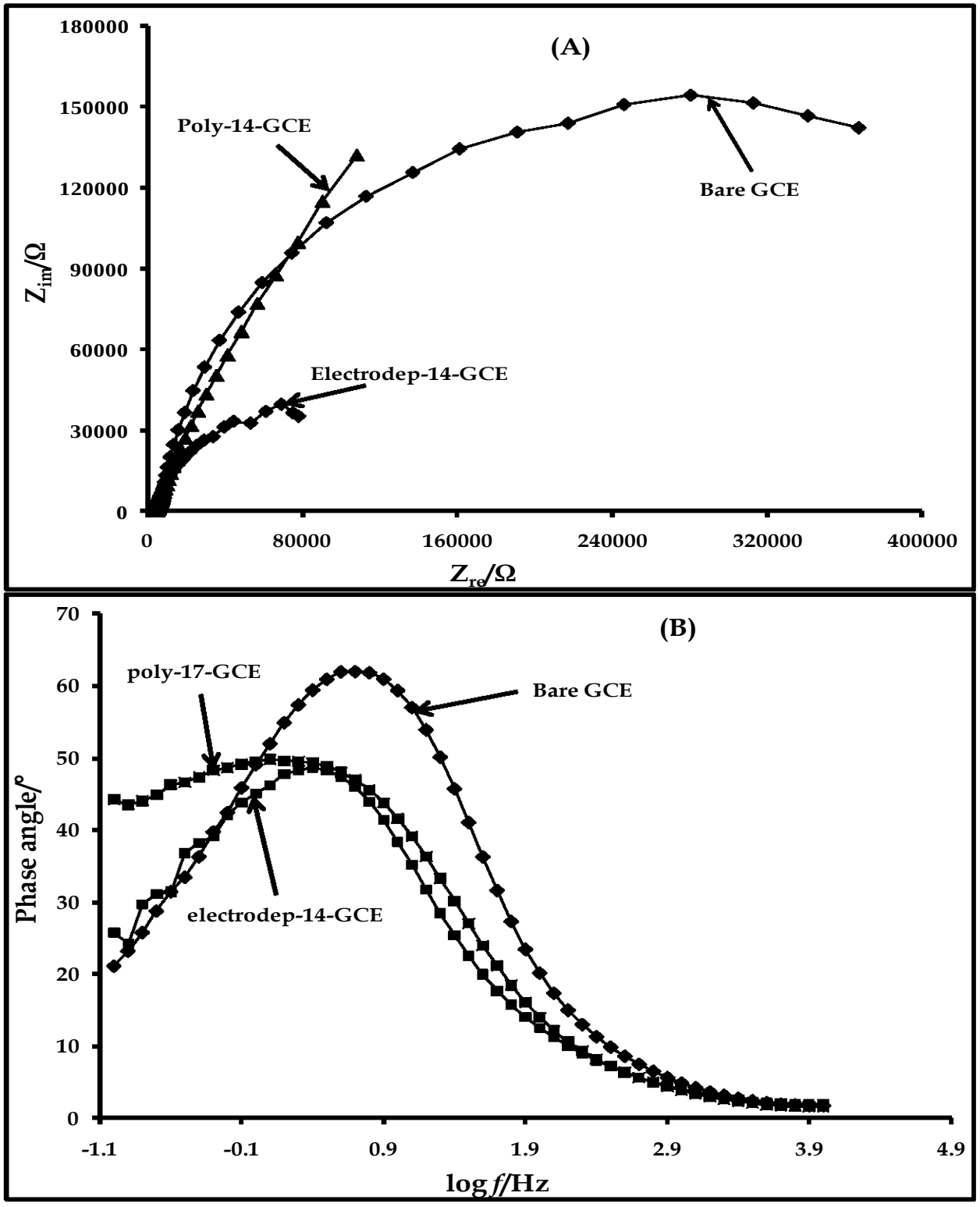

Figure 5.11: (A) Impedance spectra and (B) Bode plots (phase angle versus log *f*) of bare and MnPc-modified GCEs in 100 µM hydrolyzed solution of bendiocarb (pH 4). Applied potential = 0.50 V vs. Ag | AgCl.

The relatively porous film of complex **14**, Fig. 4.19C, may have positively influenced percolation of charged species within this film, facilitating a better charge transfer process that results in better response of bendiocarb than that observed on poly-**17**-GCE film. As expected, values of R_S are within narrow range (3.33 – 7.39 KΩ); no significant change is expected due to electrode modification. The values of CPE for the modified electrode are significantly greater than that for the bare electrode, due to the presence of the films. The value of 'n' for each of the films and the bare electrode is less than 1 (Table 5.4). This is in agreement with the non-ideal capacitive behavior of the bare and the MnPc-film-modified glassy carbon electrodes, as represented by the CPE in the equivalent circuit.

Table 5.4 also contains values obtained from the Bode plot (plot of phase angle versus log *f*) (Fig. 5.11B). The phase angle and frequency of a particular maximum are representative of the relaxation process of the electrode. The maximum on the bare electrode corresponds to a phase angle of 62° at a frequency of 5.01 Hz. The phase angles of the maxima on poly-**17**-GCE and electrodep-**14**-GCE are 49° and 50°, respectively, with corresponding frequencies of 2.51 and 1.26 Hz, respectively. The difference in phase angle and frequency of the maxima on the films, relative to the bare electrode, suggests that electro-oxidation of bendiocarb occurred, not on the bare electrode, but on the films.

5.2.2 Kinetics of electro-oxidation

Kinetics of electro-oxidation of bendiocarb on the films was investigated by hydrodynamic techniques, using rotating disc electrode (RDE) voltammetry. Figs. 5.12A and B show the RDE voltammograms for the electro-oxidation of bendiocarb (200 μM) on electrodep-**14**-GCE and poly-**17**-GCE films, respectively, at different rotation rates (250 – 1250 rpm). The voltammograms were recorded within the potential range of 0 to 600 mV vs. Ag|AgCl, at a scan rate of 20 mVs^{-1}. Fresh films of each of the complexes (**14** and **17**) were used to record the RDE voltammogram at each rotation rate. Insets in the

figures are the Levich plots (plots of transport limiting current, I_L, (measured at 0.60 V) vs. square root of angular speed, $\omega^{1/2}$) for the electro-oxidation of bendiocarb on the different films. The plots fulfill the expected linear dependence of I_L on $\omega^{1/2}$, predicted by the Levich equation (equation 5.8) [152], indicative of diffusion-controlled mass transport. The quantities in equation 5.8 have the same meanings as

Table 5.5: Kinetic data for the oxidation of 200 µM hydrolyzed solution of bendiocarb, pH 4.

Electrode	Tafel slope (mV/decade)	k_o (cm s^{-1})	α	*E*p (V) vs. Ag|AgCl	I_p (µA)
electrodep-**14**-GCE	77	8.92×10^{-6}	0.77	0.44	1.64
poly-**17**-GCE	92	1.51×10^{-6}	0.64	0.52	1.05

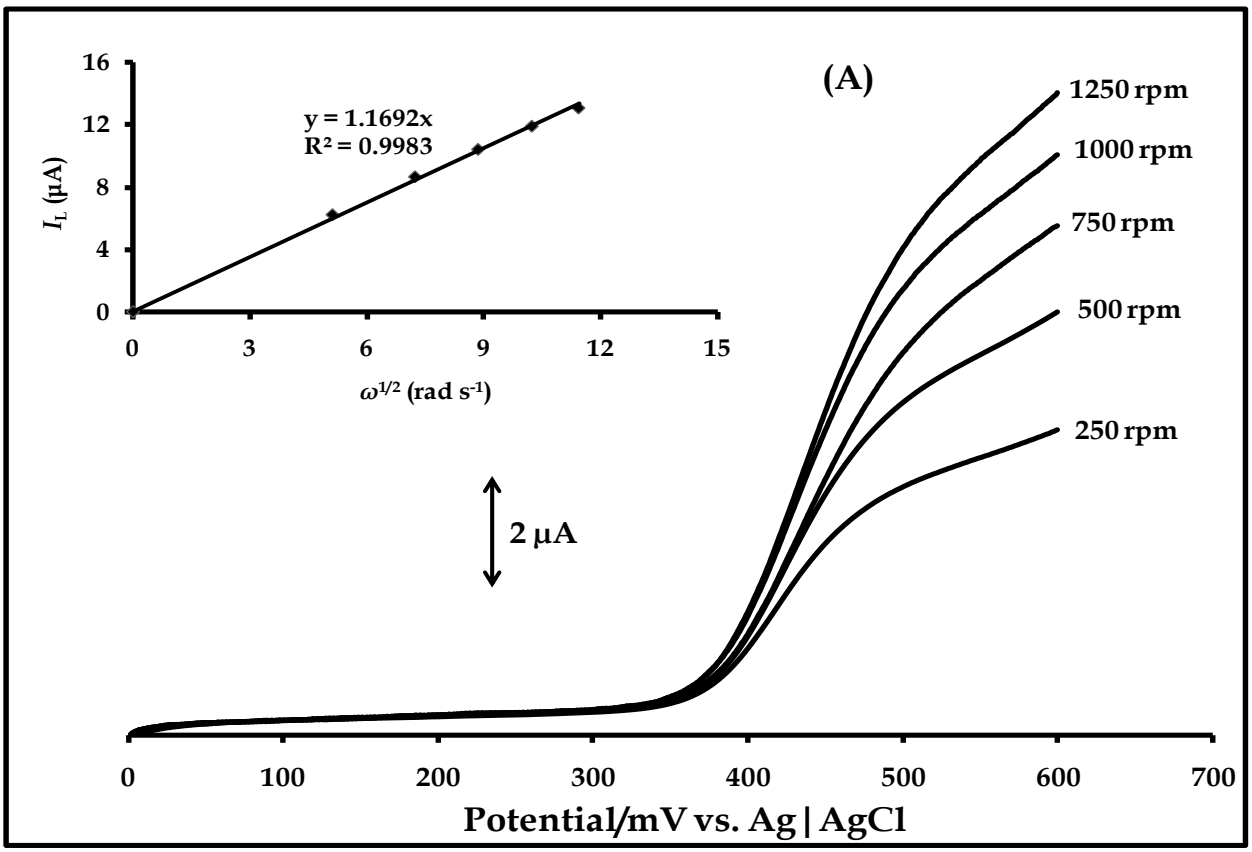

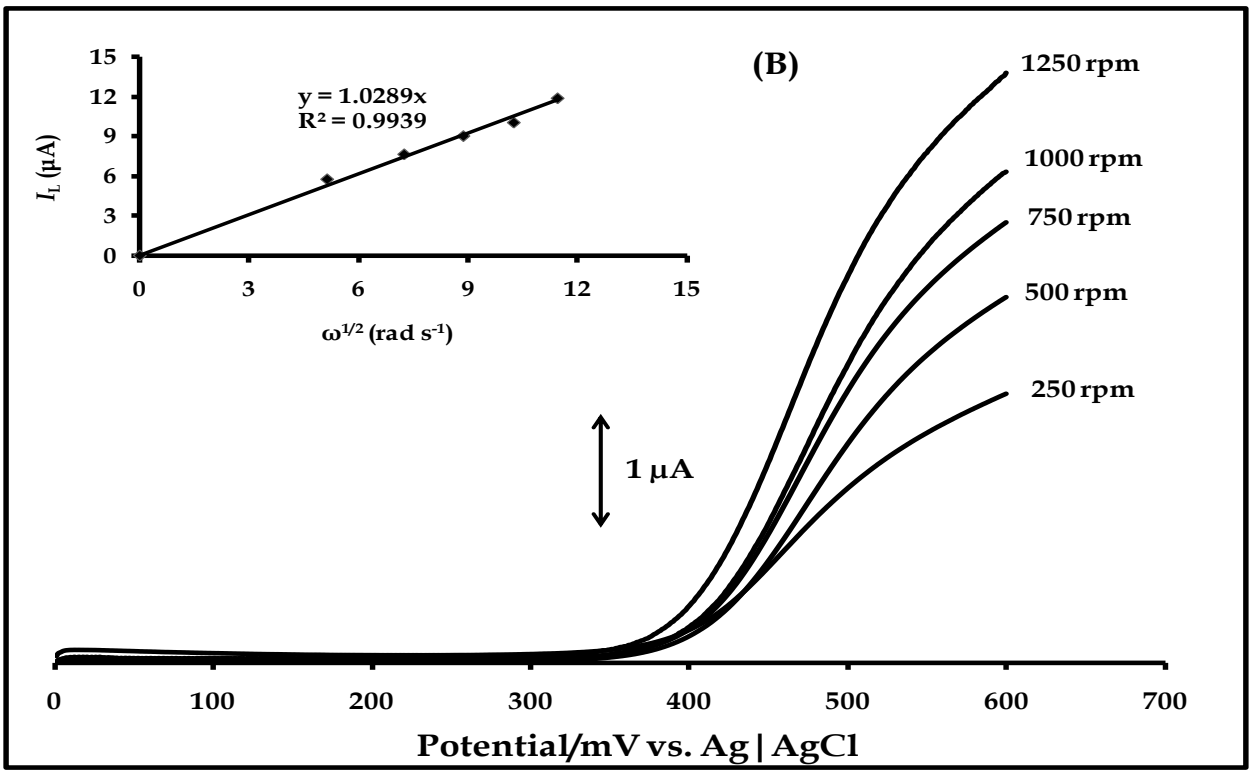

Figure 5.12: RDE voltammograms (250-1250 rpm) for the oxidation of 200 μM hydrolyzed solution of bendiocarb (pH 4) on (A) electrodep-**14**-GCE and (B) poly-**17**-GCE. Scan rate = 20 mVs^{-1}.

defined previously for carbofuran, but *A* is the effective surface area of the glassy carbon electrode (0.071 cm^2) and *C* is the bulk concentration of bendiocarb (2 × 10^{-7} mol cm^{-3}).

Koutecky-Levich equation (equation 5.9) was also used to further investigate the kinetics of oxidation of bendiocarb on the films. Figs. 5.13A and B are the Koutecky-Levich plots (ω = 250-1000 rpm) for the oxidation of 200 μM hydrolyzed solution of bendiocarb on electrodep-**14**-GCE and poly-**17**-GCE, respectively, at different potential {(a) 480 mV, (b) 500 mV, (c) 520 mV and (d) 540 mV versus Ag|AgCl}. The kinetic current, I_k, (inverse of the intercept of the respective plots in Fig. 5.13) for the oxidation of bendiocarb, on each film, at different potential, was estimated. The corresponding values of heterogeneous rate constant, *k*, were calculated from I_k, using equation 5.10. Values of standard heterogeneous constant, k_o, for the oxidation of bendiocarb on these

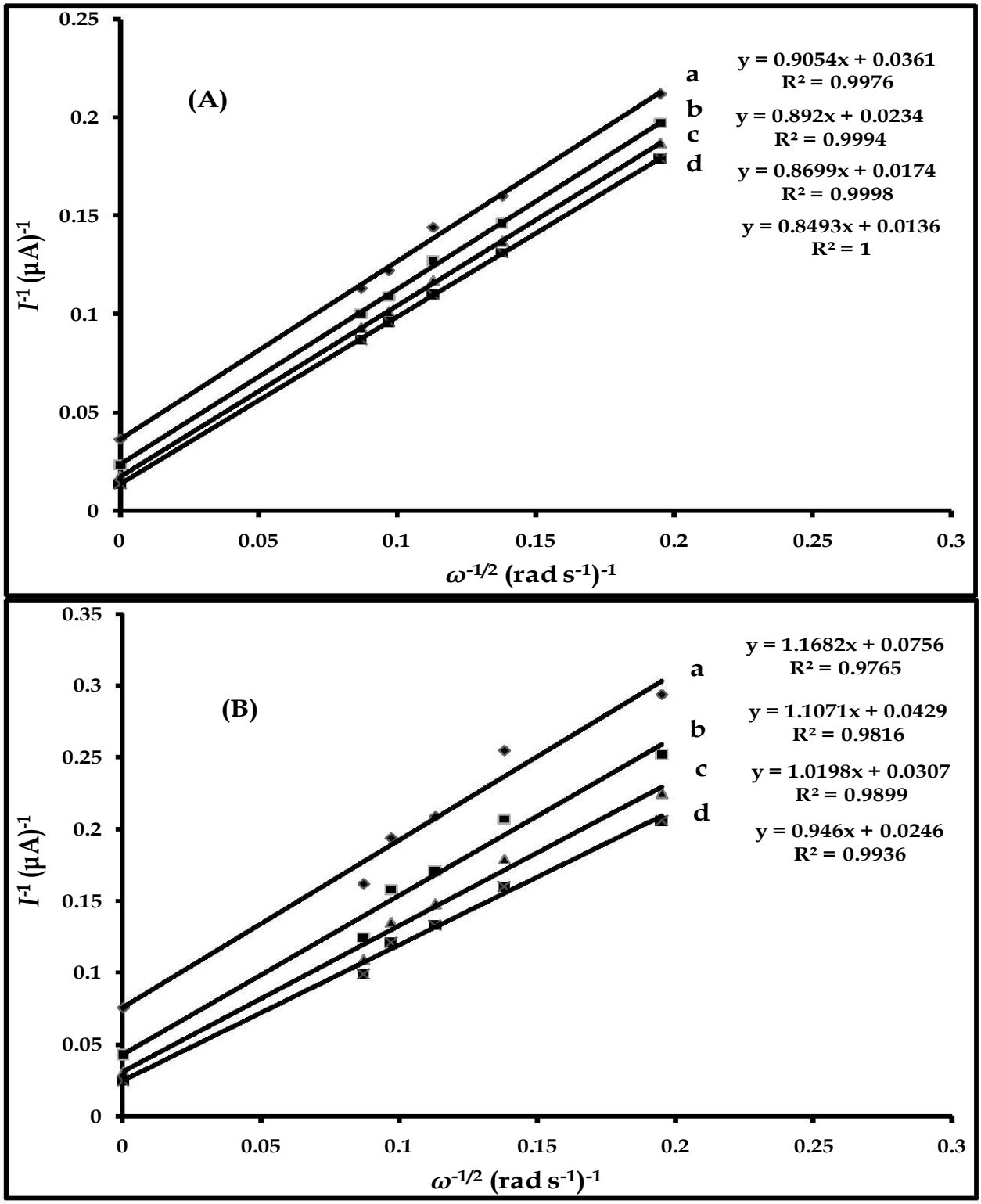

Figure 5.13: Koutecky-Levich plots for the oxidation of 200 µM hydrolyzed solution of bendiocarb (pH 4) on (A) electrodep-**14**-GCE and (B) poly-**17**-GCE at different potential: (a) 480 mV, (b) 500 mV, (c) 520 mV and (d) 540 mV versus Ag | AgCl.

films were evaluated from the intercepts (ln k_o) of the plots of ln k versus potential (equation 5.11), Fig. 5.14a (electrodep-**14**-GCE) and b (poly-**17**-GCE). The values obtained are 8.92×10^{-6} and 1.51×10^{-6} cm s^{-1} on electrodep-**14**-GCE and poly-**17**-GCE, respectively (Table 5.5). These values are consistent with the current responses of bendiocarb observed on these films (Tables 5.4 and 5.5). A larger standard rate constant is obtained for the oxidation of bendiocarb on the more porous electrodeposited film of complex **14**.

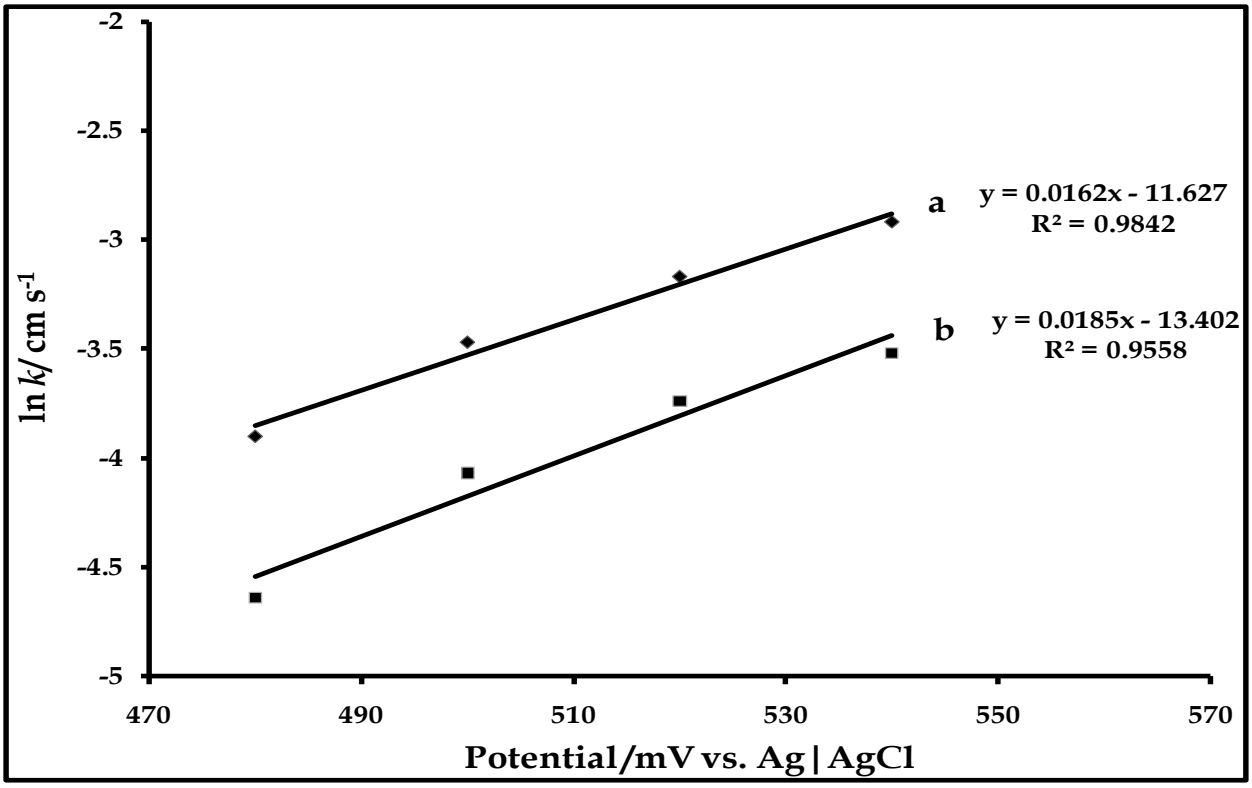

Figure 5.14: Plots of ln k versus potential for the oxidation of 200 µM hydrolyzed solution of bendiocarb (pH 4) on (a) electrodep-**14**-GCE and (b) poly-**17**-GCE.

Further kinetic information was obtained from the Tafel plots shown in Fig. 5.15, for the oxidation of bendiocarb on electrodep-**14**-GCE (a) and poly-**17**-GCE (b). The plots (log I_k versus potential) were obtained from the RDE voltammograms at 1250 rpm (Fig. 5.12). I_k, kinetic current corrected for mass transport (in this case), is as defined previously {$I_k = (I \times I_L)/(I_L - I)$}. Tafel slopes (Fig. 5.15) of 77 and 92 mV/decade are obtained for the

oxidation of bendiocarb on electrodep-**14**-GCE and poly-**17**-GCE, respectively, Table 5.5. These values suggest that the rate-determining step in the electro-oxidation of bendiocarb on these films is a one-electron process [249]. Substrate-catalyst interaction is also ruled out, as highlighted previously for the oxidation of carbofuran on **15**-SAM, SWCNT-**18**-SAM and (**22-24)**-SAM-modified gold electrodes. Values of α were calculated, using equation 5.3. The values obtained are 0.77 and 0.64 for the oxidation of bendiocarb on electrodep-**14**-GCE and poly-**17**-GCE, respectively. These values are consistent with the range for most systems (0.3 and 0.7) [248], as discussed previously.

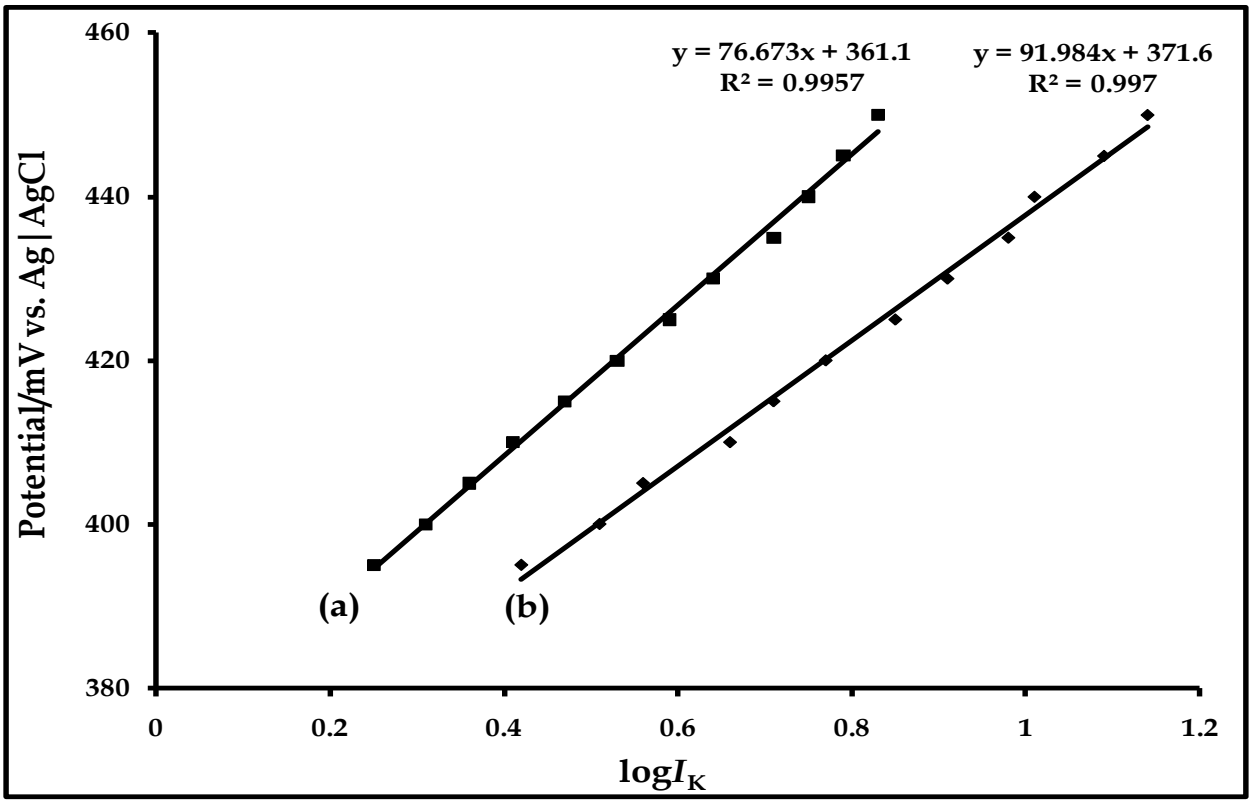

Figure 5.15: Tafel plots for the oxidation of 200 µM hydrolyzed solution of bendiocarb (pH 4) on (a) electrodep-**14**-GCE and (b) poly-**17**-GCE.

Oxidation of bendiocarb is suggested to be the rate-determining step (the slow step), since the rate of electron transfer between the films and the electrode is assumed to be very fast. The oxidation potential of bendiocarb on each film is within the range for metal oxidation ($Mn^{IV}Pc^{-2}/Mn^{III}Pc^{-2}$). This redox process was observed on the films of

complexes **17** and **14** (Table 4.5). The mechanism below is proposed for the catalysis of bendiocarb on these films (equation 5.14 and 5.15).

$Mn^{III}Pc^{-2} \longrightarrow Mn^{IV}Pc^{-2} + e^{-}$ 5.14

$Mn^{IV}Pc^{-2} + \mathbf{RO}^{-} \longrightarrow Mn^{III}Pc^{-2} + \mathbf{RO}^{\cdot}$ 5.15

where **R** is the remaining portion of the analyte in Scheme 5.2.

5.3 Bentazon

5.3.1 Voltammetry response

Electrocatalytic oxidation of the herbicide, bentazon (Fig. 1.23C), was carried out on poly-**20**-GCE. Prior to voltammetry measurement, the modified electrode (poly-**20**-GCE) was conditioned in 0.1 M phosphate buffer solution, pH 5, (Fig. 5.16A), by repetitive cycling, until a reproducible scan was obtained. The best voltammetry response of bentazon was obtained at this pH. Conditioning improves stability of the electrode, but resulted in decrease in the current of process **IV** (Fig 5.16A). The current

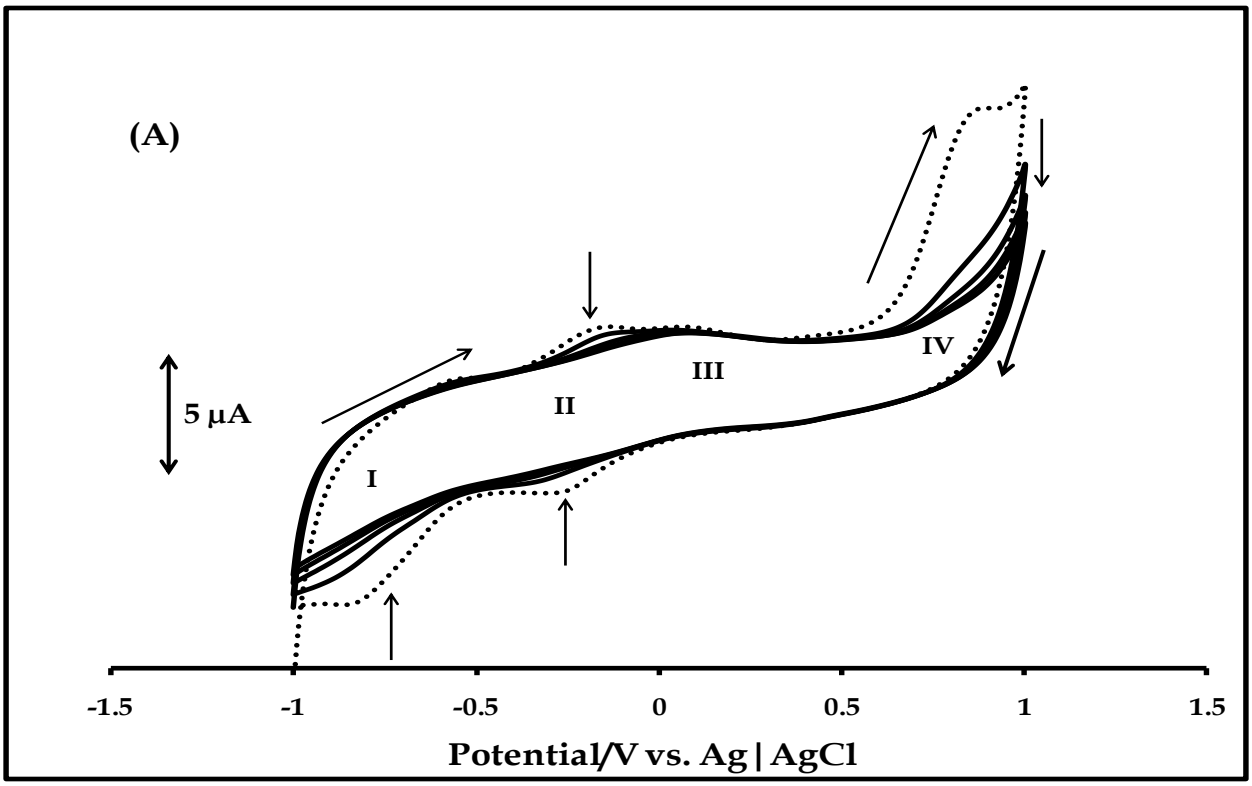

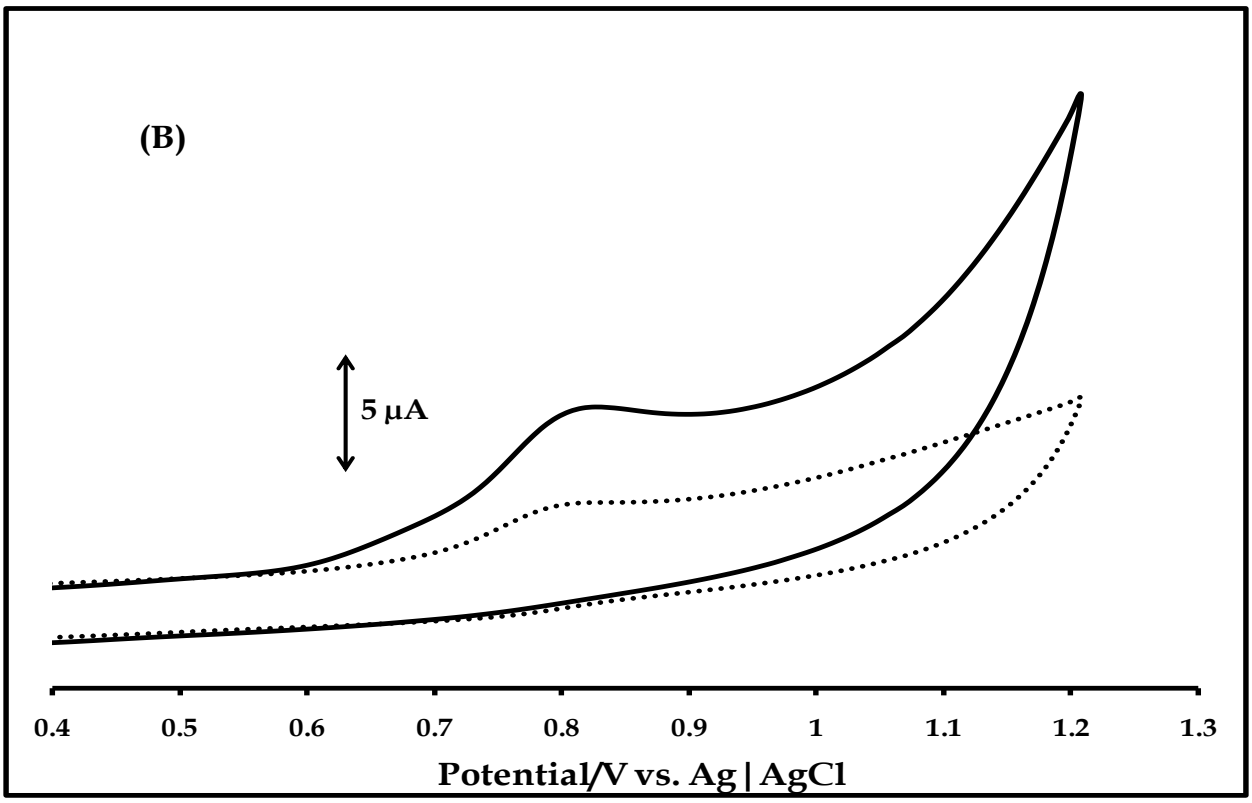

Figure 5.16: (A) Repetitive cycling of poly-**20**-GCE in pH 5 buffer solution (dashed line = first scan) and (B) voltammetry responses of bare GCE (dashed line) and poly-**20**-GCE (solid line) in 100 µM solution of bentazon (pH 5). Scan rate = 100 mVs^{-1}.

signal due to bentazon appeared at potentials of process **IV** on the modified electrode. This process was not observed after conditioning, hence no contribution from the background peak. The current signals observed in Fig. 5.16B (3.88 µA, 0.80 V) (solid line) can be adequately assigned to the oxidation bentazon. The current response of the herbicide on the film was better than that observed on the bare electrode (1.3 µA, 0.80 V) (dashed line). This indicates electrocatalytic behavior of the film towards the herbicide. Square wave voltammetry technique was used for quantitative determination of the herbicide, because of its more sensitive nature compared to cyclic voltammetry. Fig. 5.17A shows the square wave voltammetry profiles of bentazon, on the modified electrode, at different concentrations (50 to 750 µM). Interestingly, oxidation of the herbicide occurred at more favorable potential (~+0.74 V versus Ag | AgCl) in Fig. 5.17A

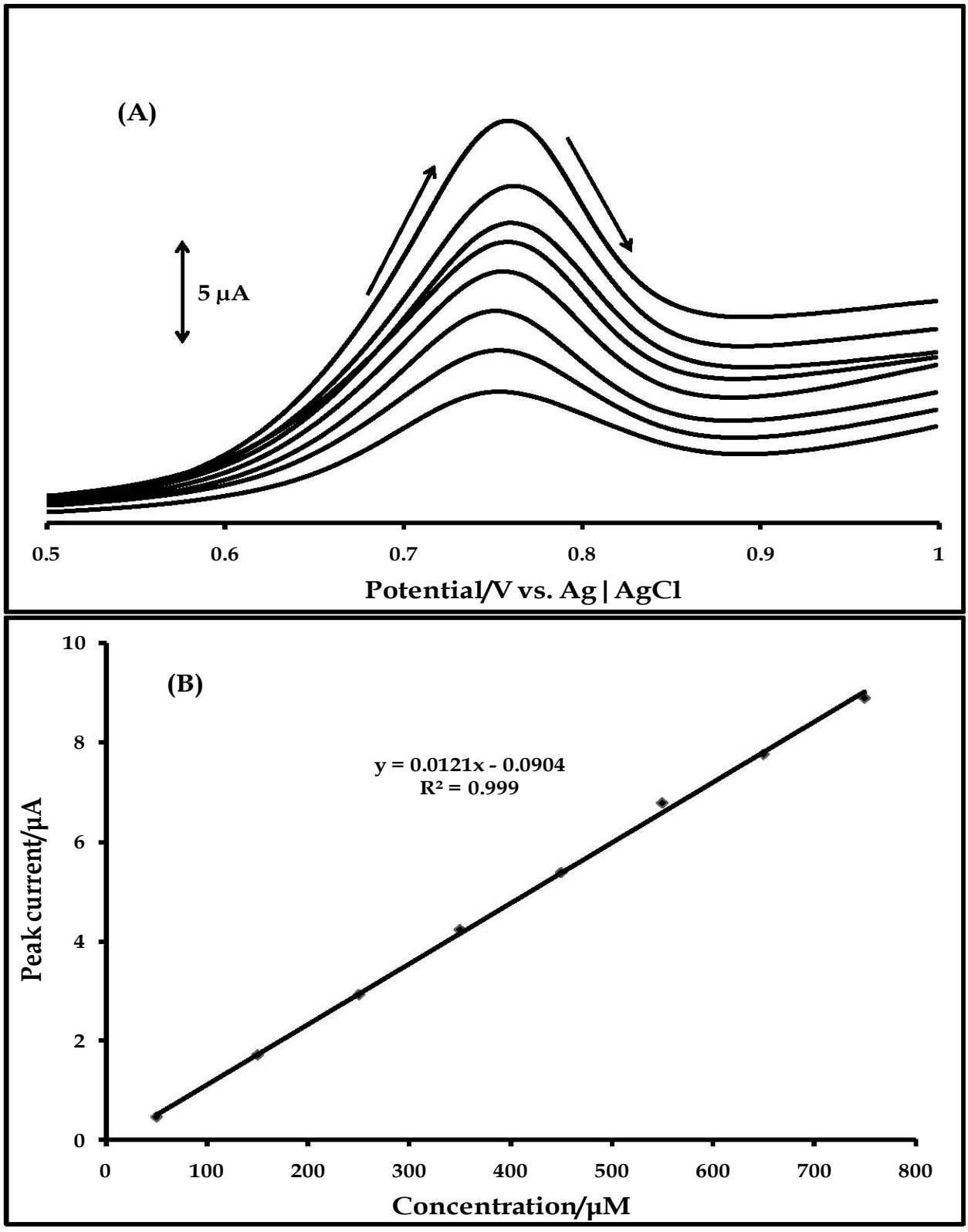

Figure 5.17: (A) Square wave voltammetry profiles and (B) calibration curve of bentazon (50 to 750 µM) (pH 5) on poly-**20**-GCE.

relative to that observed in Fig. 5.16B. A linear relationship was obtained between current response and concentration, Fig. 5.17B, with detection limit of 2.48 × 10^{-7} M, using 3δ criterion [253] (where δ is the standard deviation of the blank). The relationship between current response and concentration is expressed linearly by equation 5.16

$$I_p = (0.0121 \pm 0.00012)\ [\text{bentazon}] - (0.0904 \pm 0.001) \qquad 5.16$$

The detection limit obtained was less than the value reported using bare glassy carbon electrode (1.0 × 10^{-5} M) [205]. The modified electrode showed better stability compared to the bare electrode. 63% of the original herbicide signal was observed on the modified electrode, compared to 24% for the bare electrode, when the used electrodes were rinsed in excess acetone.

5.3.2 Mechanism of oxidation

Amplification of current response of bentazon on poly-**20**-GCE, relative to the response on bare GCE, suggests electrocatalytic behavior of the film towards the herbicide. Also,

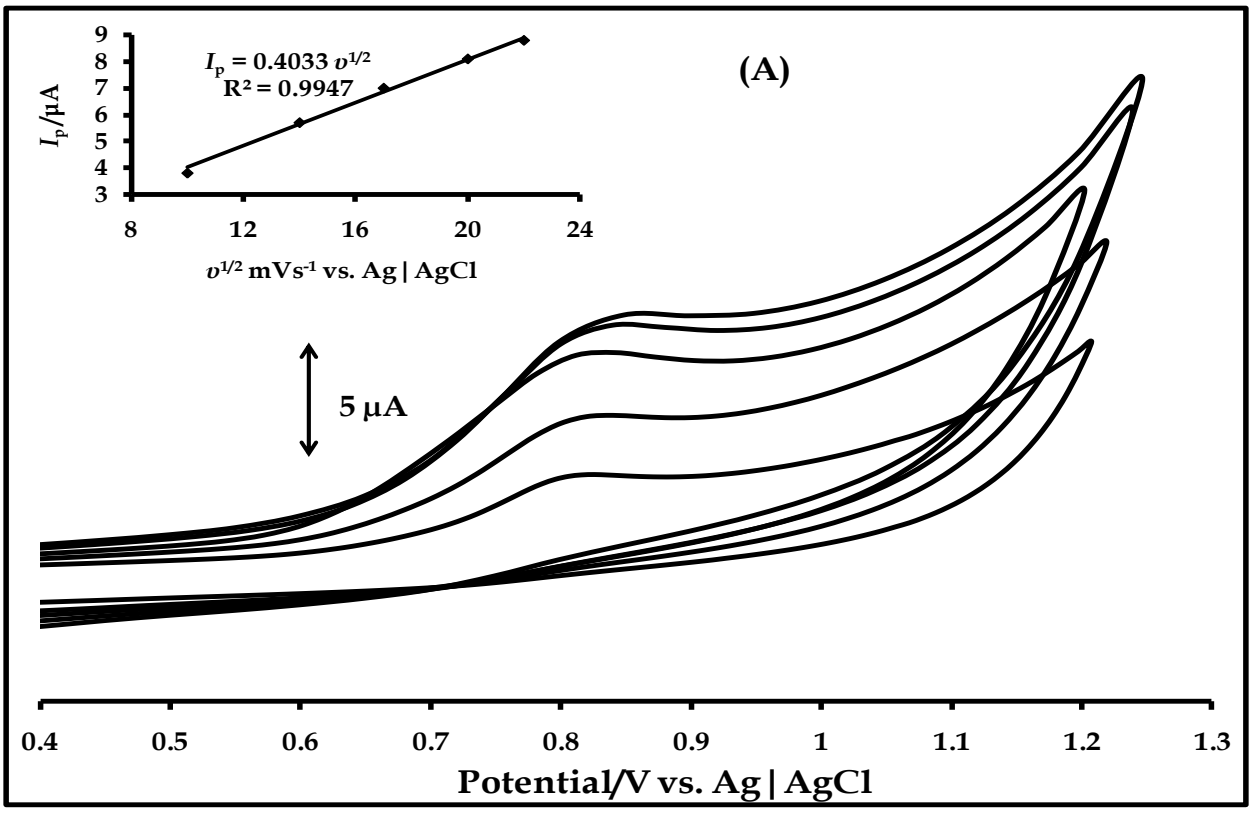

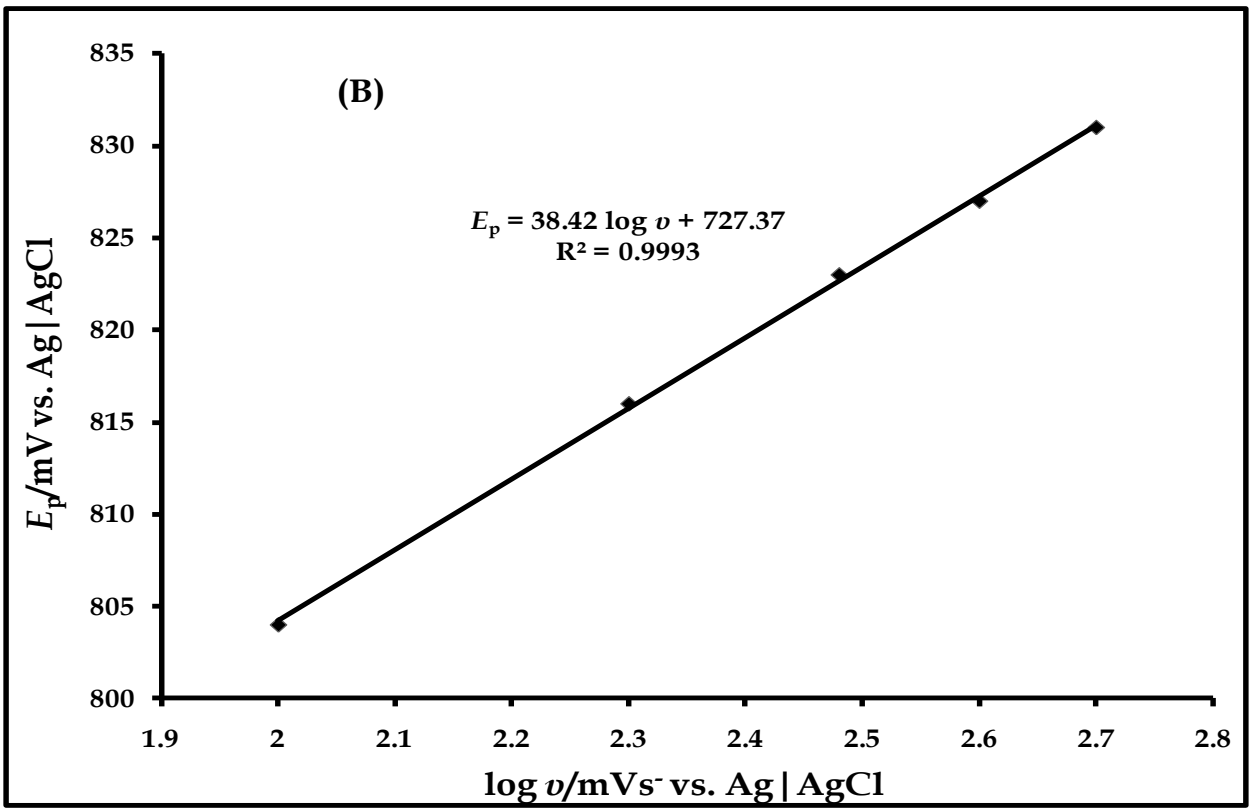

Figure 5.18: (A) Cyclic voltammetry profiles of poly-**20**-GCE in 100 µM solution of bentazon (pH 5) at different scan rate (100-500 mVs^{-1}) (inset = I_p vs. $\upsilon^{1/2}$) and (B) Plot of E_p vs. log υ

the voltammetry signal of bentazon, observed at ~+0.80 V (versus Ag|AgCl) on the film indicates the involvement of MPc ring redox process in catalysis, Fig. 5.17A. This value is same as the potential for the first ring oxidation process on the polymeric film (Fig. 4.17C, Table 4.5), hence the involvement of this species in the suggested mechanism. Cyclic voltammetry, and not RDE, was employed for the elucidation of mechanism of electrocatalysis of this herbicide. Fig. 5.18A shows the cyclic voltammetry profiles obtained for poly-**20**-GCE in 100 µM solution of bentazon at different scan rate (100 – 500 mVs^{-1}), the inset is a linear plot of peak current (I_p) versus the square root of scan rate ($\upsilon^{1/2}$), indicating that the catalysis of the herbicide on this film is diffusion-controlled. Plots of peak potential (E_p) versus log υ (Fig. 5.18B) were used to further investigate the mechanism of electrocatalysis of bentazon on the film. For a totally

irreversible diffusion-controlled system, the anodic peak potential can be represented as shown in equation 5.17 [248].

$$E_p = \frac{2.3RT}{2(1-\alpha)n_aF}\log \upsilon + K \qquad 5.17$$

where E_p is the oxidation peak potential of bentazon in mV, υ is the scan rate in mVs^{-1}, K is a constant, other quantities have their usual meanings. Equation 5.17 can be represented as shown in equation 5.18, where b is the Tafel slope.

$$E_p = \frac{b}{2}\log \upsilon + K \qquad 5.18$$

A Tafel slope of 77 mV/decade (Fig. 5.18B) was obtained, a value which is close to 60 mV/decade, suggesting that a fast one-electron transfer is followed by a slow chemical step. This is represented by the mechanism shown in equations 5.19-5.21. Bentazon is represented as RNHNR^1, where R^1 is the isopropyl group and R is the remaining portion of the molecule (see Fig. 1.23C for structure). Based on the reported dimerization of the oxidation product of bentazon [205], oxidation may involve any of the two nitrogen atoms in the molecule (Fig. 1.23C). In this work, the nitrogen of the tertiary amine (nitrogen atom attached to the isopropyl group) is involved in the suggested mechanism. The higher electron density of the lone pair of the nitrogen of the tertiary amine group, compared to that of the nitrogen of the secondary amine, makes it more susceptible to oxidation, hence its involvement in the suggested mechanism. Dimerization resulted in the poisoning of electrode after oxidation [205]. Electrode poisoning was also observed in the present study, but appreciably reduced due to the presence of the polymeric film on the electrode.

$$Mn^{III}Pc^{-2} \longrightarrow Mn^{III}Pc^{-1} + \mathbf{e^-} \qquad 5.19$$

$$Mn^{III}Pc^{-1} + \mathbf{RNHNR^1} \longrightarrow Mn^{III}Pc^{-2} + \mathbf{RNHN\cdot} + \mathbf{R^1} \qquad 5.20$$

$$\mathbf{RNHN\cdot} + \mathbf{RNHN\cdot} \longrightarrow \mathbf{RNHN\text{-}NHNR} \qquad 5.21$$

Regeneration of $Mn^{III}Pc^{-2}$ species in equation 5.20 describes catalysis while equation 5.21 indicates the dimerization of the oxidation product.

CHAPTER 6

CONCLUSIONS AND RECOMMENDATIONS

6.1 Conclusions

The synthesis, spectral, electrochemical and spectroelectrochemical properties of new alkylthio- and arylthio-substituted cobalt (**13**, **16 19** and **22**), manganese (**14**, **17**, **20** and **23**) and iron (**15**, **18**, **21** and **24**) phthalocyanine complexes are reported. Electrochemical properties of the diethylaminoethanethio-substituted derivatives (**13-21**) are reported for the first time. A nano-composite of SWCNT and complex **18** (SWCNT-**18**) was fabricated, in an attempt to enhance the electrocatalytic application of the complex (representative of complexes **13-21**). The structural integrity of the nano-composite was extensively investigated. The complexes and the nano-composite were used for the design of chemically modified electrodes (MPc-SAM-modified gold electrodes and MPc-modified glassy carbon electrodes), and the surface properties of the modified electrodes investigated. The electrodes were employed for the electrocatalytic oxidation of carbofuran, bendiocarb and bentazon.

The spectral qualities of the complexes were marginally affected by the molecular make-up of the substituents (diethylaminoethanethio versus benzylthio), but substantially influenced by the nature of metal center, and position of substituent on the phthalocyanine ligand. As expected, non-peripheral substitution resulted in red-shifted Q-band, relative to peripheral substitution. The Q-bands of the MnPc complexes were also significantly red-shifted with respect to those of the Co and Fe analogues, while the spectral qualities of the FePc complexes were more complicated, characteristic of the presence of stacked monomers in DMF.

Electrochemical and spectroelectrochemical properties of the complexes were substantially determined by the nature of central metal, point of substitution and molecular identity of the substituents. Effects of the nature and position of substituent were more pronounced on the electrochemical behaviors of the CoPc complexes (**13**, **16** and **22**), with significant correlation with the extent of spectral resolution, during spectroelectrochemical investigation. For the MnPc complexes, spectral transformations

during spectroelectrochemical studies were substantially affected by the presence of the μ-oxo species in DMF, while the extent of this occurrence was dependent on point of substitution, number of substituent and concentration of molecular oxygen in the medium. Non-peripheral substitution resulted in restriction to coplanar association of the Pc ligands, via oxo bridge, thus the absence of the μ-oxo species in DMF solution of the non-peripheral complex. The μ-oxo species was prominent in oxygen-saturated DMF solution of the peripheral derivatives. Interestingly, there was a significant reduction in the intensity of the Q-band due to the μ-oxo species, in a N_2-dearated DMF solution of the tetra-substituted derivative. However, this species persisted in a N_2-dearated DMF solution of the octa-substituted analogue.

The nano-composite obtained from covalent integration of SWCNT with complex **18** showed structural integrity suggesting the formation of the composite. Spectroscopic (IR and XRD) and microscopic (TEM) properties of the nano-composite, relative to that of its individual units, confirmed its successful fabrication. Structural properties of this composite, revealed by its XRD spectrum, showed a marked departure from those of its constituent units, further confirming its formation.

Differences in surface properties of the bare and modified electrodes confirmed successful modification. Cyclic voltammetry properties of the modified electrodes, in relevant electrolytes were significantly influenced by the type of metal center, nature and position of substituent on the Pc ligand of the adsorbed MPc complexes. Expectedly, SAMs formed from alkylthio-substituted MPc complexes (**13**, **14** and **15**) exhibited more blocking characteristics than those of benzylthio-substituted complexes (**22**, **23** and **24**). For the MnPc-modified GCEs, AFM images of complexes **14** and **17**, on ITO (representative of GCE), showed that non-peripheral substitution resulted in the formation of relatively porous molecular films, while peripheral substitution gave more compact film morphology. SEM images of **18**-SAM, representative of other SAMs, depicted the self-assembled nature of this complex on gold-coated glass (representative of its nature on gold disc electrode). The differences in morphologies of **18**-SAM and

SWCNT-**18**-SAM, as revealed by their SEM images, indicated differences in their structural properties.

The surface properties of the bare and SAM-modified gold electrodes were further evaluated by EIS. The electrical properties of the SAM/electrode interfaces were probed, using this technique. The presence of SWCNT in the SWCNT-**18**-SAM was confirmed by lower charge transfer resistance in the SWCNT-**18**-SAM, relative to **18**-SAM. Generally, electrical properties of the SAM/electrode interfaces, judging by the nature of their impedance spectra and the fitted impedance data, were influenced by the molecular identity of the substituent and nature of central metal of the adsorbed MPc complexes.

Electrocatalytic activity of the MPc-modified electrodes was substantiated by better voltammetry responses of carbofuran, bendiocarb and bentazon on these electrodes, relative to their responses on bare electrodes. The use of MPcs as electrocatalysts for these pesticides is reported for the first time.

Amplification of the current signal of carbofuran on the SAM-modified gold electrodes, at more energetically favorable oxidation potential, relative to the signal on bare gold electrode, enhances the prospect of designing MPc-based electrochemical sensor for this insecticide. Importantly, regeneration of 95% of the original signal of the insecticide, on rinsing the used electrodes in excess acetone, is a testimony to the resistance of the electrodes to fouling, and the prospect of reproducing the signals of the insecticide on these electrodes. Enhanced sensitivity and significant degree of selectivity for carbofuran, observed on SWCNT-**18**-SAM-modified gold electrode, brightens the prospect of employing this nano-composite in the design of electrochemical sensor for carbofuran.

This work has also shown that the mechanism of formation, surface integrity and potential use of MPc-based films, as electrochemical sensors for electroactive analytes, are dependent on the molecular architecture of the MPc complex. A highly porous and

permeable film was formed from non-peripherally substituted MPc complex, while peripheral substitution formed compact and less-permeable film. Better signal of the carbamate insecticide, bendiocarb, on electrodeposited film of complex **14**, relative to that observed on electropolymerized film of complex **17**, showed that non-peripherally substituted MPc complexes may be more desirable for designing MPc-based electrochemical sensors for this insecticide. This submission was attested to by the lower charge transfer resistance obtained for bendiocarb on electrodep-**14**-GCE.

Investigation of the kinetics of oxidation of these pesticides gave better understanding of their voltammetry behaviors on the modified electrodes. Their mechanisms of oxidation are closely related: involvement of one-electron process, as the rate determining step, and presence (in few cases) or absence (in most cases) of analyte-catalyst intermediate.

6.2 Recommendations

The following are recommended based on the results of this work

(1) The synthesis and investigation of the UV-Vis spectral properties of the non-peripheral octa-substituted derivatives of diethylaminoethanethio-substituted Mn and TiPc complexes may produce new set of interesting NIR absorbing MPc complexes.

(2) More studies need to be conducted in order to have a better understanding of the UV-Vis spectral properties of the FePc complexes studied in this work. This will also be helpful for spectroelectrochemical evaluation of these complexes

(3) Direct comparative studies of the surface properties of MPc-SAM and MPc-polymer modified electrodes will be useful in evolving the best strategy for forming MPc-based thin films for particular electrocatalytic application.

(4) Based on the results of this work, the use of MPc-SAM-modified gold electrodes as carbofuran sensor is very promising. More work should be done on how to enhance the sensitivity, selectivity and reproducibility of these sensors.

(5) Successful integration of SWCNT with complex **18** (diethylaminoethanethio-substituted complex), via amide bond, suggests the prospect of coordinating this type of MPc complex with functional molecules, like proteins, enzymes, nucleotides and peptide, for possible biological applications.

REFERENCES

[1] P. Gregory, *J. Porphyrins Phthalocyanines* 1999, **3**, 468.

[2] D.H.R. Barton, H.N. Rydon and J.A. Elvidge, *Biographical Memoirs of Fellows of the Royal Society* 1968, **14**, 309.

[3] J.M. Robertson, R.P. Linstead and C.E. Dent, *Nature* 1935, 219.

[4] J.M. Robertson, *J. Chem. Soc*. 1936, 1195.

[5] J.M. Robertson and I. Woodward, *J. Chem. Soc*. 1937, 219.

[6] J.M. Robertson and I. Woodward, *J. Chem. Soc*. 1940, 36.

[7] W.R. Scheidt and Y.J. Lee, *Structure and Bonding* 1987, **64**, 1

[8] W.R. Scheidt, K.M. Kadish, K.M. Smith and R. Guilard in: *The Porphyrin Handbook* (Eds.); Academic Press: Boston, 2000; Vol. 3, p. 49.

[9] R.D. Shannon, *Acta Crystallogr. A* 1976, **32**, 751.

[10] J.L. Hoard, *Ann. N. Y. Acad. Sci*. 1973, **206**, 18.

[11] G. Booth in: *The Chemistry of Synthetic Dyes*. K. Venkataraman (Eds.); Academic Press: New York, 1971; p. 241-282.

[12] J.S. Aderson, E.F. Bradbrook, A.H. Cook, R.P. Linstead, *J. Chem. Soc.* 1938, 1151.

[13] P.A. Barrett, D.A. Frye, R.P. Linstead, *J. Chem. Soc.* 1938, 1157.

[14] G.T. Bryrne, R.P. Linstead, A.R. Lowe, *J. Chem. Soc.* 1934, 1017.

[15] R.P. Linstead, A.R. Lowe, *J. Chem. Soc*. 1934, 1031.

[16] R.P. Linstead, E.G. Noble, J.M. Wright, *J. Chem. Soc*. 1937, 911.

[17] R.P. Linstead, *Ber. Dtsch. Chem. Ges*. 1939, **72A**, 93.

[18] B.D. Berezin, *Coordination Compounds of the Porphyrins and Phthalocyanines*; Wiley: Chichester, 1981

[19] A.B.P. Lever, *Adv. Inorg. Radiochem*. 1965, **27**, 27.

[20] R.P. Linstead, A.R. Lowe, *J. Chem. Soc*. 1934, 1022.

[21] C.E. Dent, R.P. Linstead, *J. Chem. Soc*. 1934, 1033.

[22] F.H. Moser, A.L. Thomas, *The Phthalocyanines: Properties*, vol. 1, CRC Press: Boca Raton, Florida, 1983.

[23] F.H. Moser, A.L. Thomas, *The Phthalocyanines: Manufacture and Applications*, vol. 2, CRC Press: Boca Raton, Florida, 1983

[24] A.G. Gürek, Ö. Bekaroglu, *J. Chem. Soc., Dalton Trans*. 1994, 1419.

[25] M. Brewis, G.J. Clarkson, P. Humberstone, S. Makhseed, N.B. McKeown, *Chem. Eur. J*., 1998, **4,** 1633.

[26] S.A. Mikhalenko, V.M. Derkacheva, E.A. Luk'yanets, *J. Gen. Chem. USSR (Engl. Transl.)*, 1981, **51**, 1405

[27] N.B. McKeown, Phthalocyanine Materials: *Synthesis, Structure and Functions*, 1998, Cambridge University Press, Cambridge.

[28] K. M. Kadish, K. M. Smith, and R. Guilard, *The Porphyrin Handbook (Eds.)*, 2003, Vol. 16, Academic Press, Boston.

[29] E.F. Perez, G. Neto, A.A. Tanaka, L.T. Kubota, *Electroanalysis* 1998, **10**, 111.

[30] J.A. Thomson, K. Murata, D.C. Miller, J.L. Stanton, W.E. Broderick, B.M. Hoffman, J.A. Ibers, *Inorg. Chem*. 1993, **32**, 3546.

[31] I. Gürol, V. Ahsen, Ö. Bekaroglu, *J. Chem. Soc., Dalton Trans*. 1994, 497.

[32] N. Jagerovic, I. Alkorta, J. Elguero, C. Fernandez Castano, C. Foces, A.L. Llamas Saiz, *New J. Chem*. 1996, **20**, 1081.

[33] P.J. Brach, S.J. Grammatica, O.A. Ossanna, L.J. Weinberger, *Heterocycl. Chem*. 1970, **7**, 1403

[34] W.S. Struve in: *Phthalocyanine Pigments*. H.A. Lubs (Eds.); Reinhold Press: New York, 1955; p. 577.

[35] M. Hanack, G. Schmid, M. Sommerauer, *Angew. Chem. Int. Ed. Engl.* 1993, **32**, 1442.

[36] M. Sommerauer, C. Rager, M. Hanack, *J. Am. Chem. Soc.* 1996, **118**, 10085.

[37] J.G. Young, W. Onyebuagu, *J. Org. Chem.* 1990, **55**, 2155.

[38] S. Öztürk, S. Isik, H.-K. Fun, E. Kendi, E. Agar, S. Sasmaz, A.A. Ibrahim, *Acta Cryst*. 1999, **C55**, 395.

[39] I.G. Abramov, V.V. Plakhtinskii, M.B. Abramova, A.V. Smirnov, G.G. Krasovskaya, *Chem. Hetero. Comp*. 1999, **35**, 1342.

[40] S. Öztürk, S. Isik, E. Agar, S. Sasmaz, H.-K. Fun, *Spectro. Lett*. 2000, **33**, 245.

[41] C.G. Claessens, T. Torres, *Eur. J. Org. Chem*. 2000, 1603.

[42] G. Gümüs, A. Gül, Ö. Bekaroglu, *J. Chem. Res.* 1994, 430.

[43] C.C. Leznoff in: Phthalocyanines: *Properties and Applications*, C.C. Leznoff, A.B.P. Lever, (Eds.); VCH: Weinheim, 1989, vol. 1, p. 1-54.

[44] C. Dent, *J. Chem. Soc*. 1938, 1.

[45] I. Owen, M. Kenney, *Inorg. Chem*. 1962, **1**, 331.

[46] T. J. Hurley, M.A. Robinson, S.I. Trotz, *Inorg. Chem*. 1967, **6**, 389.

[47] S. Gaspard, P. Maillard, *Tetrahedron* 1987, **43**, 1083.

[48] D. Wöhrle, G. Schrnurpfeil, G. Knothe, *Dyes and Pigm.* 1992, **18**, 91.

[49] A.H. Jackson in: The Porphyrins, D. Dolphin (Eds.); Academic Press: New York, 1978; p. 374-388.

[50] P.A. Barrett, C.E. Dent, R.P. Linstead, *J. Chem. Soc*. 1936, 1719.

[51] C.E. Dent, R.P. Linstead, *J. Chem. Soc*. 1934, 1027.

[52] J.M. Robertson, *J. Chem. Soc*. 1935, 615.

[53] J.M. Robertson, Organic Crystals and Molecules; Cornell University Press: Ithaca, New York, 1953.

[54] G.J. Clarkson, N.B. McKeown, K.E. Treacher, *J. Chem. Soc., Perkin Trans. 1* 1995, 1817.

[55] W. Eberhardt, M. Hanack, *Synthesis* 1997, 95.

[56] G.C. Bryant, M.J. Cook, T.G. Ryan, A.J. Thorne, *Tetrahedron* 1996, **52**, 809.

[57] R.B. Freas, J.E. Campana, *Inorg. Chem*. 1984, **23**, 4654.

[58] T.W.B. Healy, C.T. Ewins, *J. Porphyrins Phthalocyanines* 1999, **3**, 522.

[59] N. Srinivasan, C.A Haney, J. S. Lindsey, W.Z. Zhang, B.T. Chait, *J. Porphyr. Phthalocyan.* 1999, **3**, 283.

[60] R. Lidgard, M.W. Duncan, *Rapid Commun. Mass Spectrom*. 1995, **9**, 128

[61] J. Mark, M.J. Stillman in: Porphryin Handbook: *Phthalocyanine properties and materials*, K.M. Kadish, K.M. Smith, R. Guilard (Eds.), Academic Press, New York, 2003, vol. 16, Chap 103.

[62] M. Gouterman in: The Porphyrins. D. Dolphin (Eds.); Academic Press: New York, 1978; vol. 3, Part A, p. 1.

[63] S.G. Makarov, O.N. Suvorova, C. Litwinski, E.A. Ermilov, B. Roeder, O. Tsaryova, T. Duelcks, D. Woehrle, *Eur. J. Inorg. Chem*. 2007, **4**, 546.

[64] S.G. Makarov, A.V. Piskunov, O.N. Suvorova, G. Schnurpfeil, G.A. Domrachev, D. Woehrle, *Chem. Eur. J.* 2007, **13**, 3227.

[65] S.G. Makarov, C. Litwinski, E.A. Ermilov, O. Suvorova, B. Roeder, D. Woehrle, *Chem. Eur. J.* 2006, **12**, 1474.

[66] Y. Chen, M. Hanack, W.J. Blau, D. Dini, Y. Liu, J. Bai, *J. Mater. Sci*. 2006, **41**, 2169

[67] C.C. Leznoff, L.S. Black, A. Hiebert, P.W. Causey, D. Christendat, AB.P. Lever, *Inorg. Chim. Acta* 2006, **359**, 2690.

[68] S. Knecht, K. Durr, G. Schmid, L.R. Subramania, M. Hanack, *J. Porphyrins Phthalocyanines* 1999, **3**, 292.

[69] P. Tau, T. Nyokong, *Polyhedron* 2006, **25**, 1802

[70] P. Tau, T. Nyokong, *Electrochim. Acta* 2007, **52**, 3641.

[71] R. Taube, *Pure Appl. Chem*. 1974, **38**, 427

[72] A.B.P. Lever, S.R. Pickens, P.C. Minor, L. Licoccia, B.S. Ramaswamy and K. Magnell*, J. Am. Chem. Soc*. 1981, **103**, 6800.

[73] T. Tsuzuki, Y. Kuwabara, N. Noma, Y. Shirota, M.R. Willis, *Jpn. J. Appl. Phys*. 1996, **35**, L447.

[74] B.O. Agboola, K.I. Ozoemena, T. Nyokong, *Electrochim. Acta* 2006, **51**, 4379

[75] K. Ozoemena, T. Nyokong, *Electrochim. Acta* 2002, **47**, 4035.

[76] J. Obirai, T. Nyokong, *Electrochim. Acta* 2004, **49**, 1417.

[77] D.W. Clack, N.S. Hush, I.S. Woolsey, *Inorg. Chim. Acta* 1976, **19**, 129.

[78] A. Giruadeau, F. Fau, A.J. Bard, *J. Am.Chem. Soc*. 1980, **102**, 5137.

[79] S.-I. Mho, B. Ortiz, N. Doddapaneni, S.-M. Park, *J. Electrochem. Soc*. 1995, **142**, 1047

[80] W.A. Nevin, M.R. Hempstead, W. Liu, C.C. Leznoff, A.B.P. Lever, *Inorg. Chem*. 1987, **26**, 570.

[81] F. Matemadomboa, M. D. Maree, K. I. Ozoemena, P.Westbroek, T Nyokong, *J. Porphyrins Phthalocyanines* 2005, **9**, 484.

[82] K. Ozoemena, P. Westbroek, T. Nyokong, *J. Porphyrins Phthalocyanines* 2002, **6**, 98.

[83] M. Idowu, T. Nyokong, *Polyhedron* 2009, **28**, 416

[84] A.B.P. Lever, P.C. Minor, J.P. Wilshire, *Inorg. Chem*. 1981, **20**, 2550.

[85] A.B.P. Lever, P.C. Minor, *Adv. Mol. Relax. Proc*. 1980, **18**, 115.

[86] S. Sievertsen, B. Moubaraki, K.S. Murray, H. Homborg, Z. Anorg, *Allg. Chem*. 1994, **620**, 682.

[87] J. Zhu. F. Gu, J. Zhag, *Mater. Lett*. 2007, **16**, 1296.

[88] W. Posiuk-Bronikoswska, M. Krajewska, I. Pfis-Kabulska, *Polyhedron* 1998, **18**, 561.

[89] D.K. Rittenberg, L. Baarrs-Hibbe, A. Böhm, J.S. Miller, *J. Mater. Chem*. 2000, **10**, 241

[90] G. Mbambisa, P. Tau, E. Antunes, T. Nyokong, *Polyhedron* 2007, **26**, 5355.

[91] M.J. Stillman, T. Nyokong, in: C.C. Leznoff, A.B.P. Lever (Eds.), *Phthalocyanines: Properties and Applications*, vol. 1, VCH, New York, 1989 (Chapter 3)

[92] A.B.P. Lever, J.P. Wilshire, S.K. Quan, *Inorg. Chem*. 1981, **20**, 761.

[93] P.C. Minor, A.B.P. Lever, *Inorg. Chem*. 1983, **22**, 826.

[94] N. Sehlotho, M. Durmuş, V. Ahsen, T. Nyokong, *Inorg. Chem. Comm***.** 2008, **11**, 479.

[95] B.O. Agboola, K.I. Ozoemena, T. Nyokong, *Electrochim. Acta* 2007, **52**, 2520

[96] M. Kandaz, A. Koca, *Polyhedron* 2009, **28**, 2933.

[97] Y. Orihashi, M. Nishikawa, H. Ohno, E. Tsuchida, H. Matsuda, H. Nakahashi, M. Kato, *Bull. Chem. Soc., Jpn*. 1987, **60**, 3731.

[98] L.A. Bottomley, C. Ercolani, J.N. Gorce, G. Pennesi, G. Rossi, *Inorg. Chem*. 1986, **25**, 2338

[99] K.M. Kadashi, L.A. Bottomley, J.S. Cheng, *J. Am. Chem. Soc*. 1978, **100**, 2731.

[100] A.B.P. Lever, J.P. Wilshire, *Inorg. Chem*. 1978, **17**, 1145.

[101] B.O. Agboola, T. Nyokong, *Anal. Chim. Acta* 2007, **587**, 116.

[102] N. Nombona, P. Tau, N. Sehlotho, T. Nyokong, *Electrochim. Acta* 2008, **53**, 3139.

[103] R.F. Lane, A.T. Hubbard, *J. Phys. Chem*. 1973, **77**, 1401.

[104] R.F. Lane, A.T. Hubbard, *J. Phys. Chem*. 1973, **77**, 1411.

[105] P.R. Moses, L. Wier, R.W. Murray, *Anal. Chem.* 1975, **47**, 1882.

[106] L.L. Miller, B.F. Watkins, J.R. Behling, E. Kariv, *J. Am. Chem. Soc.* 1975, **97**, 3549

[107] R.W. Murray, *Acc. Chem. Res*. 1980, **13**, 135.

[108] R.W. Murray in: *Electroanalytical Chemistry* (Ed.: A.J. Bard), Marcel Dekker, New York, 1980, Vol. 13.

[109] A.M. Titse, A.M. Timinov, G.A. Shagisultanova, *Coord. Chem. Rev*. 1993, **125**, 43.

[110] T. Osa in: *New Challenges in Organic Chemistry* (Ed.: T. Osa), Gordon and Breach Scientific Publishers, Amsterdam, 1998, pp. 183-219.

[111] R.W. Murray, (Eds.), Molecular design of electrode surface in: *Techniques of Chemistry*, Wiley, New York, 1992, Vol. 22.

[112] D. Xie, Y. Jiang, J. Jiang, Z. Wu, Y. Li, *Sensor Actuator B: Chem.* 2001, **77**, 260.

[113] M.A. Meineke, J.D. Gezelter, *J. Phys. Chem. B* 2001, **105**, 6515.

[114] P. Gomez-Romero, M. Lira-Cantru, *Adv. Mater*. 1997, **9**, 144.

[115] P. Gomez-Romero, M. Lira-Cantru, *Proc. Electrochem. Soc.* 1997, **96**, 158.

[116] A. Aurian, B. Blajeni, S.C. Holleck, *J. Appl. Electrochem.* 1989, **19**, 331.

[117] V.V. Guliants, M.A. Carreon, Y.S. Lin, *J. Member Sci.* 2004, **235**, 53.

[118] D. Belanger, G. Laperriere, L. Gravel, *J. Electrochem. Soc.* 1990, **137**, 365.

[119] F. Girard, S. Ye, G. Laperriere, *J. Electroanal. Chem.* 1992, **334**, 35.

[120] S. Ye, F. Girard, D. Belanger, *J. Phys. Chem.* 1993, **97**, 12373.

[121] H. Yoneyama, Y. Li, S. Kuwabata, *J. Electrochem. Soc.* 1992, **139**, 28.

[122] G. Bidan, M.-A Niel, *Synth. Met.* 1997, **85**, 1387.

[123] G. Bidan, E.M. Genies, M. Lapkowski, *J. Electroanal. Chem. Interfacial Electrochem.* 1988, **251**, 297.

[124] M. Lapkowski, G. Bidan, M. Fournier, *Synth. Met.* 1991, **41**, 411

[125] M. Hasik, A. Pron, I. Kulszewicz-Bajer, *Synth. Met*. 1993, **55**, 972.

[126] G. Bidan, E.M. Genies, M. Lapkowski, *J. Chem. Soc., Chem. Commun*. 1988, 533.

[127] R. Koncki, O.S. Wolfbeis, *Anal. Chem.* 1994, **370**, 301.

[128] O. Ikeda, H. Yoneyama, *J. Electroanal. Chem. Interfacial Electrochem.* 1989, **265**, 323.

[129] R.A. Bull, F.R. Fan, A.J Bard, *J. Electrochem. Soc.* 1983, **130**, 1636.

[130] Y. Tse, P. Jadan, H. Lam, A.B.P. Lever, *Anal. Chem.* 1995, **67**, 981

[131] J. Obirai, T. Nyokong, *J. Electroanal. Chem.* 2004, **573**, 77

[132] A. Goux, F. Bedioui, L. Robbiola, M. Pontie, *Electroanalysis* 2003, **15**, 969

[133] E.E. Polymeropoulos, J. Sagiv, *J. Chem. Phys.* 1978, **69**, 1836

[134] J. Sagiv, *J. Am. Chem. Soc.* 1980, **2**, 102.

[135] J. Sagiv, *Isr. J. Chem.* 1979, **18**, 339

[136] K. Ozoemena, P. Westbroek, T. Nyokong, *Electrochem. Comm*. 2001, **3**, 529.

[137] B. Agboola, P. Westbroek, K.I. Ozoemena, T. Nyokong, *Electrochem Commun*. 2007, **9**, 310.

[138] T.R.E. Simpson, M.J. Cook, M.C. Petty, S.C. Thorpe, D.A. Russell, *Analyst* 1996, **121**, 1501

[139] S. Kurosawa, E. Tawara-Kondo, N. Kamo, *Anal. Chim. Acta* 1997, **337**, 1.

[140] M.J. Cook *Pure Appl. Chem*. 1999, **71**, 2145.

[141] J. Obirai, N. Pereira-Rodrigues, F. Bedioui, T. Nyokong *J. Porphyrins Phthalocyanines* 2003, **7**, 508.

[142]K.L. Brown, J. Shaw, M. Ambrose, H.A. Mottola, *Microchem. J.* 2002, **72**, 285.

[143] N. Tromach, O. Hild, D. Schlettwein, D.Wöhrle, *J. Mat. Chem*. 2002, **12**, 879

[144] G. Kalyuzhny, A. Vaskevich, G. Ashkenasy, A. Shanzer, I. Rubinstein, *J. Phys. Chem. B* 2000, **104**, 8238.

[145] K. Ozoemena, T. Nyokong, P. Westbroek, *Electroanalysis* 2003, **15**, 1762.

[146] H.O. Finklea, S. Avery, M. Lynch, T. Furtsch, *Langmuir* 1987, **3**, 409.

[147] N. Sehlotho, T. Nyokong, S. Griveau, F. Bedioui, *Electroanalysis* 2007, **19**, 103.

[148] J. Barsoukov, R. Macdonald, Impedance Spectroscopy: Theory, Experiment, and Applications, second ed., John Wiley and Sons, Inc., Hoboken, New Jersey, 2005.

[149] D.A. Geraldo, C.A. Togo, J. Limson, T. Nyokong, *Electrochim. Acta* 2008, **53**, 8051.

[150] W.J. Albery, M.L. Hitchman, *Ring-Disc Electrodes*, Clarendon Press, Oxford, 1971

[151] W.J. Albery, S. Bruckenstein, *J. Electroanal. Chem*. 1983, **144**, 105.

[152] V.G. Levich, *Physicochemical Hydrodynamics*, Prentice Hall, Englewood Cliffs, N.J., 1962, pp. 60-78.
[153] J. Koutecky, V.G. Levich, *Zh. Fiz. Khim*. 1956, **32**, 1565.

[154] K. Ozoemena, T. Nyokong, *J. Chem. Soc., Dalton Trans.* 2002, 1806

[155] S. Iijima, *Nature*, 1991, **56**, 354.

[156] J.M. Carlsson, *Nature Materials*, 2007, **6**, 801.

[157] J.C. Meyer, A.K. Geim, M.I. Katsnelson, K.S. Novoselov, T.J. Booth, S. Roth, A. K. Geim, *Nature*, 2007, **446**, 60.

[158] French National Centre for Scientific Research (CNRS), http://www.cnrs.fr

[159] J. Liu, S. Fan, H. Dai, *MRS Bull*., 2004, **29**, 244.

[160] C. Journet, P. Bernier, *Appl. Phys. A*., 1998, **67**, 1.

[161] S. Niyogi, M.A. Hamon, H. Hu, B. Zhao, P. Bhowmik, R. Sen, M.E. Itkis, R.C. Haddon, *Acc. Chem. Res*., 2003, **35**, 1105.

[162] M.S. Dresselhaus, G. Dresselhaus, P. Eklund, *Science of Fullerenes and Carbon Nanotubes*, Academic Press, New York, 1996.

[163] R. Saito, M.S. Dresselhaus, G. Dresselhaus, *Physical Properties of Carbon Nanotubes*, Imperial College Press, London, 1998.

[164] H. Paloniemi, T. Aaritalo, T. Laiho, H. Liuke, N. Kocharova, K. Haapakka, F. Terzi, R. Seeber, J. Lukkari, *J. Phys. Chem. B*, 2005, **109**, 8634.

[165] H. Li, A. Adronov, *Carbon*, 2007, **45**, 984.

[166] S.J. Tans, A.R.M. Verschueren, C. Dekker, *Nature*, 1998, **393**, 49.

[167] Y. Nakayama, S. Akita, *Synth. Met*., 2001, **117**, 207.

[168] R.H. Baughman, A.A. Zakhidov, W.A. de Heer, *Science*, 2002, 297, 787.

[169] H. Dai, J.H. Hafner, A.G. Rinzler, D.T. Colbert, R.E. Smalley, *Nature*, 1996, **384**, 147.

[170] J. Kong, N.R. Franklin, C. Zhou, M.G. Chapline, S. Peng, K. Cho, H. Dai, *Science*, 2000, **287**, 622.

[171] C.S. Li, D.Z. Wang, T.X. Liang, X.F. Wang, L. Ji, *Mater. Lett*., 2004, **58**, 3774.

[172] B. Zhang, J. Liang, C.L. Xu, B.Q. Wei, D.B. Ruan, D.H. Wu, *Mater. Lett*., 2001, **51**, 539.

[173] H.J. Ahn, J.I. Sohn, Y.S. Kim, H.S. Shim, W.B. Kim, T.Y. Seong, *Electrochem. Commun*, 2006, **8**, 513.

[174] C.E. Banks, R.R. Moore, T.J. Davies, R.G. Compton, *Chem. Commun*, 2004, 1804.

[175] L. Sheeney-Haj-Ichia, B. Basnar, I. Willner, *Angew. Chem. Int. (Eds.)*, 2005, **44**, 78.

[176] J.J. Gooding, *Electrochim. Acta*, 2005, **50**, 3049.

[177] J.J. Gooding, R. Wibowo, J. Liu, W. Yang, D. Losic, S. Orbions, F.J. Meams, J.G. Shapter, D.B. Hibbert, *J. Am. Chem. Soc*., 2003, **125**, 9006.

[178] F. Patolsky, Y. Weizmann, I. Willner, *Angew. Chem. Int. (Eds.)*, 2004, **43**, 2113.

[179] S.M. Lee, K.S. Park, Y.C. Choi, Y.S. Park, J.M. Bok, D.J. Bae, K.S. Nahm, Y.G. Choi, S.C. Yu, N-G. Kim, T. Frauenheim, Y.H. Lee, *Synth. Met.*, 2000, **113**, 209.

[180] P-X. Hou, S-T. Xu, Z. Ying, Q-H. Yang, C. Liu, H-M. Cheng, *Carbon*, 2003, **41**, 2471.

[181] H-M. Cheng, Q-H. Yang, C. Liu, *Carbon*, 2001, **39**, 1447.

[182] M. Carmo, V.A. Paganin, J.M. Rosolenb, E.R. Gonzalez, *J. Power Sources*, 2005, **142**, 169.

[183] R.P. Raffaelle, B.J. Landi, J. D. Harris, S.G. Bailey, A.F. Hepp, *Mater. Sci. Eng. B*, 2005, **116**, 233.

[184] J. Zhang, J.K. Lee, Y. Wu, R.W. Murray, *Nano Lett.*, 2003, **3**, 403.

[185] K.I. Ozoemena, T. Nyokong, D. Nkosi, I. Chambrier, M.J. Cook, *Electrochim. Acta*, 2007, **52**, 4132.

[186] H. Li, B. Zhou, Y. Lin, L. Gu, W. Wang, K.A.S. Fernando, S. Kumar, L.F. Allard, Y.P. Sun, *J. Am. Chem. Soc.*, 2004, **126**, 1014.

[187] M. Hazani, R. Naaman, F. Hennrich, M.M. Kappes, *Nano Lett.*, 2003, **3**, 153

[188] S. Li, P. He, J. Dong, Z. Guo, L. Dai, *J. Am. Chem. Soc.*, 2005,**127**, 14.

[189] Y. Lin, L.F. Allard, Y.P. Sun, *J. Phys. Chem. B*, 2004, **108**, 3760.

[190] V. Zorbas, A.L. Smith, H. Xie, A. Ortiz-Acevedo, A.B. Dalton, G.R. Dieckmann, R.K. Draper, R.H. Baughman, I.H. Musselman, *J. Am. Chem. Soc.*, 2005, **127**, 12323.

[191] W. Zhao, C. Song, P.E. Pehrsson, *J. Am. Chem. Soc.*, 2002, **124**, 760.

[192] D. Tasis, N. Tagmatarchis, A. Bianco, M. Prato, *Chem. Rev.*, 2006, **106**, 1105.

[193] D. Reznik, C.H. Olk, D.A. Neumann, J.R.D. Copley, *Phys. Rev. B* 1995, **52**, 116.

[194] Y. Zhang, X. Sun, L. Pan, H. Li, Z. Sun, C. Sun, B.K. Tay, *J. Alloys Compd*. 2009, **480**, 17.

[195] C. Bower, A. Kleinhammes, Y. Wu, O. Zhou, *Chem. Phys. Lett*. 1998, **288**, 481.

[196] The United Nations Committee of Experts on the Transport of Dangerous Goods and on Globally Harmonized System of Classification and Labeling of Chemicals (UNCETDG/GHS), December, 2002.

[197] R.J. Argauer, R.T. Brown, *J. Agric. Food Chem*., 1994, **42**, 1920.

[198] R.F. Cook, R.P. Stanovick, C.C. Cassil, *J. Agric. Food Chem*., 1969, **17**, 277

[199] T.N. Rao, B.H. Loo, B.V. Sarada, C. Terashima, A. Fujishima, *Anal. Chem*., 2002, **74**, 1578

[200] W. Hang, S. Jian-Jun, W. Yan-Min, L. Xiao and C. Guo-Na, *Analyst*, 2008, **133**, 1619.

[201] K. Kadokami, M. Morimoto, K. Haraguchi, M. Koja, R. Shinohara, *Anal. Sci*. 1991, **7**, 247.

[202] G. Durand, V. Bouvot and D. Barcelo, *J. Chromatogr*. 1992, **607**, 319.

[203] S. Chiron, E. Martinez and D. Barcelo, *J. Chromatogr*. 1994, **A 665**, 283.

[204] R.B. Geerdink, A.M.B.C. Graumans, J. Viveen, *J. Chromatogr*. 1991, **547**, 478.

[205] E.M. Garrido, L.C. Lima, C.M. Delerue-Matos, A.M. Oliveira Brett, *Talanta*, 1998, **46** 1131.

[206] S.F. Ruiz, M.L. Henrique, V.M. Pedro, *Sensor Letters*, 2006, **4**, 319.

[207] M.P. Somashekarappa, S. Sampath, *Chem. Comm*. 2002, 1262.

[208] K.I. Ozoemena, T. Nyokong, *Talanta* 2005, **67**, 162.

[209] J. Obirai, F. Bedioui, T. Nyokong, *J. Electroanal. Chem*. 2005, **576**, 323.

[210] J. Xue, X. Ying, J. Chen, Y. Xian, L. Jin, J. Jin, *Anal. Chem*. 2000, **72**, 5313.

[211] S. Griveau, M. Gulppi, J. Pavez, J.H. Zagal, F. Bedioui, *Electroanalysis* 2003, **15**, 779

[212] B.N. Acher, G.M. Fohlen, J.A. Parker, J. Keshavayya, *Polyhedron* 1967, **6**, 1463.

[213] Z.A. Bayur, *Dyes and Pigm.* 2005, **65**, 235

[214] N.B. McKeown in: Kadish KM, Smith KM, Guilard R (eds) *Porphyrin Handbook, Phthalocyanines: Synthesis*, Vol 15, Chpt. 98, 2003, Academic Press, New York.

[215] J. Liu, A.G. Rinzler, H. Dai, J.H. Hafner, R.K. Bradley, P.J. Boul, A. Lu, T. Iverson, K. Shelimov, C.B. Huffman, F. Rodriguez-Macias, T.Y-S. Shon, R. Lee, D.T. Colbert, R.E. Smalley, *Science* 1998, **280**, 1253.

[216] B.A. Boukamp**,** *Solid State Ionics* 1986, **20,** 31.

[217] I. Chambrier, M.J. Cook, P.T. Wood, *Chem Commun* 2000, 2133

[218] T. Muto, T. Temma, M. Kimura, K. Hanabusa, H. Shirai, *J. Org. Chem.* 2001, **66**, 6102.

[219] N. Kobayashi, O. Toshie, M. Sato, N. Shin-ichiro, *Inorg. Chem*. 1993, **32**, 1803.

[220] N. Kobayashi, T. Ishizaki, K. Ishii, H. Konami, *J. Am. Chem. Soc*. 1999, **121**, 9096.

[221] A. Hadasch, A. Sorokin, A. Rabion and B. Meunier, *New J. Chem*. 1998, **22**, 45.

[222] N. Grootboom, T. Nyokong, *J. Mol. Cat. A: Chem*. 2002, **179**, 113.

[223] A.R. Ozkaya, A.G. Gurek, A. Gul A, O. Bekaroglu, *Polyhedron* 1997, **16**, 1877.

[224] M.J. Stillman in: C.C. Leznoff, A.B.P. Lever (Eds.), *Phthalocyanines: Properties and Applications*, vol. 3, VCH Publishers, New York, 1993 (Chapter 5).

[225] K. Takahashi, M. Kawashima, Y. Tomita and M. Itoh, *Inorg. Chim. Acta*. 1995, **232**, 69.

[226] A.B.P. Lever, E.R. Milaeva, G. Speier in *Phthalocyanines: Properties and Applications*, C.C. Leznoff, A.B.P. Lever (eds), VCH Publishers, New York Vol. 3 (1993).

[227] J. Mack and M.J. Stillman, *J. Porphyrins Phthalocyanines* 2001, **5**, 67.

[228] K. Ban, K. Nishizawa, K. Ohta, H. Shirai, *J. Mater Chem.* 2000, **10**, 1083.

[229] K. Daniel, A. Volker, Patent cooperation treaty, PCT/EP/011145, 2006.

[230] M. Terrones, W.K. Hsu, A. Schwoerer, K. Prassides, H.W. Kroto, D.R.M. Walton, *Appl. Phys. A* 1998, **66**, 307.

[231] K. Nishiyama, S. Tahara, Y. Uchida, S. Tanoue, I. Taniguchi, *J. Electroanal. Chem*. 1999, **478**, 83.

[232] M.D. Porter, T.B. Bright, D.L. Allara, C.E.D Chidsey, *J. Am. Chem. Soc.* 1987, **109**, 3568.

[233] S. Griveau, J. Pavez, J.H. Zagal, F. Bedioui, *J. Electroanal. Chem.* 2001, **497**, 75.

[234] X. Wu, W. Zang, *J. Electroanal. Chem.* 1995, **383**, 1.

[235] X. Wu, W. Zang, H. Yu, *J. Electroanal. Chem.* 1995, **398**, 1.

[236] C.S. Hsu, F. Manfeld, *Corrosion* 2001, **57**, 747.

[237] J.E. Hutchison, T.A. Postlethwaite, R.W. Murray, *Langmuir* 1993, **9**, 3277.

[238] J. Zak, H. Yuan, M. Ho, L.K. Woo, M.D. Porter, *Langmuir* 1993, **9**, 2772.

[239] H.O. Finklea in: Bard AJ, Rubinstein I (Eds.) *Electroanalytical Chemistry*, Marcel Dekker, New York, vol. 19 (1996), p. 109.

[240] R.R. Durand, F.C. Anson, *J. Electroanal. Chem.* 1982, **134**, 273.

[241] J.H. Zagal, M.A. Guilppi, C. Depretz, D. Lelievre, *J. Porphyrins Phthalocyanines* 1999, **3**, 355

[242] N. Kobayashi, P. Janda, A.B.P. Lever, *Inorg. Chem.* 1992, **31**, 5172.

[243] D.A. Van Galen, M. Majda, *Anal Chem.* 1988, **60**, 1549.

[244] T.F. Otero, E.D. Larreta-Azelain, *Polymer* 1988, **29**, 1522.

[245] T. Nyokong in: *N_4-macrocyclic metal complexes: electrocatalysis, electrophotochemistry, and biomimetic electrocatalysis* (Eds.) J.H. Zagal, F. Bedioui, J-P. Dodelet, Springer, 2006, Chpt. 7.

[246] M.E. Sanchez Vergara, I.F. Islas Bernal, M. Rivera, A. Ortiz Rebollo, J.R. Alvarez Bada, *Thin Solid Films*, 2007, **515**, 5374.

[247] N. Al-Dahoudi, M.A. Aegerter, *Thin Solid Films* 2006, **502**, 193.

[248] A.J. Bard, L.R. Faulkner, *Electrochemical Methods: fundamentals and applications*, John Wiley & Sons, Inc., New York (2nd edition) (2001).

[249] M. Ebadi, *Electrochim. Acta* 2003, **48**, 4233.

[250] J.-M. Zen, A.S. Kumar, M.-R. Chang, *Electrochim. Acta* 2000, **45**, 1691.

[251] M.E.G. Lyons, C.A. Fitzerald, M.R. Smyth, *Analyst* 1994, **119**, 855.

[252] B. Wermeckers, F. Beck, *Electrochim. Acta* 1985, **30**, 1491.

[253] J.C. Miller, J.N. Miller, P.J. Worsfold, *Statistics for Analytical Chemists*, Horwood, Chichester, 1984.

[254] R.I. Stefan, J.F. Van Staden, H.Y. Abdoul-Enein, *Electrochemical Sensors in Bioanalysis*, Marcel Dekker, New York, 2001.

[255] A.J. Fry, M.A. Mitnick, *J. Am. Chem. Soc.* 1969, **91**, 6207.